

**TWO-PHASE FLOW IN HIGH-HEAT-FLUX MICRO-CHANNEL
HEAT SINK FOR REFRIGERATION COOLING APPLICATIONS**

(Contract No. N00014-05-1-0408)

by

Issam Mudawar

Jaeseon Lee

Myung Ki Sung

Boiling and Two-Phase Flow Laboratory
School of Mechanical Engineering
Purdue University
West Lafayette, Indiana 47907
Tel. (765) 494-5705

September 2008

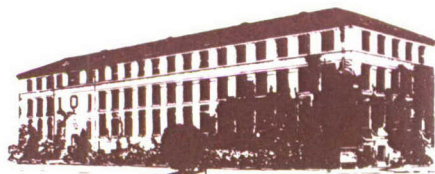
Final Report

Prepared for

Dr. Mark Spector
Office of Naval Research
Physical Science S&T Division, Code 331
800 N. Quincy St.
Arlington VA 22217-5660

Boiling and Two-Phase Flow Laboratory

**Boiling and
Two-Phase Flow
Laboratory**



School of Mechanical Engineering

**Purdue University
West Lafayette, Indiana 47907**



REPORT DOCUMENTATION PAGE				Form Approved OMB No. 0704-0188	
<p>The public reporting burden for this collection of information is estimated to average 1 hour per response, including the time for reviewing instructions, searching existing data sources, gathering and maintaining the data needed, and completing and reviewing the collection of information. Send comments regarding this burden estimate or any other aspect of this collection of information, including suggestions for reducing the burden, to Department of Defense, Washington Headquarters Services, Directorate for Information Operations and Reports (0704-0188), 1215 Jefferson Davis Highway, Suite 1204, Arlington, VA 22202-4302. Respondents should be aware that notwithstanding any other provision of law, no person shall be subject to any penalty for failing to comply with a collection of information if it does not display a currently valid OMB control number.</p> <p>PLEASE DO NOT RETURN YOUR FORM TO THE ABOVE ADDRESS.</p>					
1. REPORT DATE (DD-MM-YYYY) 09-11-2008	2. REPORT TYPE Final	3. DATES COVERED (From - To) 04-01-20074 to 09-30-2008			
4. TITLE AND SUBTITLE Two-Phase Flow in High-Heat-Flux Micro-Channel Heat Sink for Refrigeration Cooling Applications <i>Part II</i>			5a. CONTRACT NUMBER NA		
			5b. GRANT NUMBER N00014-04-1-0408		
6. AUTHOR(S) Mudawar, Issam Lee, Jaeseon Sung, Myung Ki			5c. PROGRAM ELEMENT NUMBER NA		
			5d. PROJECT NUMBER NA		
			5e. TASK NUMBER NA		
7. PERFORMING ORGANIZATION NAME(S) AND ADDRESS(ES) Purdue University Boiling and Two-Phase Flow Laboratory Mechanical Engineering Building, 585 Purdue Mall West Lafayette, IN 47907			5f. WORK UNIT NUMBER NA		
			8. PERFORMING ORGANIZATION REPORT NUMBER N00014-04-1-0408-FR		
9. SPONSORING/MONITORING AGENCY NAME(S) AND ADDRESS(ES) Office of Naval Research ATTN: Mark Spector, ONR Code 331 One Liberty Center 875 N. Randolph Street Arlington, VA 22203-1995			10. SPONSOR/MONITOR'S ACRONYM(S) ONR		
			11. SPONSOR/MONITOR'S REPORT NUMBER(S) NA		
12. DISTRIBUTION/AVAILABILITY STATEMENT Unlimited					
13. SUPPLEMENTARY NOTES NA					
14. ABSTRACT <p>This report examines the pressure drop and heat transfer characteristics of two-phase micro-channel heat sinks. New models and correlations are proposed for both saturated and subcooled boiling conditions. These tools are shown to provide accurate predictions of pressure drop, two-phase heat transfer coefficient and critical heat flux. Also discussed in this report is a new hybrid cooling system that combines the cooling attributes of micro-channel flow and jet impingement. It is shown this system is very effective at meeting the cooling demands of high-flux defense electronics, including the ability to dissipate in excess of 1000 W/cm². Detailed predictive tools are provided to tackle the design of a hybrid cooling module.</p>					
15. SUBJECT TERMS phase change, electronics cooling, micro-channel,jet impingement, hybrid cooling, refrigeration cooling					
16. SECURITY CLASSIFICATION OF: a. REPORT U b. ABSTRACT U c. THIS PAGE U		17. LIMITATION OF ABSTRACT UU	18. NUMBER OF PAGES 465	19a. NAME OF RESPONSIBLE PERSON Mudawar, Issam 19b. TELEPHONE NUMBER (Include area code) 765-494-5705	

PART II

LOW TEMPERATURE HYBRID MICRO-CHANNEL/MICRO-JET IMPINGEMENT

COOLING

(Contract No. N00014-05-1-0408)

by

Prof. Issam Mudawar

Myung Ki Sung

Boiling and Two-Phase Flow Laboratory

School of Mechanical Engineering

Purdue University

West Lafayette, Indiana 47907

Tel. (765) 494-5705

September 2008

Final Report

Prepared for

Dr. Mark Spector

Office of Naval Research

Physical Science S&T Division, Code 331

800 N. Quincy St.

Arlington VA 22217-5660

20080918325

TABLE OF CONTENTS

	Page
LIST OF TABLES	v
LIST OF FIGURES.....	vi
NOMENCLATURE	xi
ABSTRACT.....	xvi
CHAPTER 1. INTRODUCTION.....	1
1.1. Selection of Cooling Geometry and Single-Phase Heat Transfer Characteristics	1
1.2. Effect of Circular-Jet Patterns on Single-Phase Heat Transfer Characteristics	3
1.3. Two-Phase Heat Transfer Characteristics.....	4
1.4. Critical Heat Flux	5
1.5. Objectives of Present Study	8
CHAPTER 2. EXPERIMENTAL METHODS.....	10
2.1. Flow Loop	10
2.2. Test Module.....	10
2.2.1. Micro-Jet Plates	14
2.3. Operating Procedure and Measurements	15
CHAPTER 3. NUMERICAL METHODS	17
3.1. Standard $k-\epsilon$ Turbulent Model.....	17
3.2. Determination of Extent of Laminar Zone.....	22
CHAPTER 4. SINGLE-PHASE NUMERICAL RESULTS.....	26
4.1. Effects of Micro-Channel Geometry	26
4.1.1. Circular Jets	26
4.1.2. Slot Jets	31
4.2. Comparison of Numerical Predictions with Experimental Results	33

	Page
4.3. Parametric Trends of Cooling Characteristics.....	36
4.3.1. Circular Jets	36
4.3.2. Slot Jets	42
4.4. Different Circular-Jet-Pattern Configurations.....	45
4.4.1. Determination of Jet Velocities	45
4.4.2. Validation of Numerical Predictions	49
4.4.3. Predicted Trends of Cooling Performance	49
CHAPTER 5. SINGLE-PHASE EXPERIMENTAL RESULTS	57
5.1. Overall Cooling Performance.....	57
5.1.1. Circular Jets	57
5.1.2. Slot Jets	57
5.1.3. Different Circular-Jet-Pattern Configurations	60
5.2. Correlation of Single-Phase Heat Transfer Data	60
5.2.1. Circular Jets	60
5.2.2. Different Circular-Jet-Pattern Configurations	67
5.2.3. Slot Jets	69
5.3. Comparison of Single-Phase Performance of Two Hybrid Cooling Schemes.....	73
CHAPTER 6. TWO-PHASE RESULTS.....	77
6.1. Boiling Curve Trends.....	77
6.1.1. Circular Jets	77
6.1.2. Slot Jets	81
6.1.3. Different Circular-Jet-Pattern Configurations	81
6.2. Flow Visualization Results for Slot Jets	89
6.3. Comparison of Pressure Drop and Two-Phase Heat Trasnfer Coefficients for Different Circular-Jet Patterns.....	89
6.4. Subcooled Nucleated Boiling Region	94
6.5. Comparison of Two-Phase Performance of Two Hybrid Cooling Schemes	100
6.6. Critical Heat Flux.....	100
6.6.1. Developing Homogeneous Layer Model	103
6.6.2. CHF Prediction Procedure.....	109
CHAPTER 7. CONCLUSIONS.....	113
7.1. Selection of Cooling Geometry and Single-Phase Heat Transfer Characteristics	113
7.2. Effect of Circular-Jet Patterns on Single-Phase Heat Transfer Characteristics	114
7.3. Two-Phase Heat Transfer Characteristics.....	115
7.4. Effect of Circular-Jet Patterns on Two-Phase Heat Transfer Characteristics	116
7.5. Critical Heat Flux	117

	Page
LIST OF REFERENCES	119
APPENDICES	
Appendix A. HFE 7100 Properties.....	125
Appendix B. Single-Phase and Two-Phase Data	128

LIST OF TABLES

Table	Page
2.1: Experimental operating conditions.....	16
3.1: Dimensions of unit cell for circular jets.....	17
3.2: Key dimensions of unit cell for slot jets.....	20
4.1: Dimensions tested in numerical parametric study for circular jets.....	26
4.2: Dimensions tested in numerical parametric study for slot jets.....	31
4.3: Experimental operating conditions	23
5.1: Operating conditions for two-phase experiment.....	40

Appendix Table

A.1: Saturated HFE 7100 property data.....	126
A.2: Liquid HFE 7100 property data.....	127
B.1: Single-phase and two-phase experimental data for slot jets.....	129
B.2: Single-phase and two-phase experimental data for equal-size-jet pattern.	138
B.3: Single-phase and two-phase experimental data for decreasing-size-jet pattern..	141
B.4: Single-phase and two-phase experimental data for increasing-size-jet pattern...	144
B.5: Critical heat flux data for equal-size-jet pattern.	147

LIST OF FIGURES

Figure	Page
2.1: Schematic of flow loop	11
2.2: (a) Test module construction. (b) Cross-section of module assembly	12
2.3: Details of copper heating block	13
3.1: Schematic of unit cell illustrating (a) overall dimensions and thermocouple locations and (b) jet patterns consisting of single row of circular micro-jets and single micro-channel.	18
3.2: Schematic of unit cell consisting of single slot jet and single micro-channel.....	19
3.3: Fluid flow regimes for free circular impinging jet with $Pr_f > 1$	24
4.1: Numerical predictions of the effects of micro-channel height on surface temperature for jet velocities of (a) $U_{jet} = 1$ m/s, (b) $U_{jet} = 5$ m/s, and (c) $U_{jet} = 10$ m/s.	27
4.2: Streamline plots for $H_{ch} = 1$ mm, $W_{ch} = 1$ mm and jet velocities of (a) $U_{jet} = 1$ m/s and (b) $U_{jet} = 5$ m/s.	28
4.3: Numerical predictions of the effects of micro-channel width on surface temperature for $U_{jet} = 5$ m/s and $H_{ch} = 3$ mm.....	29
4.4: Numerical predictions of the effects of (a) channel height and (b) jet width and channel width on centerline temperature distribution along the micro-channel. ..	32
4.5: Comparisons of numerical prediction along the thermocouple line with measured temperatures for the equal-size-circular jet configuration.....	34
4.6: Comparisons of numerical prediction along the thermocouple line with measured temperatures for the micro-slot-jet configuration.	35

Figure	Page
4.7: Numerical predictions of micro-channel bottom wall temperature distribution for (a) $q''_{eff} = 53.39 \text{ W/cm}^2$ and $U_{jet} = 0.90 \text{ m/s}$, and (b) $q''_{eff} = 162.15 \text{ W/cm}^2$ and $U_{jet} = 4.53 \text{ m/s}$	37
4.8: Numerical predictions of wall temperature, including sidewall region, at four axial locations for (a) $q''_{eff} = 53.39 \text{ W/cm}^2$ and $U_{jet} = 0.90 \text{ m/s}$, and (b) $q''_{eff} = 162.15 \text{ W/cm}^2$ and $U_{jet} = 4.53 \text{ m/s}$	38
4.9: Streamline plots for (a) $U_{jet} = 0.90 \text{ m/s}$ and (b) $U_{jet} = 4.53 \text{ m/s}$	40
4.10: Numerical predictions of micro-channel bottom wall heat flux distribution for (a) $q''_{eff} = 53.39 \text{ W/cm}^2$ and $U_{jet} = 0.90 \text{ m/s}$, and (b) $q''_{eff} = 162.15 \text{ W/cm}^2$ and $U_{jet} = 4.53 \text{ m/s}$	41
4.11: Numerical predictions of micro-channel bottom wall Nusselt number distribution for (a) $q''_{eff} = 53.39 \text{ W/cm}^2$ and $U_{jet} = 0.90 \text{ m/s}$, and (b) $q''_{eff} = 162.15 \text{ W/cm}^2$ and $U_{jet} = 4.53 \text{ m/s}$	43
4.12: Numerical predictions of micro-channel bottom wall temperature distribution including sidewall for (a) $Re_{jet} = 2892$ and $q''_{eff} = 20.58 \text{ W/cm}^2$, and (b) $Re_{jet} = 26764$ and $q''_{eff} = 76.37 \text{ W/cm}^2$	44
4.13: Numerical predictions of micro-channel bottom wall heat flux distribution for (a) $Re_{jet} = 2892$ and $q''_{eff} = 20.58 \text{ W/cm}^2$, and (b) $Re_{jet} = 26764$ and $q''_{eff} = 76.37 \text{ W/cm}^2$	46
4.14: Numerical predictions of micro-channel sidewall heat flux distribution for (a) $Re_{jet} = 2892$ and $q''_{eff} = 20.58 \text{ W/cm}^2$, and (b) $Re_{jet} = 26764$ and $q''_{eff} = 76.37 \text{ W/cm}^2$	47
4.15: Numerical predictions of micro-channel bottom wall Nusselt number distribution for (a) $Re_{jet} = 2892$ and $q''_{eff} = 20.58 \text{ W/cm}^2$, and (b) $Re_{jet} = 26764$ and $q''_{eff} = 76.37 \text{ W/cm}^2$	48
4.16: Comparison of numerical predictions of temperatures along thermocouple line and measured temperatures	50
4.17: Streamlines and wall temperature plots at $q''_{eff} = 36.0 \text{ W/cm}^2$, $\dot{m} = 11.1 \text{ g/s}$ for (a) decreasing jet size, (b) equal jet size, and (c) increasing jet size	51
4.18: Streamline and wall temperature plots at $q''_{eff} = 67.6 \text{ W/cm}^2$, $\dot{m} = 33.6 \text{ g/s}$ or (d) decreasing jet size, (e) equal jet size, and (f) increasing jet size.....	52

Figure	Page
4.19: Streamlines and wall temperature plots at $q''_{eff} = 121.5 \text{ W/cm}^2$, $\dot{m} = 55.9 \text{ g/s}$ for (h) decreasing jet size, (i) equal jet size, and (j) increasing jet size.	53
4.20: Variation of wall temperature along micro-channel for (a) $q''_{eff} = 36.0 \text{ W/cm}^2$, $\dot{m} = 11.1 \text{ g/s}$, (b) $q''_{eff} = 67.6 \text{ W/cm}^2$, $\dot{m} = 33.6 \text{ g/s}$, and (c) $q''_{eff} = 121.5 \text{ W/cm}^2$, $\dot{m} = 55.9 \text{ g/s}$	56
5.1: Thermocouple readings in copper heating block versus jet Reynolds number for different heat fluxes and inlet temperatures for circular jets.	58
5.2: Thermocouple readings in copper heating block versus jet Reynolds number for different heat fluxes and inlet temperatures for slot jets.	59
5.3: Variation of heat transfer coefficient with mean jet Reynolds number for different jet patterns.	61
5.4: Schematic of superpositioning technique for correlating single-phase heat transfer data.	65
5.5: Comparison of predictions of single-phase heat transfer correlation and experimental data for equal-size-circular jet pattern.	66
5.6: Comparison of predictions of single-phase heat transfer correlation and experimental data for different circular-jet-pattern configurations.	70
5.7: Schematic of superpositioning technique for correlating single-phase heat transfer for slot jets.	72
5.8: Comparison of predictions of single-phase heat transfer coefficient correlations with slot jet HFE-7100 data.	74
5.9: Numerical predictions of micro-channel sidewall temperature distribution for (a) circular jets at $q''_{eff} = 162.15 \text{ W/cm}^2$ and $Q = 3.71 \times 10^{-5} \text{ m}^3/\text{s}$, and (b) slot jet at $q''_{eff} = 76.37 \text{ W/cm}^2$ and $Q = 4.51 \times 10^{-5} \text{ m}^3/\text{s}$	75
5.10: Variation of heat transfer coefficient with mean jet Reynolds number for different jet patterns.	76
6.1: Boiling curves for equal-size-circular jet pattern with four axial wall locations at (a) $\Delta T_{sub} = 88.7 \text{ }^\circ\text{C}$ and $U_{jet} = 0.90 \text{ m/s}$, and (b) $\Delta T_{sub} = 48.2 \text{ }^\circ\text{C}$ and $U_{jet} = 0.91 \text{ m/s}$	79

Figure	Page
6.2: (a) Subcooling effects on boiling curve at $U_{jet} = 1.04$ m/s. (b) Flow rate effects on boiling curve at $T_{in} = -20$ °C.....	80
6.3: (a) Boiling curves measured at x_{tc1} , x_{tc2} , x_{tc3} and x_{tc4} for $U_{jet} = 0.87$ m/s at (a) $\Delta T_{sub} = 88.1$ °C and (b) $\Delta T_{sub} = 68.1$ °C.....	82
6.4: Subcooling effects on boiling curve at $U_{jet} = 0.86$ m/s. (b) Jet velocity effects on boiling curve at $\Delta T_{sub} = 107.8$ °C.....	83
6.5: Boiling curves corresponding to increasing and decreasing heat flux for decreasing-jet-size pattern.....	85
6.6: Effects of flow rate on boiling curve for patterns of (a) decreasing jet size, (b) equal jet size, and (c) increasing jet size.....	86
6.7: Effects of subcooling on boiling curve for patterns of (a) decreasing jet size, (b) equal jet size, and (c) increasing jet size.....	87
6.8: Flow visualization and flow patterns inside hybrid module for $U_{jet} = 0.44$ m/s and $\Delta T_{sub} = 0$ °C with (a) $q''_{eff} = 43$ W/cm ² and (b) $q''_{eff} = 63$ W/cm ²	90
6.9: (a) Variation of pressure drop with heat flux for different inlet temperatures for decreasing-jet-size pattern. (b) Variation of pressure drop with heat flux for different jet patterns.....	92
6.10: Schematic representation of vapor growth and variation of void fraction along micro-channel for (a) conventional micro-channel and (b) hybrid cooling configuration.....	93
6.11: Variation of micro-channel outlet temperature with heat flux for different jet patters at $Q = 2.33 \times 10^{-5}$ m ³ /s and $T_{in} = 0$ °C.....	94
6.12: (a) Variation of surface temperature with heat flux for tree jet patterns at $Q = 3.87 \times 10^{-5}$ m ³ /s and $T_{in} = -40$ °C. (b) Variation of two-phase heat transfer coefficient with wall superheat for three jet patterns at tow flow rate and $T_{in} = 0$ °C.	96
6.13: Comparison of predictions of two-phase heat transfer coefficient correlation with HFE 7100 data for different circular-jet-pattern configurations.....	98
6.14: Comparison of predictions of two-phase heat transfer coefficient correlation with HFE 7100 data for slot jets.	99

Figure	Page
6.15: Bubble growth and condensation inside hybrid module for (a) circular jets and (b) slot jet.....	101
6.16: Variation of CHF with jet velocities with different subcoolings.....	102
6.17: (a) Cross-sectional representation of Developing Homogeneous Layer Model (DHLM). (b) Mass conservation for liquid and homogeneous layer control volumes. (c) Energy conservation for homogeneous layer control volume. (d) Slide view representation of DHLM for hybrid cooling configuration.....	104
6.18: Variations of homogeneous layer thickness and liquid layer velocity along micro-channel for $T_{in} = -20^{\circ}\text{C}$ at (a) $U_{jet} = 3.2 \text{ m/s}$ and (b) $U_{jet} = 6.1 \text{ m/s}$	107
6.19: (a) Partitioning of one segment of the heated wall micro jet-impingement and micro-channel flow portions. (b) Comparison of CHF data and predictions based on CHF superpositioning scheme.	111

NOMENCLATURE

a	empirical constant
A_{ch}	portion of test surface area of unit cell dominated by channel flow
A_{jet}	portion of test surface area of unit cell dominated by jet impingement
A_H	flow area of homogeneous two-phase layer
A_t	top test surface area of copper heating block
A_{total}	surface area of unit cell
b	empirical constant
c	empirical constant
C_1, C_2, C_3	empirical constants
C_1, C_2, C_μ	turbulence model constants
c_p	specific heat at constant pressure
C_{sub}	empirical constant
d_h	hydraulic diameter of channel
D	tube diameter
D_{jet}	diameter of micro-jet
g	gravitational acceleration
G	production of turbulent energy
G_H	mass velocity of homogeneous two-phase layer
H	height of unit cell
H_{ch}	height of micro-channel
H_{jet}	height (length) of micro-jet
H_{th}	height from thermocouple hole to unit cell bottom boundary
H_w	height from unit cell bottom boundary to test surface

h	height of wall jet
	convective heat transfer coefficient, $\dot{q}_{eff}^* / (T_s - T_{in})$
h_{fg}	latent heat of vaporization
\bar{h}_{ch1}	mean convective heat transfer coefficient for micro-channel region 1
\bar{h}_{ch2}	mean convective heat transfer coefficient for micro-channel region 2
\bar{h}_{jet}	mean convective heat transfer coefficient for jet-impingement region
\bar{h}_L	mean convective heat transfer coefficient inside micro-channel
\bar{h}_{ip}	mean two-phase heat transfer coefficient
Ja	Jacob number
k	thermal conductivity; turbulent kinetic energy
K_i	Interfacial mass flux
l	parameter used in determining laminar layer thickness
L	length of unit cell (also length of micro-channel)
$L_{jet,i}$	length of micro-channel associated with jet i
L_{jet}	pitch of circular jets
L_1, L_2, L_3, L_4	distance between thermocouple holes
\dot{m}	mass flow rate
m	empirical constant
n	outer normal coordinate at interface between solid and liquid
	empirical constant
N_i	number of jets of size i in single micro-channel
Nu	Nusselt number
N_{jet}	number of micro-jets per single micro-channel
\bar{Nu}_L	average Nusselt number
p_h	channel perimeter
P	pressure
Pr	Prandtl number
Pr_t	turbulent Prandtl number
P_W	electrical power supplied to copper heating block

q''	heat flux
\dot{q}_{eff}''	effective heat flux based on top test surface area of copper block, $\dot{q}_{eff}'' = \dot{P}_W / A_t$
\dot{q}_m''	critical heat flux based on top test surface area of copper block (based on P_W/A_t)
$\dot{q}_{m,p}''$	critical heat flux based on channel perimeter
Q	volumetric flow rate, $Q = \dot{m}/\rho_f$
r	radius measured from point of jet impact
r_j	radius of circular jet
r_s	radius extent of stagnation zone
r_b	radial location at boundary layer reaches film thickness
r_t	critical radius for onset of turbulence zone
Re_{jet}	jet Reynolds number, $U_{jet} D_{jet} / \nu_f$
$Re_{jet,m}$	jet Reynolds number based on mean velocity of all jets in a given jet pattern
T	temperature
T_{in}	jet inlet temperature
T_{tci}	temperature measured by thermocouple tci ($i = 1$ to 4)
\bar{T}_s	mean wall temperature
ΔT_{sat}	superheat, $T_s - T_{sat}$
ΔT_{sub}	subcooling, $T_{sat} - T_f$
u	velocity component in x direction
U	characteristic velocity of flow boiling system
U_i	Cartesian components of velocity
U_{jet}	jet inlet velocity, $U_{jet} = Q / (N_{jet} A_{jet})$
v	velocity component in y direction
w	velocity component in z direction
W	width of unit cell
W_{ch}	width of micro-channel

W_{jet}	slot jet width
W_w	half-width of copper wall separating micro-channels
x	Cartesian coordinate
x'	apparent quality
y	Cartesian coordinate
z	Cartesian coordinate
Z	dimensionless stream-wise coordinate

Greek symbols

α	void fraction
δ	hydrodynamic boundary layer thickness, thickness of homogeneous two-phase layer
δ_{th}	thermal boundary layer thickness
ε	dissipation rate of turbulent kinetic energy
ϕ	fluid phase (vapor or liquid)
μ	dynamic viscosity
μ_t	eddy viscosity
ν	kinematic viscosity
ρ	density
σ_ε	empirical constant in k and ε transport equations
σ_k	empirical constant in k and ε transport equations

Subscripts

bd	bubble departure
ch	channel
$corr$	correlated
exp	experimental
f	fluid
g	vapor
H	homogeneous layer

<i>in</i>	inlet
<i>m</i>	maximum (CHF)
<i>out</i>	outlet
<i>pred</i>	predicted
<i>s</i>	test surface; solid
<i>sat</i>	saturation
<i>sub</i>	subcooling
<i>t</i>	turbulent
<i>tci</i>	thermocouple ($i = 1$ to 4)
<i>th</i>	thermocouple reading
<i>w</i>	channel sidewall
Γ	interface between solid and liquid.

ABSTRACT

This research proposes a new hybrid cooling scheme for high-flux thermal management of electronic and power devices. This scheme combines the cooling benefits of micro-channel flow and micro-jet impingement with those of indirect refrigeration cooling. Experiments were performed to assess single-phase cooling performance using HFE 7100 as a working fluid. Excellent numerical predictions of this performance was achieved using the standard k - ε model. The proposed cooling scheme is shown to involve complex interactions of impinging jets with micro-channel flow. Increasing jet velocity allows jets to penetrate the micro-channel flow toward the surface, especially in shallow micro-channels, greatly decreasing wall temperature. In addition to the numerical predictions, a superpositioning technique is introduced that partitions the heat transfer surface into zones that are each dominated by a different heat transfer mechanism, and assigning a different heat transfer coefficient value to each zone. This study also examined the two-phase cooling performance of the hybrid cooling scheme. Vapor layer development along the micro-channel is shown to be fundamentally different from that encountered in conventional micro-channels. In the hybrid scheme, subcooled jet fluid produces repeated regions of bubble growth followed by collapse, rather than the continuous growth common to conventional micro-channel flow. By reducing void fraction along the micro-channel, the hybrid scheme contributes greater wall temperature uniformity. Increasing subcooling and/or flow rate delay the onset of boiling to higher heat fluxes and higher wall temperatures, but also increase critical heat flux considerably. By dividing the test surface into a portion that is dominated by jet impingement and another by micro-channel flow, and applying the appropriate CHF correlation for each portion, the CHF data for this hybrid cooling configuration is predicted with a mean absolute error of 15.2%. This study also explores the single-phase and two-phase cooling

performance of a hybrid cooling module in which a series of micro-jets deposit coolant into each channel of a micro-channel heat sink. This creates symmetrical flow in each micro-channel, and the coolant is expelled through both ends of the micro-channel. Three micro-jet patterns are examined, decreasing-jet-size (relative to center of channel), equal-jet-size and increasing-jet-size.

CHAPTER 1. INTRODUCTION

1.1. Selection of Cooling Geometry and Single-Phase Heat Transfer Characteristics

Spurred by micro-miniaturization of electronic components and greatly increased component and circuit density in electronic and power devices, heat dissipation has become a primary concern in the design of such devices. High performance cooling schemes are therefore becoming increasingly important to the development of these devices.

To combat these cooling challenges, a myriad of liquid cooling schemes have been developed and tested, mostly since the early 1980s. Of those, jet impingement and micro-channel heat sinks have emerged as the two most powerful thermal solutions for such next generation devices as microprocessors, laser diodes, radars and x-ray anodes (Mudawar, 2001).

Jet impingement cooling has been investigated both experimentally (Martin, 1977; Jiji and Dagan, 1987; Wadsworth and Mudawar, 1990; Estes and Mudawar, 1995) and numerically (Craft *et al.*, 1993; Park *et al.*, 2003; Baydar and Ozmen, 2005). These studies demonstrated the effectiveness of jet impingement at maintaining very low thermal resistances, especially in the jet's stagnation zone. A key drawback in using a single jet to cool the surface of an electronic device is large variation of surface temperature caused by a sharp reduction in the heat transfer coefficient away from the stagnation zone. Multiple jets are often used to attenuate those variations by creating multiple, closely spaced stagnation zones. Here too, problems arise due to flow blockage between closely spaced jets especially for jets that are situated towards the center of the device surface. Blockage for the central jets can also greatly complicate coolant distribution and exit of the spent fluid (Jiji and Dagan, 1987). Clearly, better means are

needed to capitalize upon the merits of multiple jet impingement while facilitating a more advantageous flow distribution inside of, and exit from, a cooling module.

Micro-channel heat sinks have been studied quite extensively for chip cooling applications. In an early highly cited study, Tuckerman and Pease (1981) demonstrated heat removal rates up to 790 W/cm^2 using water as working fluid. A key advantage of micro-channel heat sinks is their ability to achieve high heat transfer coefficients using coolant flow rates that are far smaller than those required with jet impingement. However, this advantage is realized with a very large temperature rise along the direction of fluid flow as well as large pressure drop, both of which are very undesirable in electronics cooling. In addition to experimental work, several numerical studies have been published on the fluid flow and heat transfer characteristics of micro-channel heat sinks (Kim and Kim, 1999; Fedorov and Viskanta, 2000; Qu and Mudawar, 2002). Qu and Mudawar (2002) demonstrated that the conventional Navier-Stokes and energy equations provide accurate prediction of a heat sink's heat transfer characteristics.

Clearly, both jet-impingement and micro-channel heat sinks can dissipate the high heat fluxes anticipated in future high performance devices. However, as explained above, both have drawbacks. In a previous study, the author of the present study proposed an effective means for capitalizing upon the merits of cooling schemes while alleviating some of their shortcomings (Sung and Mudawar, 2006). They showed how a "hybrid" cooling scheme consisting of a single slot jet that fed fluid into micro-channels can meet the challenges of future high performance electronic devices by facilitating the dissipation of high heat fluxes while also maintaining uniformity in the device surface temperature.

Regardless of which cooling scheme is used, dissipating very large heat fluxes can lead to unacceptably high device temperatures. All electronic devices have upper temperature limits that are dictated by material and performance constraints. One effective means for maintaining the device temperature below this limit during high-flux heat dissipation is to greatly decrease the coolant temperature. One example of a successful low temperature cooling system is the Kleemenko cooler, which provides 80 W of refrigeration for device cooling at -96 °C (Little, 2000). Aside from thermal

benefits, low temperatures provide significant enhancement in device functionality and reliability. Naeemi and Meindl (2004) demonstrated 4.3 times higher CMOS chip performance at -100°C than at 85°C. Schmidt and Notohardjono (2002) showed low temperature cooling offers orders of magnitude improvement in reliability. Overall, low temperatures facilitate faster switching times of semiconductor devices, increase circuit speed (due to lower electrical resistance of interconnecting materials), reduce thermally induced failures, and improve device performance by decreasing current leakage.

Refrigeration cooling can be implemented in one of two configurations, direct-refrigeration cooling and indirect-refrigeration cooling. Direct refrigeration involves inserting the cooling module as an evaporator in a vapor compression cycle, and using the refrigerant as coolant for the electronic device. Indirect-refrigeration cooling involves using a separate cooling loop in which a liquid coolant is used to remove the dissipated heat, which is rejected a separate vapor compression cycle. While the direct-refrigeration system is simpler and more compact, the indirect-refrigeration system provides greater flexibility in coolant selection, as well as allows the use of a non-pressurized cooling module.

1.2. Effect of Circular-Jet Patterns on Single-Phase Heat Transfer Characteristics

With the hybrid cooling scheme, the coolant is introduced gradually as a series of jets into each micro-channel of a micro-channel heat sink, and is expelled symmetrically through both ends of the micro-channel. Unlike conventional micro-channels, where the temperatures of both the coolant and the device to which the micro-channel heat sink is attached increase along the direction of fluid flow, the hybrid scheme supplies low temperature coolant at various locations along the micro-channel. This helps enhance temperature uniformity of both coolant and device. Another benefit of the hybrid scheme is a reduction in pressure drop compared to conventional micro-channel heat sinks. The hybrid cooling scheme is also superior to multi-jet-impingement modules in its ability to better manage the flow of spent coolant, prevent flow instabilities, and reduce flow blockage. In the examination of the effect of the jet pattern configurations, three different

jet patterns are compared. The first, decreasing-jet-size pattern, consists of jets that decrease in size symmetrically from the center of the micro-channel towards the two ends. The second, equal-jet-size pattern, consists of jets of equal size uniformly distributed along the micro-channel, like those used in the authors' earlier studies. The third, increasing-jet-size pattern, consists of jets that increase in size from the center of the micro-channel towards the two ends. The same total flow area of all jets is used for each jet pattern.

1.3. Two-Phase Heat Transfer Characteristics

Phase change greatly enhances the cooling performance of both micro-channel flow and jet impingement. This enhancement is of paramount importance for applications requiring the removal of large amounts of heat from very small device surface areas. With single-phase liquid cooling, increasing heat flux produces a proportional increase in device-to-fluid temperature difference. On the other hand, phase change produces only a mild increase in temperature difference corresponding to large increases in heat flux. This attractive cooling performance is realized within the nucleate boiling regime as long as the device heat flux is safely below critical heat flux (CHF).

Bowers and Mudawar (1994) provided the earliest framework for designing and modeling micro-channel heat sinks. Since their study, many other studies were published, which examined various performance and modeling aspects of two-phase micro-channel cooling. Qu and Mudawar (2003) conducted an experimental study of two-phase micro-channel heat sinks. The two types of hydrodynamic instabilities, severe pressure oscillation and mild parallel channel instability, were classified from the observations of the two-phase flow patterns inside the micro-channels. Lee and Mudawar (2005) carried out a two-phase experiment of the micro-channel heat sinks of R134a for refrigeration cooling applications. In their experimental study, the parallel channel instability could be reduced by increasing the amount of throttling upstream and a heat flux.

Researchers have also investigated two-phase boiling heat transfer characteristics of impinging jets. Wadsworth and Mudawar (1990) conducted single-phase and two-

phase experiments of a confined slot jet impingement of subcooled FC 72 on a 12.7 mm \times 12.7 mm heat source. The use of multiple jets enhanced cooling uniformity by creating several impingement zones. However, multiple jets promoted flow blockage between the jets and complicate fluid distribution downstream from the impinging zone. Wolf *et al.* (1996) presented two-phase heat transfer characteristics of a free slot jet impingement with inlet velocity of 2 to 5 m/s. They indicated the two-phase heat transfer coefficient was independent of jet velocities in fully developed boiling regime. Yang *et al.* (2001) showed bubble growth on the surface was affected by high subcooling due to the vapor condensation by experimental study with a free circular jet. Tay *et al.* (2002) indicated the non-uniform temperature distribution at jet impingement might cause additional thermal stress on the chip package.

1.4. Critical Heat Flux

Convective cooling with phase change is especially attractive for high performance devices because of the enormous heat transfer coefficients that can be realized. For a given coolant temperature, such high convection coefficients facilitate the removal of large heat fluxes while maintaining relatively small device surface temperatures. Another important advantage of phase change stems from the strong dependence of the heat transfer coefficient on heat flux. Large increases in the magnitude of the heat transfer coefficient with increasing heat flux implies the device will incur only modest temperature increases corresponding to fairly substantial increases in power dissipation. Minimizing the fluctuations in device temperature is paramount to both the reliability and the structural integrity of an electronic package.

However, phase change systems are not without drawbacks. They are typically more difficult to implement and more expensive than their single-phase counterparts. This is why they are favored only in situations where single-phase systems are deemed incapable of meeting the cooling requirements of a given device or system. Furthermore, the aforementioned advantages of convective phase change cooling are realized only within the nucleate boiling regime. This regime is maintained only as long as the coolant

can adequately replenish the surface region where the liquid is rapidly converted to vapor. Intense vapor effusion ultimately begins to restrict liquid access to this region, triggering appreciable deterioration in the cooling effectiveness. This process reaches its most dangerous state at the critical heat flux (CHF), where the bulk liquid is no longer able to replenish the surface region. Should the device heat flux exceed this limit, most of the heat dissipated in the device will be trapped in the device itself, causing a sudden unsteady escalation in the device temperature, which can lead to catastrophic failure. The ability to both predict and prevent CHF is therefore of paramount importance to the safety and integrity of any two-phase electronic cooling system.

Flow-boiling CHF can be classified as either saturated or subcooled, depending upon the bulk fluid temperature at the outlet (Qu and Mudawar, 2002). Saturated CHF is generally encountered with small flow rates, low inlet subcoolings and large length-to-diameter ratios; conditions where a significant fraction of the liquid flow is converted into a continuous vapor core. The remaining liquid is divided between a thin film that persists upon the heated wall and droplets that are entrained in the vapor core. Under these conditions, CHF takes the form of dryout of the liquid film. Micro-channel flows are especially prone to this type of CHF since they are used in applications demanding low flow rates and large length-to-diameter ratios (Qu and Mudawar, 2002).

Subcooled CHF is generally associated with high flow rates, small length-to-diameter ratios and high inlet subcoolings. Here, the bulk fluid maintains a predominantly liquid state at the outlet with a relatively small mass of vapor confined to the heated wall. Subcooling plays a vital role in all stages of the vaporization process. Subcooled liquid can absorb an appreciable fraction of the heat supplied at the wall before it is converted to vapor. This is why subcooled CHF can be far greater than saturated CHF for the same flow rate (Collier and Thome, 1994).

Decades of research have culminated in several useful correlations for CHF in both jet impingement and mini/micro-channel flows. Most of these correlations are based on Katto's formulation for saturated flow boiling CHF, which provides a generic dimensionless form adaptable to different flow configurations, coolants, flow rates, and pressures (Katto, 1983).

$$\frac{q_{m,sat}/\rho_g h_{fg}}{U} = f \left[\frac{\rho_g}{\rho_f}, \frac{\rho_f U^2 d}{\sigma}, \frac{g(\rho_f - \rho_g)d}{\rho_f U^2}, \frac{\mu_g}{\mu_f}, \frac{\rho_f U d}{\mu_f} \right], \quad (1.1)$$

where U and d are the characteristic velocity and characteristic length associated with the two-phase system. Additional dimensionless geometrical terms are also incorporated where the system involves more than one characteristic length. Observing a negligible dependence of experimental CHF data on viscosity or gravity, Katto suggested simplifying Eq. (1.1) to the following form:

$$\frac{q_{m,sat}/\rho_g h_{fg}}{U} = f \left[\frac{\rho_g}{\rho_f}, \frac{\rho_f U^2 d}{\sigma} \right]. \quad (1.2)$$

What is lacking in Eq. (1.2) is the strong dependence of CHF on subcooling. Mudawar *et al.* (1987) and Mudawar and Maddox (1989) modified an earlier theoretical CHF model that was developed by Haramura and Katto (1983) for both pool boiling and flow boiling. The modified model incorporated the effects of subcooling on both the hydrodynamic instability between the liquid and vapor phases, and the energy required to vaporize the near-wall liquid just prior to CHF. They showed the ratio of subcooled to saturated CHF can be expressed as

$$\frac{q_m}{q_{m,sat}} = \left[1 + \frac{c_{p,f} \Delta T_{sub}}{h_{fg}} \right]^n \left[1 + C_{sub} \frac{\rho_f c_{p,f} \Delta T_{sub}}{\rho_g h_{fg}} \right]^m, \quad (1.3)$$

where C_{sub} , m , and n are empirical constants.

As discussed below, two flow configurations that are important to the present study are slot jets and micro-channel flow. Following is a brief discussion of CHF findings concerning these specific flows.

The vast majority of jet impingement studies concern single and multiple free circular jets. In one of the most comprehensive studies, Monde (1987) identified different CHF regimes (V -, L -, I - and HP -regimes) for circular jets corresponding to different flow rates and different pressures. Monde and Mitsutake (1996) extended these findings to multiple circular jets. Johns and Mudawar (1996) showed the nozzle-to-surface distance has a negligible effect on CHF.

Mudawar and Wadsworth (1991) developed a module that provided uniform cooling to a 3×3 array of heat sources, each cooled by a confined rectangular jet of FC-72. They developed a correlation for CHF independent of nozzle-to-surface distance and which showed CHF is proportional to $U^{0.7}$. A key practical finding from their study is that CHF is a far stronger function of jet velocity than flow rate. In other words, CHF can be increased for a fixed flow rate simply by decreasing the jet width. Recently, Meyer *et al.* (1996) extended these findings to a heat source that is cooled by multiple slot jets.

Far fewer CHF studies are available for micro-channel heat sinks. Qu and Mudawar (2002) recently examined CHF for a heat sink containing parallel rectangular micro-channels. They showed the interaction between micro-channels is responsible for drastic differences in CHF compared to a single micro-channel.

1.5. Objectives of Present Study

A new hybrid cooling scheme is discussed that ensures excellent heat removal capability while maintaining fairly uniform surface temperature. This scheme involves feeding coolant from a series of circular micro-jets or slot jets to each micro-channel in a modified micro-channel heat sink module. Numerical simulation is first used to select key geometrical parameters, and the selected geometry is then examined experimentally. A super-positioning technique is used to develop a single-phase heat transfer correlation for this new cooling scheme.

The single-phase heat transfer characteristics and the flow field of the hybrid scheme are explored both numerically and experimentally. The laminar zone thickness of jet flow on the surface was calculated and imposed into the commercial FLUENT code (2005) to capture the heat transfer characteristics induced by strong jet interactions. The accuracy of the numerical results with laminar zones was first assessed against experimental data for HFE 7100. The single-phase heat transfer characteristics of micro-circular-jet configuration are then discussed at two different flow rates. An experimental investigation of the two-phase heat transfer characteristics is also conducted, and a new

empirical two-phase heat transfer correlation is developed for accurate predictions in the hybrid scheme.

The objective in examining these three configurations is to explore any potential cooling benefits that may be realized as a result of modulating the relative contributions of jet impingement and micro-channel flow in various regions of the micro-channel. To further enhance cooling performance, the three jet patterns are tested in an indirect-refrigeration cooling system. Two ultimate cooling objectives are to achieve, for a given flow rate, the highest possible heat transfer coefficient (*i.e.*, lowest wall temperature) and lowest wall temperature gradients. Numerical simulation is used to predict both the complex micro-jet/micro-jet flow interactions and wall temperature distribution. Also presented is a simple, yet very effective scheme for correlating single-phase heat transfer coefficient data. The performances of the three patterns are compared relative to the magnitude of two-phase heat-transfer coefficient, average surface temperature, pressure drop and CHF.

This study also explores the parametric trends of CHF for a new hybrid cooling scheme whose single-phase cooling performance was recently examined by the authors (2006). This scheme capitalizes upon the merits of both jet impingement and micro-channel flow. An area-averaged CHF correlation is constructed by applying CHF correlations for the portions of the heated surface that are influenced by jet impingement and channel flow.

CHAPTER 2. EXPERIMENTAL METHODS

2.1. Flow Loop

Figure 2.1 shows the flow loop that was configured to supply 3M Novec liquid HFE 7100 to a test module that housed the hybrid cooling configuration. This dielectric liquid was supplied from a reservoir with the aid of a centrifugal pump. The liquid first passed through a heat exchanger, where its temperature was greatly reduced by sensible heat exchange to refrigerant in a two-stage cascade chiller. The mass flow rate of HFE 7100 was measured by a Coriolis flow meter before the liquid entered the test module. The coolant flow was throttled using two control valves, one located upstream and the second downstream of the test module. The downstream valve also set the desired test module outlet pressure. After exiting the test module, the liquid returned to the reservoir to complete a full flow cycle.

2.2. Test Module

Figure 2.2 illustrates the layered construction and assembly of the test module. The micro-channels were machined into the top surface of a copper heating block. The test module also included a micro-jet plate, an upper plenum plate, a lower support plate, and 16 cartridge heaters. Figure 2.3 shows further details and key dimensions of the heating block. This block was tapered in two steps to improve temperature uniformity along its top $1.0 \times 2.0 \text{ cm}^2$ test surface. Machined into its top surface were five 1 mm wide and 3 mm deep slots. Six copper-constantan (type-T) thermocouples were inserted below the test surface to monitor its temperature. Sixteen holes were drilled into the

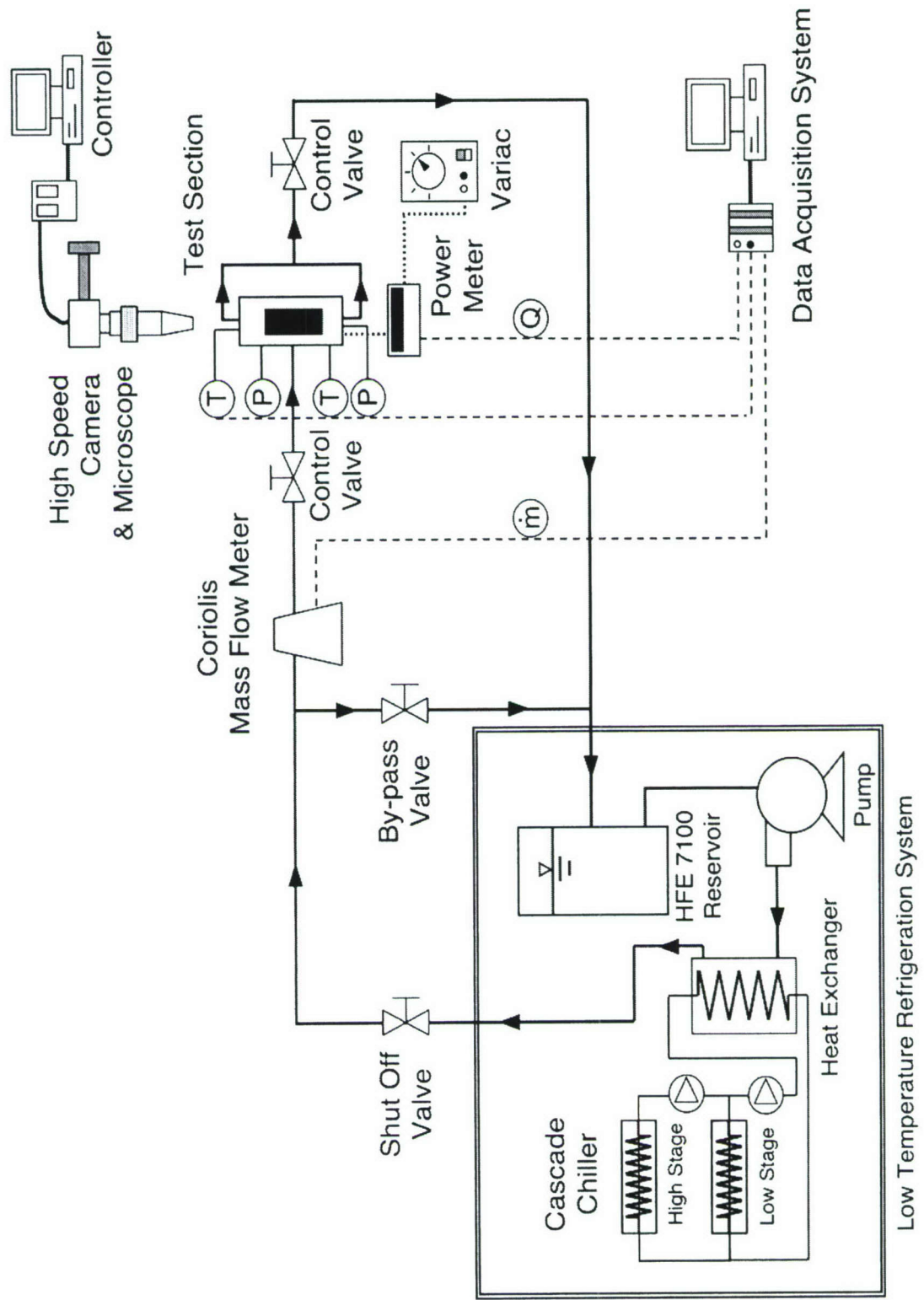


Figure 2.1 Schematic of flow loop.
Low Temperature Refrigeration System

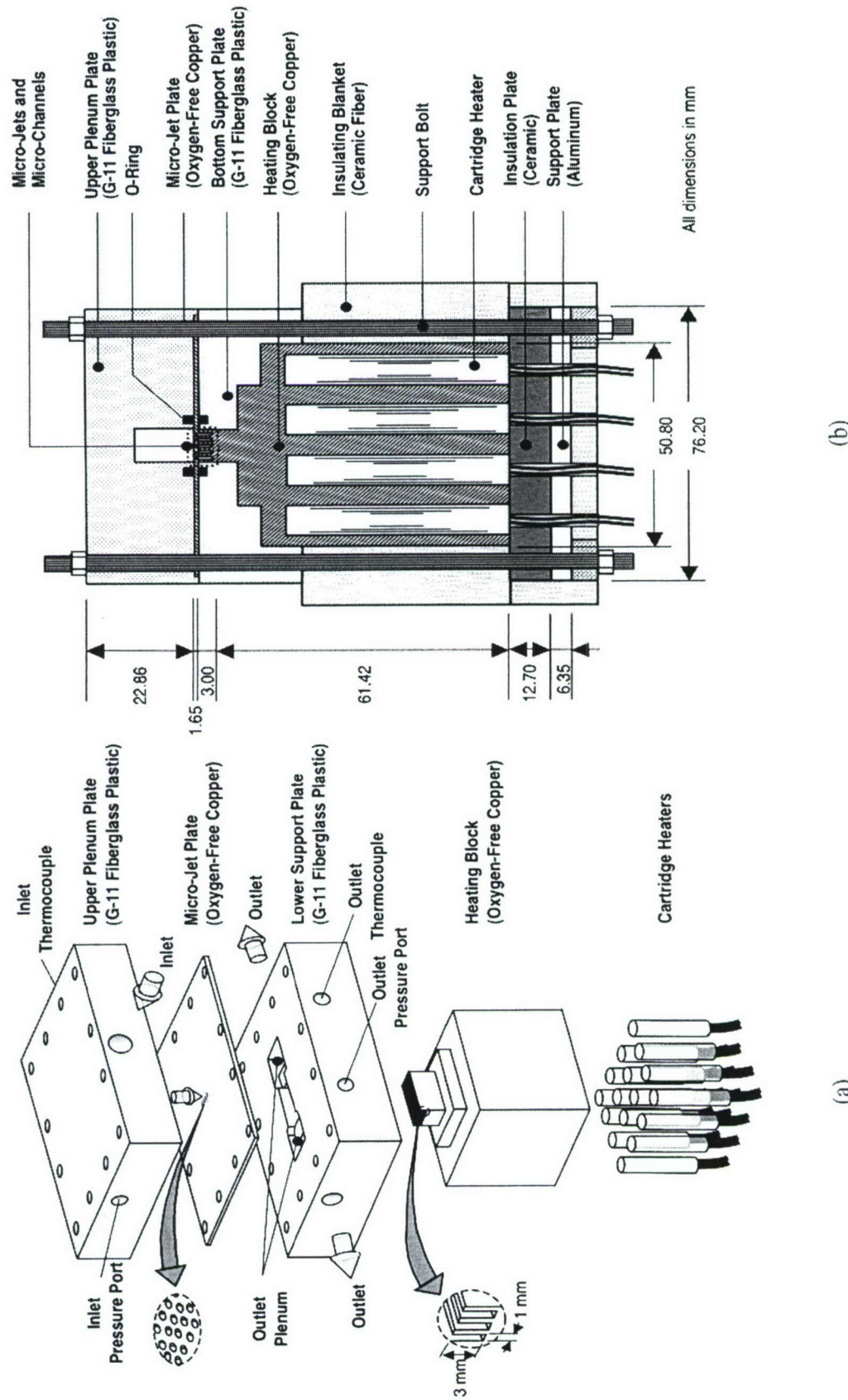


Figure 2.2 (a) Test module construction. (b) Cross-section of module assembly.

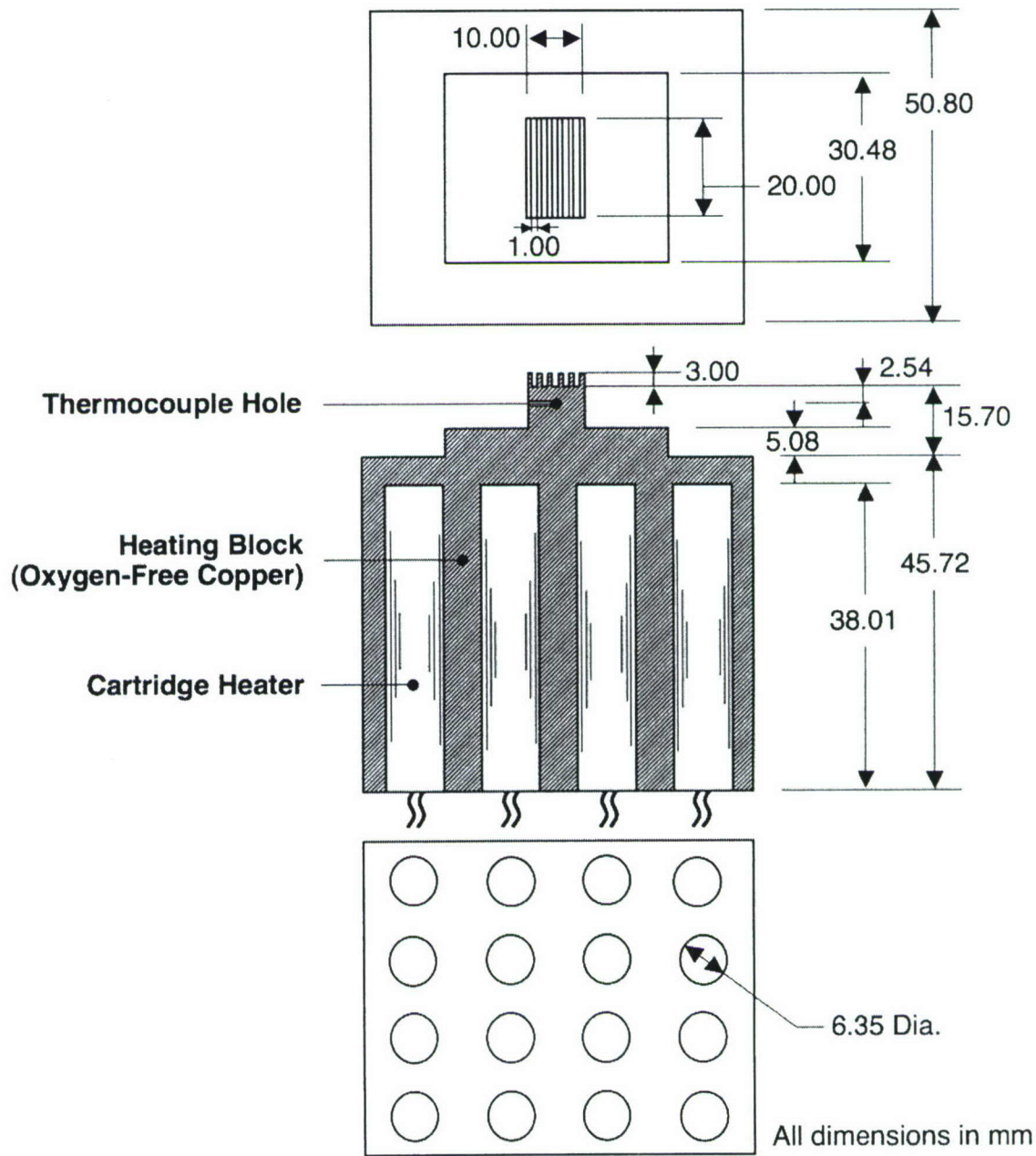


Figure 2.3 Details of copper heating block.

large underside of the heating block to accommodate the cartridge heaters. These heaters were connected in a combined series/parallel circuit and powered by a single 0-110 VAC variac. Total power dissipation from the cartridge heaters was measured by a Yokogawa WT 210 wattmeter. The top plenum plate and lower support plate of the test module were fabricated from high temperature fiberglass plastic (G-11). Blanket insulation around the circumference, and solid ceramic insulation at the bottom of the copper block helped minimize heat loss to the ambient. RTV silicone rubber was applied along the interface between the heating block and lower support plate to prevent liquid leakage.

O-rings were used to prevent liquid leakage between the jet plate and the upper plenum plate and lower support plate. An absolute pressure transducer and a type-T thermocouple were connected to the inlet plenum in the top plenum plate. Another absolute pressure transducer and a second type-T thermocouple were connected to the outlet plenums in the lower support plate. Four stainless steel pins were used to align the cover plate with the housing to ensure accurate placement of the jets relative to the micro-channels.

2.2.1. Micro-Jet Plates

The micro-jet plates were fabricated from oxygen-free copper. Five parallel arrays of fourteen 0.39 mm diameter circular holes were drilled equidistantly within the 1 cm width facing the five micro-channels in the circular-jet plate. The slot-jet plate, which is also fabricated from oxygen-free copper, has five parallel 0.6 mm wide by 1.65 mm deep and 2.94 mm long slots machined equidistantly, facing the micro-channels of the heating block. For the jet pattern configurations, three different micro-jet patterns are examined; each pattern is formed in a separate micro-jet plate. In the first micro-jet plate, jets decrease in size along each side of the micro-channel. The second plate has equally-sized jets, and, in the third plate, jets increase in size along each side of the micro-channel. In each plate, five parallel arrays of circular holes are drilled within the 1-cm width facing the five micro-channels. It is important to emphasize that the sum of flow

areas of all jets is the same for all three micro-jet plates. The micro-jet plates are fabricated from oxygen-free copper.

2.3. Operating Procedure and Measurements

Once the required operating conditions were achieved, electric power was supplied to the test module's cartridge heaters in small increments up to CHF. Key parameters were measured after steady state was achieved following each power increment. These include module inlet pressure, P_{in} , outlet pressure, P_{out} , inlet temperature, T_{in} , outlet temperature, T_{out} , heating block thermocouple temperatures, and heater power input, P_w . The total volumetric flow rate was determined from the measured mass flow rated, \dot{m} , and coolant density, ρ_f ,

$$Q = \frac{\dot{m}}{\rho_f}. \quad (2.1)$$

The effective heat flux, \bar{q}_{eff} , from the top test surface of the copper heating block was determined by dividing the total electrical power input, P_w , by the test surface area, $A_t = 10 \times 20 \text{ mm}^2$. Thus,

$$\bar{q}_{eff} = \frac{P_w}{A_t}. \quad (2.2)$$

The heat transfer coefficient was calculated from

$$\bar{h} = \frac{\bar{q}_{eff}}{(\bar{T}_s - T_{in})}, \quad (2.3)$$

where \bar{T}_s is the mean temperature of the test surface.

Special attention was given to minimizing heat loss from the copper block. A 3-D numerical model of the entire test module yielded a heat loss to the ambient of less than 4% of the electrical power input during the two-phase region. The heat fluxes reported in the present paper are therefore based on the measured electrical power input.

Measurement uncertainties associated with the pressure transducers, flow meter, wattmeter, and thermocouples are 0.5%, 0.1%, 0.5%, and 0.3°C, respectively. Table 2.1 summarizes the operating conditions of the study.

Table 2.1 Experimental operating conditions.

Working fluid	Inlet temperature	Jet velocity	Outlet Pressure	Effective heat flux
	T_{in} (°C)	U_{jet} (m/s)	P_{out} (bar)	q''_{eff} (W/cm²)
HFE 7100	- 40 to 20	0.48 to 7.35	1.31 to 1.67	16.06 to 1,127.00

CHAPTER 3. NUMERICAL METHODS

3.1. Standard k - ε Model

Figures 3.1 and 3.2 show unit cells that were used in the numerical simulation for circular jets and slot jets, respectively. Each unit cell consists of one of the five micro-channels along with the associated array of circular micro-jets or slot micro-jets and surrounding solid. Key dimensions of the unit cells are given in Table 3.1 and Table 3.2. The unit cell figures show both top and side cross-sectional views of the unit cell and corresponding coordinate system and key notations. Because of symmetry, a computational domain consisting of only one quarter of the unit cell is required.

Table 3.1 Dimensions of unit cell for circular jets.

L (mm)	L_1 (mm)	L_2 (mm)	L_3 (mm)	L_4 (mm)	W (mm)	W_{ch} (mm)	W_w (mm)
20.00	4.00	6.00	3.00	6.00	1.83	1.00	0.42
H (mm)	H_{jet} (mm)	H_{ch} (mm)	H_w (mm)	H_h (mm)	D_{jet1} (mm)	D_{jet2} (mm)	D_{jet3} (mm)
14.27	1.65	3.00	7.62	5.08	0.60	0.45	0.30
D_{jet4} (mm)	L_{jet1} (mm)	L_{jet2} (mm)	L_{jet3} (mm)	L_{jet4} (mm)	L_{jet5} (mm)		
0.39	1.84	1.62	1.44	1.23	1.43		

Flow profiles and heat transfer characteristics of the computational domain were predicted using FLUENT 6.2.16 (2005), which is based on the finite volume method

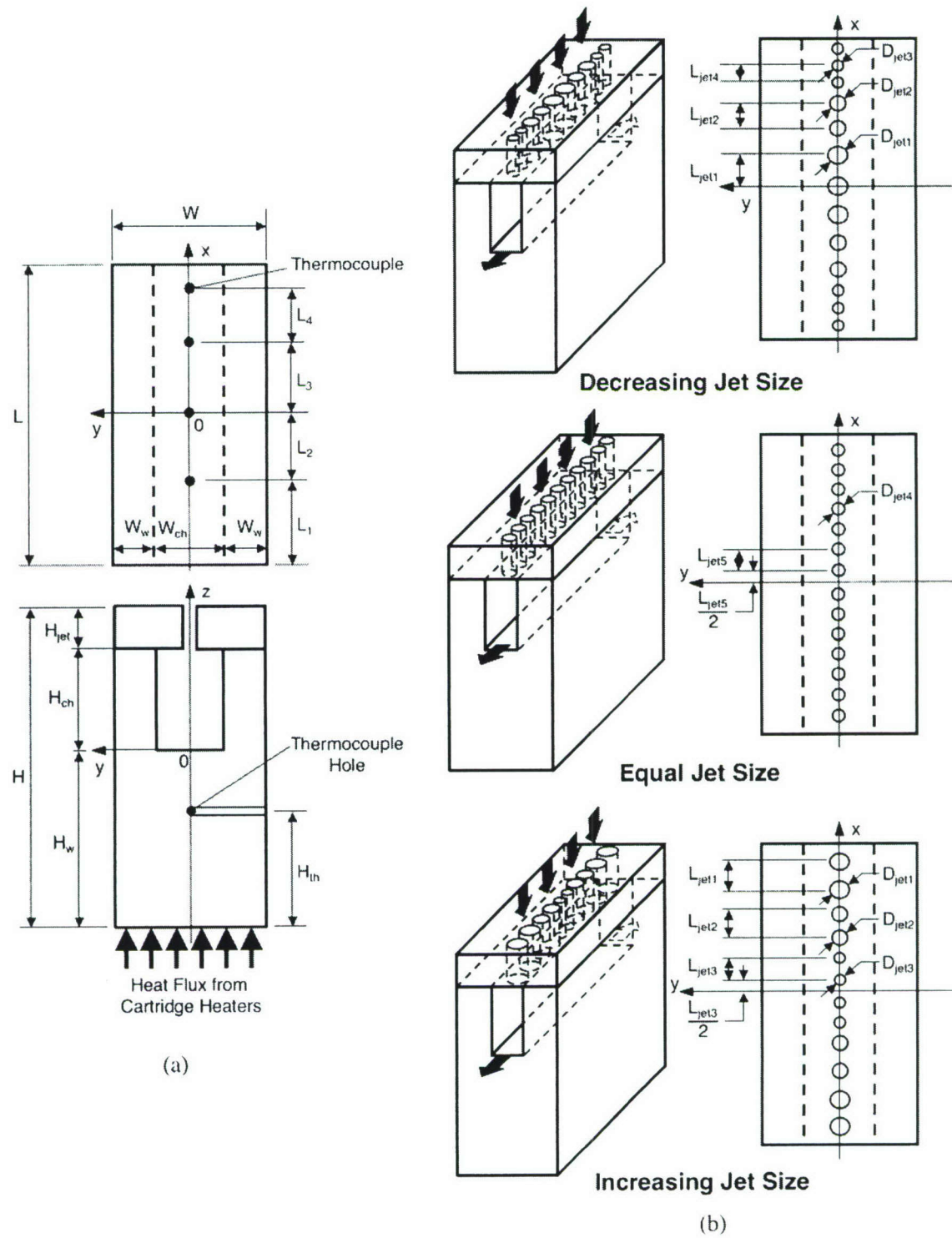


Figure 3.1 Schematic of unit cell illustrating (a) overall dimensions and thermocouple locations and (b) jet patterns consisting of single row of circular micro-jets and single micro-channel.

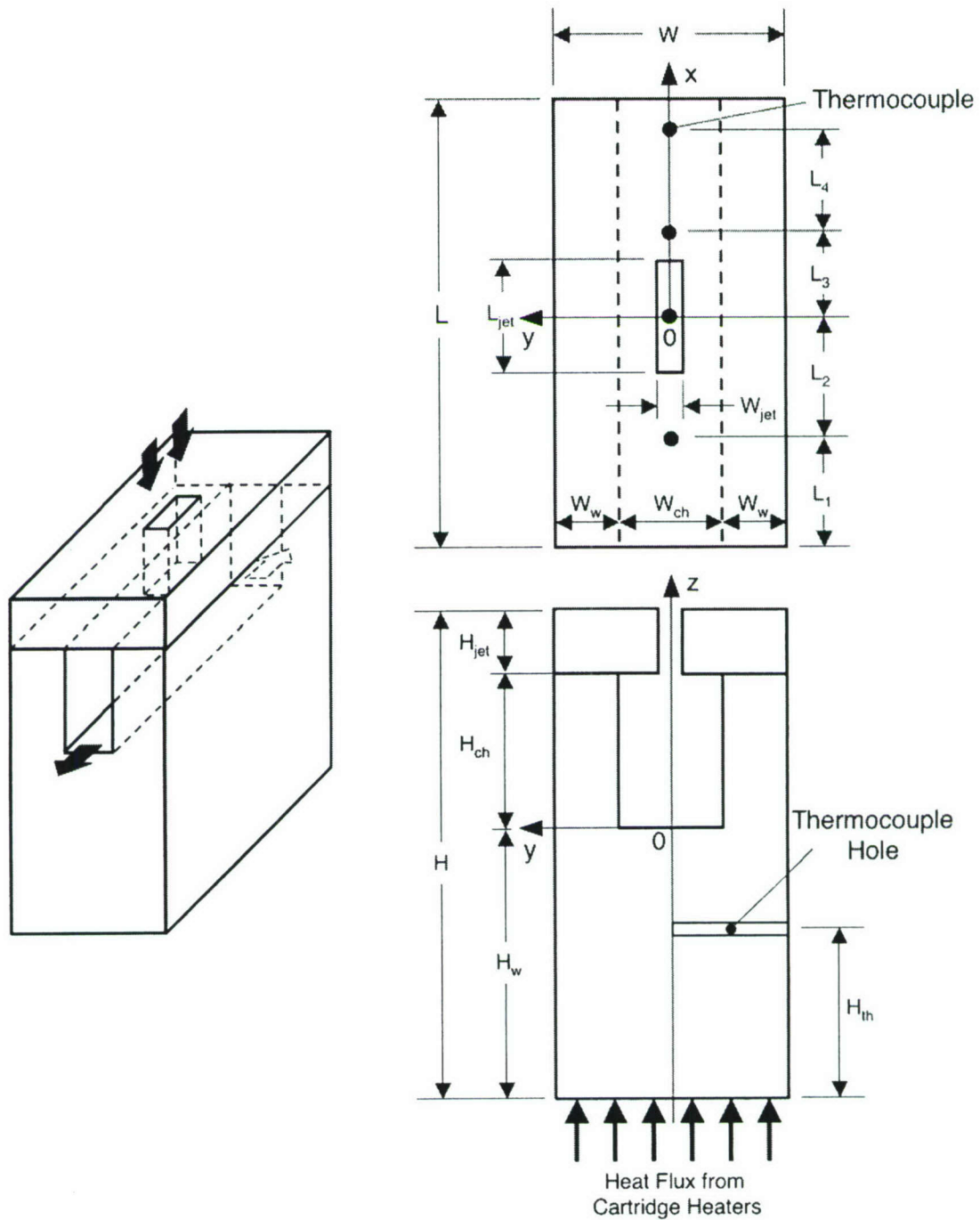


Figure 3.2 Schematic of unit cell consisting of single slot jet and single micro-channel.

(FVM). The geometry and meshes for the computational domain were generated using Gambit 2.2.30 (2006). The standard two-equation k - ε turbulent model (Launder and Spalding, 1974) was used for the closure of the Reynolds stress tensor.

Table 3.2 Key dimensions of unit cell for slot jets.

L (mm)	L_1 (mm)	L_2 (mm)	L_3 (mm)	L_4 (mm)	L_{jet} (mm)	W (mm)	W_{jet} (mm)
20.00	4.00	6.00	3.00	6.00	2.94	1.83	0.60
<hr/>							
W_{ch} (mm)	W_w (mm)	H (mm)	H_{jet} (mm)	H_{ch} (mm)	H_w (mm)	H_{th} (mm)	
1.00	0.42	14.27	1.65	3.00	7.62	5.08	

Solid-liquid interfaces are governed by continuities of both temperature and heat flux,

$$T_{s,\Gamma} = T_{f,\Gamma}, \quad (3.1)$$

and

$$-k_s \frac{\partial T_s}{\partial n} \Big|_\Gamma = -k_f \frac{\partial T_f}{\partial n} \Big|_\Gamma. \quad (3.2)$$

Conservation equations are expressed in the Cartesian tensor notation for steady, turbulent and incompressible flow with constant properties as follows.

For the fluid region:

$$\frac{\partial U_i}{\partial x_i} = 0, \quad (3.3)$$

$$\rho_f U_j \frac{\partial U_i}{\partial x_j} = -\frac{\partial P}{\partial x_i} + \frac{\partial}{\partial x_j} \left((\mu_f + \mu_t) \frac{\partial U_i}{\partial x_j} \right), \quad (3.4)$$

and

$$\rho_f c_{p,f} U_j \frac{\partial T}{\partial x_j} = \frac{\partial}{\partial x_j} \left(\left(k_f + \frac{c_{p,f} \mu_t}{Pr_t} \right) \frac{\partial T}{\partial x_j} \right), \quad (3.5)$$

where

$$\mu_t = \frac{C_\mu \rho_f k^2}{\varepsilon}, \quad (3.6)$$

$$\rho_f U_j \frac{\partial k}{\partial x_j} = \frac{\partial}{\partial x_j} \left(\left(k_f + \frac{\mu_t}{\sigma_k} \right) \frac{\partial k}{\partial x_j} \right) + G - \rho_f \varepsilon, \quad (3.7)$$

and

$$\rho_f U_j \frac{\partial \varepsilon}{\partial x_j} = \frac{\partial}{\partial x_j} \left(\left(k_f + \frac{\mu_t}{\sigma_\varepsilon} \right) \frac{\partial \varepsilon}{\partial x_j} \right) + C_1 G \frac{\varepsilon}{k} - C_2 \rho_f \frac{\varepsilon^2}{k}. \quad (3.8)$$

The production of turbulent energy is defined as $G = -\overline{u_i u_j} \partial U_i / \partial x_j$. The following values are used for the coefficients in the above equations: $C_\mu = 0.09$, $C_1 = 1.44$, $C_2 = 1.92$, $\sigma_k = 1.0$, $\sigma_\varepsilon = 1.3$, and $Pr_t = 0.85$.

For the solid region:

$$U_i = 0, \quad (3.9)$$

and

$$\frac{\partial}{\partial x_j} \left(k_s \frac{\partial T}{\partial x_j} \right) = 0. \quad (3.10)$$

Heat transfer in the unit cell is a conjugate one combining conduction and convection effects. The boundary conditions were specified as follows:

$$u = 0, v = 0, w = -U_{jet}, \text{ and } T = T_{in}, \text{ for the jet inlet} \quad (3.11)$$

$$\dot{m} = \dot{m}_{in}, \frac{\partial v}{\partial x} = 0, \frac{\partial w}{\partial x} = 0, \text{ and } \frac{\partial T}{\partial x} = 0, \text{ for the channel outlet.} \quad (3.12)$$

For the solid regions, a constant heat flux was applied along the copper bottom boundary of the unit cell:

$$-k_s \frac{\partial T}{\partial z} = \overline{q_{eff}}, \quad (3.13)$$

where $\overline{q_{eff}}$ was determined from measured electrical power input as

$$\overline{q_{eff}} = \frac{P_w}{A_t}. \quad (3.14)$$

A zero heat flux condition was applied to all solid thermal boundaries except the interfaces between fluid and copper. The SIMPLE (Semi-Implicit Method for Pressure-Linked Equations) algorithm by Patankar (1980) was used to couple velocities and pressure. A total of 593,460 mesh cells was used in the selection of geometry numerical simulation. Three different mesh sizes were tested using 195,720, 414,656 and 693,500 elements for circular jets. To examine the effects of mesh size for slot jets, 84,000, 288,000 and 517,500 mesh elements were also tested. The middle mesh size was used because temperature differences were less than of the finer mesh. The middle mesh sizes of both jet schemes were employed in single-phase heat transfer characteristic study because temperature differences between the two finer mesh sizes in circular jets and slot jets were less than 2.27% and 3.2%, respectively.

3.2. Determination of Extent of Laminar Zone

Two concerns in implementation of the numerical methods described in this study are (1) the suitability of the standard $k-\varepsilon$ model to the present flow configuration, which involves complex interaction of jets with parallel channel flow, and (2) determination of the radial extent from the jet's stagnation point where the turbulent zone commences. To determine the upstream radial location of the turbulent zone, laminar flow is imposed on the computational domain from the jet inlet to the stagnation zone, and a portion of the wall jet surrounding the stagnation zone. The computational domain in FLUENT is therefore divided into two sub-zones, a laminar zone and a turbulent zone.

Determining the extent of the laminar zone away from the stagnation zone based on first principles is quite elusive. However, lot of insight may be gained from a related flow configuration involving a free circular impinging liquid jet. For a circular free jet, Fig. 3.3 shows the flow field along a heated surface can be classified into four regions: a stagnation zone, a boundary layer region, a similarity or fully viscous region and a turbulent region. Within the stagnation zone, the circular jet flow decelerates normal to the surface but accelerates radially, and the flow is laminarized flow by a strong radial pressure gradient (Incropera, 1999). Watson (1964) used inviscid theory to determine

thickness h of the wall jet on the surface in the stagnation zone. For inviscid Bernoulli flow, mass conservation yields

$$\frac{\pi D_{jet}^2}{4} U_{jet} = 2\pi r h U_{jet}, \quad (3.16)$$

which can be simplified into

$$h = \left(\frac{D_{jet}^2}{8r} \right) + \left\{ 1 - \frac{2\pi}{3\sqrt{3} c^2} \right\} \delta \quad \text{for } r_s < r < r_b, \quad (3.17)$$

where

$$\delta^2 = \frac{\sqrt{3} c^3}{\pi - c \sqrt{3}} \frac{r}{D_{jet} \text{Re}_{jet}} \quad \text{and } c = 1.402. \quad (3.18)$$

In the fully viscous region, hydrodynamic boundary layer thickness is the same as the thickness of liquid wall layer, $d = h$. Here, viscous effects extend across the entire liquid film, and the mean liquid velocity decreases r . Watson (1964) derived the following relation for liquid layer thickness in this region based on the velocity similarity profile with a Jacobi elliptic function as follows:

$$h = \frac{8\pi}{3\sqrt{3}} \frac{(r^3 + l^3)}{D_{jet} \text{Re}_{jet} r}, \quad \text{for } r_b < r < r_c, \quad (3.19)$$

where

$$l = 0.3296 D_{jet} \text{Re}_{jet}^{1/3}. \quad (3.20)$$

The radius between the developing boundary layer region and fully viscous region is given as

$$r_b = 0.1834 D_{jet} \text{Re}_{jet}^{1/3}. \quad (3.21)$$

Returning to the present hybrid cooling configurations, it must be noted, for the minimum jet velocity tested of $U_{jet} = 2.68$ m/s, the distance L_{jet} between jets feeding liquid into a single micro-channel is shorter than the radius, r_b , where the fully viscous region begins. This means only the stagnation and boundary layer regions of the wall

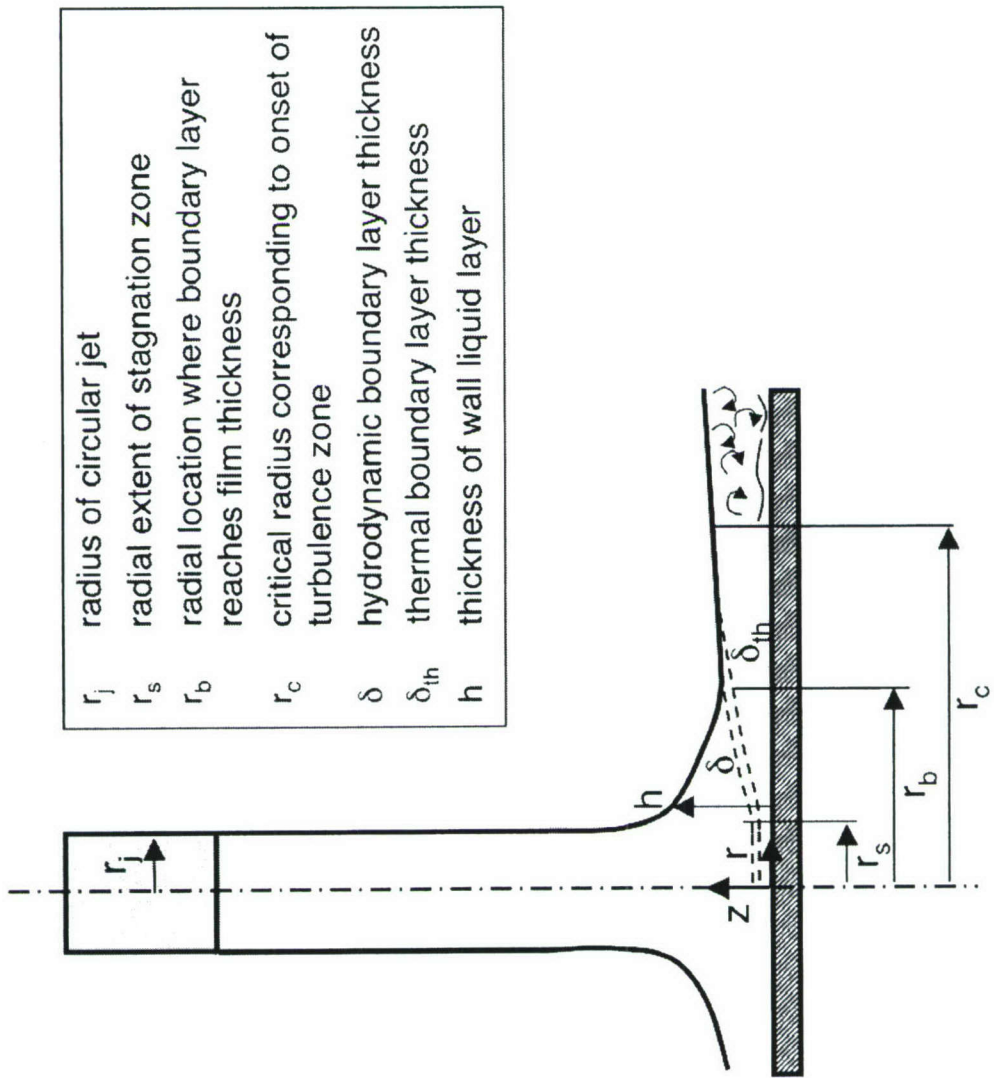


Figure 3.3 Fluid flow regimes for free circular impingement jet with $Prf > 1$.

liquid layer are of importance there. Therefore, the laminar flow was imposed on the flow domain between the jet inlet and stagnation zone, as well as up to height $h(r)$ from the wall as given by Eqs. (3.17) and (3.16). Turbulence was permitted everywhere else in the computational domain.

For examining the effects of jet patterns on single-phase heat transfer, the computational domain in FLUENT is therefore divided into two sub-zones, a laminar zone and a turbulent zone. For each jet pattern, the laminar thickness for each jet size is determined and the smallest laminar zone height is used for all jets.

CHAPTER 4. SINGLE-PHASE NUMERICAL RESULTS

4.1. Effects of Micro-Channel Geometry

As discussed earlier, high temperatures and large spatial temperature gradients are two key obstacles to the implementation of many seemingly effective high-flux cooling schemes (Mudawar, 2001). In this study, the effects of liquid inlet velocity and cooling geometry on both maximum surface temperature and spatial temperature variations were investigated for different values of jet velocity in pursuit of optimal geometry.

4.1.1. Circular Jets

Referring to Fig. 3.1, the performance of the hybrid configuration was examined by varying two key geometrical parameters: micro-channel width (W_{ch}) and micro-channel height (H_{ch}). The performance predictions were repeated for three jet velocities, 1, 5 and 10 m/s for an inlet HFE 7100 liquid temperature of 0 °C and a heat flux of $q''_{eff} = 300 \text{ W/cm}^2$. Both the diameter and pitch of the circular jets were held constant in this parametric study. Geometrical parameters used in the circular jet optimization are summarized in Table 4.1.

Table 4.1 Dimensions tested in numerical parametric study for circular jets.

H_{ch} (mm)	W_{ch} (mm)	D_{jet} (mm)	U_{jet} (m/s)
1.00, 3.00, 6.00	1.00, 1.40	0.39	1, 5, 10

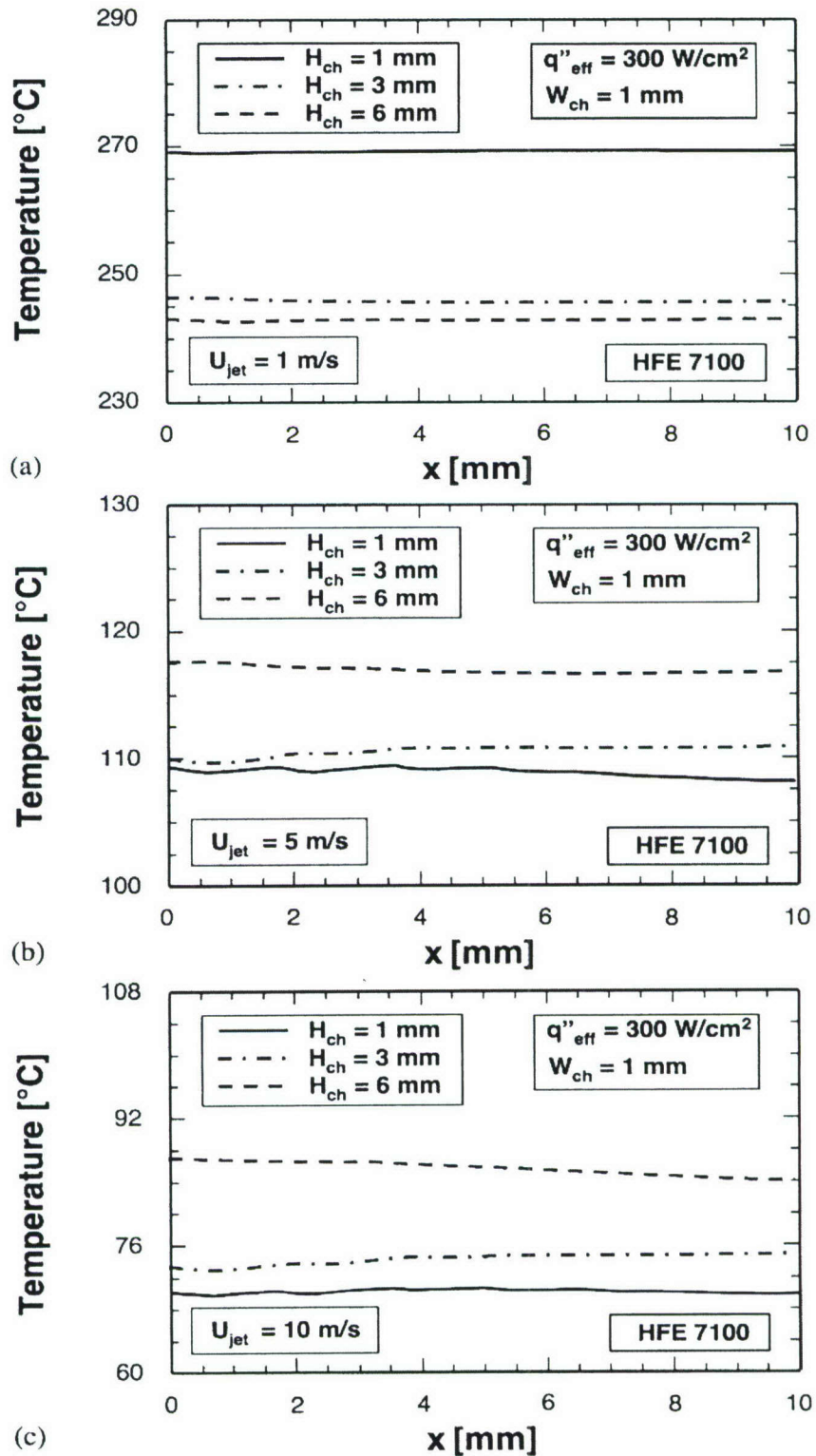


Figure 4.1 Numerical predictions of the effects of micro-channel height on surface temperature for jet velocities of (a) $U_{jet} = 1 \text{ m/s}$, (b) $U_{jet} = 5 \text{ m/s}$, and (c) $U_{jet} = 10 \text{ m/s}$.

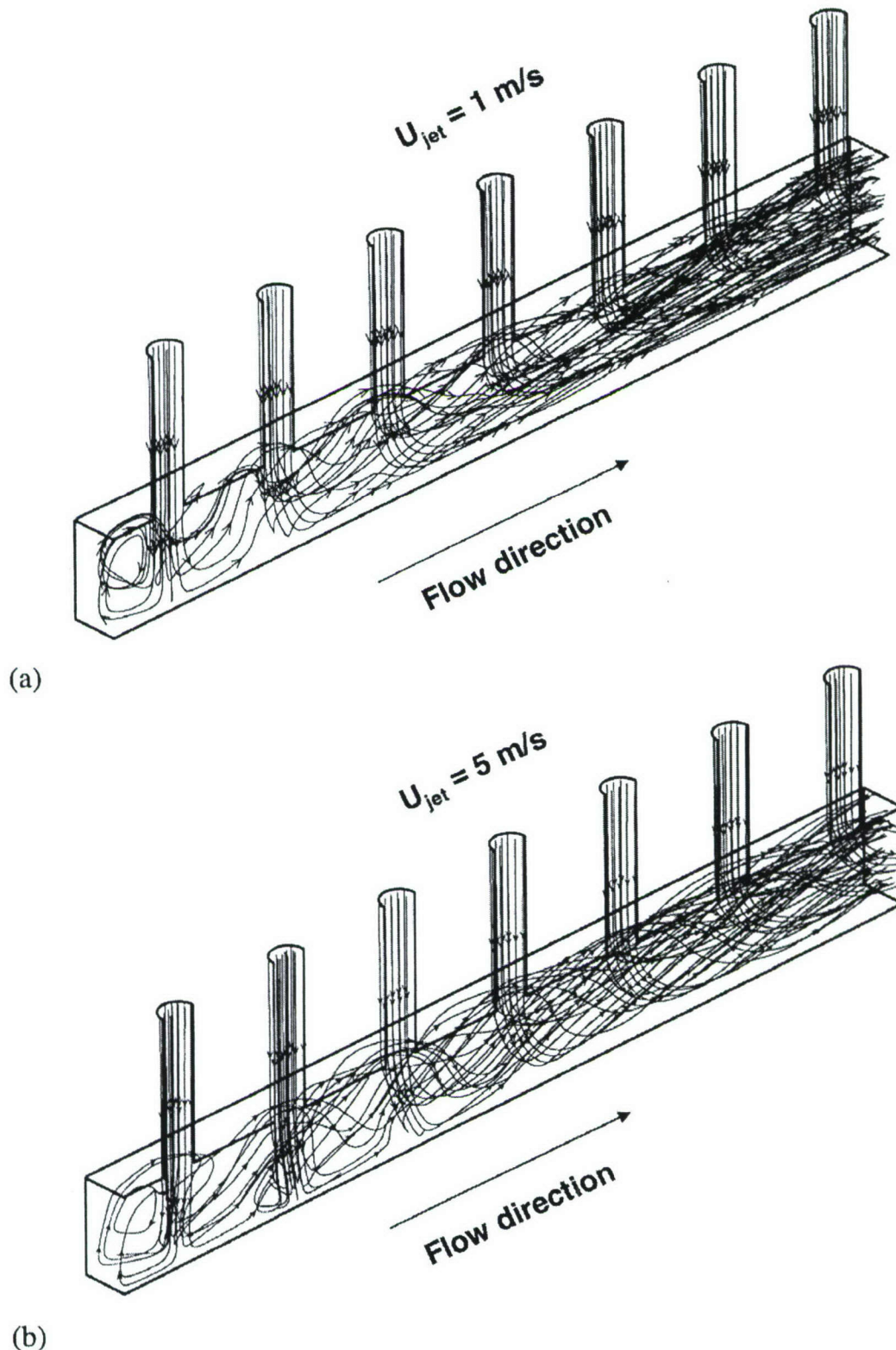


Figure 4.2 Streamline plots for $H_{ch} = 1 \text{ mm}$, $W_{ch} = 1 \text{ mm}$ and jet velocities of (a) $U_{jet} = 1 \text{ m/s}$ and (b) $U_{jet} = 5 \text{ m/s}$.

Figure 4.1 shows the parametric effects of micro-channel height for a fixed width of $W_{ch} = 1$ mm and three jet velocities. Notice the large overall decrease in surface temperature as jet velocity is increased from $U_{jet} = 1$ to 10 m/s caused by the large dependence of the convective heat transfer coefficient on jet velocity. For $U_{jet} = 5$ and 10 m/s, Fig. 4.1 shows an advantageous decrease in the maximum surface temperature with decreasing channel height. By reducing channel height, the jet flow is better able to penetrate the liquid flow in the micro-channel, and the impingement effect is felt more strongly at the surface. However, the decrease in maximum surface temperature realized by reducing micro-channel height is accompanied by more appreciable temperature gradients both locally and along the entire length of the micro-channel. The local gradients are the result of the aforementioned strong impingement effects, while the overall gradient is due to increased flow rate along the micro-channel. However, Fig. 4.1(a) shows reducing micro-channel height from 3 to 1 mm *increases* surface temperature.

To explain these seemingly opposite trends, streamline plots were generated for the smallest micro-channel height of $H_{ch} = 1$ mm for $U_{jet} = 1$ m/s, Fig. 4.2(a), and $U_{jet} = 5$ m/s, Fig. 4.2(b). Notice in Fig. 4.2(a) for the low velocity case that while the upstream jet (close to central region of micro-channel, where flow rate is zero) can easily impact the surface, its spent fluid makes it difficult for the second jet to penetrate towards the surface. The spent fluid from the first and second jets makes it even more difficult for the third jet to reach the surface, and so on. On the other hand, Fig. 4.2(b) shows that despite the increasing flow rate of spent fluid from upstream, jets at $U_{jet} = 5$ m/s are better able to penetrate the micro-channel flow. In other words, heat removal is dominated more by micro-channel flow at $U_{jet} = 1$ m/s and by jet impingement at $U_{jet} = 5$ m/s. Clearly, the effects of jet impingement must diminish even at $U_{jet} = 5$ m/s had longer micro-channels been tested. For the lower jet velocity, the reduced surface temperature achieved by increasing micro-channel height from 1 to 3 mm (see Fig. 4.1(a)) is apparently the result of the increased heat transfer area available for the micro-channel flow.

Figure 4.3 shows the effects of micro-channel width, W_{ch} , on surface temperature for $H_{ch} = 3.0$ mm and $U_{jet} = 5$ m/s while maintaining a fixed pitch of $W = 1.83$ mm

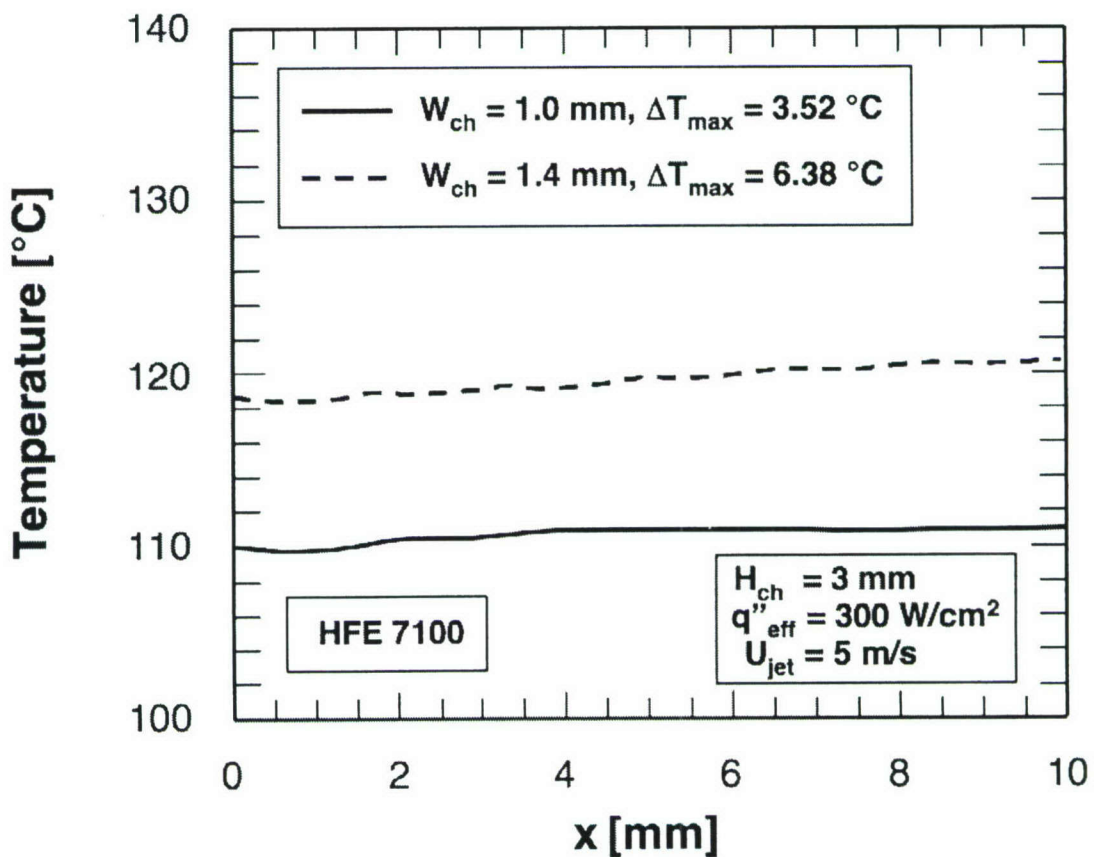


Figure 4.3 Numerical predictions of the effects of micro-channel width on surface temperature for $U_{jet} = 5 \text{ m/s}$ and $H_{ch} = 3 \text{ mm}$.

between micro-channels. As shown in Fig. 3.1, increasing W_{ch} decreases the micro-channel wall thickness W_w . Figure 4.3 shows increasing W_w by reducing W_{ch} from 1.4 to 1.0 mm decreases both surface temperature and temperature gradient along the Figure 4.3 shows the effects of micro-channel width, W_{ch} , on surface temperature for $H_{ch} = 3.0$ mm and $U_{jet} = 5$ m/s while maintaining a fixed pitch of $W = 1.83$ mm between micro-channels. This behavior is believed to be the result of the increased contribution of conduction through the thicker sidewalls.

4.1.2. Slot Jets

A numerical parametric study for the hybrid micro-channel/micro-slot jet cooling module was conducted by varying micro-channel height, H_{ch} , micro-channel wall thickness, W_w , and jet width, W_{jet} , as indicated in Table 4.2.

Table 4.2 Dimensions tested in numerical parametric study for slot jets.

H_{ch} (mm)	W_{ch} (mm)	W_{jet} (mm)	U_{jet} (m/s)
1.00, 3.00	1.00, 1.40	0.30, 0.60	5, 10

Figure 4.4(a) shows the effects of micro-channel height on surface centerline temperature for $W_w = 0.43$ mm, $W_{jet} = 0.6$ mm and jet velocities of $U_{jet} = 5$ and 10 m/s. The higher jet velocity is shown decreasing the maximum surface temperature appreciably. Due to the fin effect of the micro-channel copper sidewall, a lower axial temperature gradient is achieved at $U_{jet} = 5$ m/s for $H_{ch} = 3$ mm compared to 1 mm. This effect appears to subside appreciably for $U_{jet} = 10$ m/s because of apparent dominance of jet impingement with the channel's bottom wall compared to the fin effect.

Figure 4.4(b) shows that surface temperature is reduced for $U_{jet} = 5$ m/s by decreasing channel width because stronger jet vorticity along the channel sidewalls increases the contribution of sidewall conduction. Additionally, mean flow velocity

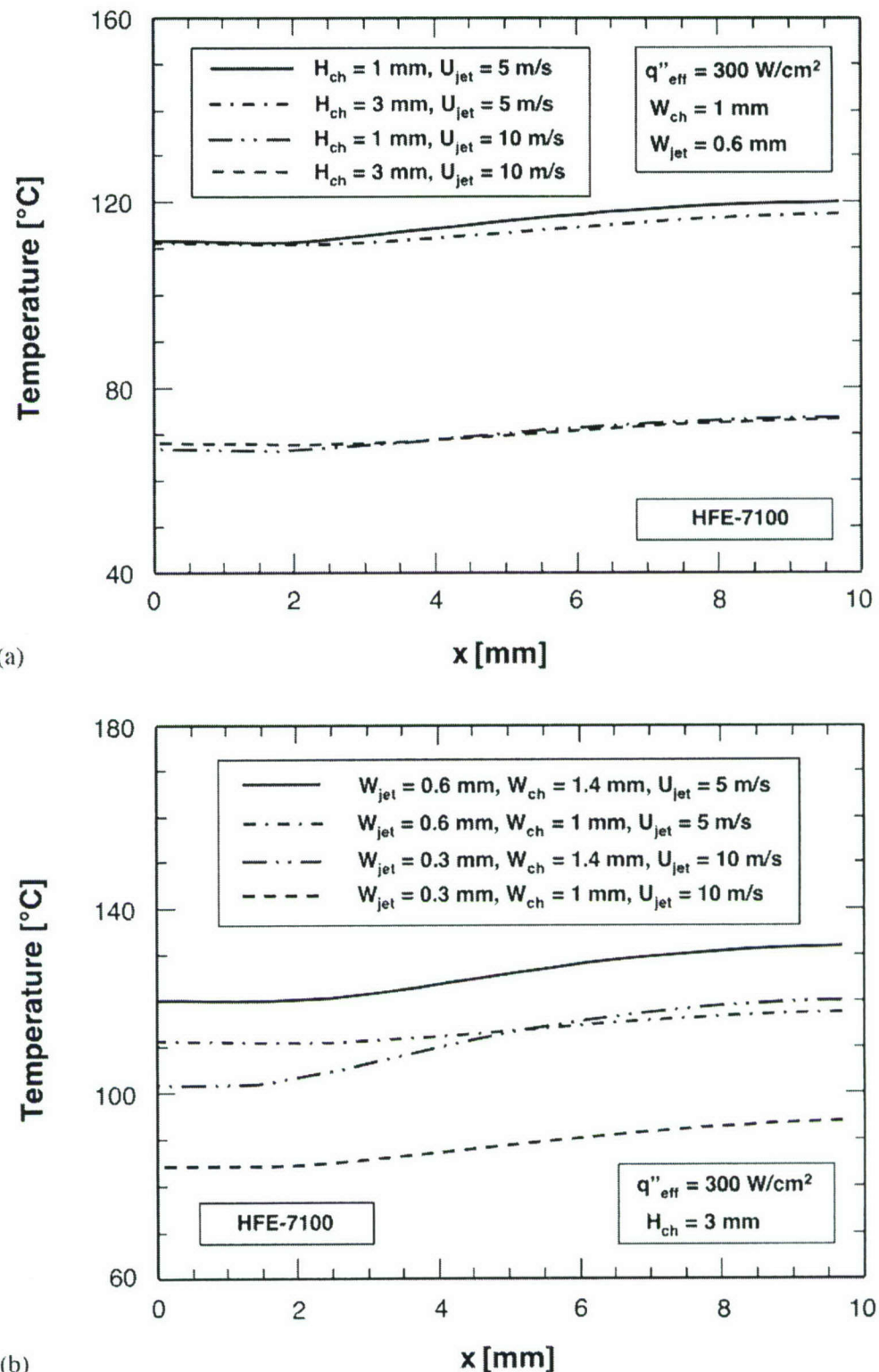


Figure 4.4 Numerical predictions of the effects of (a) channel height and (b) jet width and channel width on centerline temperature distribution along the micro-channel.

along the micro-channel increases with decreasing W_{ch} , which helps decrease the axial temperature gradient as well. For a fixed W_{ch} , decreasing jet width, W_{jet} , in half while maintaining the same flow rate requires doubling jet velocity. Figure 4.4(b) shows higher jet velocity decreases surface temperature, although the axial temperature gradient is greater. This trend points to a very important practical conclusion concerning maximum surface temperature: for a given flow rate, higher heat transfer coefficients and lower surface temperatures are possible simply by decreasing jet width. Obvious limits to how small jet width can be made are manufacturability and high pressure drop.

Using these parametric trends of micro-channel geometry as a guide to achieving favorable cooling performance, experiments were performed using the geometry detailed in Table 3.1 and Table 3.2.

4.2. Comparison of Numerical Predictions with Experimental Results

Figures 4.5 and 4.6 compare numerical predictions of temperature distribution along the thermocouple line inside the copper heating block with the thermocouple measurements for circular jets and slot jet, respectively. Both the numerical predictions and experimental data show wall temperature decreases with decreasing liquid inlet temperature for about the same jet velocity and wall heat flux. Both predictions and experimental data also show strong influence of jet velocity on cooling performance. For an inlet temperature of $T_{in} = 0$ °C in Fig. 4.5, increasing jet velocity from $U_{jet} = 2.68$ to 4.53 m/s, facilitates the removal of nearly twice the wall heat flux while incurring only a mild increase in wall temperature.

Close agreement between predicted and measured temperatures proves the single-phase performance of the present hybrid cooling scheme can be accurately predicted with the Navier-Stokes and energy equations using the standard $k-\varepsilon$ model. This agreement also demonstrates the effectiveness of the technique discussed earlier in relation to determining the extent of the laminar zone of the computational domain.

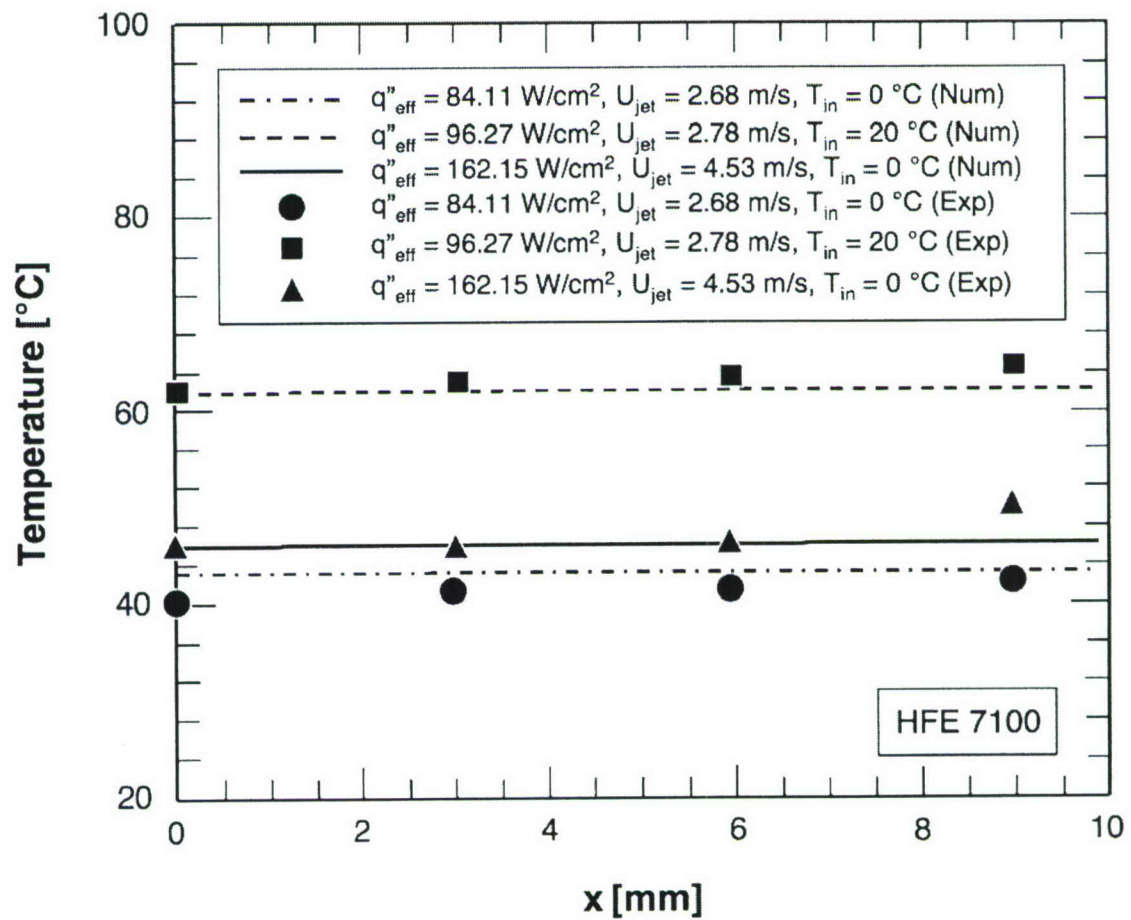


Figure 4.5 Comparisons of numerical prediction along the thermocouple line with measured temperatures for the equal-size-circular jet configuration.

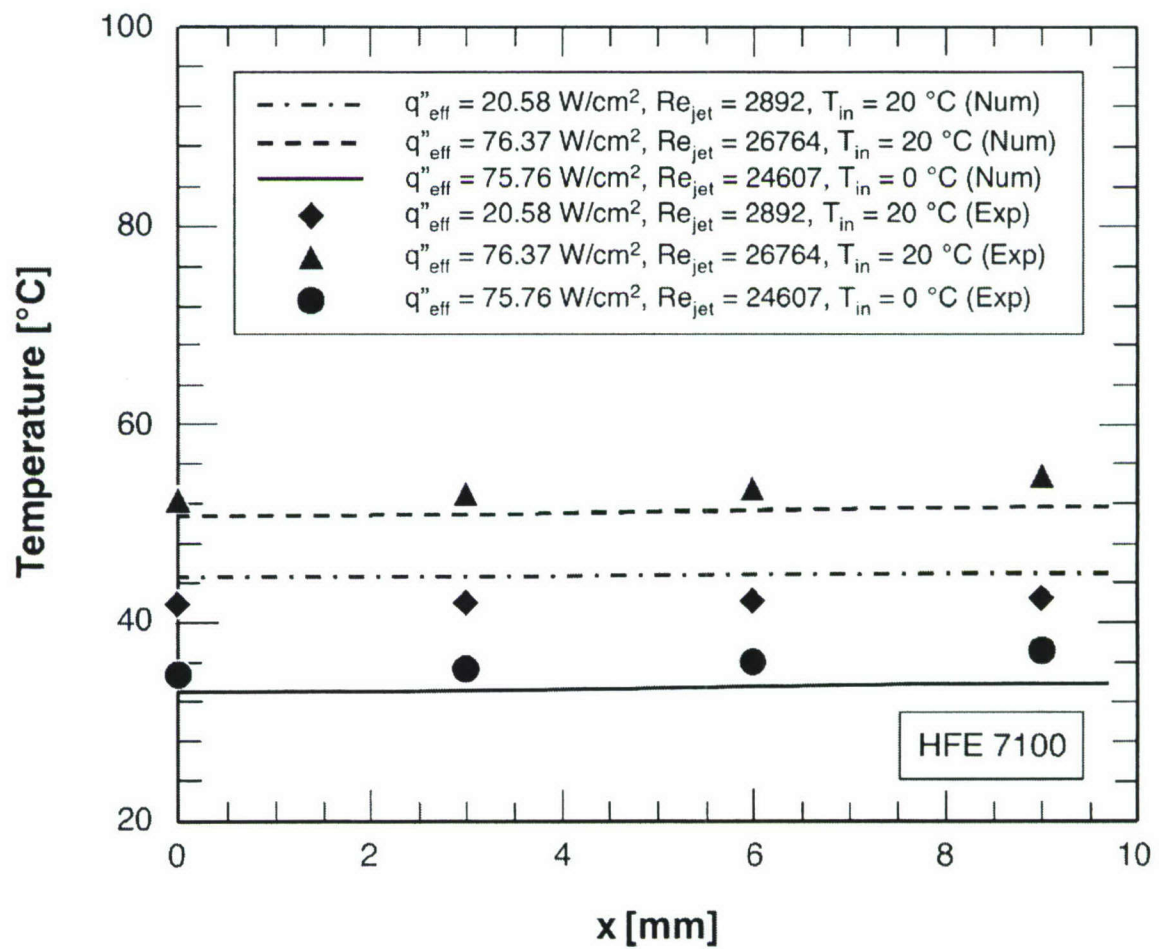


Figure 4.6 Comparisons of numerical prediction along the thermocouple line with measured temperatures for the micro-slot-jet configuration.

4.3. Parametric Trends of Cooling Characteristics

4.3.1. Circular Jets

Table 4.3 summarizes the different numerical simulation tests that were used to examine the cooling performance of the hybrid cooling scheme.

Table 4.3 Numerical simulation cases using HFE 7100 as working fluid.

Inlet temperature T_{in} ($^{\circ}\text{C}$)	Flow rate Q (m^3/s)	Jet velocity U_{jet} (m/s)	Effective heat flux q''_{eff} (W/cm^2)
0	7.34×10^{-6}	0.90	53.39
20	2.19×10^{-5}	2.68	84.11
0	2.28×10^{-5}	2.78	96.27
0	3.71×10^{-5}	4.53	162.15

Figures 4.7(a) and 4.7(b) show temperature distributions along the micro-channel's bottom wall for $q''_{eff} = 53.39 \text{ W/cm}^2$ and $U_{jet} = 0.90 \text{ m/s}$, and $q''_{eff} = 162.15 \text{ W/cm}^2$ and $U_{jet} = 4.53 \text{ m/s}$, respectively. For the weak jet case, Fig. 4.7(a), heat transfer appears dominated more by the micro-channel flow than by jet impingement. Since coolant flow rate increases along the flow direction, the heat transfer coefficient is highest and wall temperature lowest near the outlet ($x = 10 \text{ mm}$). The reverse is true for the strong jet case, Fig. 4.7(b). Here, heat transfer is influenced more by jet impingement than by the micro-channel flow, evidenced by both the local depressions in wall temperature immediately below the jets as well as lower overall wall temperatures.

Due to the fin effect of the micro-channel sidewall, lower temperatures are achieved along the corner of the micro-channel's bottom wall for both weak and strong jet cases.

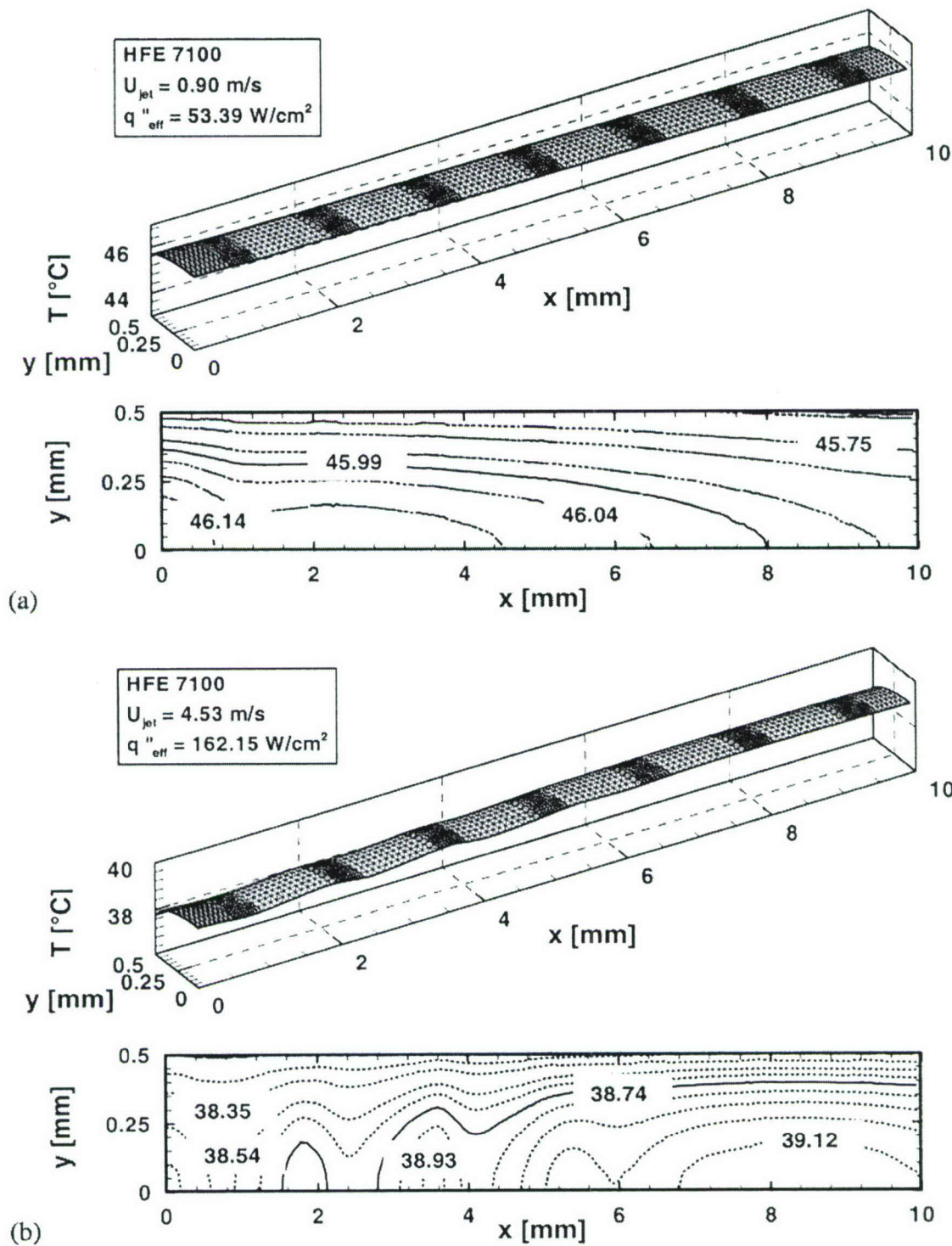


Figure 4.7 Numerical predictions of micro-channel bottom wall temperature distribution for (a) $q''_{eff} = 53.39 \text{ W/cm}^2$ and $U_{jet} = 0.90 \text{ m/s}$, and (b) $q''_{eff} = 162.15 \text{ W/cm}^2$ and $U_{jet} = 4.53 \text{ m/s}$.

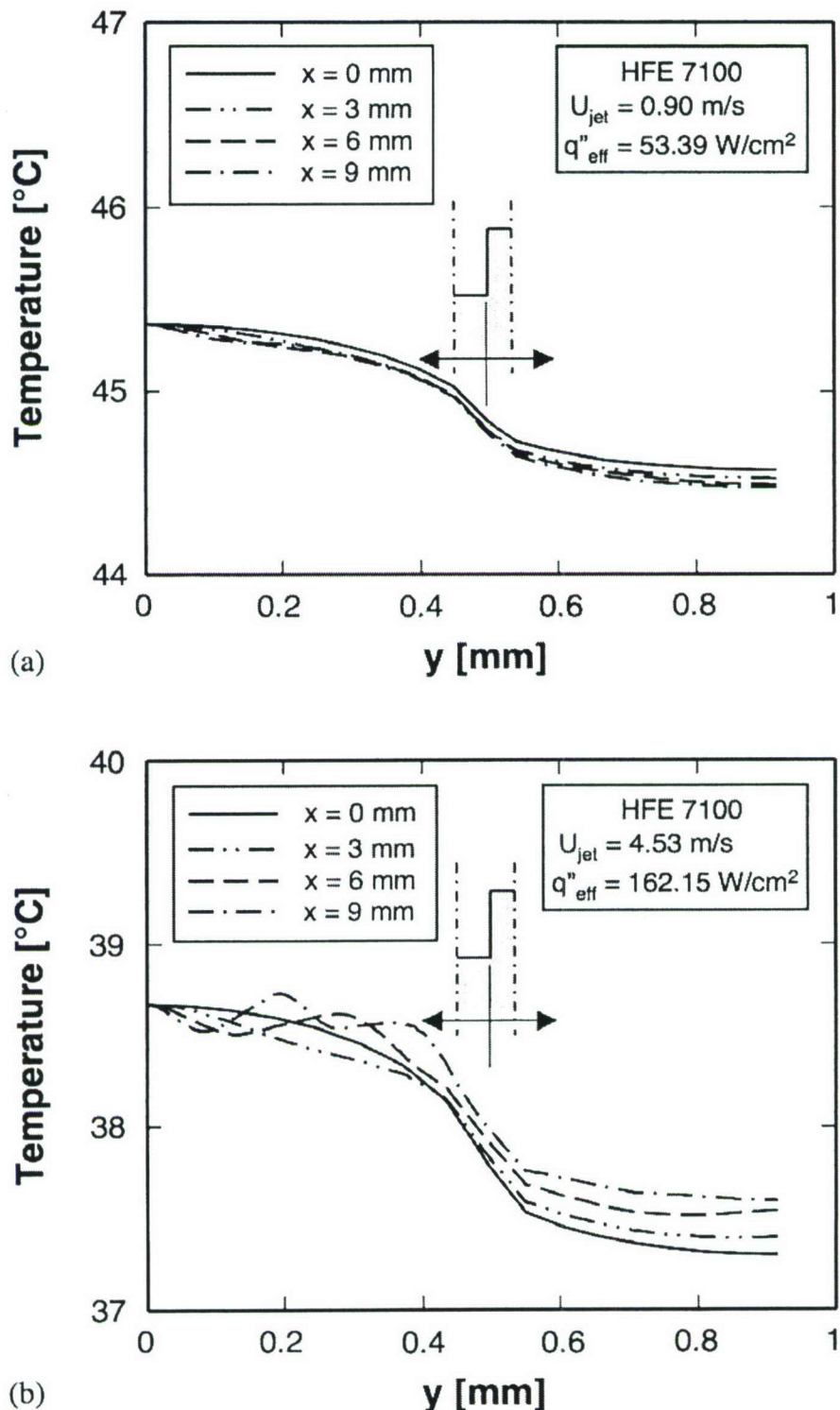


Figure 4.8 Numerical predictions of wall temperature, including sidewall region, at four axial locations for (a) $q''_{eff} = 53.39 \text{ W/cm}^2$ and $U_{jet} = 0.90 \text{ m/s}$, and (b) $q''_{eff} = 162.15 \text{ W/cm}^2$ and $U_{jet} = 4.53 \text{ m/s}$.

Figure 4.8 shows bottom wall temperature distribution including the region below the micro-channel sidewall. Temperature profiles are shown for four different axial locations, $x = 0, 3, 6$, and 9 mm. These profiles depict the aforementioned fin effect of the micro-channel sidewall. The small variations between temperature profiles corresponding to different axial locations clearly highlights the effectiveness of the hybrid cooling scheme at virtually eliminating the axial temperature gradients often associated with conventional micro-channel heat sinks.

Figure 4.9 shows further evidence of the relative contributions of jets and micro-channel flow for weak and strong jets. Streamline plots in Fig. 4.9(a) corresponding to weak jets show jet flow is barely able to penetrate the axial micro-channel flow and have its effect felt at the wall. This is especially the case for downstream jets that face increasing resistance from the gradually increasing micro-channel flow. On the other hand, Fig. 4.9(b) shows jets are better able to penetrate the micro-channel and produce strong impingement effect at the wall. Despite the increasing micro-channel flow in the x -direction, Fig. 4.9(b) shows the jet fluid approaching the wall for most jets, though downstream jets appear to be facing greater resistance from the micro-channel flow. This strong impingement effect is manifest in Fig. 4.7 in the form of greater heat transfer coefficients. These trends are further illustrated with plots of heat flux distribution along the bottom wall of the micro-channel. These distributions are shown for weak and strong jet cases in Figs. 4.10(a) and 4.10(b), respectively. In these plots, local heat flux is evaluated as

$$q'' = -k_{\Gamma} \frac{\partial T_{\Gamma}}{\partial n} \Big|_{\Gamma}, \quad (4.1)$$

where k_{Γ} is the interface thermal conductivity obtained by the harmonic mean of k_s and k_f . Both figures show higher heat fluxes are encountered near the jet centerline, but this effect is more noticeable for the strong jets. Heat flux is quite small in the corner of the micro-channel where the flow is weakest. For the weak jet case, Fig. 4.10(a), the highest heat flux is encountered near the first jet closest to the center of the micro-channel, and the lowest heat flux near the micro-channel center ($x = 0$). Notice that local heat flux peaks are damped by the micro-channel flow for all jets excepting the most upstream.

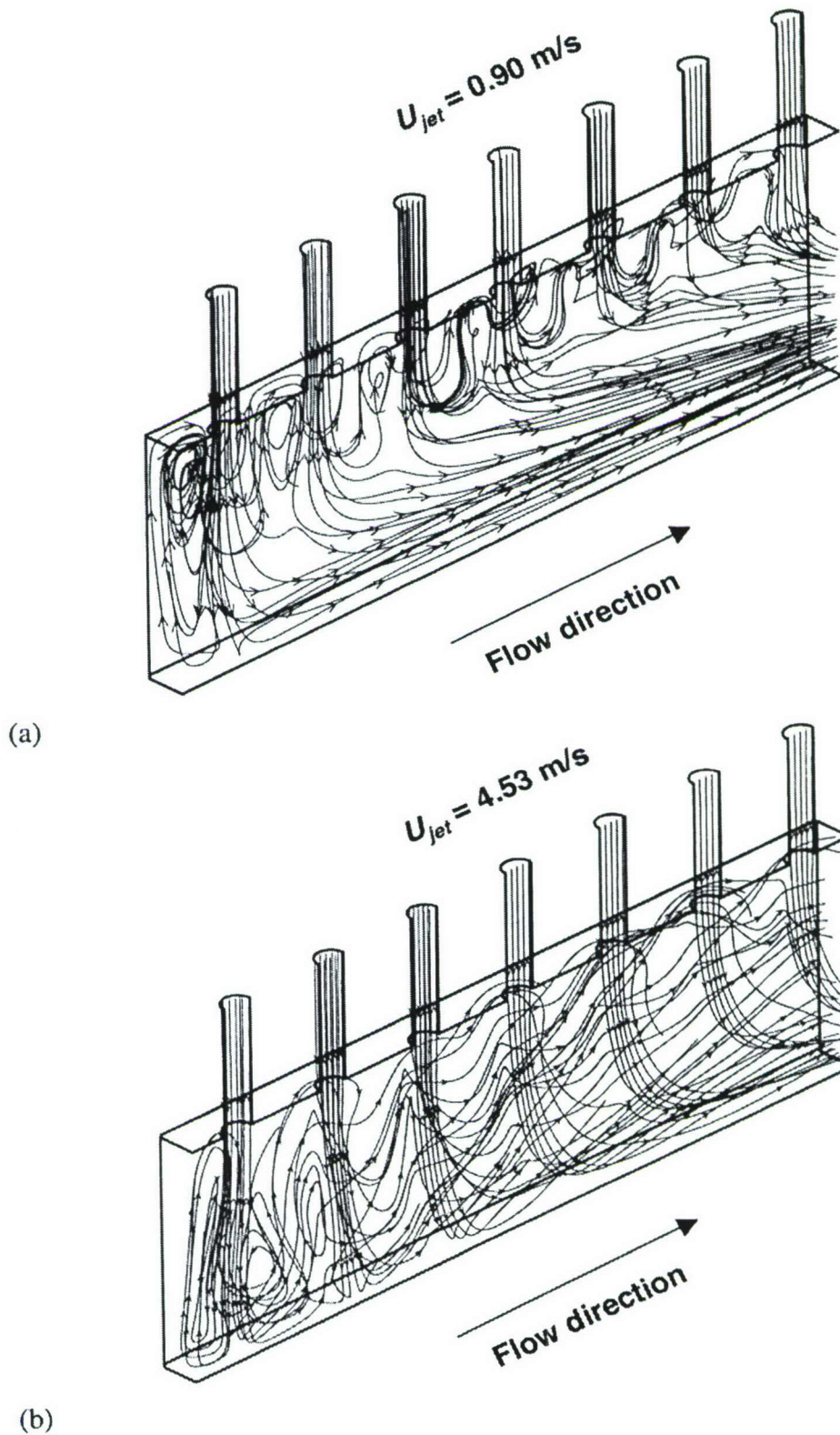


Figure 4.9 Streamline plots for (a) $U_{jet} = 0.90 \text{ m/s}$ and (b) $U_{jet} = 4.53 \text{ m/s}$.

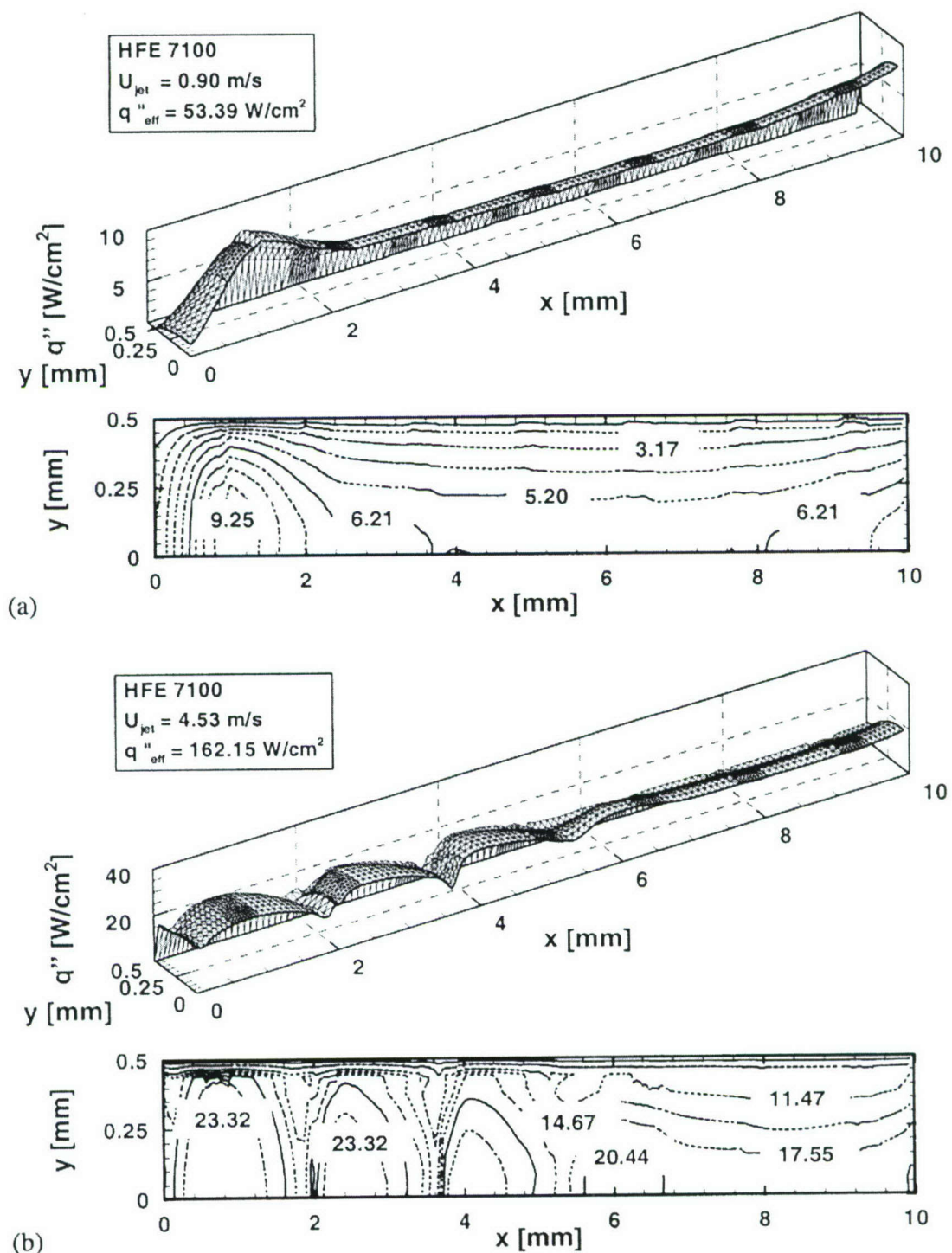


Figure 4.10 Numerical predictions of micro-channel bottom wall heat flux distribution for (a) $q''_{eff} = 53.39 \text{ W/cm}^2$ and $U_{jet} = 0.90 \text{ m/s}$, and (b) $q''_{eff} = 162.15 \text{ W/cm}^2$ and $U_{jet} = 4.53 \text{ m/s}$.

On the other hand, Fig. 4.10(b) shows strong jets produce noticeable local peaks in the heat flux distribution for several upstream jets. However, the peaks are ultimately damped for the three most downstream jets.

Similar trends also shown in Fig. 4.11 in the form of Nusselt number distribution along the bottom wall, where the local Nusselt number is defined as

$$Nu = \frac{q'' L_{jet}}{k_f(T_s - T_{in})}. \quad (4.2)$$

4.3.2. Slot Jets

Figures 4.12(a) and 4.12(b) show temperature distribution of the micro-channel bottom wall of the unit cell, including the sidewall, for $q''_{eff} = 20.58 \text{ W/cm}^2$ with $Re_{jet} = 2,892$ and $q''_{eff} = 76.37 \text{ W/cm}^2$ with $Re_{jet} = 26,764$, respectively. Overall, surface temperature increases along the micro-channel flow direction, and higher temperatures are encountered near the outlet. Comparing the two figures shows higher jet velocities decrease surface temperature. Slightly lower surface temperatures are achieved below the sidewall due to the aforementioned fin effect. Along the centerline of the micro-channel bottom wall, Fig. 4.12(a) shows the lowest surface temperature is achieved immediately below the center of the slot jet ($x = 0$). However, the lowest temperature of the channel bottom wall is located near the end of the slot jet span because of increased velocity along the micro-channel.

Figures 4.13 and 4.14 show the heat flux distribution along the micro-channel bottom wall and the sidewall, respectively. The local heat flux is evaluated from Eq. (4.1). Both distributions in Fig. 4.13 show heat flux is greatest near the jet centerline due to the impingement effect and thin boundary layer. Notice how the heat flux becomes vanishingly small in the lower corner of the micro-channel where the flow is highly weakened for the rectangular channel. Figures 4.14(a) and 4.14(b) show a sharp rise in heat flux along the sidewall a short distance above the test surface. This rise is the result of the wall jet forming away from the stagnation zone of the slot jet. Notice the stronger influence of this wall jet in Fig. 4.14(b) for the higher Reynolds number case. The wall

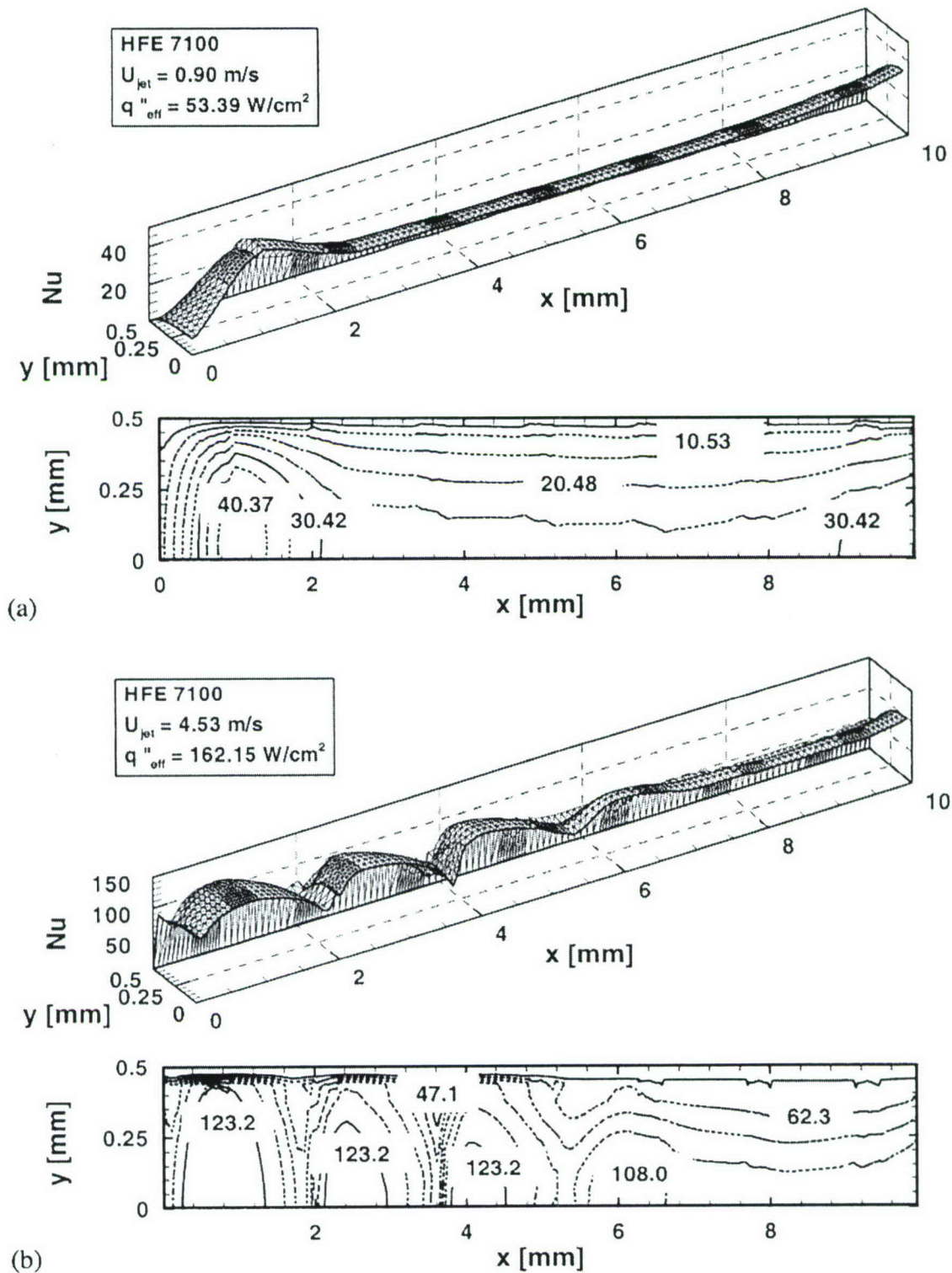


Figure 4.11 Numerical predictions of micro-channel bottom wall Nusselt number distribution for (a) $q''_{eff} = 53.39 \text{ W/cm}^2$ and $U_{jet} = 0.90 \text{ m/s}$, and (b) $q''_{eff} = 162.15 \text{ W/cm}^2$ and $U_{jet} = 4.53 \text{ m/s}$.

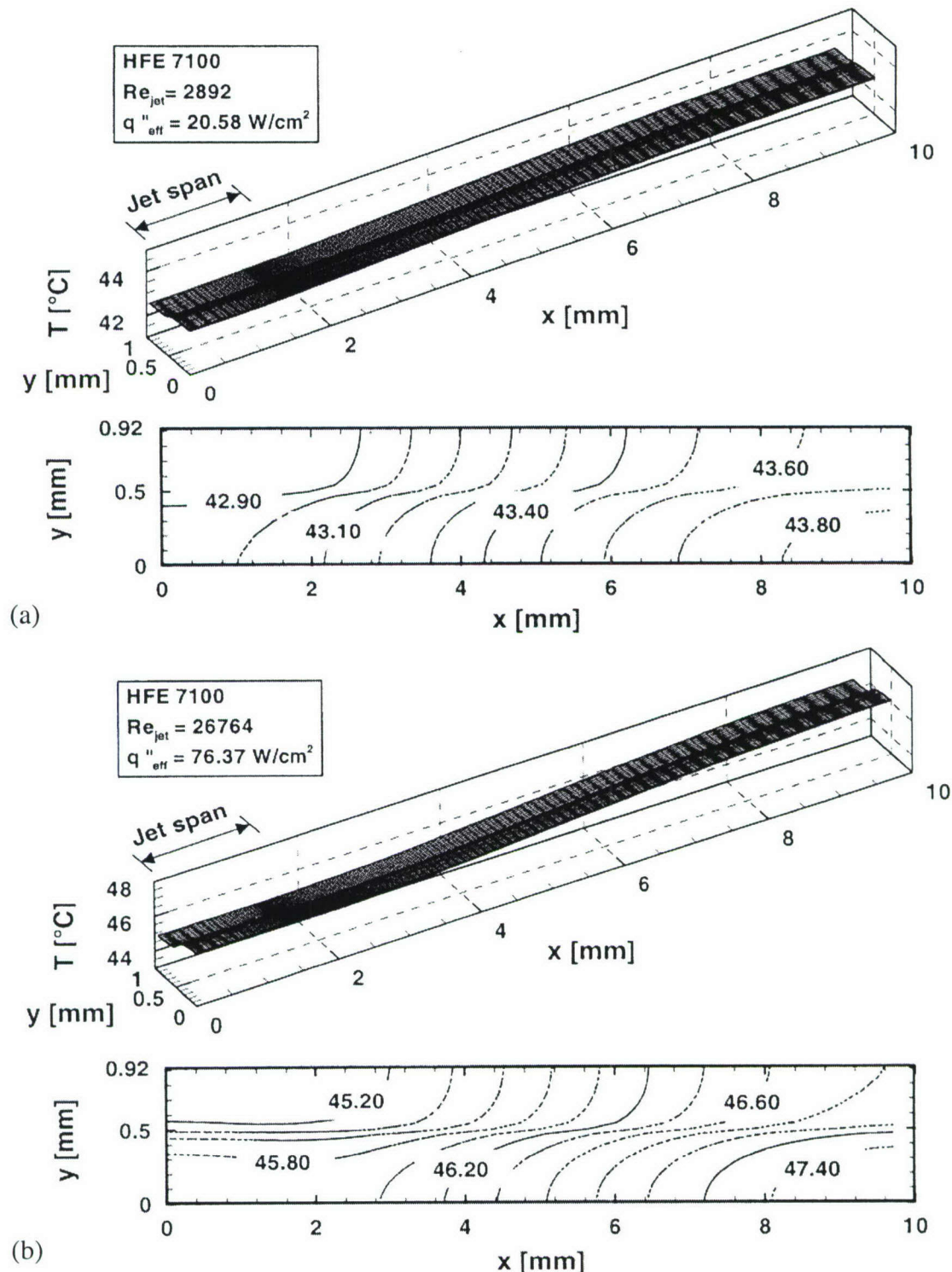


Figure 4.12 Numerical predictions of micro-channel bottom wall temperature distribution including sidewall for (a) $Re_{jet} = 2892$ and $q''_{eff} = 20.58 \text{ W/cm}^2$, and (b) $Re_{jet} = 26764$ and $q''_{eff} = 76.37 \text{ W/cm}^2$.

jet flow also induces strong circumferential recirculation, producing high fluxes along the entire sidewall, which is obviously being sustained by heat conduction along the sidewall. Figure 4.15 shows local Nusselt number along the micro-channel's bottom wall follows a distribution similar to that shown in Fig. 4.13 for heat flux. The local Nusselt number is calculated from Eq. (4.2).

4.4. Different Circular-Jet-Pattern Configurations

Numerical simulations of the different jet patterns are conducted to predict both the complex micro-jet/micro-jet flow interaction and wall temperature distribution. Two ultimate cooling objectives are to achieve, for a given flow rate, the highest possible heat transfer coefficient and lowest wall temperature gradients.

4.4.1. Determination of Jet Velocities

Jet velocities of differently sized jets can be related to one another by equating their pressure drop. Consider a cooling module that contains three different jet sizes, D_{jet1} , D_{jet2} and D_{jet3} . Equal pressure drop requires that

$$\Delta P_1 = \Delta P_2 = \Delta P_3 = f \frac{H_{jet}}{D_{jet1}} \frac{\rho_f U_{jet1}^2}{2} = f \frac{H_{jet}}{D_{jet2}} \frac{\rho_f U_{jet2}^2}{2} = f \frac{H_{jet}}{D_{jet3}} \frac{\rho_f U_{jet3}^2}{2}, \quad (4.3)$$

where the pressure drop coefficient, f , is inversely proportional to jet Reynolds (Incropera, 1999)

$$f = K \text{Re}_{jet}^{-1}, \quad (4.4)$$

and K is fairly constant for the conditions of the present study. Equations (4.3) and (4.4) allow the jet velocities to be related to one another as follows:

$$U_{jet2} = \frac{D_{jet2}^2}{D_{jet1}^2} U_{jet1} \quad (4.5a)$$

and

$$U_{jet3} = \frac{D_{jet3}^2}{D_{jet1}^2} U_{jet1}. \quad (4.5b)$$

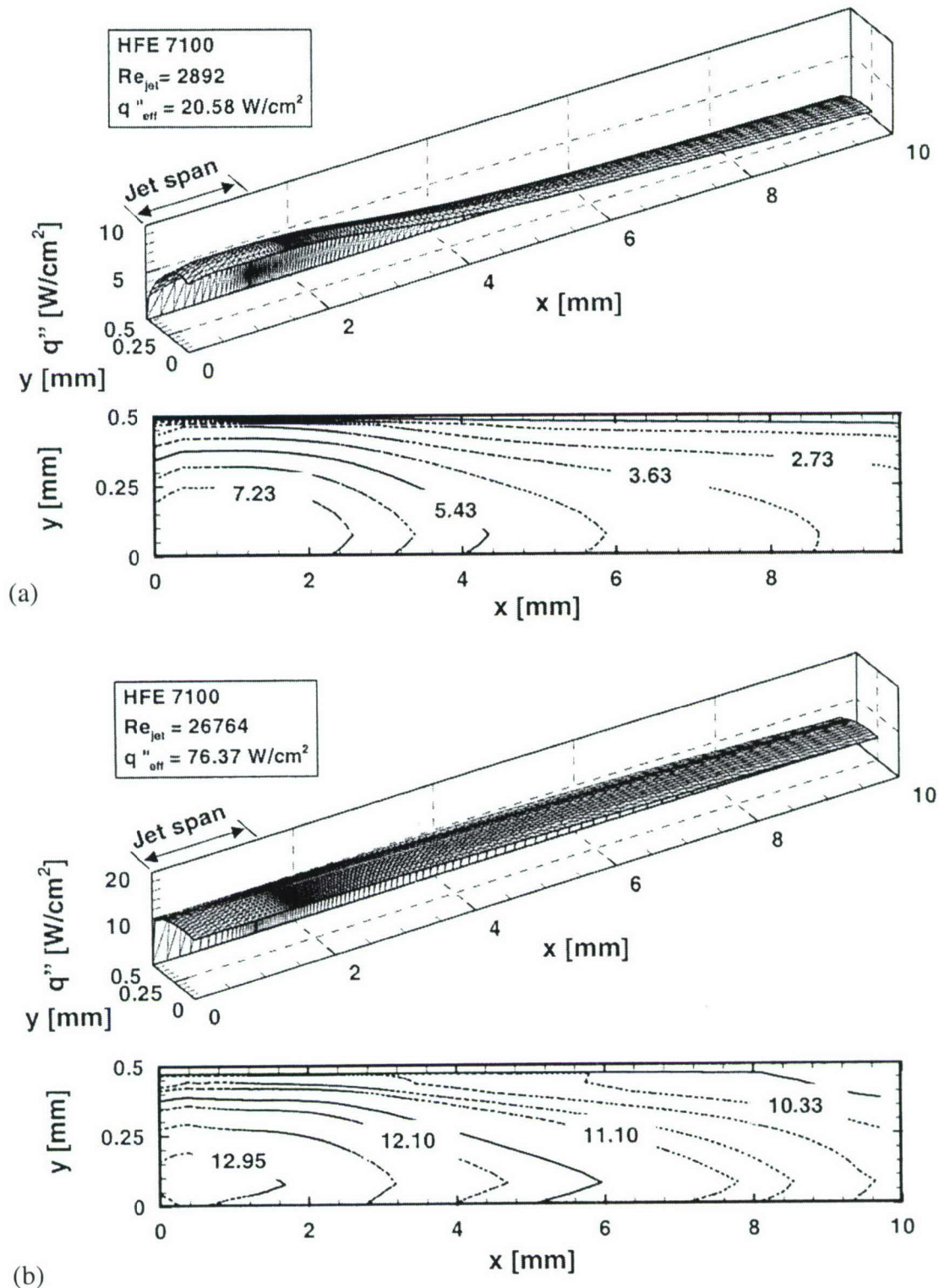


Figure 4.13 Numerical predictions of micro-channel bottom wall heat flux distribution for (a) $Re_{jet} = 2892$ and $q''_{eff} = 20.58 \text{ W/cm}^2$, and (b) $Re_{jet} = 26764$ and $q''_{eff} = 76.37 \text{ W/cm}^2$.

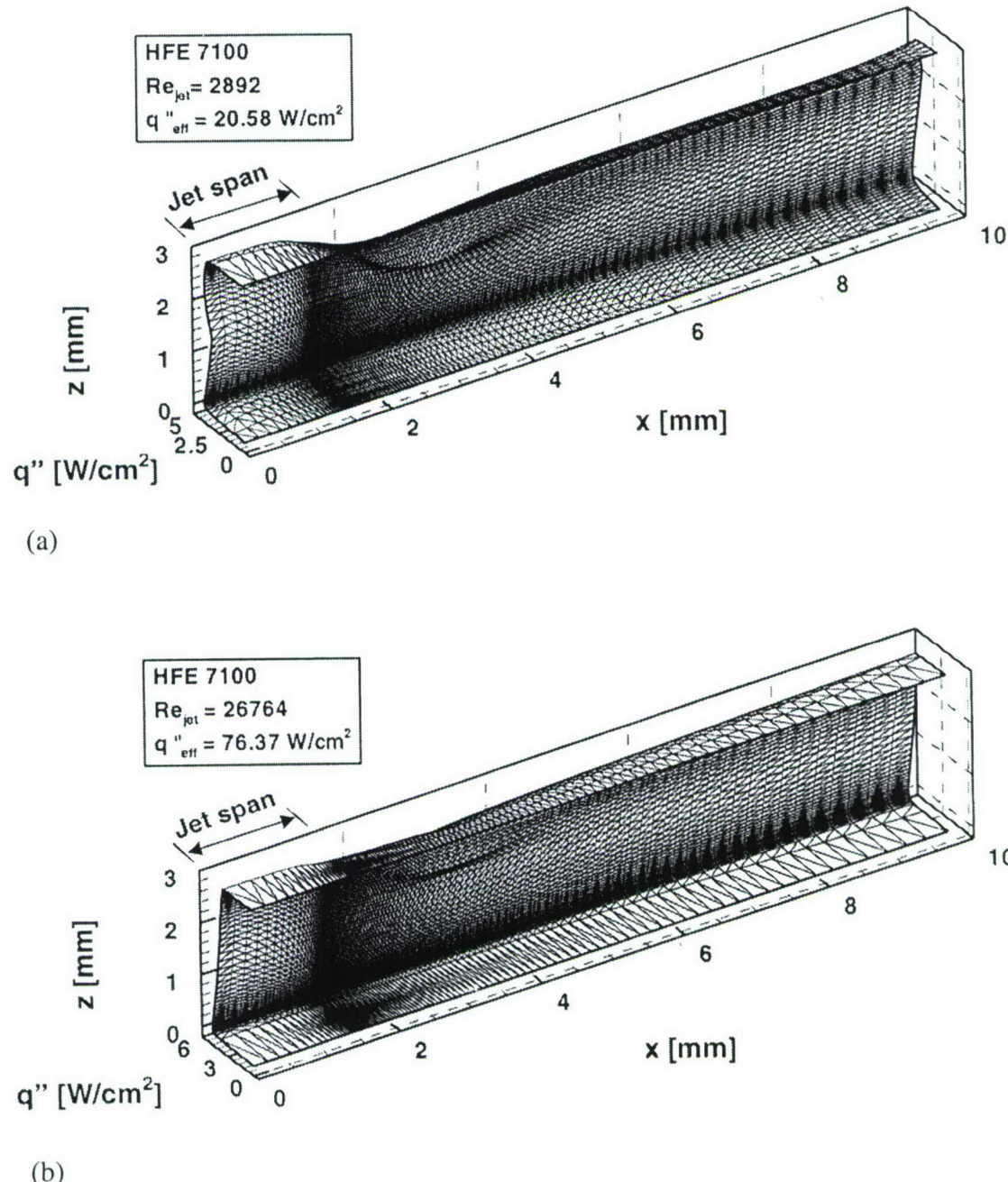


Figure 4.14 Numerical predictions of micro-channel sidewall heat flux distribution for (a) $Re_{jet} = 2892$ and $q''_{eff} = 20.58 \text{ W/cm}^2$, and (b) $Re_{jet} = 26764$ and $q''_{eff} = 76.37 \text{ W/cm}^2$.

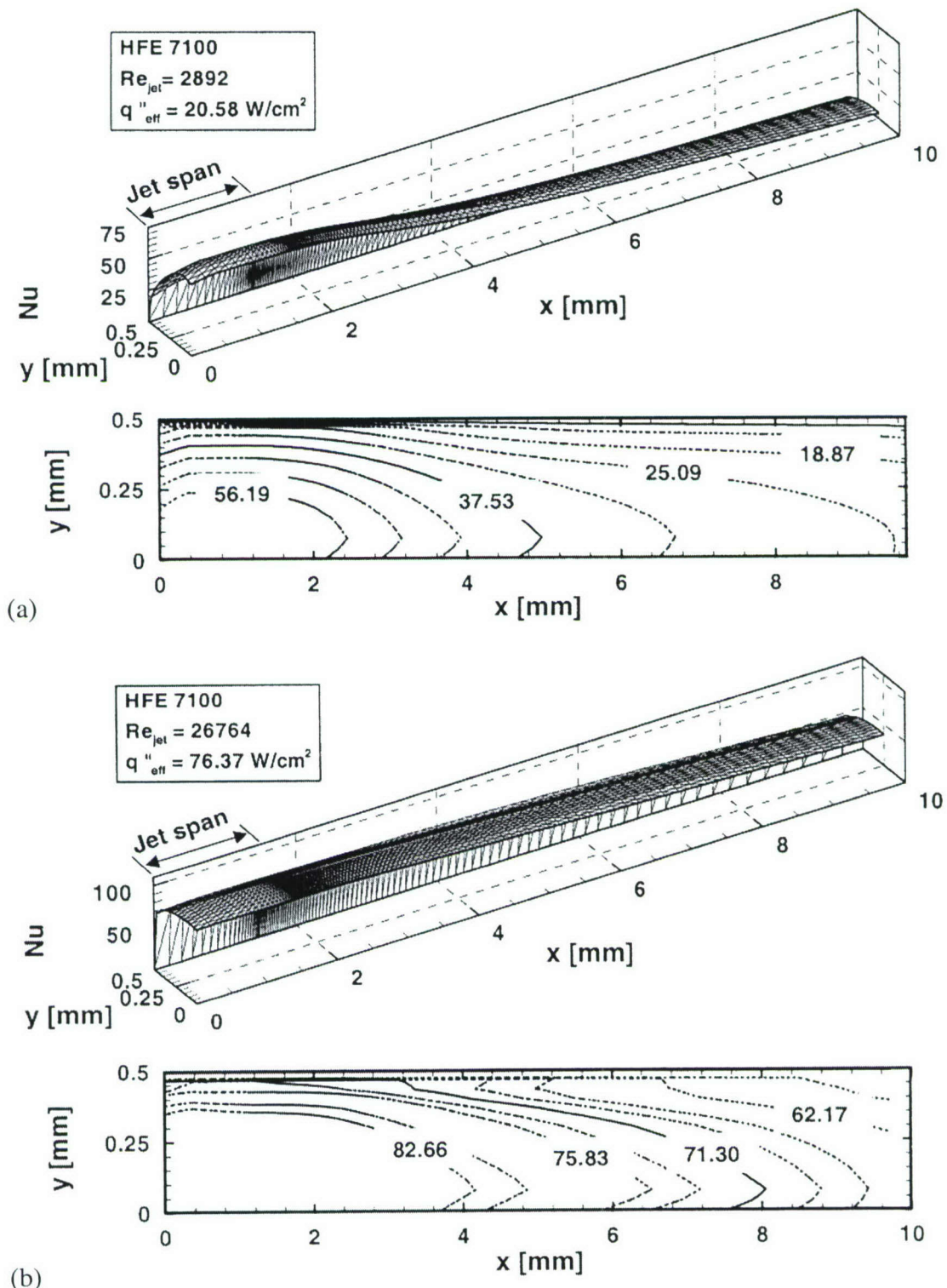


Figure 4.15 Numerical predictions of micro-channel bottom wall Nusselt number distribution for (a) $Re_{jet} = 2892$ and $q''_{eff} = 20.58 \text{ W/cm}^2$, and (b) $Re_{jet} = 26764$ and $q''_{eff} = 76.37 \text{ W/cm}^2$.

Then U_{jet1} can be determined from continuity as

$$\dot{m}_{total} = N_1 \rho_f \left(\frac{\pi D_{jet1}^2}{4} \right) U_{jet1} + N_2 \rho_f \left(\frac{\pi D_{jet2}^2}{4} \right) \left(\frac{D_{jet2}^2}{D_{jet1}^2} U_{jet1} \right) + N_3 \rho_f \left(\frac{\pi D_{jet3}^2}{4} \right) \left(\frac{D_{jet3}^2}{D_{jet1}^2} U_{jet1} \right), \quad (4.6)$$

where N_i is the total number jets of diameter D_{jeti} . The velocities of the other jets can be determined using Eqs. (4.5a) and (4.5b).

4.4.2. Validation of Numerical Predictions

Figure 4.16 compares numerical predictions of the temperature distribution along the thermocouple line in the copper block with the thermocouple measurements for the three jet patterns. The numerical scheme appears equally effective at predicting the temperature variations for the different jet patterns corresponding to different heat fluxes and flow rates. The agreement between the measured and predicted temperatures demonstrates the effectiveness of the present numerical scheme using the standard $k-\varepsilon$ model and the relations used to determine the extent of the laminar zone.

4.4.3. Predicted Trends of Cooling Performance

Figures 4.17-4.19 show flow streamlines and channel bottom wall temperature distribution for one-fourth the unit cell illustrated in Fig. 3.1. Results for the three jet patterns are provided for low, medium, high flow rates in Figs. 4.17, 4.18 and 4.19, respectively.

For the decreasing-jet-size pattern with a low flow rate, Fig. 4.17(a) shows the large jets near the center of the channel are easily able to reach the channel bottom wall, yielding lowest temperatures near the center of the channel. The spent fluid from the first jet and second jet makes it difficult for the downstream jets to reach the bottom wall. However, the heat transfer coefficient increases with increasing flow rate along the flow direction. The decreasing-jet-size pattern appears to effectively utilize both the jet flow and the channel flow to achieve excellent bottom wall temperature uniformity.

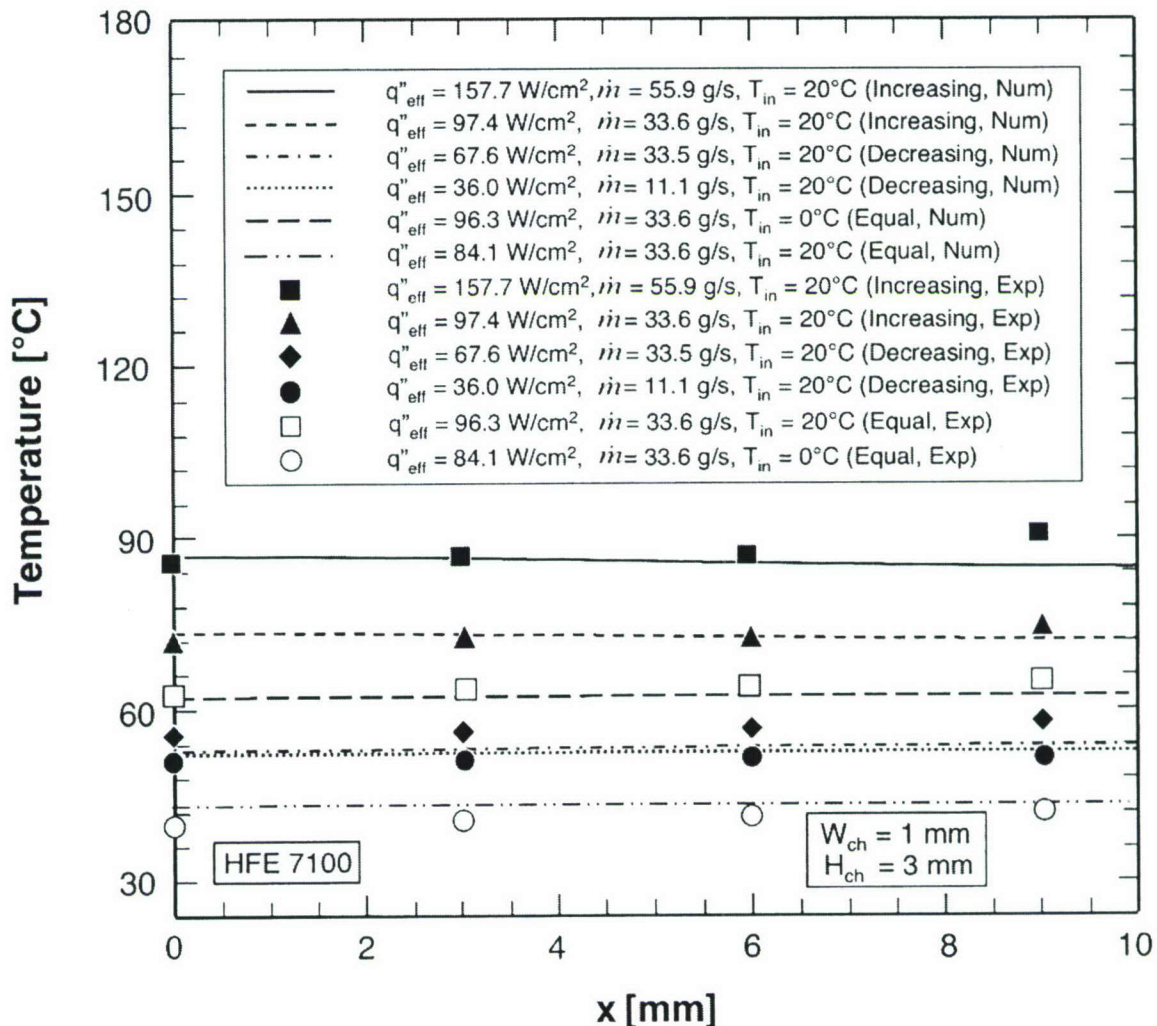


Figure 4.16 Comparison of numerical predictions of temperatures along thermocouple line and measured temperatures.

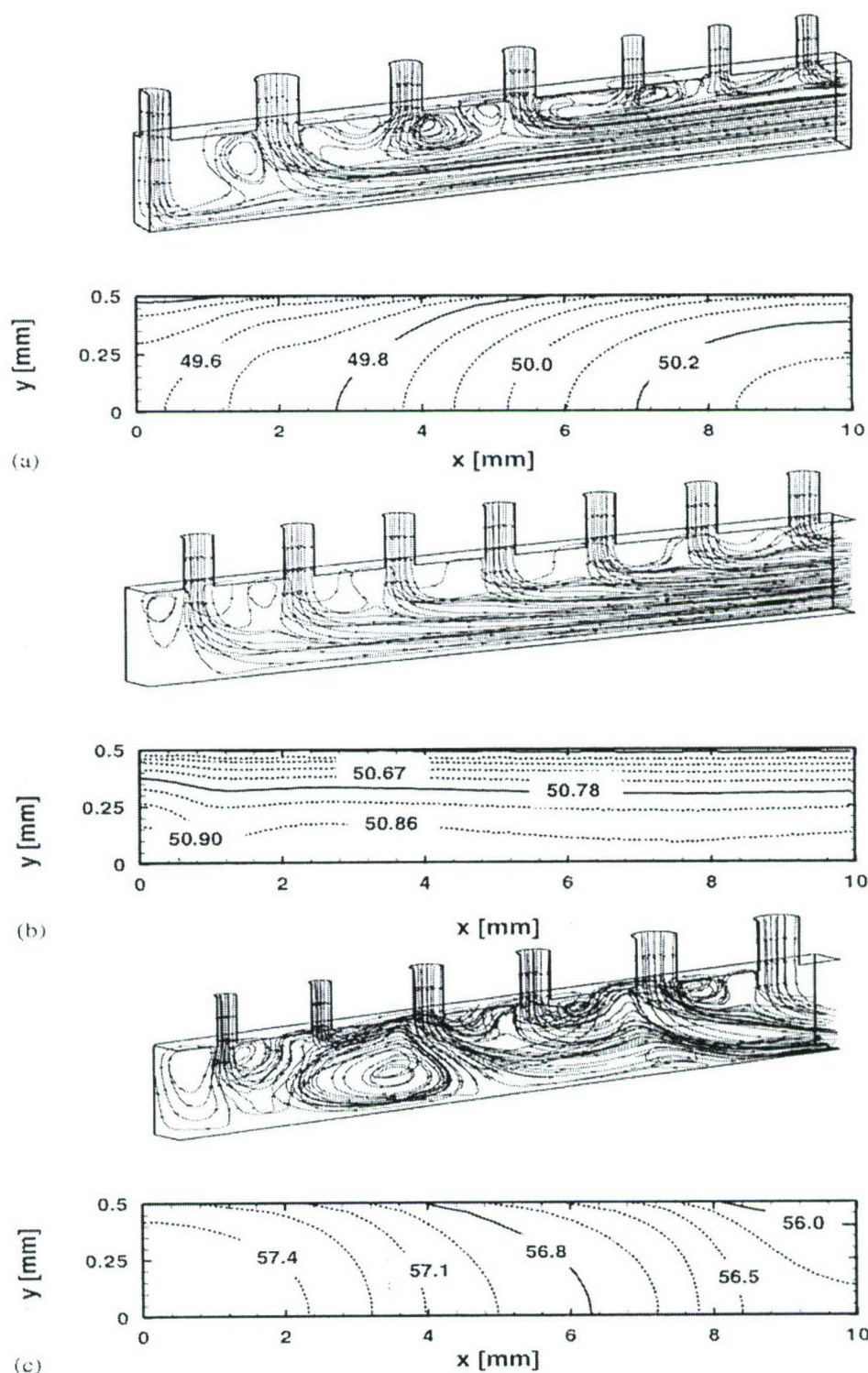


Figure 4.17 Streamlines and wall temperature plots at $q''_{eff} = 36.0 \text{ W/cm}^2$, $\dot{m} = 11.1 \text{ g/s}$ for (a) decreasing jet size, (b) equal jet size, and (c) increasing jet size.

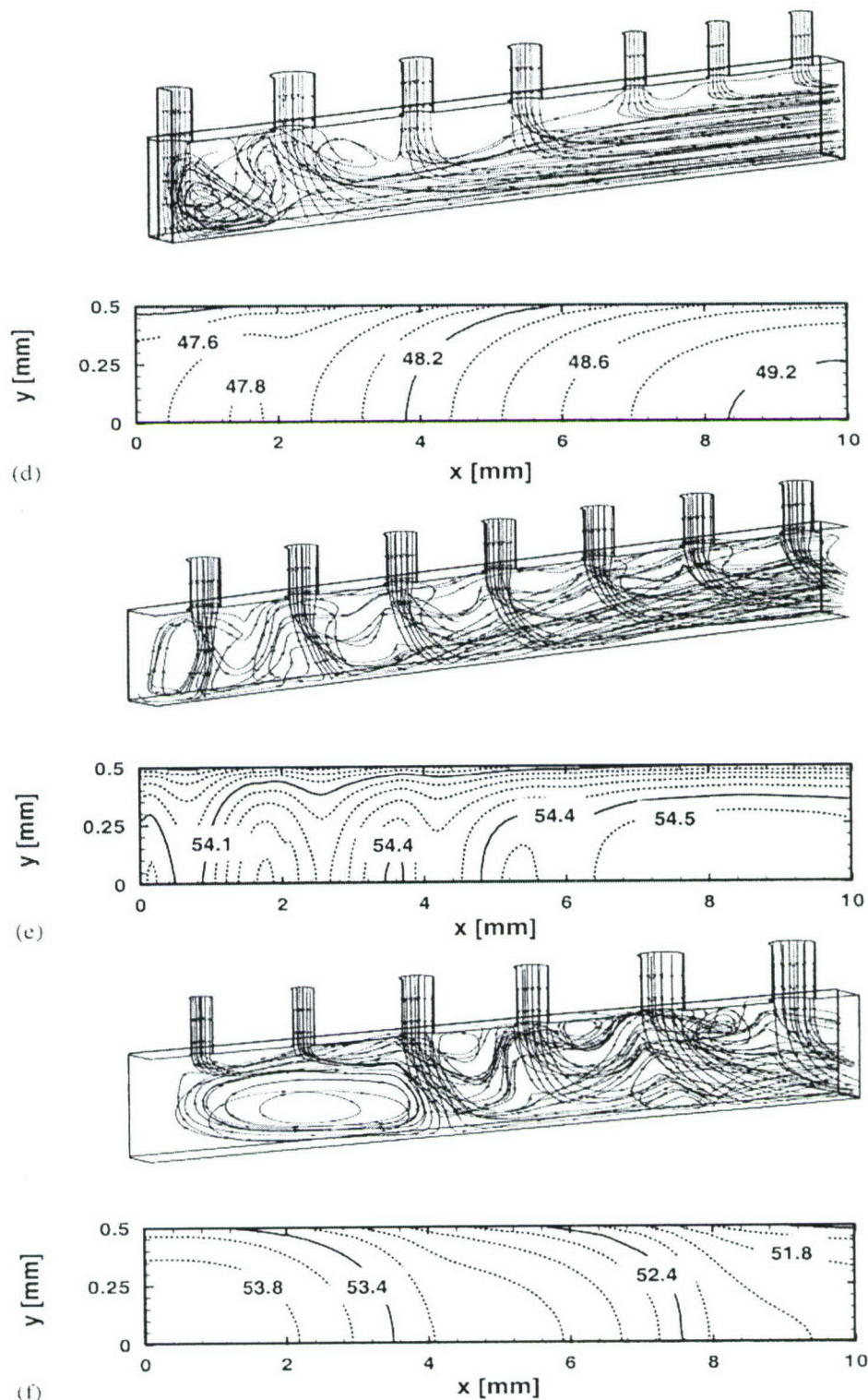


Figure 4.18 Streamline and wall temperature plots at $q''_{eff} = 67.6 \text{ W/cm}^2$, $\dot{m} = 33.6 \text{ g/s}$ for (d) decreasing jet size, (e) equal jet size, and (f) increasing jet size.

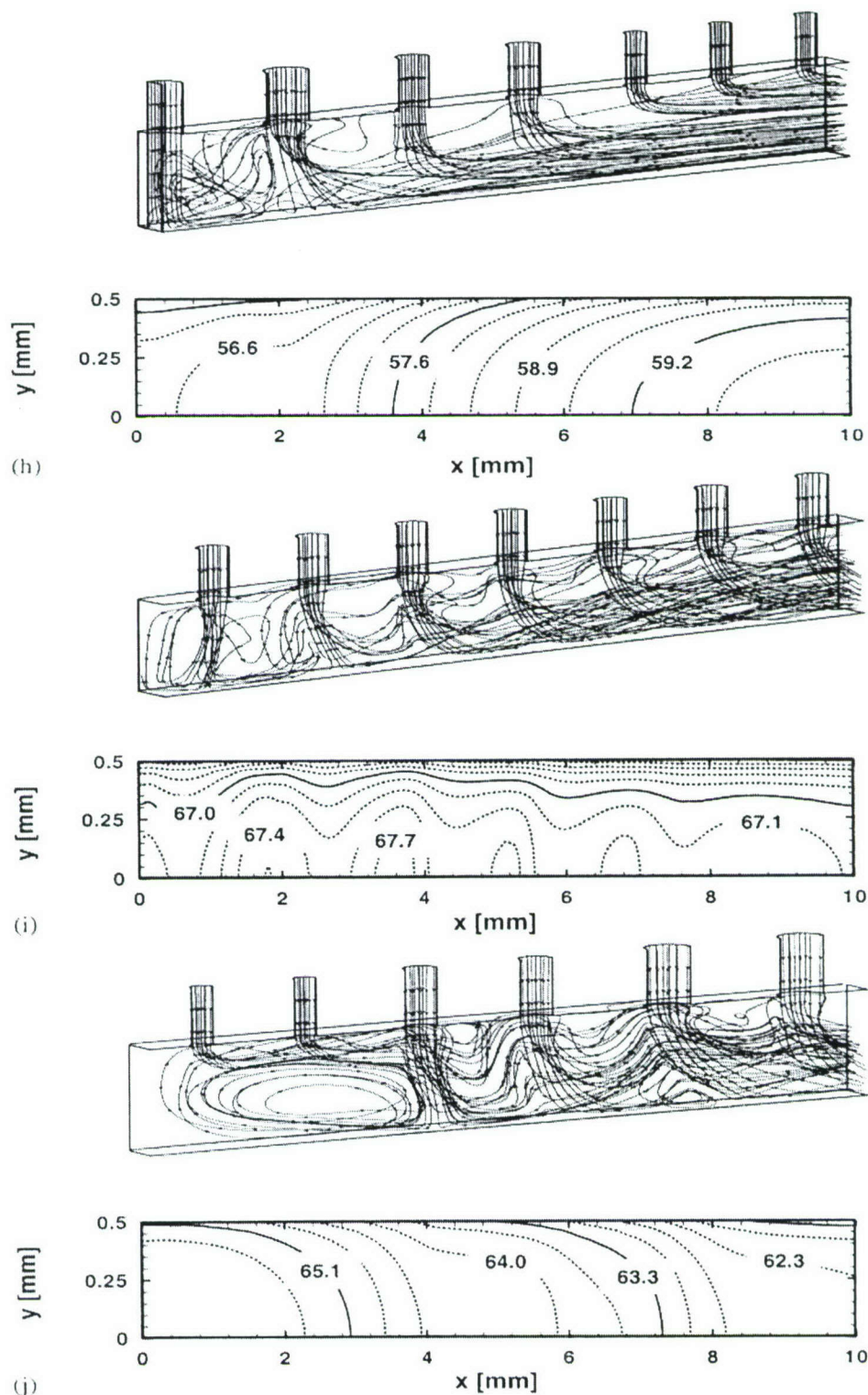


Figure 4.19 Streamlines and wall temperature plots at $q''_{eff} = 121.5 \text{ W/cm}^2$, $\dot{m} = 55.9 \text{ g/s}$ for (h) decreasing jet size, (i) equal jet size, and (j) increasing jet size.

Figure 4.17(b) shows that heat transfer for the equal-jet-size pattern is dominated more by channel flow than by jet impingement. Since the flow rate increases along the flow direction, the lowest temperature is encountered near the channel outlet. For the increasing-jet-size pattern, Fig. 4.17(c) shows the flow is complicated by interactions between neighboring jets. Large jets near the channel outlet create appreciable blockage to coolant flow from the upstream small- and medium-sized jets. Overall, the increasing-jet-size pattern provides the poorest cooling performance of the three jet patterns, evidenced by the highest wall temperatures and largest wall temperature gradients.

Figures 4.18 and 4.19 show, for medium and high flow rates, respectively, similar cooling trends for each jet patterns. One obvious difference from the low flow rate case is a greater influence of jet impingement compared to micro-channel flow for all jet patterns. Strong impingement of the largest jets reduces surface temperature for the decreasing-jet-size pattern, Figs. 4.18(a) and 4.19(a), and the increasing-jet-size pattern, Figs. 4.18(c) and 4.19(c), compared to the equal-jet-size pattern, Figs. 4.18(b) and 4.19(b). Because of the increasing flow rate along the flow direction, fairly uniform temperature is achieved with the decreasing-jet-size pattern as shown in Figs. 4.18(a) and 4.19(a). Excellent surface temperature uniformity is achieved with the equal-jet-size pattern at medium and high flow rates as shown in Figs. 4.18(b) and 4.19(b). For the increasing-jet-size pattern, the increasing flow rate escalates the aforementioned blockage effect, causing appreciable recirculation in the flow from the upstream small jets as shown in Figs. 4.18(c) and 4.19(c). Despite the ability to achieve relatively low overall wall temperatures, the flow blockage induces large wall temperature gradients for the increasing-jet-size pattern.

Figure 4.20 shows the effects of flow rate on temperature distribution along the centerline of the channel's bottom wall. For the three jet patterns, increasing flow rate decreases the bottom wall temperature at the expense of a higher temperature gradient. The medium and high flow rate cases manifest the strong impingement effects of the large jets in the form of low upstream temperatures for the decreasing-jet-size pattern, Fig. 4.20(a), and low downstream temperatures for the increasing-jet-size pattern, Fig. 4.20(c). Figure 4.20 shows, for all flow rates, the highest single-phase heat transfer

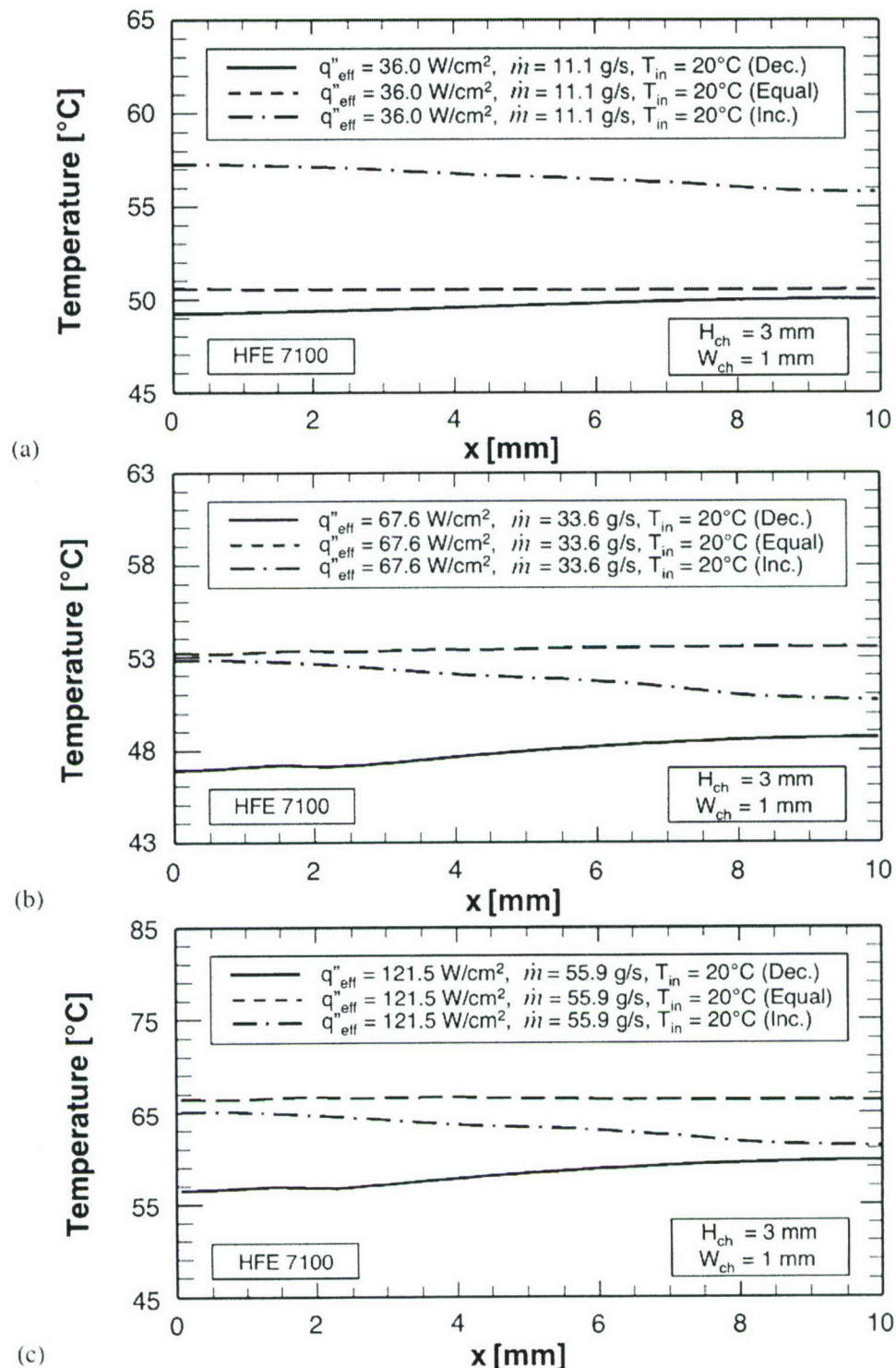


Figure 4.20 Variation of wall temperature along micro-channel for
 (a) $q''_{eff} = 36.0 \text{ W/cm}^2$, $\dot{m} = 11.1 \text{ g/s}$, (b) $q''_{eff} = 67.6 \text{ W/cm}^2$,
 $\dot{m} = 33.6 \text{ g/s}$, and (c) $q''_{eff} = 121.5 \text{ W/cm}^2$, $\dot{m} = 55.9 \text{ g/s}$.

coefficients (*i.e.*, lowest wall temperatures) are achieved with the decreasing-jet-size pattern. However, the greatest temperature uniformity is realized with the equal-jet-size pattern. These trends point to important practical trends in cooling system design. The increasing-jet-size pattern is preferred for high-heat-flux removal, while the equal-jet-size pattern is preferred for devices demanding greater temperature uniformity.

CHAPTER 5. SINGLE-PHASE EXPERIMENTAL RESULTS

5.1. Overall Single-Phase Cooling Performance

5.1.1. Circular Jets

As indicated earlier, three key objectives of the new hybrid cooling scheme are (1) dissipating large heat fluxes, (2) maintaining low surface temperatures, and (3) reducing surface temperature gradients. Figure 5.1 shows thermocouple readings of the copper heating block as a function of jet Reynolds number for $q''_{eff} = 50$ and 91 W/cm^2 . Clearly evident in this figure is the advantageous effect of increasing Re_{jet} at reducing surface temperature for a given heat flux. There is also a slight decrease in temperature gradient between thermocouples at higher Re_{jet} . However, both surface temperature and temperature gradient increase with increasing heat flux. Overall, axial surface temperature variations over the entire single-phase cooling region up to 50 W/cm^2 were less than 1.5°C .

5.1.2. Slot Jets

Choice of key geometrical parameters of the test module is based largely on the numerical findings. Key goals in the module design are to enhance heat flux removal, reduce surface temperature, and reduce surface temperature gradients. Figure 5.2 shows thermocouple readings in the copper heating block as a function of Reynolds numbers for $q''_{eff} = 32 \text{ W/cm}^2$. Increasing Reynolds number decreases both surface temperature and temperature gradient. Despite the relatively poor thermophysical properties of HFE-7100, the high cooling effectiveness of the hybrid configuration, coupled with the use of indirect refrigeration cooling, enables the dissipation of $q''_{eff} = 305.9 \text{ W/cm}^2$ at

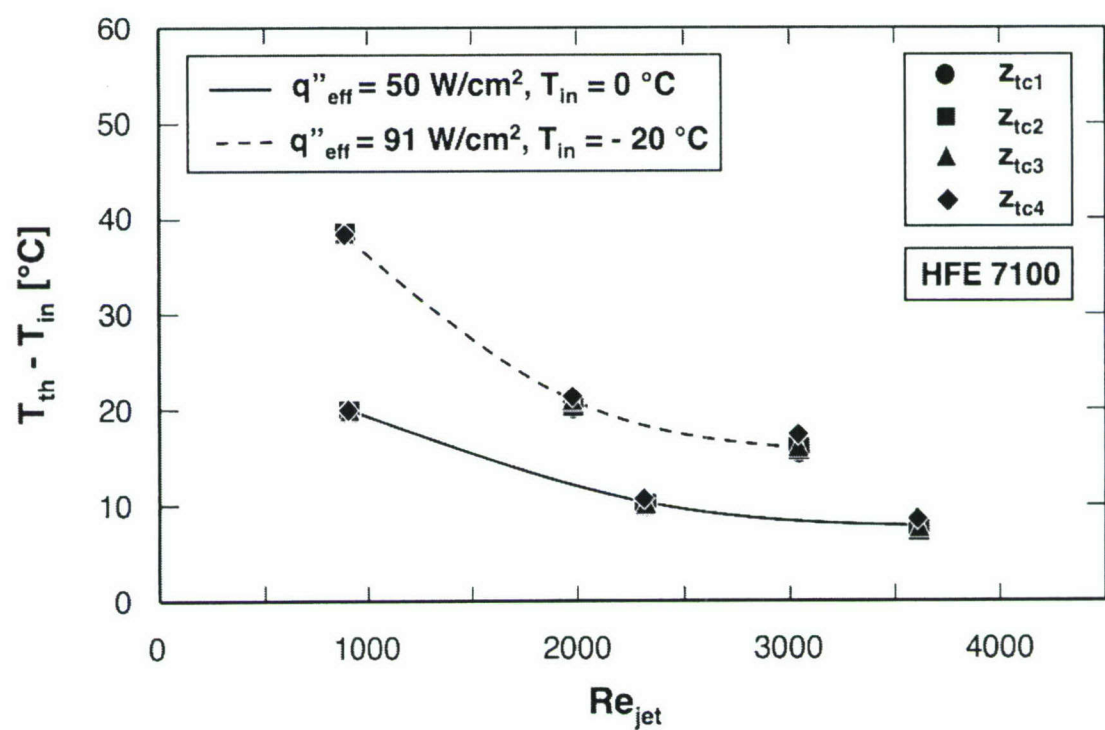


Figure 5.1 Thermocouple readings in copper heating block versus jet Reynolds number for different heat fluxes and inlet temperatures for circular jets.

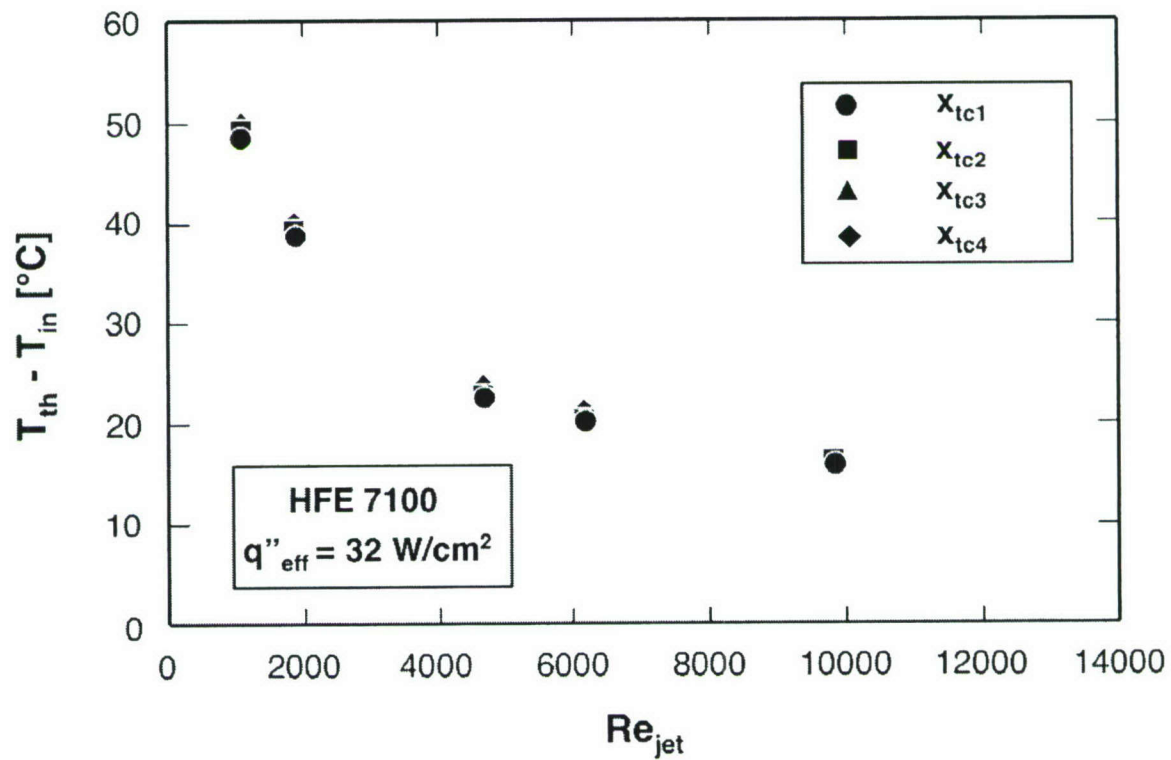


Figure 5.2 Thermocouple readings in copper heating block versus jet Reynolds number for different heat fluxes and inlet temperatures for slot jets.

$T_{in} = -40^{\circ}\text{C}$ and $U_{jet} = 7.37 \text{ m/s}$ without phase change. At this heat flux, the average surface temperature is 70.82°C , well below the maximum recommended temperature for modern electronic devices. Surface temperature variations up to $q_{eff} = 50 \text{ W/cm}^2$ are less than 2°C .

5.1.3. Different Circular-Jet-Pattern Configurations

The flow rate trends depicted in Fig. 4.20 are further substantiated in Fig. 5.3, which shows the heat transfer coefficient data plotted against $Re_{jet,m}$, the jet Reynolds number based on mean velocity of all jets in a micro-jet plate. Clearly evident in Fig. 5.3 is the advantageous effect of increasing $Re_{jet,m}$ for all jet patterns, as well as the superior heat transfer performance of the decreasing-jet-size pattern.

5.2. Correlation of Single-Phase Heat Transfer Data

5.2.1. Circular Jets

A new single-phase heat transfer correlation is sought for the new hybrid cooling scheme. Such a correlation can serve as a convenient tool for design of electronic modules utilizing the new hybrid cooling scheme, eliminating the need for much of the aforementioned numerical modeling.

A superposition technique originally developed by Wadsworth and Mudawar (1990) for slot jets can be tailored to hybrid configurations where different cooling mechanisms dominate different portions of the surface. This technique was quite effective at correlating their single-phase data, and was later used successfully to correlate data for multiple slot jets (Meyer *et al.*, 2006) as well as the present authors' own data for the aforementioned hybrid slot jet/micro-channel cooling scheme (Sung and Mudawar, 2006).

This technique consists of applying different correlations of the same general form

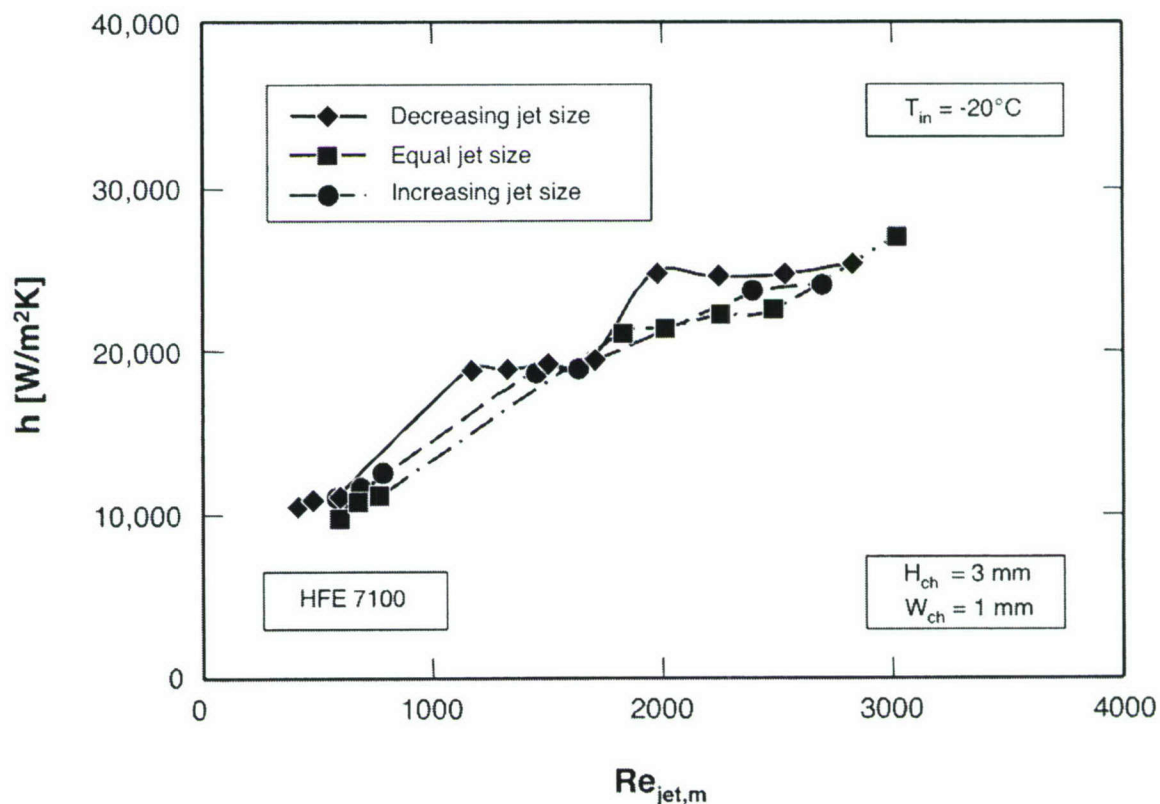


Figure 5.3 Variation of heat transfer coefficient with mean jet Reynolds number for different jet patterns.

$$\frac{\overline{Nu}}{\text{Pr}_f^{0.4}} = f(\text{Re}), \quad (5.1)$$

to the different surface regions. Figure 5.4 illustrates for a single jet cell the different surface regions associated with a single jet: an impingement region, two identical bottom wall regions on either side of the impingement region, and a micro-channel flow region.

The micro-channel flow region encompasses upstream and downstream bottom wall regions shown in Fig. 5.4, as well as the sidewalls and top wall of the micro-channel for the entire jet cell (top wall is thermally conducting in present cooling module). Assuming surface temperature is uniform across the entire wetted surface, the superpositioning technique yields the following relation for overall heat transfer coefficient, \bar{h}_L :

$$\bar{h}_L p_h L = 2 \sum_{i=1}^{N_{jet}/2} \left\{ \bar{h}_{jet,i} \left[\frac{\pi D_{jet}^2}{4} \right] + \bar{h}_{ch1,i} \left[\left(W_{ch} D_{jet} - \frac{\pi D_{jet}^2}{4} \right) \right] + \bar{h}_{ch2,i} \left[p_h \frac{L}{N_{jet}} - \left(W_{ch} D_{jet} + \frac{\pi D_{jet}^2}{4} \right) \right] \right\}, \quad (5.2)$$

where N_{jet} is the number of micro-jets per single micro-channel and p_h the micro-channel perimeter. Since channel velocity increases away from the central jets towards the outlet due to the increased flow rate, Eq. (5.2) is written to allow for variations in the values of heat transfer coefficients between successive jet cells similar to those depicted in Fig. 5.4.

Equation (5.2) can be represented in the dimensionless form

$$\overline{Nu}_L = \frac{\bar{h}_L L}{k_f} = 2 \sum_{i=1}^{N_{jet}/2} \left\{ \frac{\left[\bar{h}_{jet,i} \left(\frac{\pi D_{jet}^2}{4 p_h} \right) \right]}{k_f} + \frac{\left[\bar{h}_{ch1,i} \left(\frac{W_{ch} D_{jet} - \frac{\pi D_{jet}^2}{4}}{p_h} \right) \right]}{k_f} + \frac{\left[\bar{h}_{ch2,i} \left(\frac{\frac{L}{N_{jet}} - \frac{W_{ch} D_{jet}}{p_h} \left(1 + \frac{\pi D_{jet}^2}{4} \frac{1}{W_{ch} D_{jet}} \right)}{k_f} \right) \right]}{k_f} \right\}. \quad (5.3)$$

The Reynolds used to characterize the heat transfer in the different surface regions depicted in Fig. 5.4 are defined as

$$\text{Re}_{jet,i} = \frac{U_{jet} D_{jet}}{\nu_f}, \quad (5.4a)$$

$$\text{Re}_{ch1,i} = \frac{U_{ch1,i} \left(\frac{W_{ch} D_{jet} - \frac{\pi D_{jet}^2}{4}}{p_h} \right)}{\nu_f}, \quad (5.4b)$$

$$\text{Re}_{ch2,i} = \frac{U_{ch2,i} \left[\frac{L}{N_{jet}} - \frac{W_{ch} D_{jet}}{p_h} \left(1 + \frac{\pi D_{jet}^2}{4} \frac{1}{W_{ch} D_{jet}} \right) \right]}{\nu_f}. \quad (5.4c)$$

and

The characteristic velocity in Eq. (5.4b) is assumed equal to the jet velocity due to the strong attachment of wall jet in that region and the Bernoulli assumption as

$$U_{ch,i} = U_{jet}. \quad (5.5)$$

The characteristic velocity in $Re_{ch2,i}$ is determined from continuity, accounting for the gradual increase in flow rate away from the center of the micro-channel as follows:

$$U_{ch2,i} = \frac{U_{jet} \frac{\pi D_{jet}^2}{4} i}{W_{ch} H_{ch}}. \quad (5.6)$$

Therefore the heat transfer correlation can now be written as

$$\begin{aligned}
\frac{\overline{Nu}_L}{Pr_f^{0.4}} &= 2 \sum_{i=1}^{N_{jet}/2} \left\{ C_1 \text{Re}_{jet}^a \left(\frac{D_{jet}}{p_h} \right) + C_2 \text{Re}_{ch}^b + C_3 \text{Re}_{ch2,i}^c \right\} \\
&= 2 \sum_{i=1}^{N_{jet}/2} \left\{ C_1 \text{Re}_{jet}^a \left(\frac{D_{jet}}{p_h} \right) + C_2 \text{Re}_{jet}^b \left(\frac{W_{ch} D_{jet} - \frac{\pi D_{jet}^2}{4}}{p_h D_{jet}} \right)^b + C_3 \text{Re}_{jet}^c \left(\frac{\frac{\pi D_{jet}^2}{4}}{W_{ch} H_{ch}} \left[\frac{1}{N_{jet} D_{jet}} - \frac{W_{ch}}{p_h} \left(1 + \frac{\pi D_{jet}^2}{4} \frac{1}{W_{ch} D_{jet}} \right) \right] i \right)^c \right\} \\
&= C_1 \text{Re}_{jet}^a \left(\frac{D_{jet}}{p_h} \right) N_{jet} + C_2 \text{Re}_{jet}^b \left(\frac{W_{ch} D_{jet} - \frac{\pi D_{jet}^2}{4}}{p_h D_{jet}} \right)^b N_{jet} + \\
&\quad 2 C_3 \text{Re}_{jet}^c \left(\frac{\frac{\pi D_{jet}^2}{4}}{W_{ch} H_{ch}} \left[\frac{1}{N_{jet} D_{jet}} - \frac{W_{ch}}{p_h} \left(1 + \frac{\pi D_{jet}^2}{4} \frac{1}{W_{ch} D_{jet}} \right) \right] \right)^c \left\{ 1^c + 2^c + \dots + (N_{jet}/2)^c \right\}.
\end{aligned} \tag{5.7}$$

The exponent, a , corresponding to the impingement term is set to 0.5, which is the value recommended for the impingement zone of a jet (Wadsworth and Mudawar, 1990). The remaining empirical constants were determined from a least-squares fit to the experimental data, resulting in the following correlation for the hybrid cooling scheme:

$$\begin{aligned}
\frac{\overline{Nu}_L}{Pr_f^{0.4}} &= 63.41 \text{Re}_{jet}^{0.5} \left(\frac{D_{jet}}{p_h} \right) N_{jet} + 0.183 \text{Re}_{jet}^{0.199} \left(\frac{W_{ch} D_{jet} - \frac{\pi D_{jet}^2}{4}}{p_h D_{jet}} \right)^{0.199} N_{jet} + \\
&\quad 0.197 \text{Re}_{jet}^{0.654} \left(\frac{\frac{\pi D_{jet}^2}{4}}{W_{ch} H_{ch}} \left[\frac{1}{N_{jet} D_{jet}} - \frac{W_{ch}}{p_h} \left(1 + \frac{\pi D_{jet}^2}{4} \frac{1}{W_{ch} D_{jet}} \right) \right] \right)^{0.654} \left\{ 1^{0.654} + 2^{0.654} + \dots + (N_{jet}/2)^{0.654} \right\}.
\end{aligned} \tag{5.8}$$

Notice that D_{jet} , H_{ch} , W_{ch} , p_h , L and N_{jet} are purposely retained in Eq. (5.8) rather than replaced with the values used in the present experimental study. This is intended to allow Eq. (5.8) to be used for a hybrid scheme with different values for these parameters. Figure 5.5 shows Eq. (5.8) fits the present single-phase data with a mean absolute error (MAE) of only 6.04 %, with all data points falling within a $\pm 20\%$ error range.

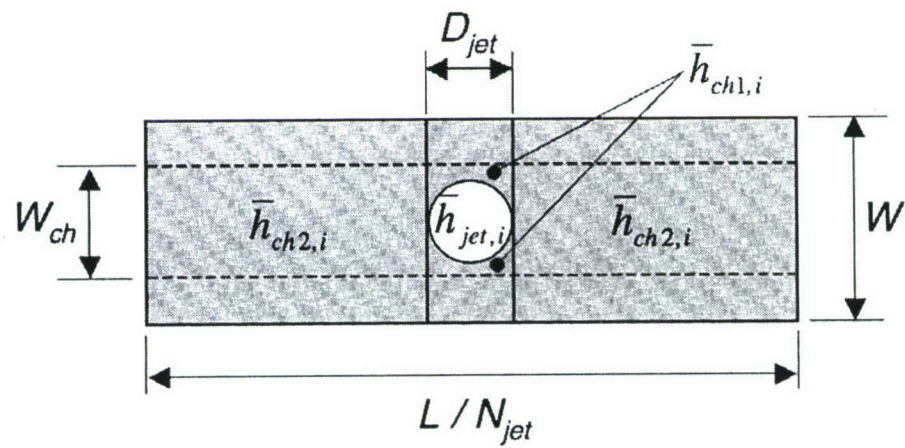


Figure 5.4 Schematic of superpositioning technique for correlating single-phase heat transfer data for circular jets.

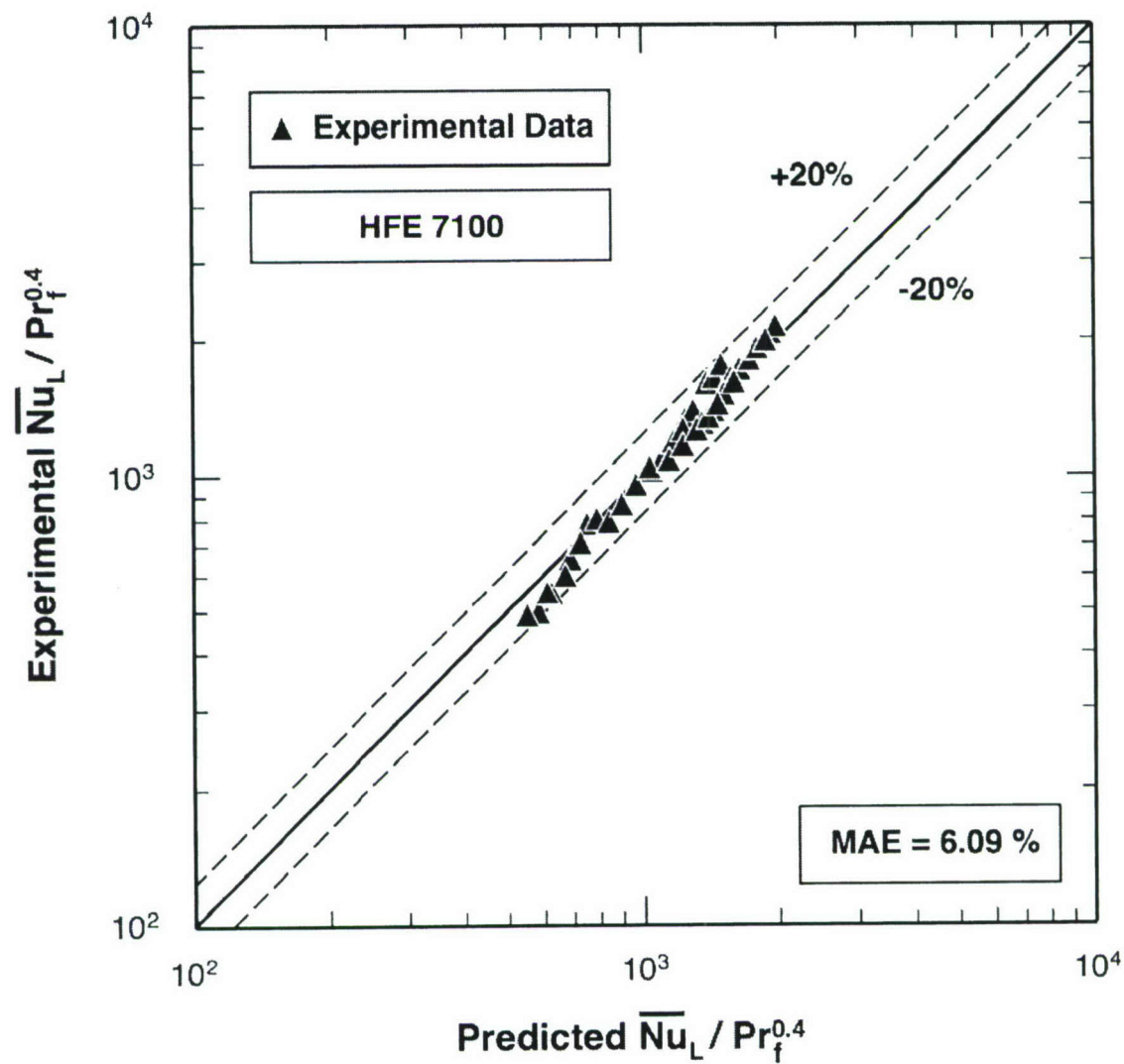


Figure 5.5 Comparison of predictions of single-phase heat transfer correlation and experimental data for equal-size-circular jet pattern.

5.2.2. Different Circular-Jet-Pattern Configurations

The previous section shows the single-phase heat transfer correlation with the superpositioning technique well predicted the experimental data of the equal-jet-size pattern. The superpositioning technique is also used to correlate the single-phase heat transfer data for the three jet patterns. The procedure of the single-phase correlation is exactly same as the previous section except calculating the channel velocity. Due to the Bernoulli effect, the sidewall characteristic velocity is assumed equal to the jet velocity. The channel velocity can be determined from mass conservation, accounting for the gradual increase in flow rate away from the center of the micro-channel as

$$U_{ch,i} = U_{jet,i} \quad (5.9a)$$

and

$$U_{ch2,i} = \sum_{j=1}^i \frac{U_{jet,j} \frac{\pi D_{jet,j}^2}{4}}{W_{ch} H_{ch}}. \quad (5.9b)$$

Therefore, the heat transfer correlation can be written as

$$\begin{aligned} \frac{\overline{Nu}_L}{Pr_f^{0.4}} &= \sum_{i=1}^{N_{jet}} \left\{ C_1 Re_{jet,i}^a \left(\frac{D_{jet,i}}{p_h} \right) + C_2 Re_{ch1,i}^b + C_3 Re_{ch2,i}^c \right\} \\ &= \sum_{i=1}^{N_{jet}} \left\{ C_1 Re_{jet,i}^a \left(\frac{D_{jet,i}}{p_h} \right) + C_2 Re_{jet,i}^b \left(\frac{W_{ch} D_{jet,i} - \frac{\pi D_{jet,i}^2}{4}}{p_h D_{jet,i}} \right)^b \right. \\ &\quad \left. + C_3 Re_{jet,i}^c \left[\sum_{j=1}^i \left(\frac{\left(\frac{U_{jet,j}}{U_{jet,i}} \right) \frac{\pi D_{jet,j}^2}{4}}{W_{ch} H_{ch}} \right) \left[\frac{L_{jet,i}}{D_{jet,i}} - \frac{W_{ch}}{p_h} \left(1 + \frac{\pi D_{jet,i}^2}{4} \frac{1}{W_{ch} D_{jet,i}} \right) \right] \right]^c \right\} \end{aligned} \quad (5.10)$$

Equation (5.10) can also be written as

$$\begin{aligned}
\frac{\overline{Nu}_L}{Pr_f^{0.4}} = & \sum_{i=1}^{N_{jet}} \sum_{j=1}^i \left\{ C_1 \text{Re}_{jet,i}^a \left(\frac{D_{jet,i}}{p_h} \right) \left(\frac{1}{i} \right) + C_2 \text{Re}_{jet,i}^b \left(\frac{W_{ch} D_{jet,i} - \frac{\pi D_{jet,i}^2}{4}}{p_h D_{jet,i}} \right)^b \left(\frac{1}{i} \right) \right. \\
& \left. + C_3 \text{Re}_{jet,i}^c \left[\frac{\left(\frac{U_{jet,j}}{U_{jet,i}} \right) \frac{\pi D_{jet,j}^2}{4}}{W_{ch} H_{ch}} \left[\frac{L_{jet,i}}{D_{jet,i}} - \frac{W_{ch}}{p_h} \left(1 + \frac{\pi D_{jet,i}^2}{4} \frac{1}{W_{ch} D_{jet,i}} \right) \right] \right]^c \right\}.
\end{aligned} \tag{5.11}$$

As indicated earlier, Eqs. (5.10) and (5.11) are valid for jet patterns that do not include a central jet. For patterns with a central jet, these equations must be modified by including the following term for each side of the micro-channel as

$$\begin{aligned}
& C_1 \text{Re}_{jet,i}^a \left(\frac{(D_{jet,i}/2)}{p_h} \right) + C_2 \text{Re}_{jet,i}^b \left(\frac{W_{ch} (D_{jet,i}/2) - \frac{\pi (D_{jet,i}/2)^2}{4}}{p_h D_{jet,i}} \right)^b \\
& + C_3 \text{Re}_{jet,i}^c \left[\frac{\pi (D_{jet,i}/2)}{W_{ch} H_{ch}} \left[\frac{(L_{jet,i}/2)}{D_{jet,i}} - \frac{W_{ch}}{p_h} \left(\frac{1}{2} + \frac{\pi (D_{jet,i}/2)^2}{4} \frac{1}{W_{ch} D_{jet,i}} \right) \right] \right]^c.
\end{aligned} \tag{5.12}$$

The rest of the single-phase correlation can be obtained by simply setting $U_{jet,1} = U_{jet,i}/2$ and $D_{jet,1} = D_{jet,i}/2$ to the third term in Eqs. (5.10) and (5.11).

The empirical constants are obtained with a least-squares' fit to the single-phase heat transfer data. The following correlation was obtained for the micro-channel/micro-circular-jet-impingement module with equal jet size from the previous section,

$$\frac{\overline{Nu}_L}{Pr_f^{0.4}} = \sum_{i=1}^{N_{jet}} \left\{ 63.41 Re_{jet,i}^{0.5} \left(\frac{D_{jet,i}}{p_h} \right) + 0.183 Re_{jet,i}^{0.199} \left(\frac{W_{ch} D_{jet,i} - \frac{\pi D_{jet,i}^2}{4}}{p_h D_{jet,i}} \right)^{0.199} \right. \\ \left. + 0.197 Re_{jet,i}^{0.654} \left[\sum_{j=1}^i \left(\frac{\left(\frac{U_{jet,j}}{U_{jet,i}} \right) \frac{\pi D_{jet,j}^2}{4}}{W_{ch} H_{ch}} \right) \left[\frac{L_{jet,i}}{D_{jet,i}} - \frac{W_{ch}}{p_h} \left(1 + \frac{\pi D_{jet,i}^2}{4} \frac{1}{W_{ch} D_{jet,i}} \right) \right] \right]^{0.654} \right\}, \quad (5.13)$$

which can also be expressed as

$$\frac{\overline{Nu}_L}{Pr_f^{0.4}} = \sum_{i=1}^{N_{jet}} \sum_{j=1}^i \left\{ 63.41 Re_{jet,i}^{0.5} \left(\frac{D_{jet,i}}{p_h} \right) \left(\frac{1}{i} \right) + 0.183 Re_{jet,i}^{0.199} \left(\frac{W_{ch} D_{jet,i} - \frac{\pi D_{jet,i}^2}{4}}{p_h D_{jet,i}} \right)^{0.199} \left(\frac{1}{i} \right) \right. \\ \left. + 0.197 Re_{jet,i}^{0.654} \left[\frac{\left(\frac{U_{jet,j}}{U_{jet,i}} \right) \frac{\pi D_{jet,j}^2}{4}}{W_{ch} H_{ch}} \left[\frac{L_{jet,i}}{D_{jet,i}} - \frac{W_{ch}}{p_h} \left(1 + \frac{\pi D_{jet,i}^2}{4} \frac{1}{W_{ch} D_{jet,i}} \right) \right] \right]^{0.654} \right\}. \quad (5.14)$$

Figure 5.6 shows Eqs. (5.13) or (5.14) fit the single-phase data for all three micro-jet patterns with a mean absolute error (MAE) of 5.26%, with all data points falling within a $\pm 20\%$ error band. This is proof of the universal validity of this correlation.

5.2.3. Slot Jets

A new single-phase heat transfer correlation is sought for the hybrid micro-channel/slot jet configuration. The superposition technique is employed here as well. Figure 5.7 illustrates the different surface heat transfer regions used in the present superpositioning technique for the hybrid micro-channel/slot jet scheme. The general single-phase correlation form

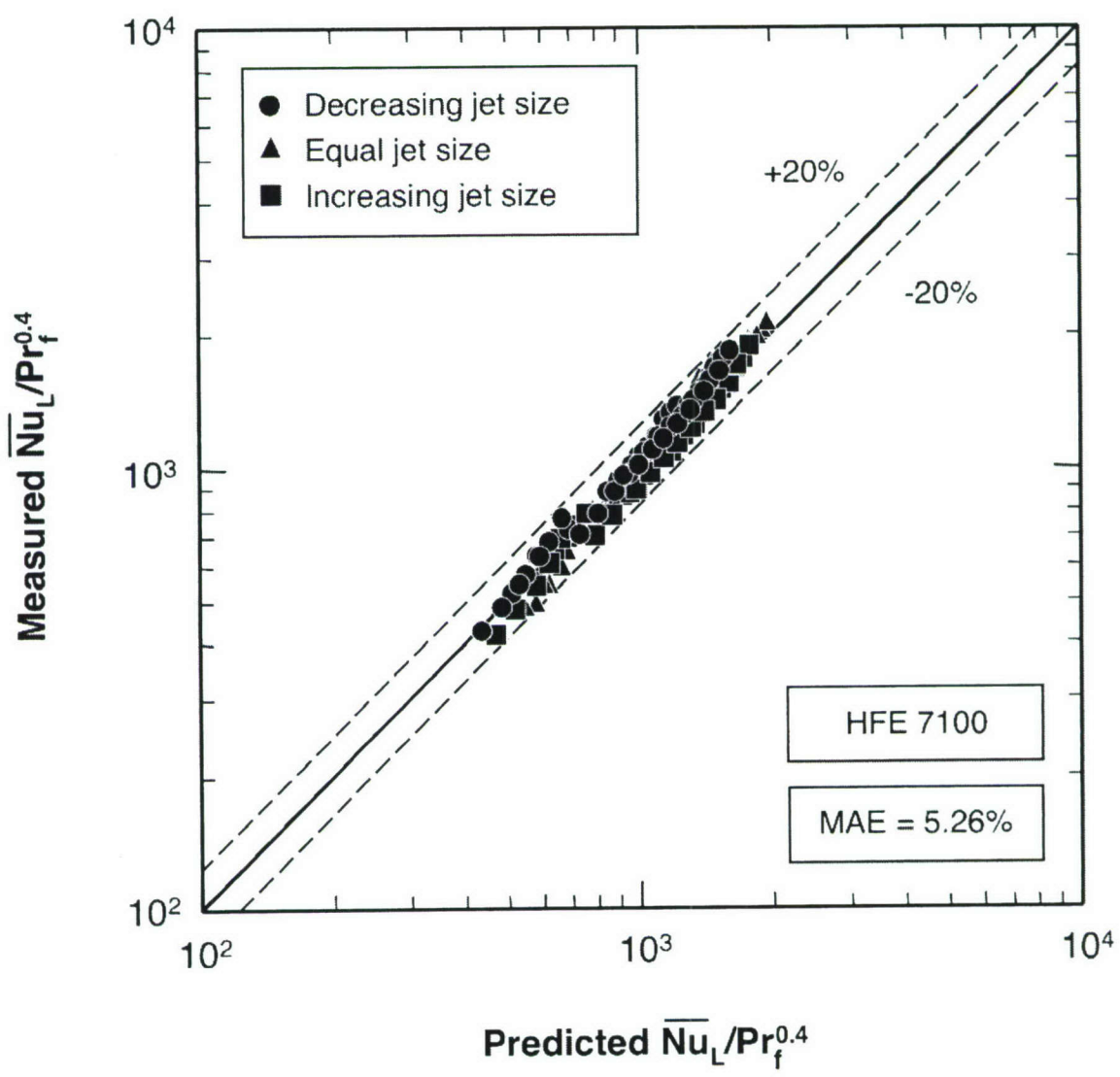


Figure 5.6 Comparison of predictions of single-phase heat transfer correlation and experimental data.

$$\frac{\overline{Nu}_L}{Pr_f^{0.4}} = f(\text{Re}), \quad (5.15)$$

is applied to each of these regions. The surface is comprised of an impingement region, two identical sidewall regions, and two identical channel flow regions. Using the superpositioning technique, the overall heat transfer is represented by the relation

$$\overline{Nu}_L = \frac{\bar{h}_L L}{k_f} = \left(\frac{\bar{h}_{jet} \left(\frac{W_{jet} L_{jet}}{p_h} \right)}{k_f} \right) + \left(\frac{\bar{h}_{ch1} \left(L_{jet} - \frac{2W_{jet} L_{jet}}{p_h} \right)}{k_f} \right) + \left(\frac{\bar{h}_{ch2} \left(L - L_{jet} \right)}{k_f} \right). \quad (5.16)$$

The Reynolds numbers for these regions are given by

$$\text{Re}_{jet} = \frac{U_{jet} (2W_{jet})}{\nu_f}, \quad \text{Re}_{ch1} = \frac{U_{ch1} \left(L_{jet} - \frac{2W_{jet} L_{jet}}{p_h} \right)}{\nu_f}, \quad \text{and} \quad \text{Re}_{ch2} = \frac{U_{ch2} (L - L_{jet})}{\nu_f}. \quad (5.17)$$

For an impinging jet, sidewall characteristic velocity is fairly equal to jet exit velocity due the Bernoulli effect. On the other hand, the channel velocity can be determined from mass conservation as

$$U_{ch1} = U_{jet}, \quad U_{ch2} = U_{jet} \frac{L_{jet} W_{jet}}{H_{ch} W_{ch}}. \quad (5.18)$$

Therefore, the hybrid module's heat transfer correlation can be written as

$$\begin{aligned} \frac{\overline{Nu}_L}{Pr_f^{0.4}} &= C_1 \text{Re}_{jet}^a \left(\frac{L_{jet}}{p_h} \right) + C_2 \text{Re}_{ch1}^b + C_3 \text{Re}_{ch2}^c \\ &= C_1 \text{Re}_{jet}^a \left(\frac{L_{jet}}{p_h} \right) + C_2 \text{Re}_{jet}^b \left(\frac{L_{jet}}{2W_{jet}} - \frac{L_{jet}}{p_h} \right)^b + C_3 \text{Re}_{jet}^c \left(\frac{L_{jet} (L - L_{jet})}{H_{ch} W_{ch}} \right)^c. \end{aligned} \quad (5.19)$$

Wadsworth and Mudawar (1990) showed the impingement term can be accurately characterized by setting $a = 0.5$, which is also adopted in the present correlation. The remaining empirical constants are determined by a least-squares' fit to the present experimental data. Two separate correlations were obtained depending on jet Reynolds number. The first is a high Re_{jet} correlation that is valid for $3,232 < Re_{jet} < 30,853$,

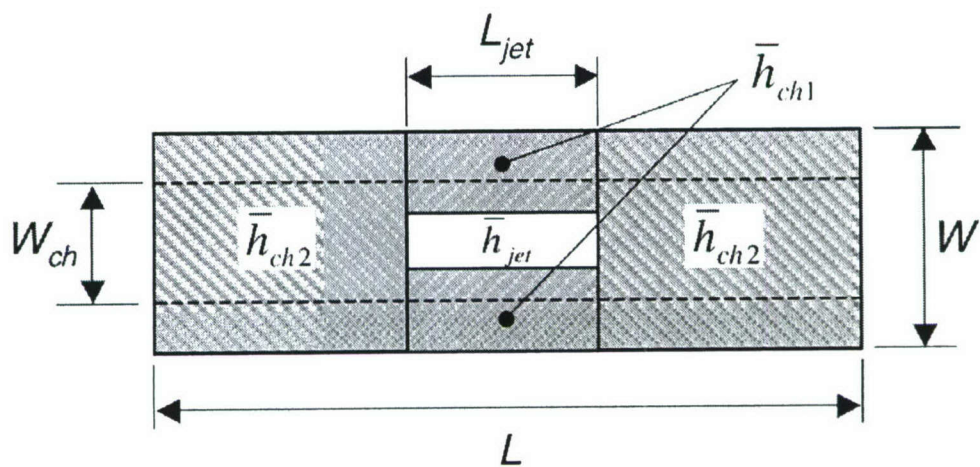


Figure 5.7 Schematic of superpositioning technique for correlating single-phase heat transfer for slot jets.

$$\frac{\overline{Nu}_L}{Pr_f^{0.4}} = 1.53 Re_{jet}^{0.5} \left(\frac{L_{jet}}{p_h} \right) + 5.01 Re_{jet}^{0.6} \left(\frac{L_{jet}}{2W_{jet}} - \frac{L_{jet}}{p_h} \right)^{0.6} + 0.18 Re_{jet}^{0.46} \left(\frac{L_{jet}(L - L_{jet})}{H_{ch}W_{ch}} \right)^{0.46}. \quad (5.20)$$

The second, low Re_{jet} correlation, is valid for $751 < Re_{jet} < 3,232$,

$$\overline{Nu}_L = 1.53 Re_{jet}^{0.5} \left(\frac{L_{jet}}{p_h} \right) Pr_f^{0.4} + 1.3 Re_{jet}^{0.45} \left(\frac{L_{jet}}{2W_{jet}} - \frac{L_{jet}}{p_h} \right)^{0.45} + 9.99 Re_{jet}^{0.52} \left(\frac{L_{jet}(L - L_{jet})}{H_{ch}W_{ch}} \right)^{0.52}. \quad (5.21)$$

Figure 5.8 shows Eqs. (5.20) and (5.21) fit the entire HFE-7100 database with a mean absolute error (MAE) of 3.90%.

5.3. Comparison of Single-Phase Performance of Two Hybrid Cooling Schemes

Both experimental study and numerical simulation are used to predict and compare the cooling performances of the two hybrid cooling configurations, circular jets and slot jets. Aside from the copper block temperature results in Fig. 5.1 and 5.2, temperature variations along the micro-channel sidewalls provide important insight into the cooling performance of each hybrid configuration. Figures 5.9(a) and 5.9(b) show sidewall temperature distributions for circular jets at $q''_{eff} = 162.15 \text{ W/cm}^2$ and $Q = 3.71 \times 10^{-5} \text{ m}^3/\text{s}$, and slot jets at $q''_{eff} = 76.37 \text{ W/cm}^2$ and $Q = 4.51 \times 10^{-5} \text{ m}^3/\text{s}$, respectively. Overall, lower temperatures are achieved with the circular jets despite a significantly higher heat flux for the circular jets compared to the slot jet. Furthermore, far better axial temperature uniformity is evident in the temperature contours of the circular jets compared to the slot jet. Figure 5.10 shows the variation of pressure drop, measured between the inlet and outlet plenums of the test module, with Re_{jet} . Figure 5.10(a) shows pressure drop for the slot jet increases with increasing Re_{jet} but decreases with increasing heat flux. The latter trend is closely related to the lower liquid viscosity at higher temperatures. Figure 5.10(b) shows, for equal Re_{jet} , lower pressure drop is encountered with the slot-jet compared to the circular jets. This can be explained by stronger contraction and expansion effects, and smaller diameter of the circular jets. These findings prove the circular jet pattern provides superior cooling performance, albeit at the expense of greater pressure drop.

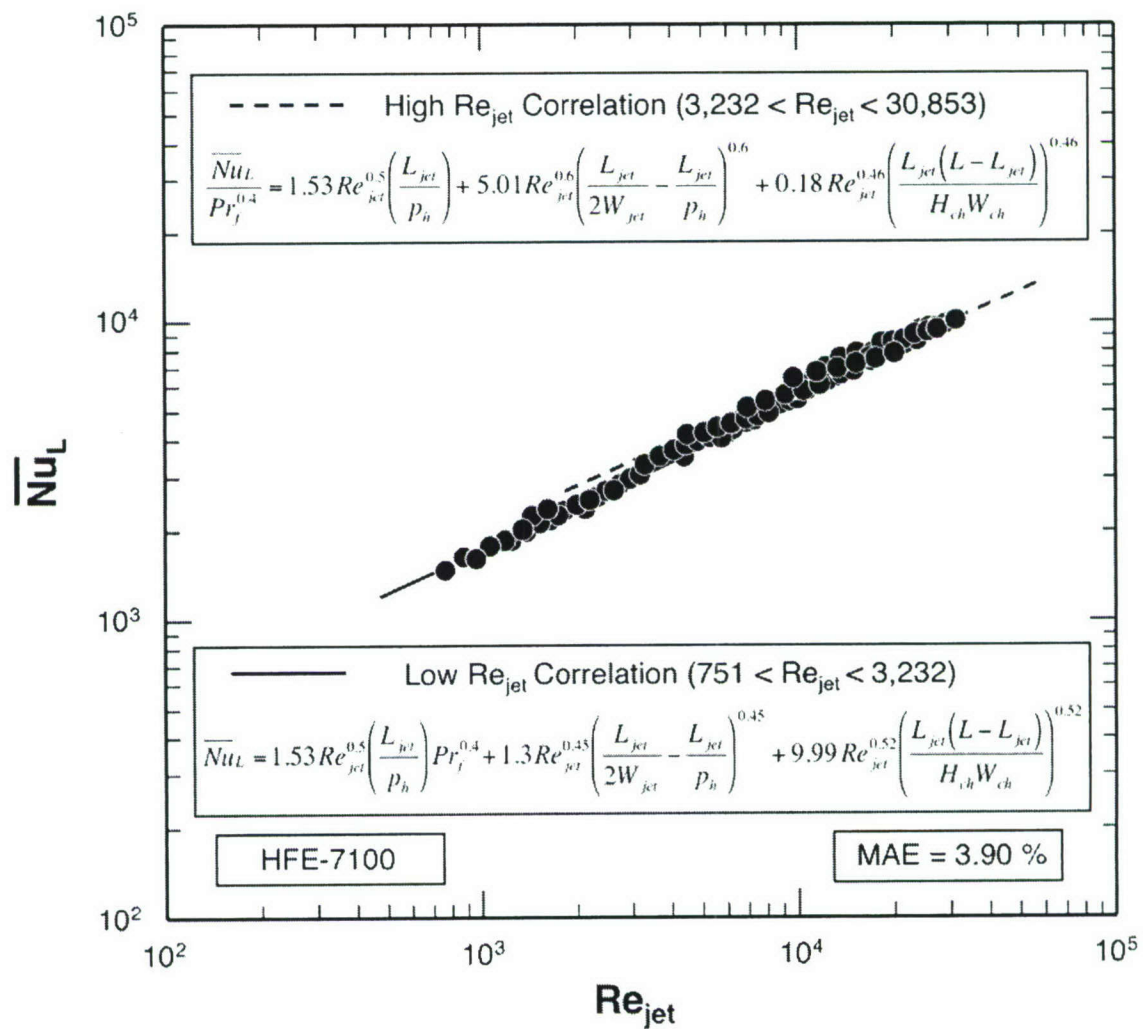


Figure 5.8 Comparison of predictions of single-phase heat transfer coefficient correlations with slot jet HFE-7100 data.

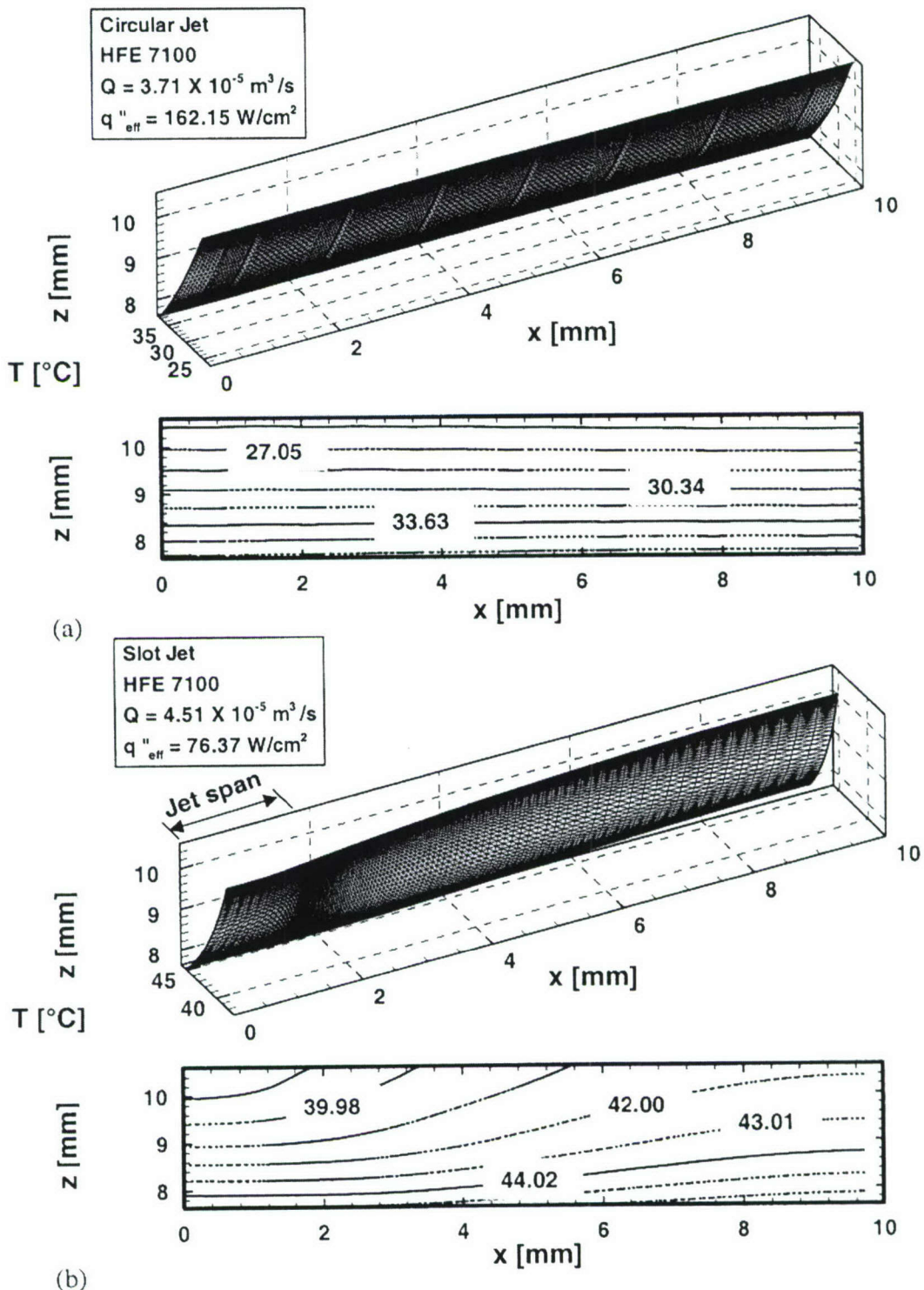


Figure 5.9 Numerical predictions of micro-channel sidewall temperature distribution for (a) circular jets at $q''_{\text{eff}} = 162.15 \text{ W/cm}^2$ and $Q = 3.71 \times 10^{-5} \text{ m}^3/\text{s}$, and (b) slot jet at $q''_{\text{eff}} = 76.37 \text{ W/cm}^2$ and $Q = 4.51 \times 10^{-5} \text{ m}^3/\text{s}$.

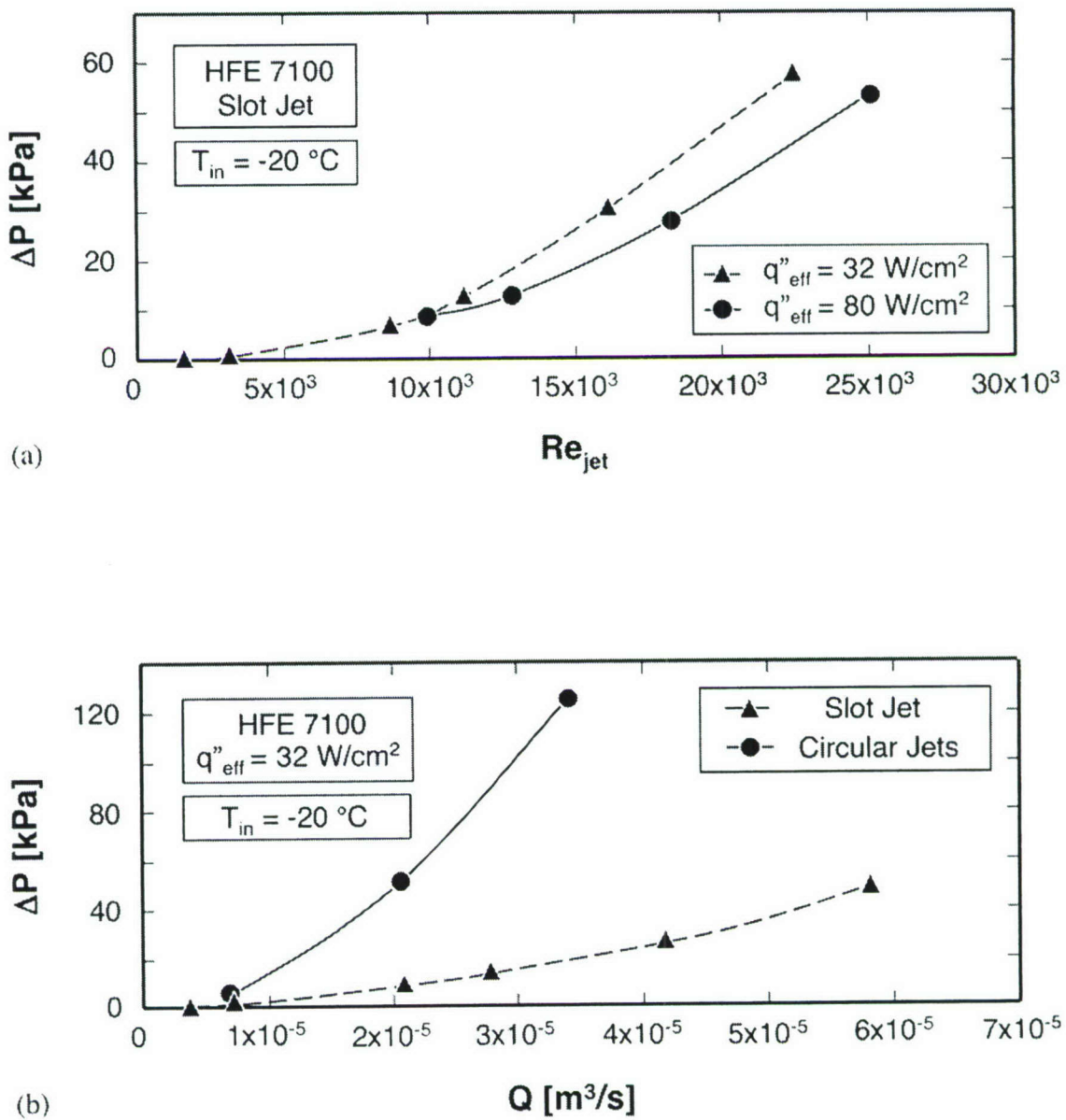


Figure 5.10 Variation of heat transfer coefficient with mean jet Reynolds number for different jet patterns.

CHAPTER 6. TWO-PHASE RESULTS

6.1. Boiling Curve Trends

6.1.1. Circular Jets

Figures 6.1(a) and 6.1(b) show boiling curves for the present hybrid cooling module for $U_{jet} = 0.9$ m/s, and inlet subcoolings of $\Delta T_{sub} = 88.7$ and 48.2°C , respectively. Wall temperature data are shown for $x_{tc1} = 0.0$, $x_{tc2} = 3.0$, $x_{tc3} = 6.0$, and $x_{tc4} = 9.0$ mm from the center of the micro-channel. Each temperature was determined from the applied heat flux, q''_{eff} , and thermocouple measurement at the same axial location by assuming one-dimensional heat conduction between the thermocouple and the micro-channel's bottom wall. The inlet temperature, T_{in} , was measured by the thermocouple inserted in the inlet plenum.

At low heat fluxes corresponding to single-phase heat transfer, Figs. 6.1(a) and 6.1(b) show fairly constant slopes for all boiling curves. With increasing heat flux, different trends are observed, depending on the magnitude of subcooling. Figure 6.1(b) shows the slope begins to increase at x_{tc4} , the most downstream of the four wall locations, indicating boiling is initiated near the micro-channel outlet. However, Fig. 6.1(a), which corresponds to highly subcooled jets, shows boiling commences at x_{tc3} , not the outlet. Numerical single-phase results show that, while the heat transfer coefficient is lowest near the center of the micro-channel, there is a second local minimum near x_{tc3} . The downstream minimum appears more favorable for nucleation because of both warmer bulk flow and lower pressure near x_{tc3} than at $x = 0$.

The decreasing slope of the boiling curves prior to CHF, albeit small, is indicative of deterioration in heat transfer effectiveness because of local vapor blanket formation.

CHF values for the cases in Fig. 6.1(a) and 6.1(b) are 276.3 and 213.2 W/cm², respectively.

Nucleate boiling inside the hybrid cooling module is fundamentally different from that encountered in conventional micro-channels. In the hybrid module, liquid supplied into the micro-channel from the jet closest to the center undergoes gradual bubble nucleation and growth. However, the micro-channel flow is influenced shortly downstream by the second jet, which can produce rapid condensation and collapse of the bubbles. The micro-channel flow produced by mixing warm upstream fluid with the cooler liquid supplied by the second jet then heats up, incurring additional nucleation, until it reaches the third jet. In this manner, the pattern of bubble growth and collapse is repeated along the micro-channel with a relatively mild overall increase in vapor void fraction. This behavior is evidenced in Figs. 6.1(a) and 6.1(b) by the relatively small variations in wall temperature along the flow direction.

The effects of subcooling and jet velocity on the boiling characteristics of the hybrid cooling module are shown in Fig. 6.2(a) and 6.2(b), respectively. An area-averaged wall temperature, T_s , is used in these plots. Figure 6.2(a) shows a relatively weak effect of subcooling on the single-phase region; this effect is the result of relatively mild variations of liquid properties with temperature. However, increasing subcooling delays the onset of boiling to both higher surface temperatures and higher heat fluxes. CHF also increases considerably with increased subcooling because of the subcooled liquid's ability to absorb an appreciable fraction of the supplied heat in the form of sensible energy; subcooled liquid also utilizes condensation to aid in delaying vapor blanket formation. Figure 6.2(b) shows increasing the flow rate delays the onset of boiling and augments single-phase heat transfer considerably. CHF also increases appreciably with increasing flow rate. Surprisingly, the higher jet velocity enabled the dissipation of an unprecedented heat flux of 1,127 W/cm². This test was terminated at this heat flux without incurring CHF. These results demonstrate the enormous cooling potential of the hybrid cooling scheme utilizing the circular jet pattern.

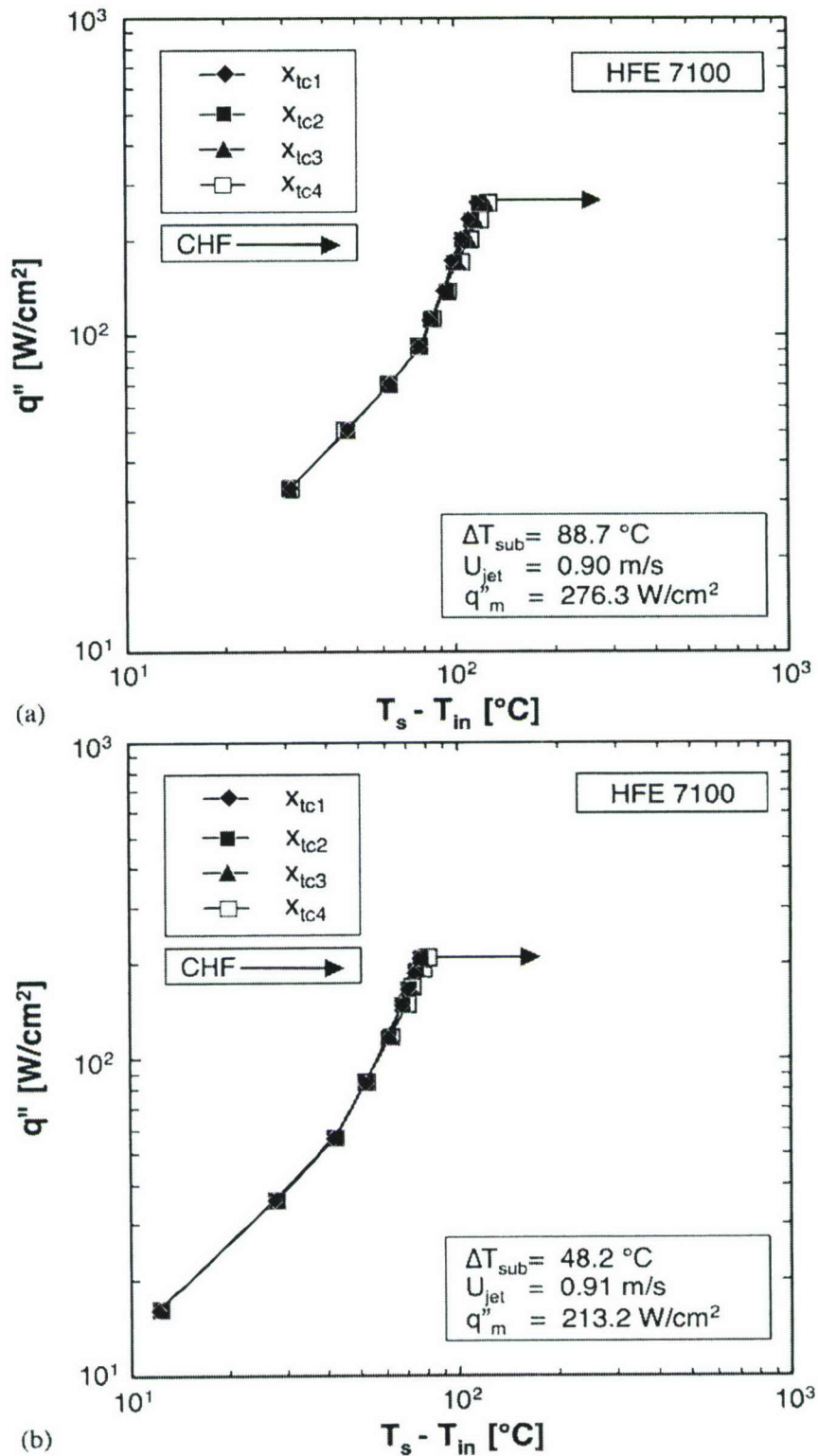


Figure 6.1 Boiling curves for equal-size-circular jet pattern with four axial wall locations at (a) $\Delta T_{sub} = 88.7 \text{ } ^\circ\text{C}$ and $U_{jet} = 0.90 \text{ m/s}$, and (b) $\Delta T_{sub} = 48.2 \text{ } ^\circ\text{C}$ and $U_{jet} = 0.91 \text{ m/s}$.

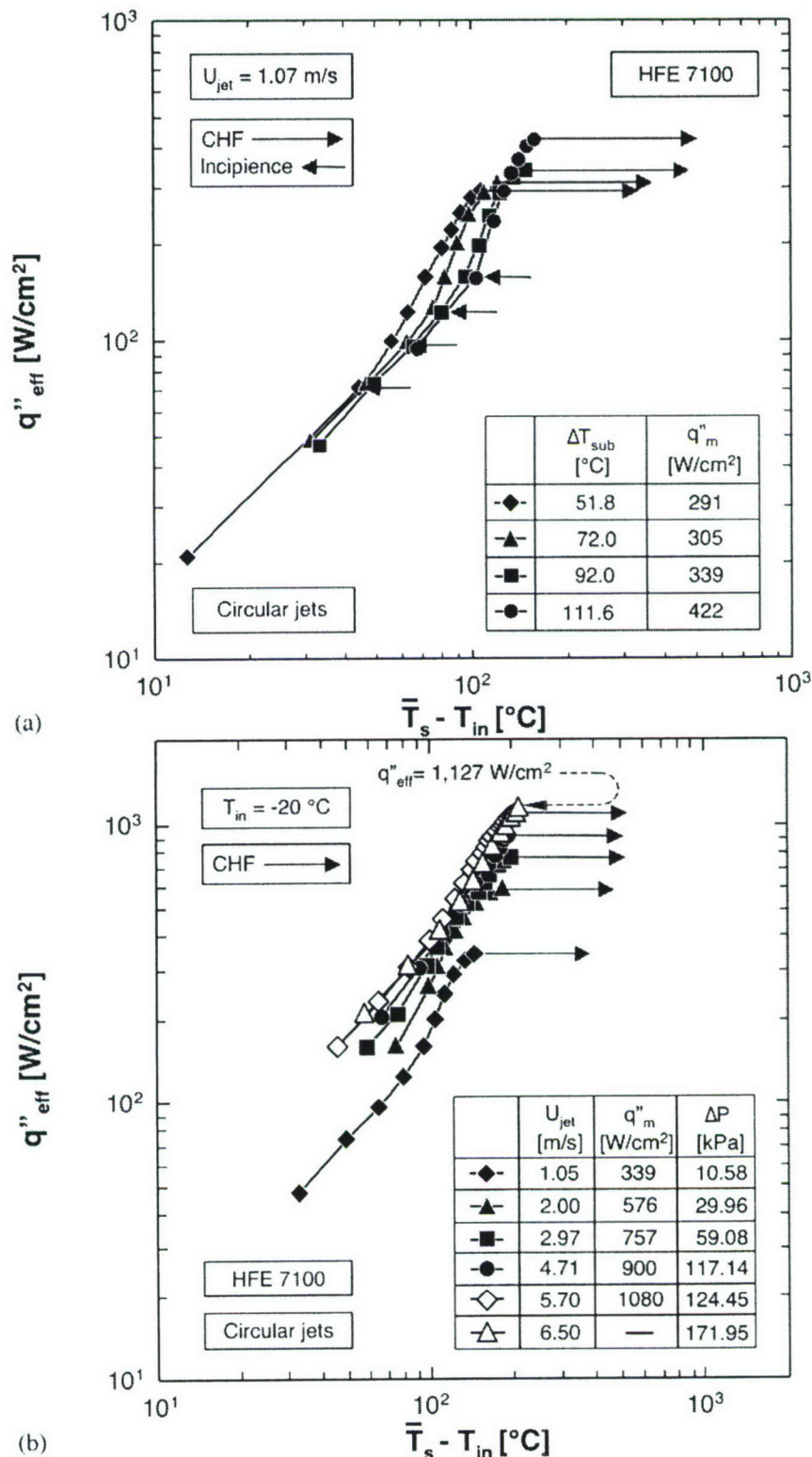


Figure 6.2 (a) Subcooling effects on boiling curve at $U_{jet} = 1.04 \text{ m/s}$. (b) Flow rate effects on boiling curve at $T_{in} = -20 \text{ }^\circ\text{C}$.

6.1.2. Slot Jets

Figures 6.3(a) and 6.3(b) show boiling curves obtained from the four thermocouple readings for a jet velocity of $U_{jet} = 0.87$ m/s and inlet subcoolings of $\Delta T_{sub} = 88.1$ and 68.1 °C, respectively. For each subcooling, the slope of the boiling curve in the single-phase region is fairly constant, indicative of a constant heat transfer coefficient. The highest temperature in the same region is encountered near the outlet, which is consistent with the previous single-phase numerical predictions. For both subcoolings, location x_{tc4} shows the earliest increase in slope, making the onset of boiling near the outlet. This location also maintains the highest temperatures throughout the nucleate boiling region and is where critical heat flux (CHF) commences. CHF values for the conditions of Figs. 6.3(a) and 6.3(b) are 310.6 and 243.3 W/cm², respectively.

Figure 6.4(a) shows the effects of subcooling on the boiling curve for $U_{jet} = 0.86$ m/s. Slight deviations in the single-phase region are the result of liquid property variations with temperature. Increasing the subcooling delays the onset of boiling incipience and enhances CHF considerably. Increased CHF is the result of the subcooled liquid's ability to absorb a substantial fraction of the wall heat flux in the form of sensible heat prior to evaporation. Figure 6.4(b) shows the effects of jet velocity (and flow rate) on the boiling curve for $\Delta T_{sub} = 107.8$ °C. Increasing U_{jet} delays the onset of boiling and broadens the single-phase heat transfer region considerably. CHF also increases appreciably with increasing U_{jet} . Because of high CHF values, higher velocity tests were terminated well before CHF to protect the test module against potential overheating or burnout.

6.1.3. Different Circular-Jet-Pattern Configurations

Since high-flux electronic and power devices for which the present cooling scheme is intended undergo power fluctuations during normal operation, it is important to determine the temperature response of the device to these power fluctuations. Of special importance is the ability to produce the same temperature for a given heat flux value regardless how this heat flux is reached. Nucleate boiling performance can manifest

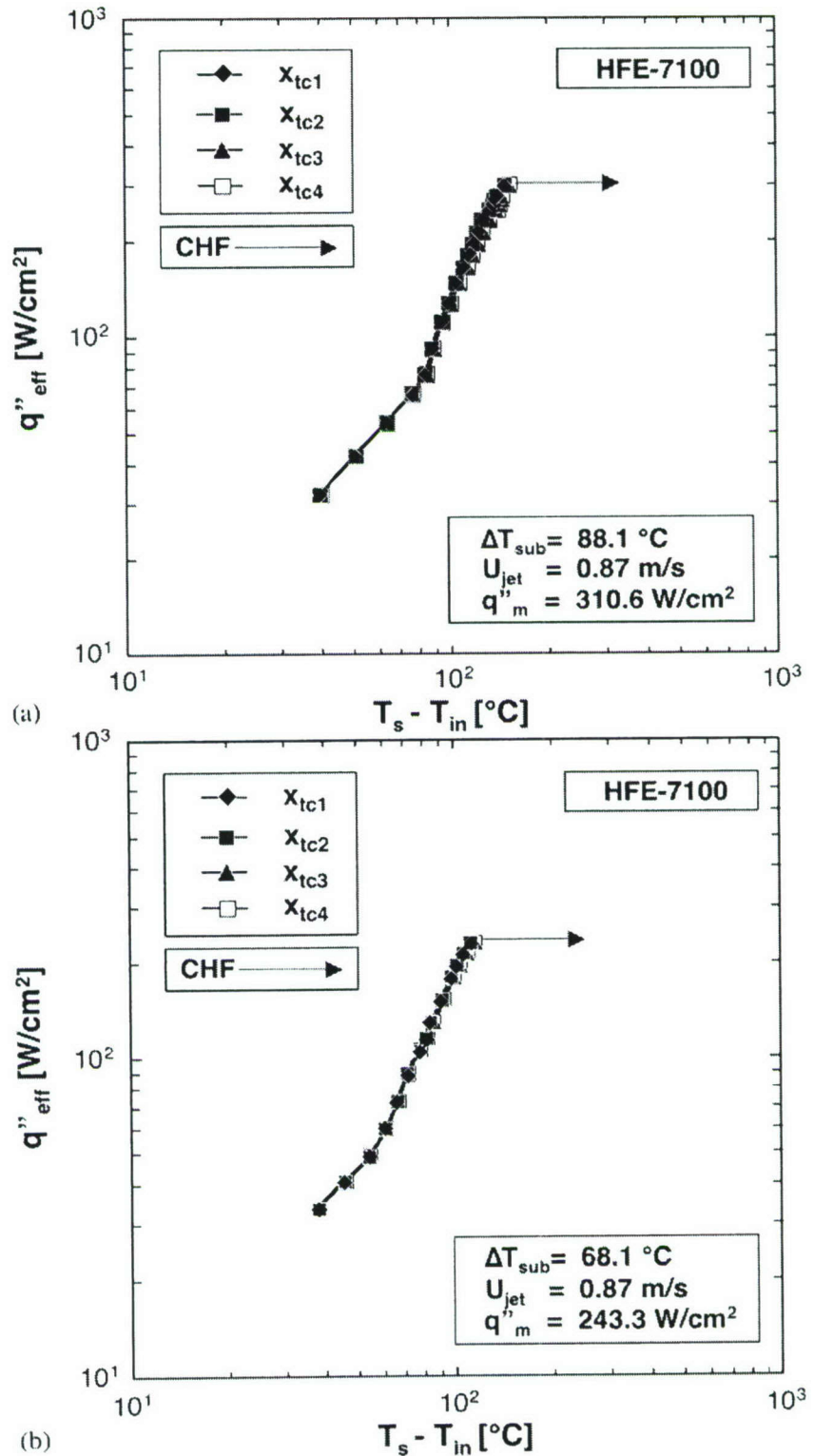


Figure 6.3 (a) Boiling curves measured at $x_{\text{tc}1}$, $x_{\text{tc}2}$, $x_{\text{tc}3}$ and $x_{\text{tc}4}$ for $U_{\text{jet}} = 0.87 \text{ m/s}$ at (a) $\Delta T_{\text{sub}} = 88.1 \text{ }^{\circ}\text{C}$ and (b) $\Delta T_{\text{sub}} = 68.1 \text{ }^{\circ}\text{C}$.

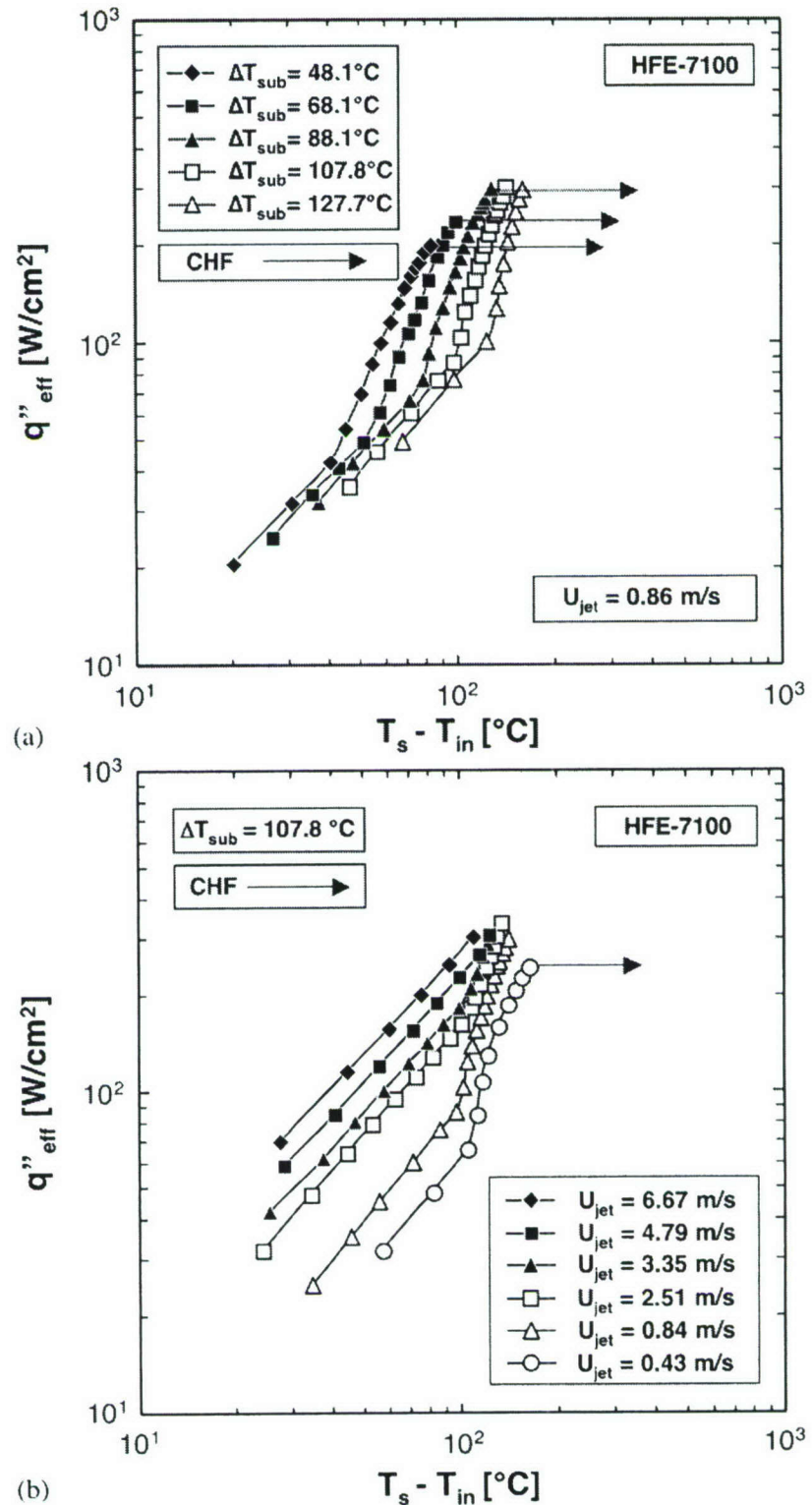


Figure 6.4 (a) Subcooling effects on boiling curve at $U_{jet} = 0.86 \text{ m/s}$. (b) Jet velocity effects on boiling curve at $\Delta T_{sub} = 107.8^\circ\text{C}$.

significant hysteresis depending on whether a particular operating condition is achieved by increasing or decreasing the heat flux. Hysteresis is encountered both at the onset of boiling and throughout the nucleate boiling region. Virtually all dielectric fluids used in electronics cooling are prone to incipient boiling hysteresis. Because of the low contact angle of these coolants, liquid can easily flood cavities, depriving potential nucleation sites from the vapor embryos necessary to initiate and sustain the boiling process (Mudawar, 2001). When increasing the heat flux from a non-boiling state, appreciable wall superheat - overshoot - is required to initiate the boiling process. Once boiling is initiated, the ensuing large increase in the heat transfer coefficient causes a sudden decrease in the wall temperature. The large incipient wall superheat and ensuing temperature drop are highly troublesome in electronics cooling because of the potential for thermal shock to the device. Increasing the heat flux beyond the incipience point follows a fairly predictable relationship between the heat flux and wall temperature. Similar behavior is achieved when decreasing the heat flux. However, the transition from nucleate boiling to single-phase cooling occurs without the aforementioned incipience overshoot, hence the term hysteresis. Another form of hysteresis is manifest in differences in the wall temperature in the nucleate boiling region when increasing versus decreasing the heat flux.

Figure 6.5 shows boiling curves that were measured by increasing and decreasing the heat flux for the decreasing-jet-size pattern at $Q = 2.33 \times 10^{-5} \text{ m}^3/\text{s}$ and $T_{in} = 0^\circ\text{C}$. Heat flux in these tests was increased in small increments up to CHF and then decreased again in small increments. The mean surface temperature, \bar{T}_s , in Fig. 6.5 was determined as follows. First, local surface temperatures were calculated by correcting the thermocouple temperatures for one-dimensional heat conduction between the thermocouple location and the test surface immediately above. These temperatures were then area-averaged to determine \bar{T}_s . The inlet temperature was measured by the thermocouple located in the inlet plenum. Figure 6.5 shows the two boiling curves are identically matched, proving the hybrid cooling scheme precludes both forms of hysteresis. Figure 6.6 shows the effects of flow rate on the boiling curve for the three jet patterns. For each pattern, increasing the flow rate augments single-phase heat transfer

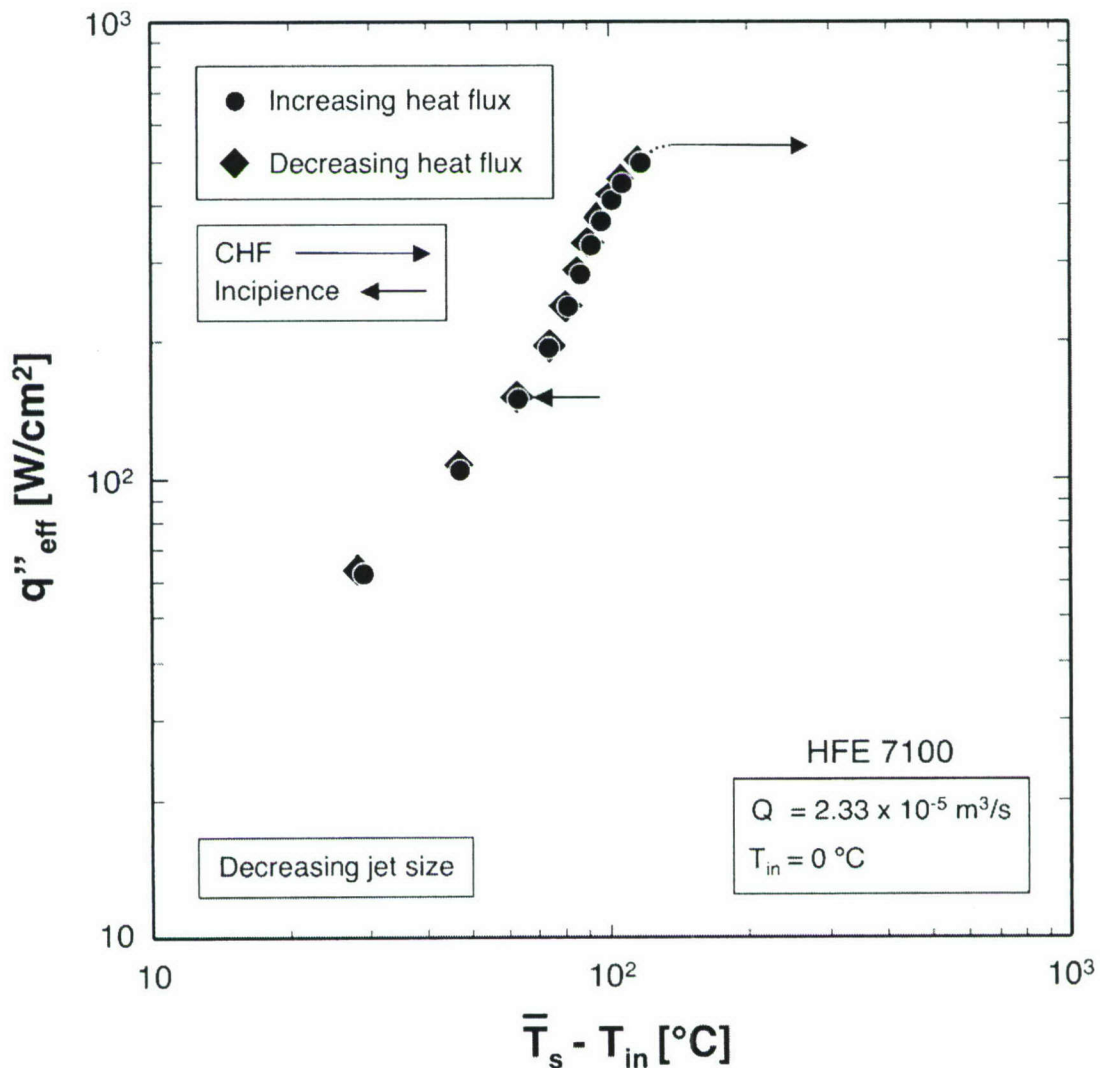


Figure 6.5 Boiling curves corresponding to increasing and decreasing heat flux for decreasing-jet-size pattern.

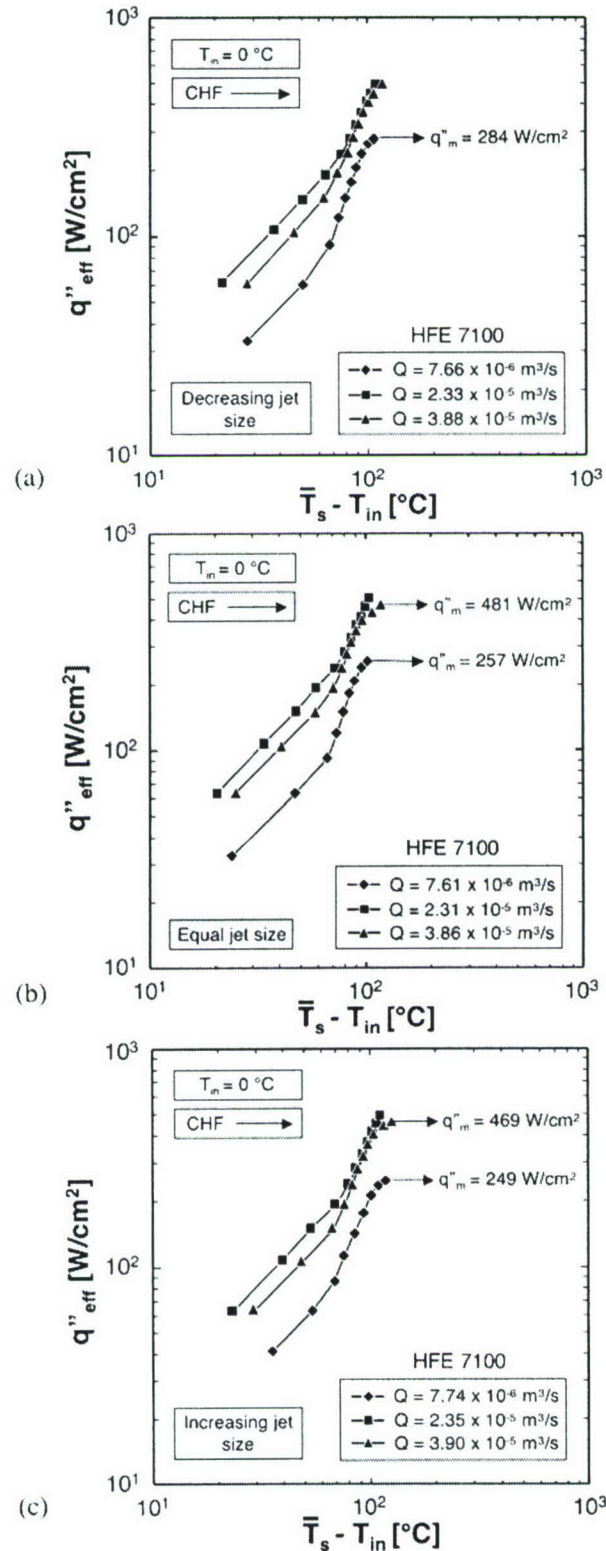


Figure 6.6 Effects of flow rate on boiling curve for patterns of (a) decreasing jet size, (b) equal jet size, and (c) increasing jet size.

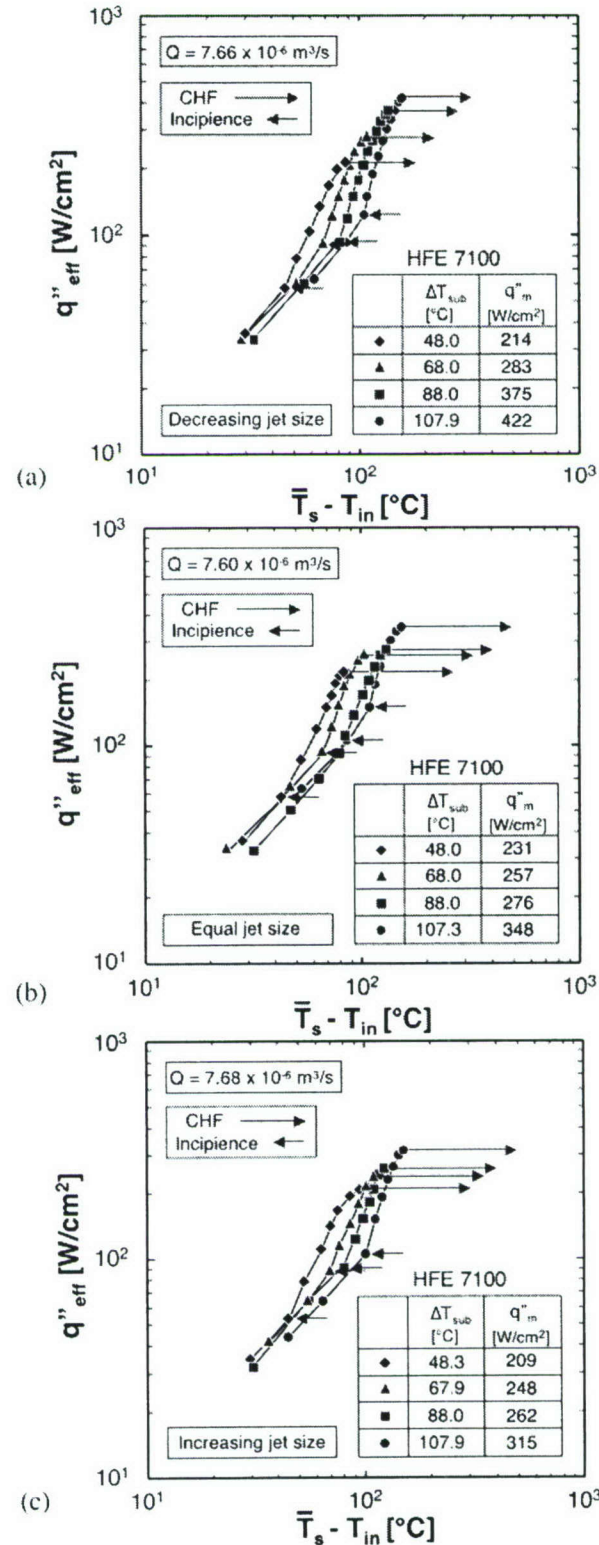


Figure 6.7 Effects of subcooling on boiling curve for patterns of (a) decreasing jet size, (b) equal jet size, and (c) increasing jet size.

considerably and delays the onset of nucleate boiling (ONB) to a higher heat flux. Boiling curves tend to converge in the nucleate boiling region, which is consistent with findings from previous sections. Increasing flow rate also enhances CHF appreciably. Notice that not all boiling curves culminate in CHF. High flow rate tests produced very high temperatures in the heating block and had to be terminated before CHF to prevent any permanent damage to the test module.

Figure 6.7 shows the effects of subcooling on the boiling curve for the three jet patterns at $Q = 7.66 \times 10^{-6} \text{ m}^3/\text{s}$. For each pattern, increasing the subcooling delayed the onset of boiling and CHF to both higher heat fluxes and higher surface temperatures. Overall, Fig. 6.7 shows the decreasing-size-jet pattern achieves the highest CHF at a given level of subcooling followed, respectively, by the equal-jet-size and increasing-jet-size patterns. Those differences in boiling behavior among the different jet patterns are closely related to the fact that the present hybrid cooling configurations are associated with very mild void fractions (this issue will be discussed later), where bulk liquid flow plays a major role even in the nucleate boiling region. In the previous numerical study on differences in single-phase performance among the three jet patterns, numerical simulations showed the decreasing-jet-size pattern yields the lowest surface temperature (*i.e.*, highest heat transfer coefficient), followed by the equal-jet-size and increasing-jet-size patterns, respectively. This also implies the decreasing-jet-size pattern delays the onset of boiling to a higher flux and decreases void fraction compared to the other two patterns. With a lower void fraction, the decreasing-jet-size pattern provides greater access of subcooled bulk liquid to the wall, resulting in the highest CHF for this pattern. The single-phase numerical simulations also showed the equal-jet-size pattern provides the greatest surface temperature uniformity, while the fluid flow with the increasing-jet-size pattern is complicated by blockage from the large jets located near the channel outlet.

6.2. Flow Visualization Results for Slot Jets

To capture two-phase flow behavior along the micro-channels, the test module's jet plate and upper housing (see Fig. 2.2) were replaced with plates made from transparent polycarbonate plastic (Lexan). A high-speed video camera fitted with close-up lenses was positioned above the test module as illustrated in Fig. 2.1. This placement facilitated viewing of three adjacent micro-channels. The relatively low melting point of polycarbonate plastic limited these flow visualization tests to low heat fluxes. Figures 6.8(a) and 6.8(b) show representative images captured at $U_{jet} = 0.44$ m/s and $\Delta T_{sub} = 48.1$ °C at $q''_{eff} = 43$ and 63 W/cm², respectively. Figure 6.8(a) shows a combination bubbly flow, caused by sidewall nucleation, and slug flow. Increasing the heat flux causes further bubble coalescence into longer slug bubbles as depicted in Fig. 6.8(b). Notice the appreciable increase in void fraction, evidenced by the large size of bubbles exiting the micro-channels in Fig. 6.8(b) compared to Fig. 6.8(a).

Qu and Mudawar (2004) classified two types of flow instability in conventional two-phase micro-channel heat sinks, severe pressure drop oscillation and mild parallel channel instability. Severe pressure drop oscillation is the result of interaction between the two-phase flow in the micro-channel heat sink and the upstream compressible volume in the flow loop. This instability causes severe fluctuations between incoming liquid and downstream two-phase mixture in all channels. The mild parallel channel instability is the result of flow interactions among micro-channels and is intrinsic to the heat sink itself. Figures 6.8(a) and 6.8(b) depict the mild parallel channel instability that causes the variations in flow pattern among adjacent micro-channels. Interestingly, the severe pressure drop oscillation was never observed in the present study.

6.3. Comparison of Pressure Drop and Two-Phase Heat Transfer Coefficients for Different Circular-Jet Patterns

Figure 6.9(a) shows the variation of pressure drop with heat flux for the decreasing-jet-size pattern at $Q = 7.45 \times 10^{-6}$ m³/s and four subcoolings. For the single-

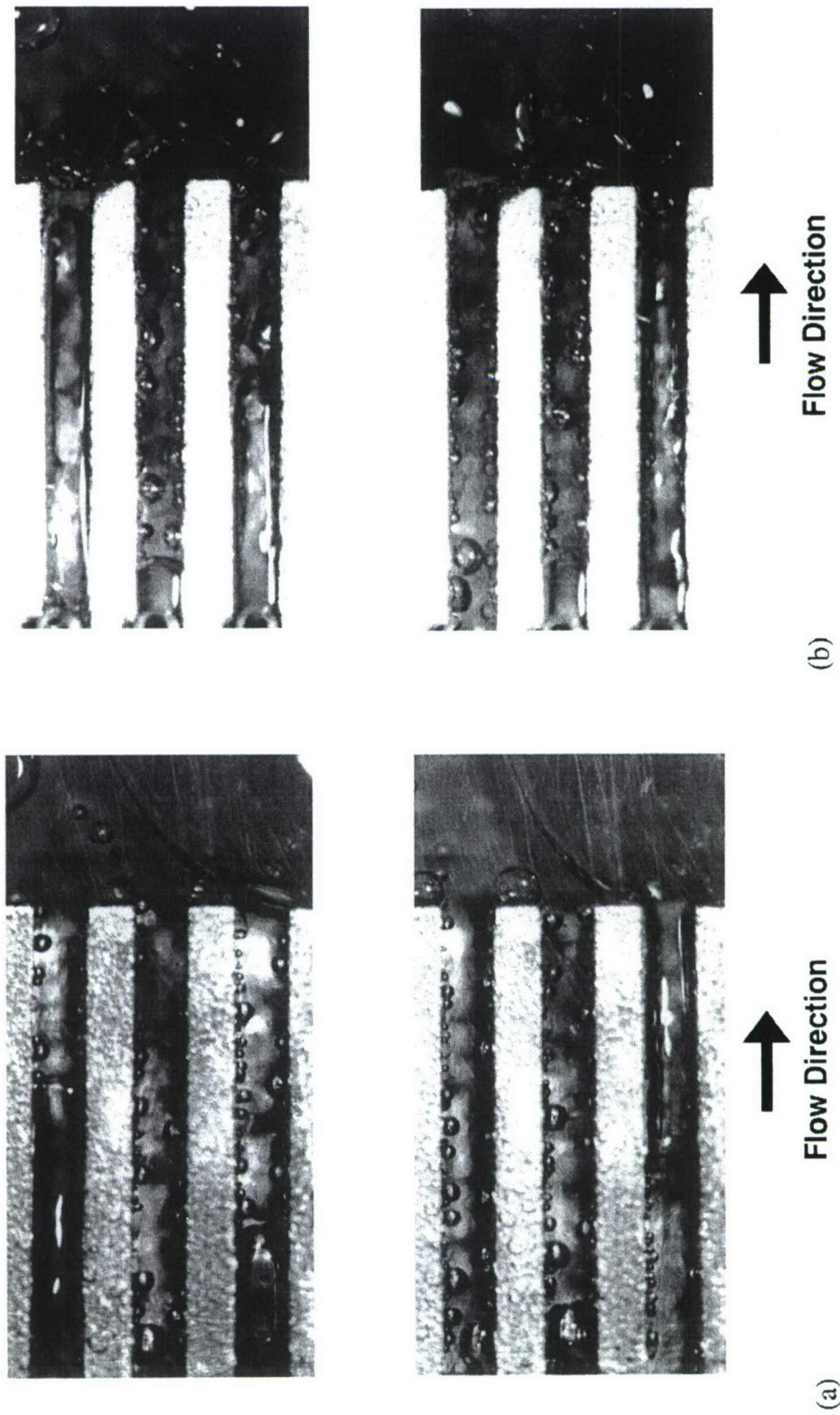


Figure 6.8 Flow visualization and flow patterns inside hybrid module for $U_{jet} = 0.44 \text{ m/s}$ and $\Delta T_{sub} = 48.1^\circ\text{C}$ with (a) $q''_{eff} = 43 \text{ W/cm}^2$ and (b) $q''_{eff} = 63 \text{ W/cm}^2$.

phase region, pressure drop decreases with increasing temperature because of reduced viscosity. Figure 6.9(a) shows pressure drop decreases with increasing heat flux for each inlet temperature because of this viscosity effect. Interestingly, this trend continues into the two-phase region, with the minimum pressure drop encountered just before CHF. This is contrary to trends found in most flow boiling situations, where pressure drop increases appreciably in the two-phase region. This unusual trend may be explained by the fundamentally different nucleate boiling pattern encountered in the hybrid cooling configuration compared to conventional micro-channel two-phase flow. As illustrated in Fig. 6.10(a), void fraction in conventional micro-channel flow increases monotonically along the micro-channel, increasing both the frictional and accelerational components of pressure drop. In the hybrid cooling configuration, Fig. 6.10(b), void fraction increases gradually between jets before being greatly reduced by condensation beneath the jets. This result is a repeated pattern of void fraction growth and collapse along the micro-channel, and a mild overall increase in void fraction along both sides of the micro-channel. Small void fraction results in both small pressure drop and pressure drop characteristics that are dominated by liquid friction.

Figure 6.9(b) shows the variation of pressure drop with heat flux for the three jet patterns at $Q = 2.33 \times 10^{-5} \text{ m}^3/\text{s}$ and $T_{in} = 0^\circ\text{C}$. Data for all patterns follow a trend of decreasing pressure drop with increasing heat flux because of the reduced liquid viscosity. This trend also persists in the two-phase region because of the mild overall increase in void fraction along the micro-channel. Feeding subcooled liquid from jets gradually along the micro-channel appears to help maintain a predominantly liquid state at the micro-channel outlet with a relatively small mass of vapor confined to the micro-channel walls. CHF is consistent with the mechanism of Departure from Nucleate Boiling (DNB) associated with highly subcooled flow boiling, high mass velocities, and small length-to-diameter ratios (Mudawar and Bowers, 1999). Figure 6.9(b) shows pressure drop is highest for the equal-jet-size pattern followed, respectively, by the decreasing-jet-size and increasing-jet-size patterns.

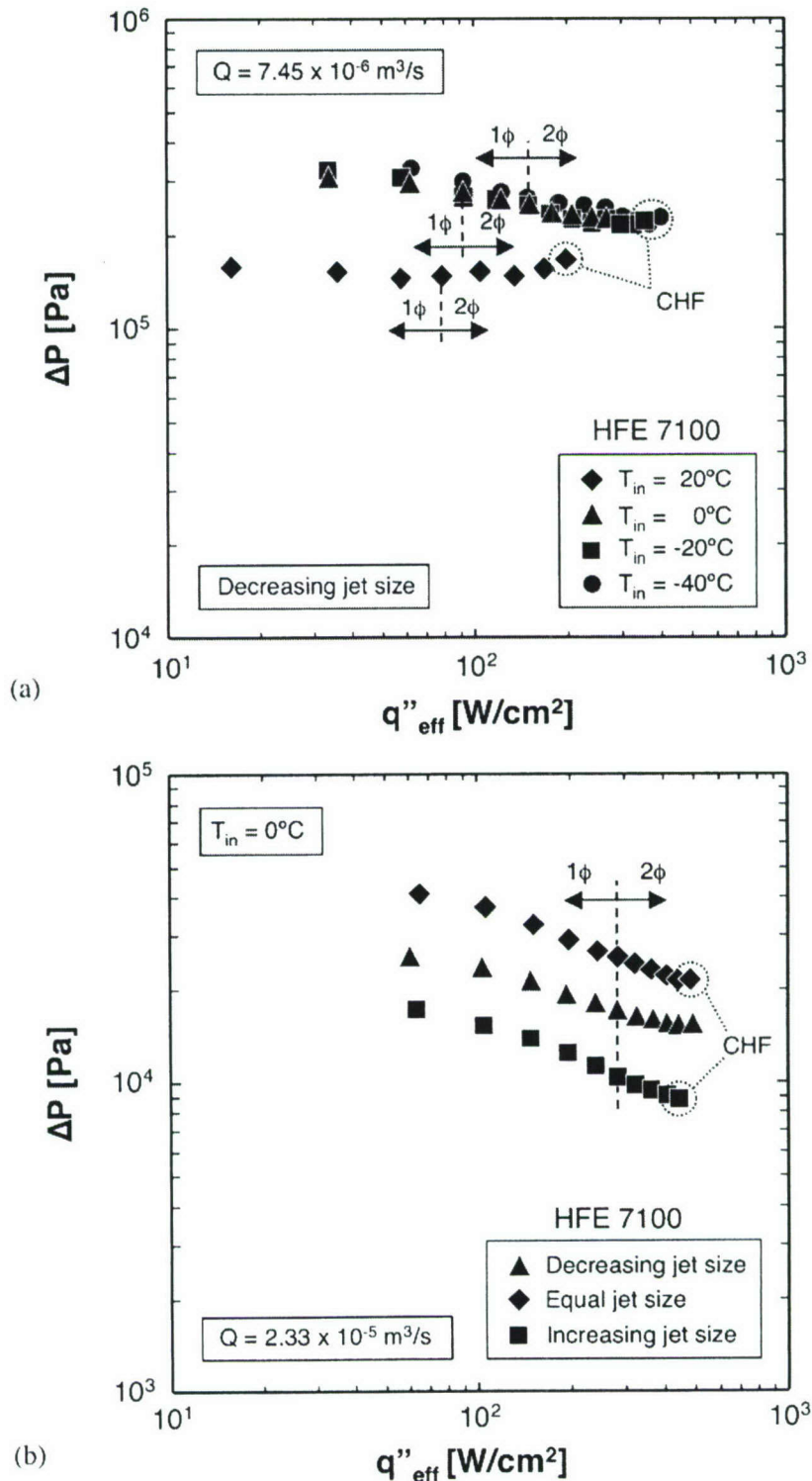


Figure 6.9 (a) Variation of pressure drop with heat flux for different inlet temperatures for decreasing-jet-size pattern. (b) Variation of pressure drop with heat flux for different jet patterns.

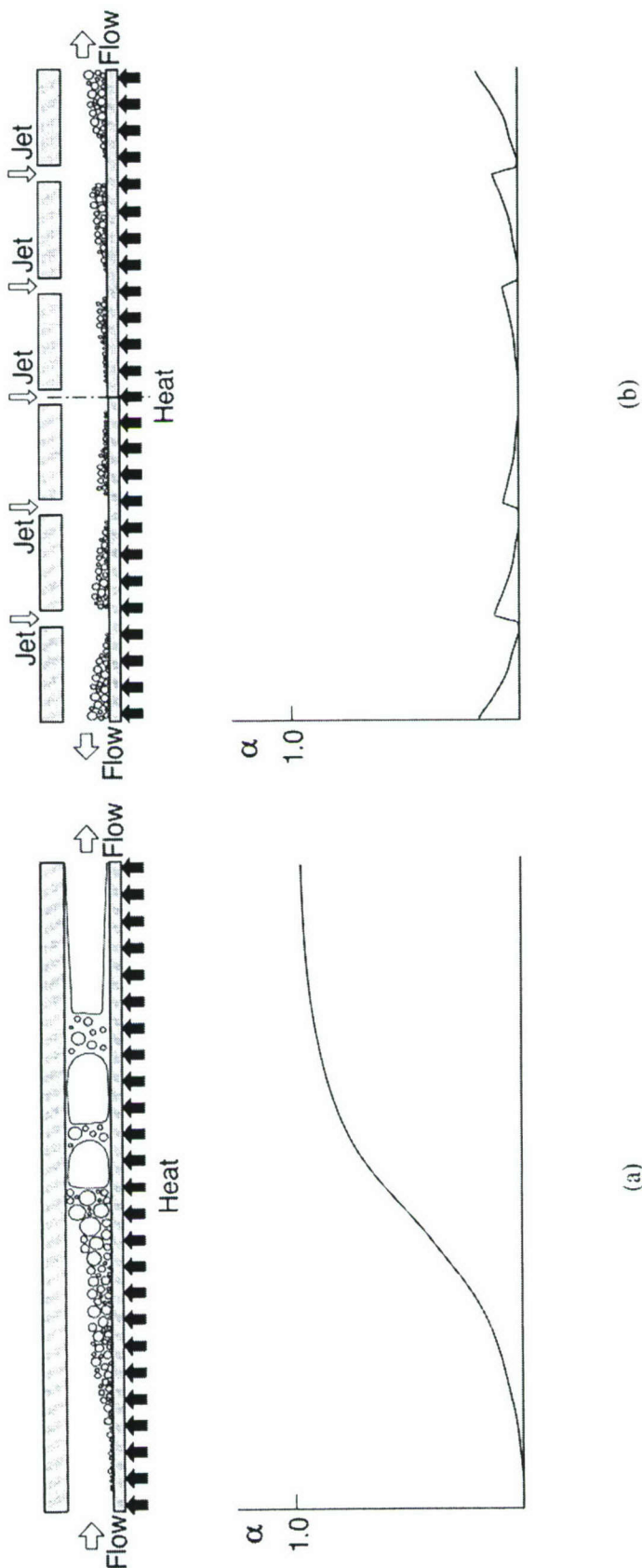


Figure 6.10 Schematic representation of vapor growth and variation of void fraction along micro-channel for (a) conventional micro-channel and (b) hybrid cooling configuration.

Figure 6.11 shows the variation of outlet fluid temperature with heat flux for the three jet patterns at $Q = 2.33 \times 10^{-5} \text{ m}^3/\text{s}$ and $T_{in} = 0^\circ\text{C}$. These trends are consistent with the earlier discussion concerning outlet surface and fluid temperatures. Figure 6.11 shows the decreasing-jet-size patterns produced the lowest temperatures followed, respectively, by the equal-jet-size and increasing-jet-size patterns. Figure 6.12(a) shows the variation of the area-averaged surface temperature with heat flux at $Q = 7.50 \pm 0.1 \times 10^{-6} \text{ m}^3/\text{s}$ and $T_{in} = -40^\circ\text{C}$. For the high flux data preceding CHF, lowest surface temperatures are achieved with the decreasing-jet-size pattern followed by the equal-jet-size and increasing jet-size patterns, respectively, in accordance with the trend captured in Fig. 6.11 for outlet fluid temperature.

Figure 6.12(b) shows the heat transfer coefficient in the two-phase region preceding CHF is also highest for the decreasing-jet-size pattern followed by the equal-jet-size and increasing-jet-size patterns, respectively. This trend is consistent with the above-mentioned (1) strong influence of single-phase liquid flow, and (2) the trend of lowest wall and fluid outlet temperatures for the decreasing-jet-size pattern. Figure 6.12(b) shows the decreasing-jet-size pattern also produces the highest CHF because of low void fraction and better access of subcooled bulk liquid to the wall.

Nonetheless, Fig. 6.12(b) shows heat transfer coefficient variations among jet patterns are relatively small; those variations are quite significant for single-phase flow. The present results point to the possibility of developing a universal two-phase heat transfer coefficient correlation applicable to all three patterns.

6.4. Subcooled Nucleated Boiling Region

Several experimental studies have been conducted to investigate the effects of impingement velocity and subcooling on two-phase heat transfer in the fully developed boiling region. Ma and Bergles (1986) showed increasing the subcooling of an R-133 jet caused a slight shift in the boiling data toward lower wall superheat. By varying subcooling of a rectangular FC-72 jet from 10 to 40 °C, Mudawar and Wadsworth (1991)

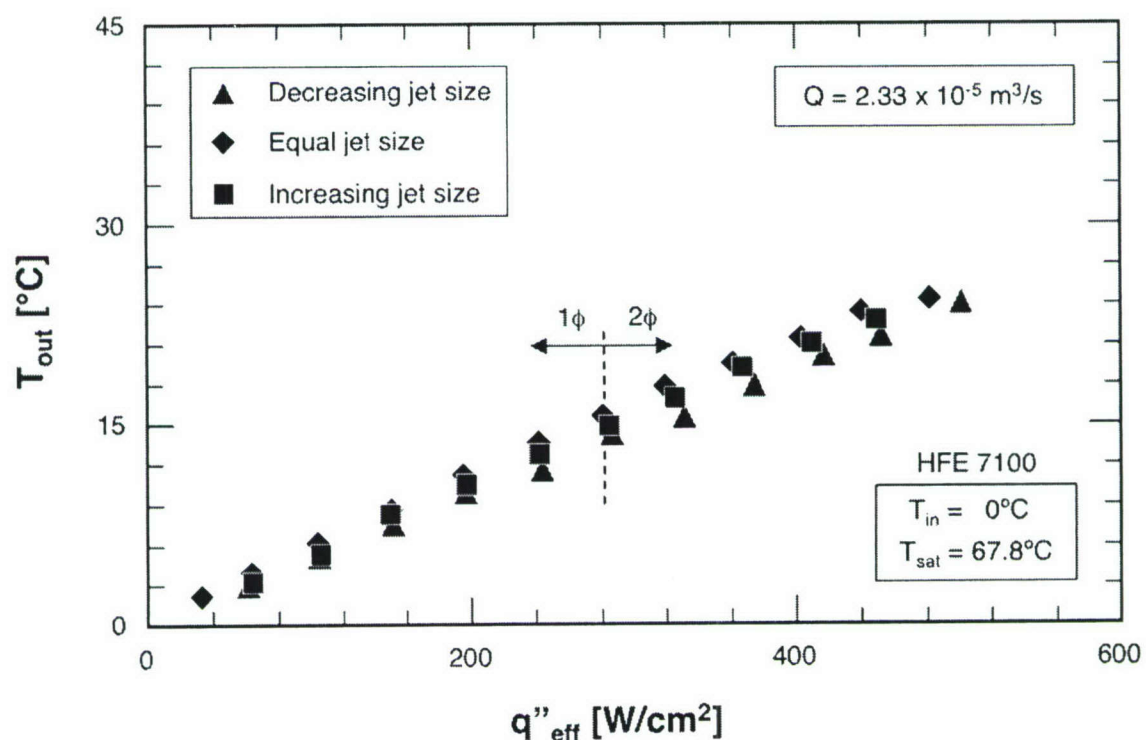


Figure 6.11 Variation of micro-channel outlet temperature with heat flux for different jet patterns at $Q = 2.33 \times 10^{-5} \text{ m}^3/\text{s}$ and $T_{in} = 0^\circ\text{C}$.

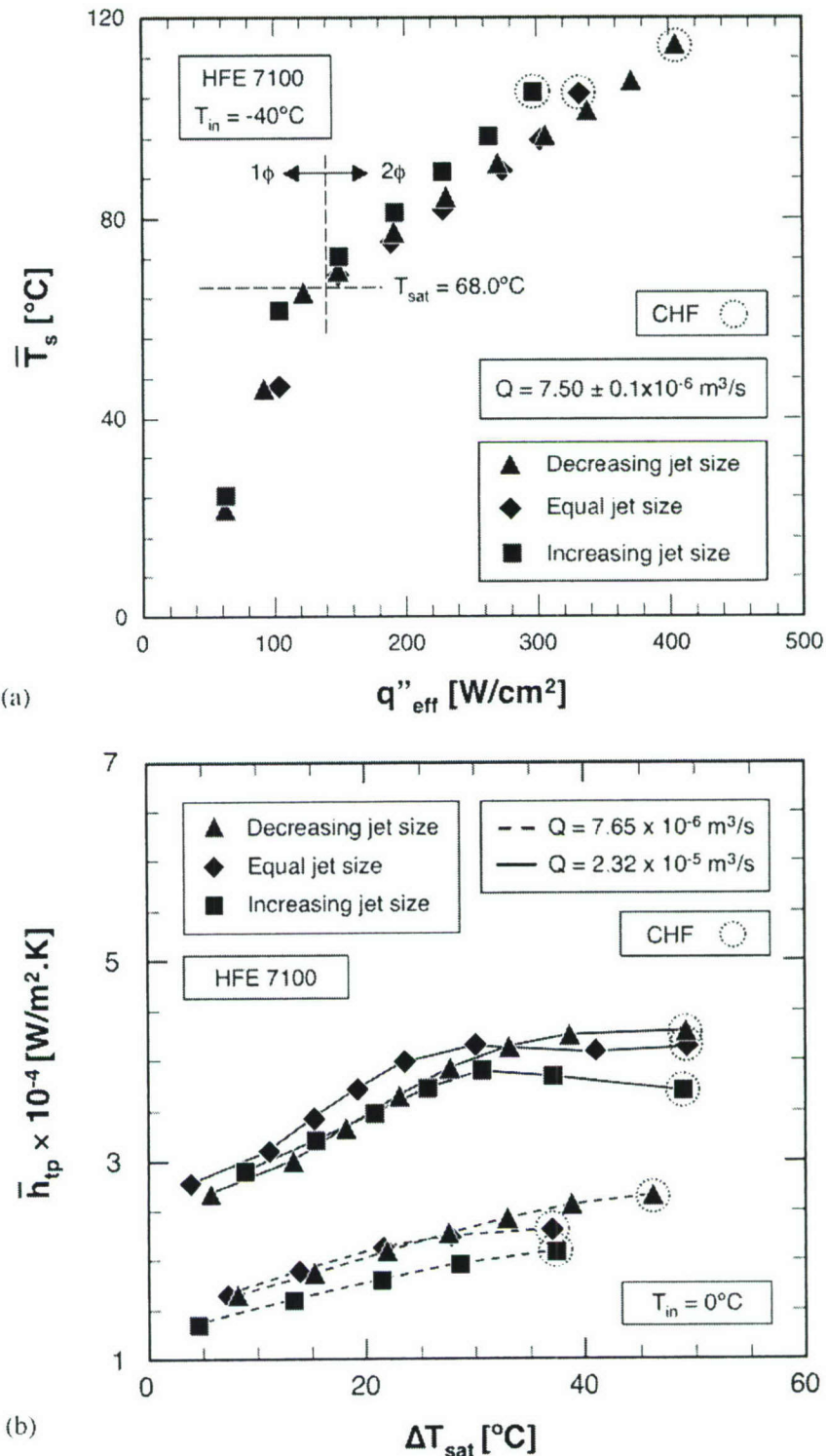


Figure 6.12 (a) Variation of surface temperature with heat flux for tree jet patterns at $Q = 3.87 \times 10^{-5}$ m³/s and $T_{in} = -40^\circ\text{C}$. (b) Variation of two-phase heat transfer coefficient with wall superheat for three jet patterns at tow flow rate and $T_{in} = 0^\circ\text{C}$.

showed a delay in boiling inception, but the nucleate boiling data had no dependence on subcooling.

Mudawar and Wadsworth (1991) also showed the nucleate boiling heat regime was independent of jet velocity, an observation shared by Katto and Kunihiro (1973) for circular jets. To derive an expression for the nucleate boiling heat transfer coefficient for the present cooling scheme, the following relationship is assumed between heat flux and wall superheat:

$$\bar{q}_{eff} = C \Delta T_{sat}^n, \quad (6.1)$$

where C and n are empirical constants. The subcooling effect is implicit in the above relation since

$$\bar{q}_{eff} = h(T_w - T_f) = h(\Delta T_{sat} + \Delta T_{sub}). \quad (6.2)$$

Combining Eqs. (6.1) and (6.2) yields

$$h = \frac{\bar{q}_{eff}}{\left(\frac{\bar{q}_{eff}}{C}\right)^{1/n} + \Delta T_{sub}}. \quad (6.3)$$

This expression reveals the two-phase heat transfer coefficient is a function of both \bar{q}_{eff} and ΔT_{sub} . The constants C and n were fitted experimentally from the present HFE 7100 data, resulting in the correlation

$$h = \frac{\bar{q}''}{\left(\frac{\bar{q}''}{64.81}\right)^{1/3.252} + \Delta T_{sub}}. \quad (6.4)$$

Figure 6.13 and Figure 6.14 compares predictions of this correlation with the present nucleate boiling data of different circular-jet-pattern configurations and slot jets, respectively. Overall mean absolute error (MEA) of 6.59% and 5.66% demonstrates excellent predictive capability for the present hybrid cooling scheme.

The two-phase heat transfer results of the present study point to many merits of the new hybrid cooling scheme, as well as provide powerful tools for thermal design of a

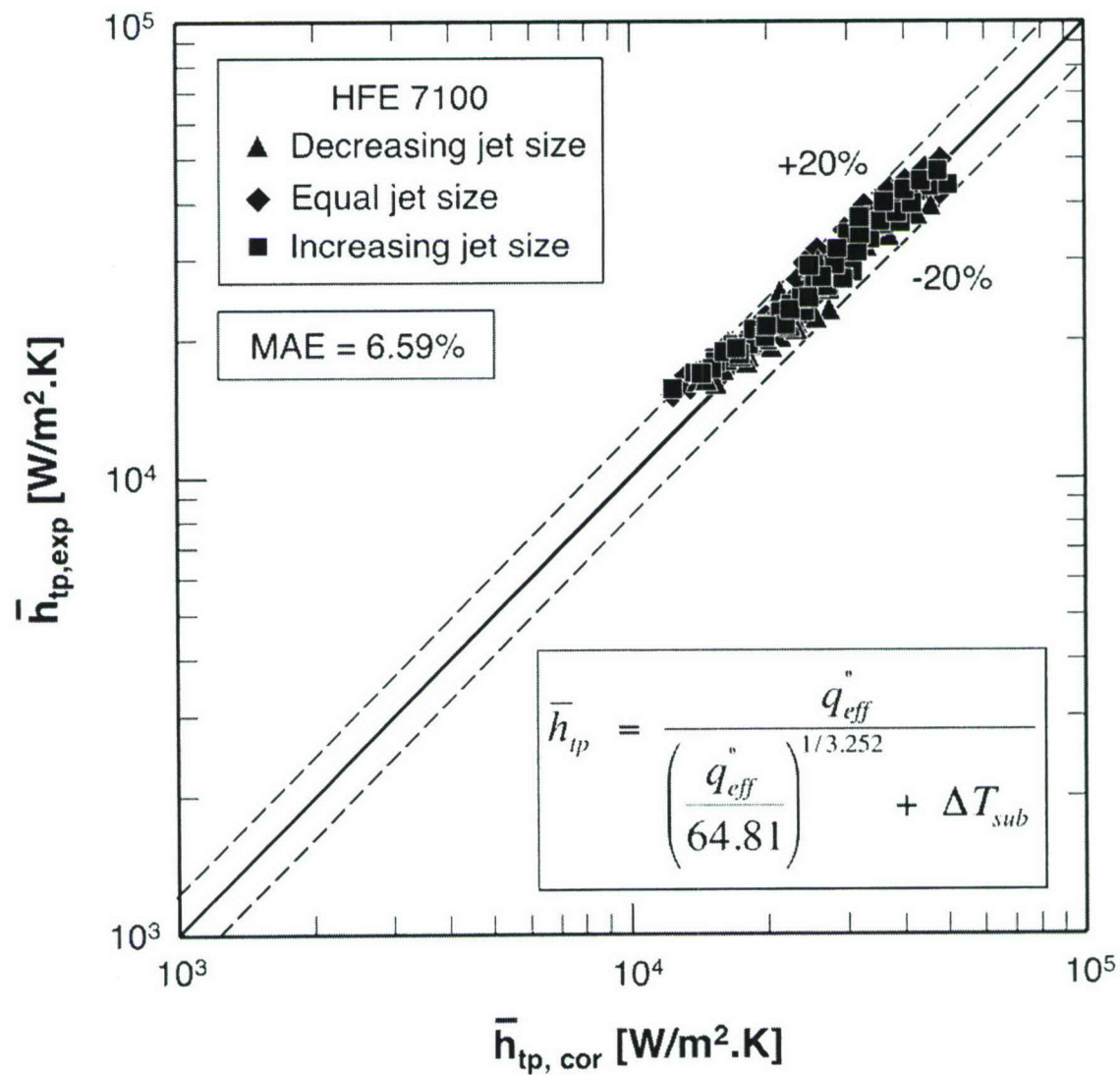


Figure 6.13 Comparison of predictions of two-phase heat transfer coefficient correlation with HFE 7100 data for different circular-jet-pattern configurations.

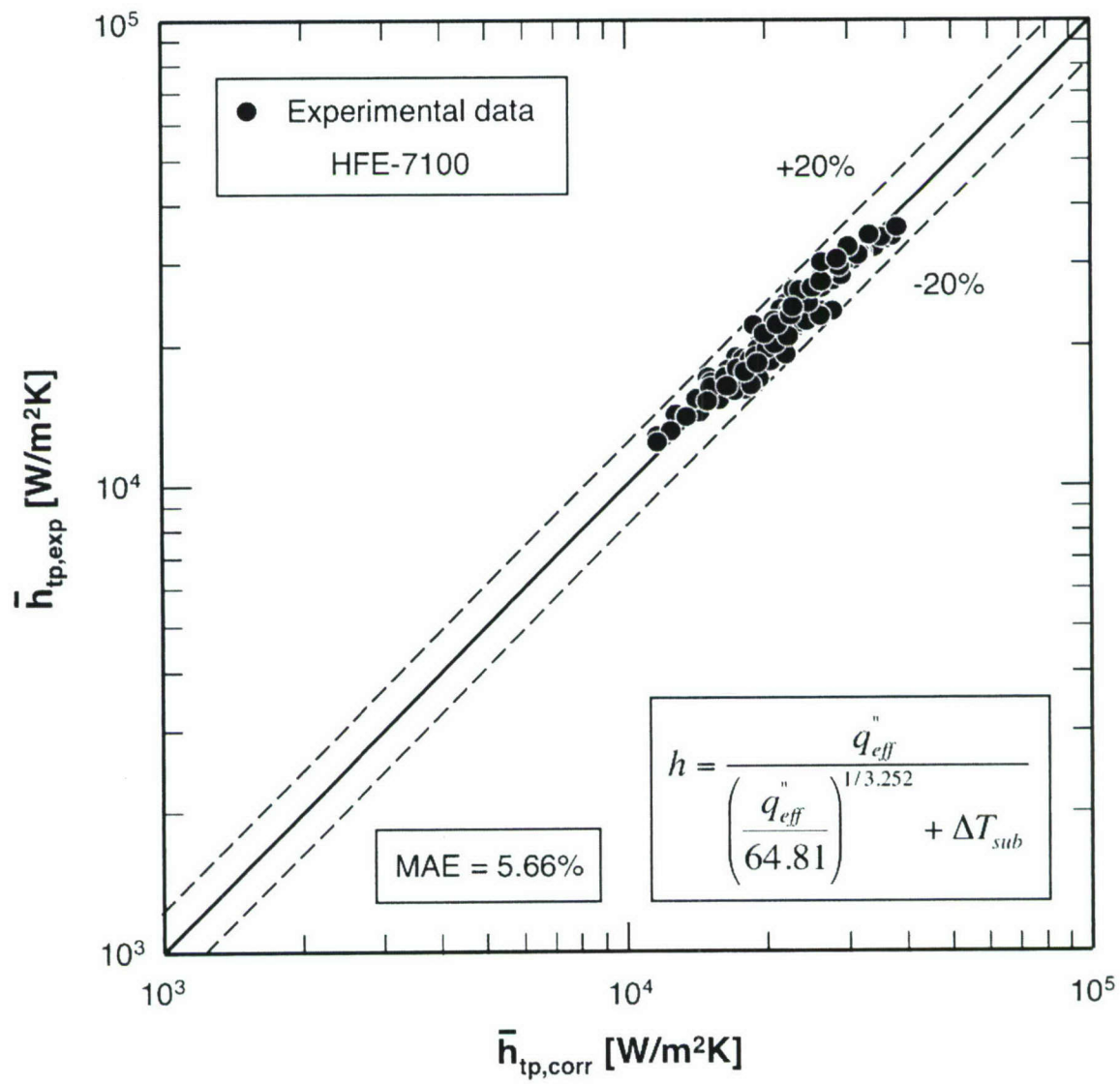


Figure 6.14 Comparison of predictions of two-phase heat transfer coefficient correlation with HFE 7100 data for slot jets.

cooling module that utilizes this scheme. However, this study also points to new important phenomena that should be carefully investigated in future work, especially that of a subcooled flow undergoing successive cycles of rapid growth and collapse of bubbles. This behavior is the subject of ongoing efforts by the authors.

6.5. Comparison of Two-Phase Performance of Two Hybrid Cooling Schemes

Overall, boiling curves in Figs. 6.1-6.6 demonstrate the circular jet pattern provides significantly better cooling performance compared to the slot jet pattern. This difference may be explained by drastic differences in the mechanisms of bubble production and growth along the micro-channel for the circular jets and slot jet as illustrated in Fig. 6.15(a) and 6.15(b), respectively. With the circular jets, liquid fed into the micro-channel from the first jet (closest to the center of the micro-channel) undergoes gradual bubble nucleation and growth. However, subcooled fluid from the second jet causes rapid condensation and collapse of upstream bubbles. This pattern of bubble growth and collapse is repeated along the micro-channel with relatively mild net overall increase in vapor void fraction. On the other hand, coolant in the slot jet case is supplied near the center of the micro-channel and loses subcooling faster than the micro-jets, resulting in an appreciable increase in void fraction near the outlet. This loss of subcooling reduces CHF for the slot jet relative to the circular jets.

6.6. Critical Heat Flux

Figure 6.16 shows CHF increases monotonically with jet velocity for each of four subcooling cases. There is also a monotonic upward shift in CHF with increased subcooling. Figure 6.16 shows $\dot{q}_m'' \sim U_{jet}^{0.624}$. Interestingly, the velocity exponent is between that for channel flow, $\dot{q}_m'' \sim U^{0.50}$ (Mudawar and Maddox, 1989), and confined jets, $\dot{q}_m'' \sim U_{jet}^{0.70}$ (Mudawar and Wadsworth, 1991). Clearly, both jet impingement and channel flow influence CHF in the present hybrid cooling configuration. The next

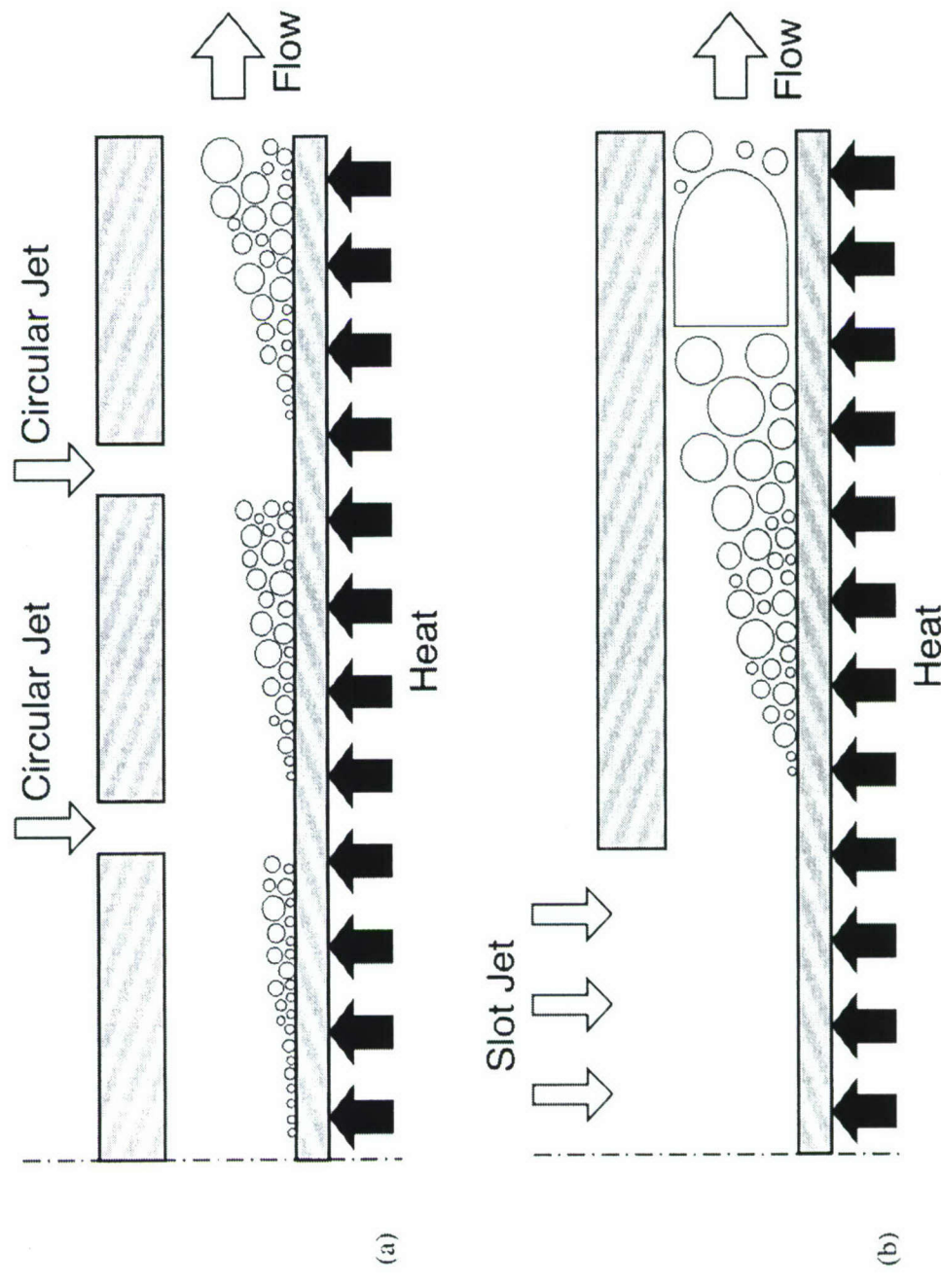


Figure 6.15 Bubble growth and condensation inside hybrid module for (a) circular jets and (b) slot jet.

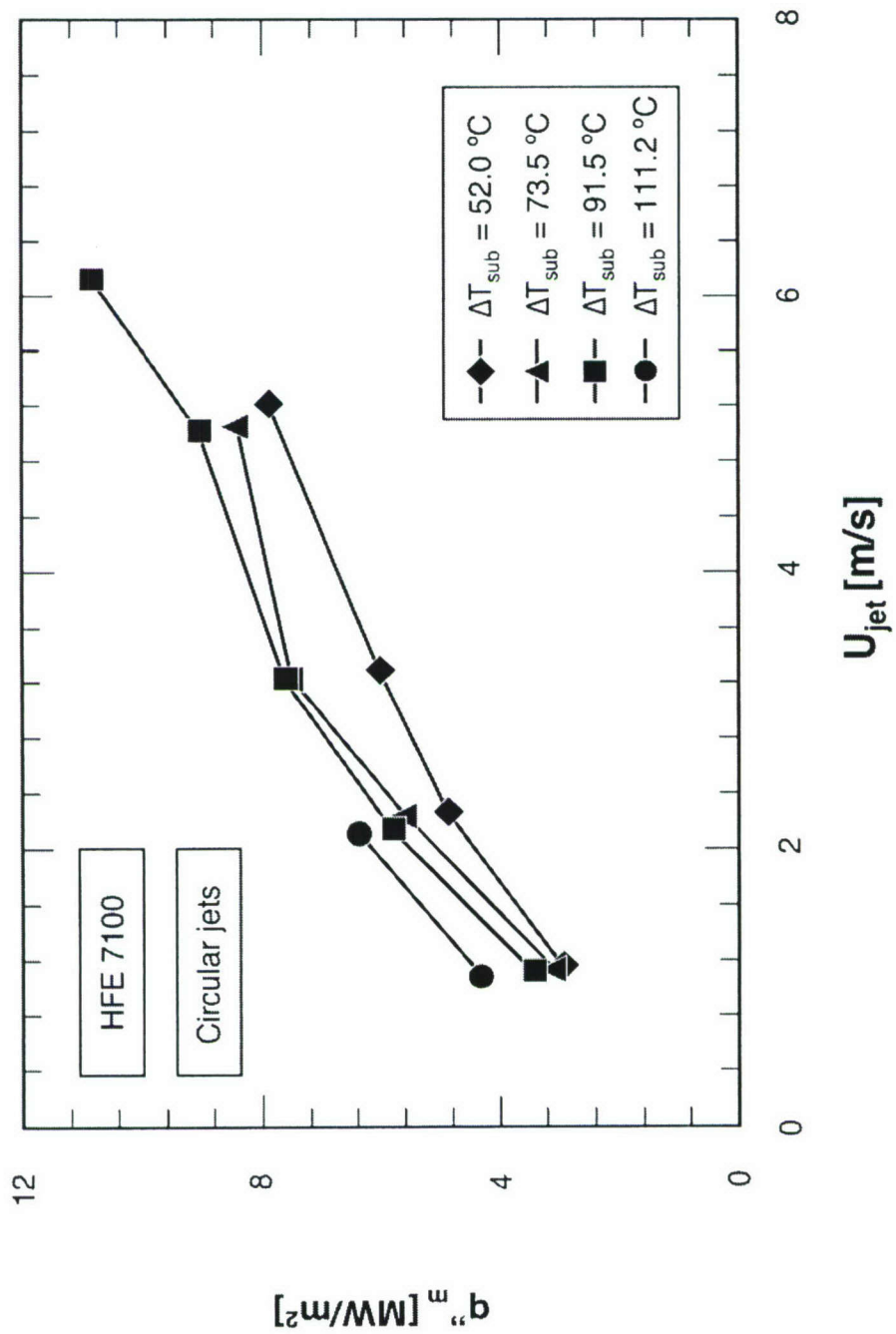


Figure 6.16 Variation of CHF with jet velocities with different subcoolings.

section will discuss means of assessing the contributions of each to the test module's CHF.

6.6.1. Developing Homogeneous Layer Model

In conventional two-phase micro-channel flow, both quality and void fraction increase monotonically along the micro-channel as liquid is gradually converted to vapor. The present hybrid cooling configuration involves complex interactions between circular jets and micro-channel flow, and unusual spatial variations of quality and void fraction. As illustrated in Fig. 6.10(b), the flow pattern is symmetrical relative to the micro-channel's centerline. On either side, jets supply subcooled liquid gradually into the micro-channel, and the flow rate is not constant but increases along the flow direction. It is therefore crucial to ascertain the spatial variations of the key flow parameters in order to determine CHF for the entire module. Achieving this goal is complicated by the fact that the flow along the micro-channel is mostly subcooled, and the liquid and vapor phases do not maintain thermodynamic equilibrium. This precludes the use of conventional parameters such as thermodynamic equilibrium quality to assess the spatial variations of void fraction and flow velocity.

Recently, Lee and Mudawar (*in review*) introduced a new technique to determine such spatial variations for subcooled two-phase flow in conventional micro-channels. Using a Developing Homogeneous Layer Model (DHLM), the flow is described as consisting of two layers, a homogeneous two-phase flow layer adjacent to the heated wall and a subcooled liquid core, as illustrated in Fig. 6.17(a). The model also assumes that because of the large density differences between liquid and vapor, the velocity of the liquid layer is fairly constant along the micro-channel. Key DHLM equations that are relevant to the present hybrid cooling configuration are discussed here. Further details of the model development can be found in ref. (Lee and Mudawar, *in review*).

As illustrated in Fig. 6.17(b), mass conservation for a control volume of the micro-channel flow between jets of length Δz requires that

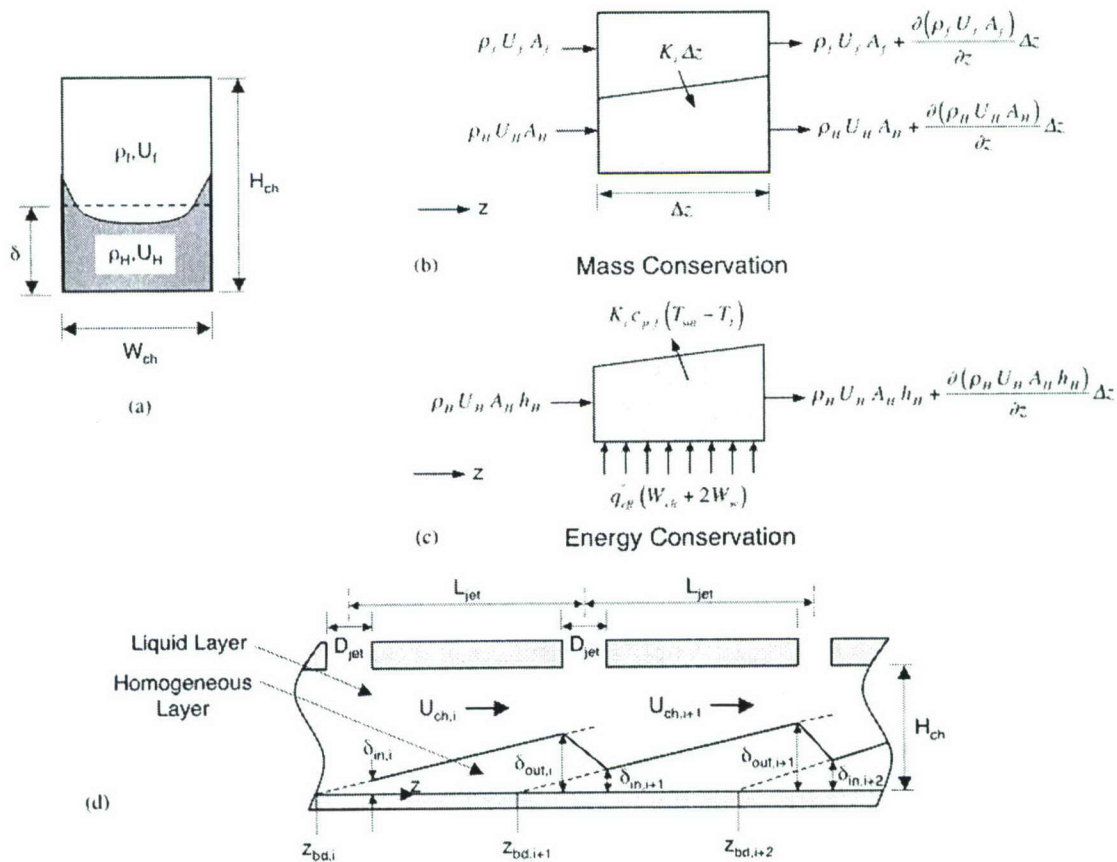


Figure 6.17 (a) Cross-sectional representation of Developing Homogeneous Layer Model (DHL). (b) Mass conservation for liquid and homogeneous layer control volumes. (c) Energy conservation for homogeneous layer control volume. (d) Side view representation of DHL for hybrid cooling configuration.

$$\frac{d(\rho_f U_f A_f)}{dz} + K_i = 0, \quad (6.5)$$

and

$$\frac{d(G_H A_H)}{dz} - K_i = 0, \quad (6.6)$$

where U_f is the mean velocity of the liquid layer, A_f the cross-sectional area of the liquid layer, $G_H (= \rho_H U_H)$ the mass velocity of the homogeneous two-phase layer, U_H the mean velocity of the homogenous layer, A_H the cross-sectional area of the homogeneous layer, and K_i the rate of mass transfer from the liquid layer to the homogeneous layer per unit distance.

As depicted in Fig. 6.17(c), energy conservation for the same control volume should account for (i) the portion of the wall heat that increases the temperature of the liquid mass transferred between the liquid layer and the homogeneous layer from T_f to T_{sat} , and (ii) a second portion that increases the latent heat of the homogeneous layer.

$$q_{eff}(W_{ch} + 2W_w) = \frac{d}{dz}(G_H A_H h_H) + K_i c_{p,f}(T_{sat} - T_f), \quad (6.7)$$

where h_H is the enthalpy of the homogenous layer.

As illustrated in Fig. 6.17(a), the flow areas for the liquid layer and the homogeneous layer can be expressed, respectively, as

$$A_f = W_{ch}(H_{ch} - \delta), \quad (6.8a)$$

and

$$A_H = W_{ch}\delta, \quad (6.8b)$$

where d is the thickness of the homogeneous layer. The area derivatives with respect to z can be expressed as

$$\frac{dA_f}{dz} = -W_{ch} \frac{d\delta}{dz} \quad (6.9a)$$

and

$$\frac{dA_H}{dz} = W_{ch} \frac{d\delta}{dz}. \quad (6.9b)$$

Combining Eqs. (6.6a), (6.6b), (6.9a) and (6.9b) and assuming the liquid layer is constant between jets yield the following relation for the spatial variation of homogeneous layer thickness:

$$\frac{d\delta}{dz} = \frac{\delta \frac{dG_H}{dz}}{(\rho_f U_f - G_H)}. \quad (6.10)$$

As indicated earlier, because vapor is generated along the micro-channel in a subcooled boiling region, thermodynamic equilibrium quality cannot be used to determine the enthalpy of the two-phase layer. According to the DHLM, the enthalpy of the homogeneous layer is expressed as

$$h_H = h_f + x_H h_{fg}, \quad (6.11)$$

where x_H is an apparent flow quality. Lee and Mudawar (*in review*) tested two different relations by Levy (1967) and Kroeger and Zuber (1968) to determine x_H and found the latter better suited for short micro-channels. The apparent flow quality according to the Kroeger and Zuber model can be expressed as

$$x_H = \frac{c_{p,f} \Delta T_{sub,in} (Z^+ - T^*)}{h_{fg} - c_{p,f} \Delta T_{sub,in} (1 - T^*)}, \quad (6.12)$$

where

$$Z^+ = \frac{z - z_{bd}}{z_{sat} - z_{bd}}, \quad (6.13a)$$

$$T^* = \tanh Z^+, \quad (6.13b)$$

and z_{bd} and z_{sat} are the axial locations corresponding to bubble departure and thermodynamic equilibrium quality of unity, respectively.

By combining Eqs. (6.6a), (6.9a), (6.9b), (6.11), (6.12) with energy conservation Eq. (6.7), the spatial variation of the homogeneous layer's mass velocity can be expressed as

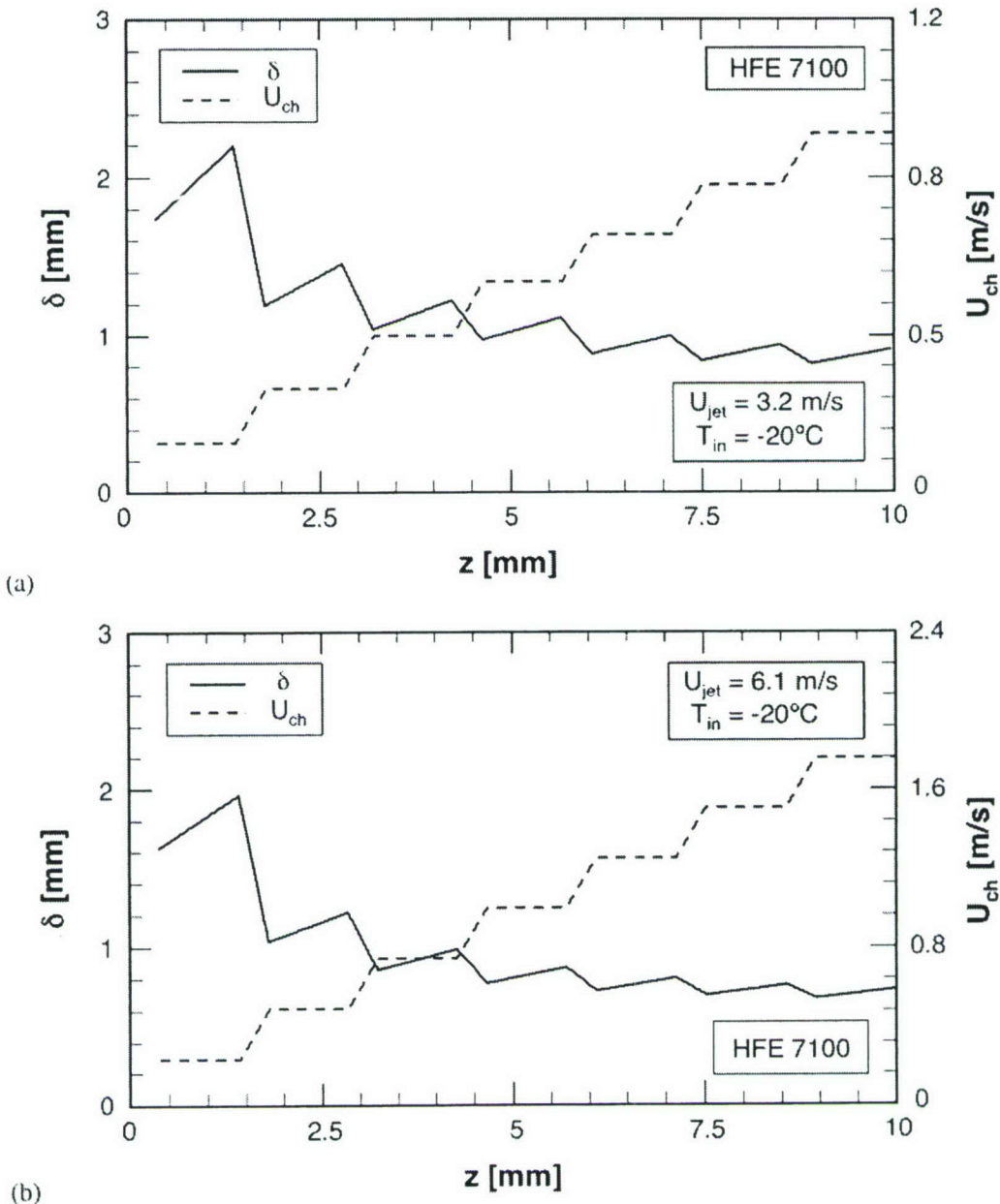


Figure 6.18 Variations of homogeneous layer thickness and liquid layer velocity along micro-channel for $T_{in} = -20^\circ\text{C}$ at (a) $U_{jet} = 3.2 \text{ m/s}$ and (b) $U_{jet} = 6.1 \text{ m/s}$.

$$\frac{dG_H}{dz} = \frac{(\rho_f U_f - G_H) \left\{ q_{eff} (W_{ch} + 2W_w) - W_{ch} \delta G_H h_{fg} \frac{dx_H}{dz} \right\}}{\rho_f U_f W_{ch} \delta [h_H + c_{p,f} (T_{sat} - T_f)]}. \quad (6.14)$$

The spatial variation of the homogeneous layer's thickness can be obtained by substituting Eq. (6.14) into Eq. (6.10).

$$\frac{d\delta}{dz} = \frac{q_{eff} (W_{ch} + 2W_w) - W_{ch} \delta G_H h_{fg} \frac{dx_H}{dz}}{\rho_f U_f W_{ch} [h_H + c_{p,f} (T_{sat} - T_f)]}. \quad (6.15)$$

Equations (6.14) and (6.15) are coupled ordinary differential equations. The homogeneous layer's thickness must satisfy the following boundary conditions:

$$\delta = \begin{cases} 0 & \text{at } z = -z_{bd} \\ H_{ch} & \text{at } z = z_{sat} \end{cases}. \quad (6.16)$$

The location of saturated boiling, z_{sat} , can be determined with the aid of a simple energy balance.

$$z_{sat} = \frac{\rho_f U_f W_{ch} H_{ch} c_{p,f} (T_{sat} - T_f)}{q_{eff} (W_{ch} + 2W_w)}. \quad (6.17)$$

The location of bubble departure, z_{bd} , is calculated from

$$z_{bd} = - \left[z_{sat} - \Delta T_{sub,bd} \frac{\rho_f U_f W_{ch} H_{ch} c_{p,f}}{q_{eff} (W_{ch} + 2W_w)} \right], \quad (6.18)$$

where $\Delta T_{sub,bd} = \frac{q_{eff}}{h_{bd}}$. (6.19)

The heat transfer coefficient at bubble departure, h_{bd} , in the micro-channel can be determined using an iterative procedure that seeks to satisfy the boundary conditions of the homogeneous layer's thickness given by Eq. (6.16).

The above DHLM development concerns the micro-channel segments between jets. As illustrated in Fig. 6.17(d), the thickness, d , of the homogeneous layer increases along the micro-channel until it encounters the next jet. This second jet deposits

additional fluid, which increases the coolant's mass flow rate for the next micro-channel segment. A new liquid layer velocity must be used for the second segment to account for the jet fluid. This new velocity can be determined from mass conservation.

$$U_{ch,i+1} = \frac{\rho_f U_{ch,i} W_{ch} (H_{ch} - \delta_{out,i}) + \rho_f U_{jet} A_{jet}}{\rho_f W_{ch} (H_{ch} - \delta_{in,i+1})}. \quad (6.20)$$

The heat transfer coefficient at bubble departure, h_{bd} , is recalculated for the micro-channel segment downstream from the jet using the updated liquid layer velocity to once again satisfy the boundary conditions given by Eq. (6.16).

Figures 6.18(a) and 6.18(b) show predicted variations of liquid layer velocity and homogeneous layer thickness along the micro-channel for $T_{in} = -20^\circ\text{C}$ and $U_{jet} = 3.2$ and 6.1 m/s, respectively. In both cases, the liquid layer velocity increases along the micro-channel. While the thickness of the homogenous layer increases between jets, its overall magnitude decreases along the micro-channel. Comparing Figs. 6.18(a) and 6.18(b) shows increasing the jet velocity, and therefore the coolant's flow rate, increase the magnitude of liquid layer velocity and, to a lesser extent, decrease the thickness of the homogenous layer.

As discussed in the next section, the liquid layer velocity given by Eq. (6.20) is key to assessing the contribution of the micro-channel flow to CHF.

6.6.2. CHF Prediction Procedure

The strategy used in predicting CHF for the hybrid cooling configuration is to superimpose the contributions of jet-impingement and micro-channel flow. In other words, the heated area is divided into two portions, one dominated by jet impingement and the other micro-channel flow. As illustrated in Fig. 6.19(a), the first portion consists of the stagnation zones of the jets and surrounding vicinity, while the second is comprised of the remaining micro-channel flow areas between jets.

To determine CHF for the hybrid cooling configuration, separate CHF correlations are used for the jet-impingement and micro-channel portions of the heat wall. For jet impingement, a correlation by Monde and Mitsutake (1996) is used.

$$\frac{q_{mw}}{q_{mw,sat}} = \frac{1 + \sqrt{1 + 4CJa}}{2}, \quad (6.21)$$

where $\frac{q_{mw,sat}}{\rho_f U_{jet} h_{fg}} = 0.221 \left(\frac{\rho_f}{\rho_g} \right)^{0.645} \left(\frac{2\sigma}{\rho_f U_{jet}^2 (l - D_{jet})} \right)^{0.343} \left(1 + \frac{l}{D_{jet}} \right)^{-0.364}, \quad (6.22)$

$$C = \frac{0.95 \left(\frac{D_{jet}}{l} \right)^2 \left(1 + \frac{l}{D_{jet}} \right)^{0.364}}{\left(\frac{\rho_f}{\rho_g} \right)^{0.43} \left(\frac{2\sigma}{\rho_f U_{jet}^2 (l - D_{jet})} \right)^{0.343}}, \quad (6.23)$$

$$Ja = \left(\frac{\rho_f}{\rho_g} \right) \left(\frac{c_{p,f} \Delta T_{sub,in}}{h_{fg}} \right), \quad (6.24)$$

l is the characteristic length of the heated surface (the length of a square heater for single jet case), and q_{mw} is CHF based on the *wetted* area. This correlation is highly effective for circular impinging jets since it is equally accurate at predicting data for a single jet or multiple jets; it is also valid for coolants with drastically different thermophysical properties. For systems involving multiple jets, Monde and Mitsutake (1996) recommended that instead of representing the length of the heated surface, the characteristic length, l , in their CHF correlation be replaced by twice the longest length between the center of a jet's stagnation zone and the edge of the portion of the heated area that is impacted by the same jet. For the present hybrid cooling configuration, l is set equal to twice the distance from the center of the jet's stagnation zone to the furthest point along the micro-channel's sidewall.

$$\frac{l}{2} = \sqrt{\left(\frac{W_{ch}}{2} \right)^2 + H_{ch}^2}. \quad (6.25)$$

For the micro-channel portion of the heated wall, the correlation by Bowers and Mudawar (1996) is used because of its suitability to subcooled micro-channel flow. For very short lengths, their correlation can be expressed as

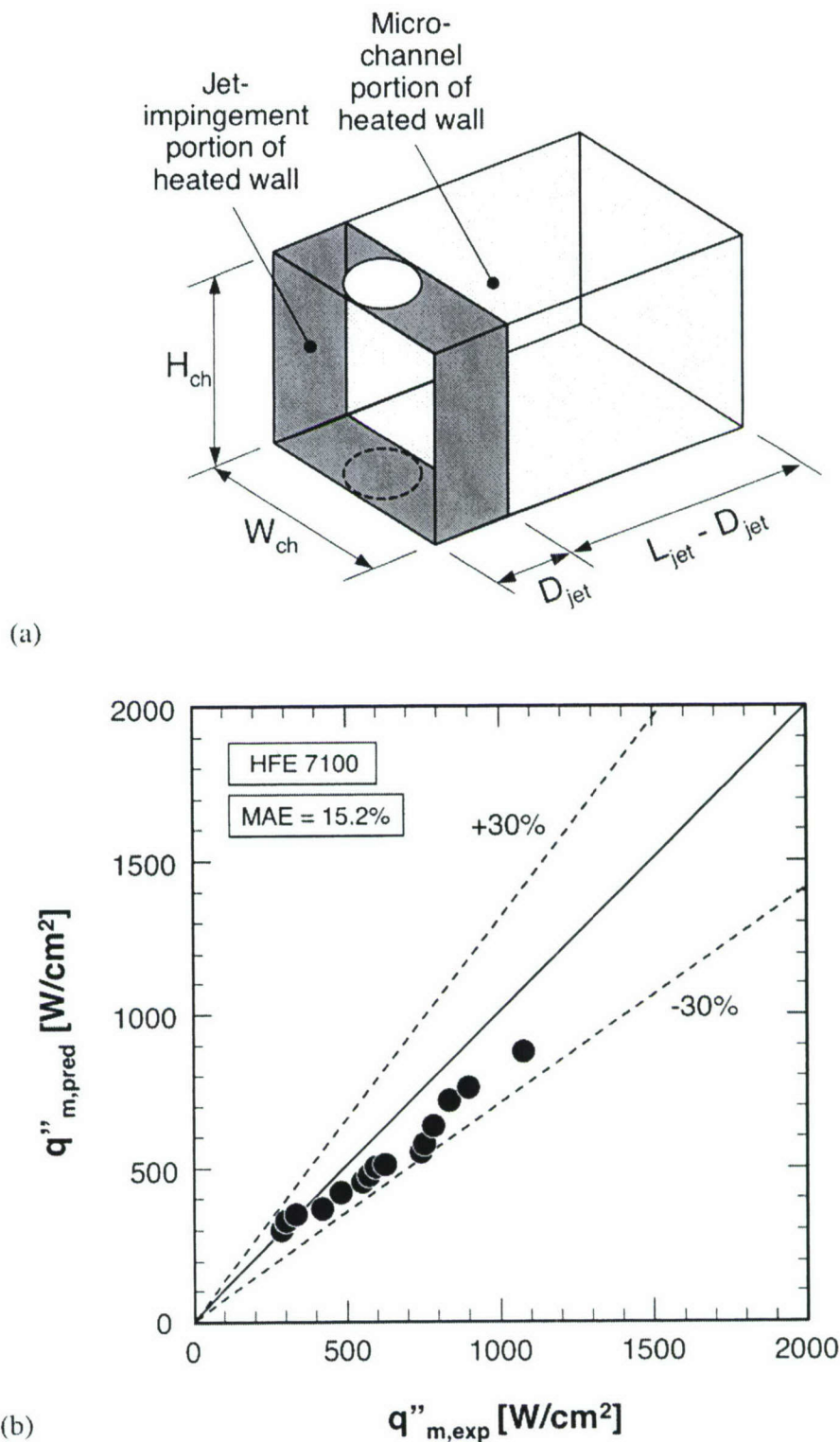


Figure 6.19 (a) Partitioning of one segment of the heated wall micro jet-impingement and micro-channel flow portions. (b) Comparison of CHF data and predictions based on CHF superpositioning scheme.

$$\frac{\dot{q}_{mw}}{\rho_f U h_{fg}} = 0.104 \left(\frac{\rho_f}{\rho_g} \right)^{-0.29} \left(\frac{\rho_f U^2 L}{\sigma} \right)^{-0.24} \left[1 + 0.4 \frac{c_{p,f} \Delta T_{sub,o}}{h_{fg}} \right], \quad (6.26)$$

where \dot{q}_{mw} is CHF based on the channel's wetted area. For the hybrid cooling configuration, the inlet velocity, U , and tube length, L , in Eq. (6.26) are replaced for each micro-channel segment between jets by $U_{ch,i}$ and $L_{jet} - D_{jet}$, respectively. The outlet subcooling, $\Delta T_{sub,o}$, in Eq. (6.26) is calculated with assuming linearly increasing liquid temperature from the center of micro-channel to the outlet based on measured inlet and outlet module temperatures.

Once CHF values are determined for all the jet impingement and micro-channel segments of the flow area, CHF for the entire test module is calculated by area-averaging these values over the top test surface area, A_t , of the module.

$$[(W_{ch} + 2W_w)L_{jet}] \dot{q}_m = [2(W_{ch} + H_{ch})(L_{jet} - D_{jet})] \dot{q}_{mw} \Big|_{Mudawar \& Bowers} + \left[2(W_{ch} + H_{ch})D_{jet} - \frac{\pi D_{jet}^2}{4} \right] \dot{q}_{mw} \Big|_{Monde \& Mitsutake}. \quad (6.27)$$

Figure 6.19(b) shows the superpositioning technique is very effective at predicting the HFE-7100 CHF data, evidenced by a mean absolute error of 15.2%.

CHAPTER 7. CONCLUSIONS

7.1. Selection of Cooling Geometry and Single-Phase Heat Transfer Characteristics

A new hybrid cooling scheme was developed that combines the benefits of both micro-jet impingement and micro-channel flow. The performance of the cooling scheme is further enhanced by indirect refrigeration cooling. Numerical analysis was used to explore the effects of key parameters of the hybrid geometry for single-phase flow. Preferred values of these parameters were used to design a test module that served to validate the predicted performance using HFE 7100 as a working fluid. Key findings from the study are as follows:

- (1) The proposed cooling scheme involves complex interactions of circular impinging jets with micro-channel flow. Numerical results show increasing jet velocity allows jets to penetrate the micro-channel flow toward the surface, especially in shallow micro-channels, greatly decreasing the average wall temperature.
- (2) Excellent agreement between numerical predictions and temperature measurements proves the standard k - ε model is very effective at predicting the heat transfer performance of the hybrid cooling scheme.
- (3) For slot jets, heat conduction along the micro-channel sidewalls is especially effective at relatively low impingement velocities. Increasing micro-channel height for low velocities reduces the temperature gradient along the micro-channel. Because of a stronger impingement effect, the influence of micro-channel height at high Reynolds numbers is less significant. For fixed micro-channel width and jet Reynolds number, decreasing jet width increases jet velocity, reducing surface temperature. However, decreasing jet width also increases surface temperature gradient along the micro-channel.

- (4) The hybrid micro-channel/slot jet module maintains a high degree of surface temperature uniformity. Surface temperature gradients are below 2 °C for heat fluxes up to 50 W/cm². Even without phase change, the hybrid module is capable of dissipating very high heat fluxes. A heat flux of 305.9 W/cm² is achieved with a jet velocity of 7.37 m/s and inlet temperature of -40 °C.
- (5) A superpositioning technique is introduced that partitions the heat transfer surface into zones that are each dominated by a different heat transfer mechanism, and assigning a different heat transfer coefficient value to each zone. Using this technique, new correlations for the three jet patterns and slot jets are developed that predict the present HFE 7100 data with the mean absolute error of 5.26% and 3.43%, respectively.

7.2. Effect of Circular-Jet Patterns on Single-Phase Heat Transfer Characteristics

This study examined a hybrid thermal management scheme that combines the cooling benefits of micro-channel flow and jet impingement. Indirect refrigeration cooling is used to achieve low coolant temperatures in order to decrease wall temperature during high-flux heat dissipation. Three micro-jet patterns are examined, decreasing-jet-size, equal-jet-size and increasing-jet-size. The performance of each pattern is examined experimentally and numerically using HFE 7100 as a working fluid. Key findings from the study are as follows:

- (1) A single-phase correlation is developed using a superpositioning technique that assigns different heat transfer coefficient values to different regions of the micro-channel based on the dominant heat transfer mechanism for each region. A single correlation is found equally effective at fitting experimental data for all three micro-jet patterns.
- (2) The three hybrid module configurations involve complex interactions of impinging jets with micro-channel flow. Increasing the flow rate (and therefore jet speed) strengthens the contribution of jet impingement to the overall cooling

performance, resulting in lower overall bottom wall temperatures. However, this advantage is realized at the expense of greater wall temperature gradients.

- (3) The highest convective heat transfer coefficients and lowest bottom wall temperatures are achieved with the decreasing-jet-size pattern, rendering this pattern most suitable for applications demanding high-heat-flux removal. The equal-jet-size pattern provides the smallest gradients in bottom wall temperature; this pattern is therefore better suited to devices demanding temperature uniformity. The increasing-jet-size pattern produces complex flow patterns and greater wall temperature gradients, which are caused by blockage of the spent fluid by larger jets near the channel outlets.

7.3. Two-Phase Heat Transfer Characteristics

This study examined the two-phase cooling performance of the hybrid micro-channel/micro-jet-impingement cooling scheme using HFE 7100 as a working fluid. Experiments were performed to investigate the parametric trend of cooling performance relative to jet velocity and fluid subcooling, as well as to obtain a correlation for two-phase heat transfer coefficient. Key findings from this portion of the study are as follows:

- (1) Bubble nucleation, growth, departure, and coalescence along the micro-channel in the hybrid scheme are fundamentally different from those encountered in conventional micro-channels. In the hybrid scheme, subcooled jet fluid can cause rapid condensation and collapse bubbles formed upstream. Therefore, this scheme involves repeated regions of bubble growth followed by collapse, rather than the continuous growth common to conventional micro-channel flow. By reducing void fraction along the micro-channel, the hybrid scheme contributes greater wall temperature uniformity.
- (2) Increasing subcooling and/or flow rate delay the onset of boiling to higher heat fluxes and higher wall temperatures. CHF also increases considerably with increased subcooling as liquid is able absorb a large fraction of the supplied heat in the form of sensible heat, and better condensation resists vapor blanket formation.

- (3) The two-phase cooling performance of the circular jet pattern is superior to that of the slot jet pattern, especially in terms of high-flux dissipation. Differences in cooling performance between the two patterns are the result of drastically different mechanisms of void fraction development along the micro-channel. The superior performance of the circular pattern is realized with a repeated pattern of bubble growth and collapse between jets that nets only a mild overall increase in vapor void fraction. Cooling fluxes as high as $1,127 \text{ W/cm}^2$ were achieved with the circular jet pattern without incurring CHF.
- (4) A correlation for the nucleate boiling region, which accounts for subcooling, fits the present HFE 7100 data of slot jets with a mean absolute error of 5.66%.

7.4. Effect of Circular-Jet Patterns on Two-Phase Heat Transfer Characteristics

This study examined a two-phase hybrid cooling scheme that combines the cooling benefits of micro-channel flow and micro-jet impingement. Three micro-jet patterns were examined, decreasing-jet-size, equal-jet-size and increasing-jet-size. The performance of each pattern was examined experimentally using HFE 7100 as a working fluid. Key findings from the study are as follows:

- (1) The hybrid cooling configuration provides a two-phase cooling performance that is free from the incipient boiling overshoot and temperature drop, which are prevalent in many boiling situations involving low contact angle liquids. Furthermore, virtually identical boiling curves are achieved by increasing and decreasing heat flux, proving this configuration is void of nucleate boiling hysteresis. These attributes render the hybrid cooling scheme highly effective for electronics cooling applications.
- (2) Feeding subcooled coolant into the micro-channel in a gradual manner greatly reduces vapor growth along the micro-channel. Void fraction increases between jets but decreases sharply beneath the jets. This creates an unusual pattern of void fraction growth followed by coalesce, and a relatively mild overall increase along the flow direction with predominantly liquid flow at outlet.

-
- (3) Pressure drop in the single-phase region decreases with increasing heat flux because of decreasing liquid viscosity. However, unlike most flow boiling situations, where pressure drop begins increasing in the nucleate boiling region, pressure drop in the hybrid configuration continues decreasing and reaches a minimum just before CHF. This behavior is closely related to the low void fraction and predominantly liquid flow. Pressure drop in the two-phase region is highest for the equal-jet-size pattern, followed by the decreasing-jet-size and increasing-jet-size patterns, respectively.
 - (4) Because of the mild void fraction, the hybrid cooling configuration is highly effective at utilizing the bulk liquid subcooling to achieve high CHF values. It is postulated CHF mechanism is similar to that of Departure from Nucleate Boiling (DNB) encountered in channel flow with high flow rates, high subcoolings and small length-to-diameter ratios. Highest CHF values are achieved with the decreasing-jet-size pattern because this pattern yields the highest outlet subcooling.
 - (5) A single correlation is constructed for the three jet patterns, which relates the two-phase heat transfer coefficient to heat flux and wall superheat. The correlation predicts the two-phase HFE 7100 data with a mean absolute error of 6.59%.

7.5. Critical Heat Flux

This study examined the two-phase heat transfer performance of a hybrid cooling scheme that combines the cooling attributes of micro-channel flow and jet impingement. A test module was constructed and tested using highly subcooled HFE-7100 to explore nucleate boiling and CHF trends. A two-phase flow model was used to ascertain liquid velocity variations along the micro-channel. Using the calculated velocities, a superpositioning technique was developed to determine CHF for the hybrid cooling configuration. Key findings from the study are as follows:

- (1) Increasing flow rate and/or subcoolings increase both the onset of boiling (ONB) and CHF to higher heat fluxes and higher temperatures. However, data appear to converge in the nucleate boiling region. The highest CHF value of $1,080 \text{ W/cm}^2$ was measured for a jet velocity of 5.70 m/s and inlet temperature of -20°C . The upper heat flux value measured in this study is $1,127 \text{ W/cm}^2$, which corresponds to

a jet velocity of 6.50 m/s and -20°C inlet temperature; this test was intentionally aborted prior to CHF to protect the test module against burnout. To the authors' knowledge, these heat flux values are the highest ever achieved with a dielectric coolant at near atmospheric pressure.

- (2) The hybrid cooling configuration involves complex interactions between circular jets and micro-channel flow, and unusual spatial variations of quality and void fraction. With the subcooled liquid supplied gradually by the jets, the flow rate is not constant, but increases along the micro-channel. Following the assumptions of the Developing Homogeneous Layer Model (DHL), the micro-channel flow is described as consisting of a homogeneous two-phase layer along the heated wall and a bulk liquid layer. This model is highly effective at determining the complex liquid velocity variations along the micro-channel.
- (3) CHF is determined with a superpositioning technique that consists of dividing the heated wall into two portions, one dominated by jet impingement and the other micro-channel flow. This technique utilizes the DHL to determine liquid velocity for each segment of the micro-channel between jets. A prior CHF correlation by Monde and Mitsutake is applied to the jet-impingement portion, and another CHF correlation by Bowers and Mudawar to the micro-channel portion. This superpositioning technique is shown to be highly effective at predicting the CHF data for the hybrid cooling configuration.

LIST OF REFERENCES

LIST OF REFERENCES

- Ambatipudi, K.K., Rahman, M.M, 2000, "Analysis of conjugate heat transfer in microchannel heat sinks", *Numer. Heat Transfer, Part A*, Vol. 37, pp. 711-731.
- Baydar, E., Ozmen, Y., 2005, "An Experimental and numerical investigation on a confined impinging air jet at high Reynolds numbers", *App. Thermal Eng.*, Vol. 25, pp. 409-421.
- Bowers, M.B., Mudawar, I., 1994, "High flux boiling in low flow rate, low pressure drop mini-channel and micro-channel heat sinks", *Int. J. Heat Mass Transfer*, Vol. 37, pp. 321-332.
- Bowers, M.B., Mudawar, I., 1994, "Two-phase electronic cooling using mini-channel and micro-channel heat sinks - Part 1. Design criteria and heat diffusion constraints", *ASME J. Electronic Packaging*, Vol. 116, pp. 290-297.
- Bowers, M.B., Mudawar, I., 1994, "Two-phase electronic cooling using mini-channel and micro-channel heat sinks - Part 2. Flow rate and pressure drop constraints", *ASME J. Electronic Packaging*, Vol. 116, pp. 298-305.
- Bowers, M.B., Mudawar, I., 1996, "Parametric study of ultra-high CHF in highly subcooled water flow inside small diameter tubes", in *Convective Flow Boiling*, J. C. Chen, Y. Fujita, F. Mayinger, and R.A. Nelson, eds., Taylor & Francis, Washington, DC, pp. 117-122.
- Collier, J.G., Thome, J.R., 1994, *Convective Boiling and Condensation*, third ed., Oxford University Press, Oxford.
- Craft, T.J., Graham, L.J.W., Launder, B.E., 1993, "Impinging jet studies for turbulence model assessment - II. An examination of the performance of four turbulence models", *Int. J. Heat Mass Transfer*, Vol. 36, pp. 2685-2697.
- Estes, K.A., Mudawar, I., 1995, "Comparison of two-phase electronic cooling using free jets and sprays", *ASME J. Electronic Packaging*, Vol. 117, pp. 323-332.

Fedorov, A.G., Viskanta, R., 2000, "Three-dimensional conjugate heat transfer in the microchannel heat sink for electronic packaging", Int. J. Heat Mass Transfer, Vol. 43, pp. 399-415.

Fluent 6.2.16., 2005, User's Guide, Fluent Inc., Lebanon, NH.

Gambit 2.2.30., 2006, User's Guide, Fluent Inc., Lebanon, NH.

Haramura, Y., Katto, Y., 1983, "A new hydrodynamic model of critical heat flux applicable to both pool and forced convection boiling on submerged bodies in saturated liquids", Int. J. Heat Mass Transfer, Vol. 26, pp. 389-399.

Incropera, F.P., 1999, Liquid Cooling of Electronic Devices by Single-Phase Convection, Wiley, New York, NY.

Jiang, L., Wong, M., Zohar, Y., 2001, "Forced convection boiling in a microchannel heat sink", J. Microelectromechanical Systems, Vol. 10, pp. 80-87.

Jiji, L.M., Dagan, Z., 1987, "Experimental investigation of single-phase multi-jet impingement cooling of array of microelectronic heat sources", Proc. Int. Symp. on Cooling Technology for Electronic Equipment, Honolulu, HI, pp. 265-283.

Johns, M.E., Mudawar, I., 1996, "An ultra-high power two-phase jet-impingement avionic clamshell module", ASME J. Electronic Packaging, Vol. 118, pp. 264-270.

Katto, Y., 1983, "Critical heat flux in forced convective flow", Proc. ASME/JSME thermal Engng Joint Conf., Hawaii, Vol. 3, pp. 1-10.

Katto, Y., Kunihiro, M., 1973, "Study of the mechanism of burn-out in boiling system of high burn-out heat flux", Bull. JSME Vol. 16, pp. 1357-1366.

Kim, S.J., Kim, D., 1999, "Forced convection in microstructures for electronic equipment cooling", ASME J. Heat Transfer, Vol. 121, pp. 639-645.

P.G. Kroeger, P.G., Zuber, N., 1968, "An analysis of the effects of various parameters on the average void fractions in subcooled boiling", Int. J. Heat Mass Transfer, Vol. 11, pp. 211-213.

Launder, B.E., Spalding, D.B., 1974, "The numerical computation of turbulent flows, Comput. Methods Appl. Mech. Eng., Vol. 3, pp. 269-289.

- Lelea, D., Nishio, S., Takano, K., 2004, "The experimental research on micro-tube heat transfer and fluid flow of distilled water", Int. J. Heat Mass Transfer, Vol. 47, pp. 4215-4231.
- Lee, J., Mudawar, I., 2005, "Two-phase flow in high-heat-flux micro-channel heat sink for refrigeration cooling applications: Part I-pressure drop characteristics", Int. J. Heat Mass Transfer, Vol. 48, pp. 928-940.
- Lee, J., Mudawar, I., in review, "Experimental investigation and theoretical model for subcooled flow boiling pressure drop in micro-channel heat sinks", ASME J. Electronic Packaging.
- Levy, S., 1967, "Forced convection subcooled boiling – Prediction of vapor volumetric fraction", Int. J. Heat Mass Transfer, Vol. 10, pp. 951-965.
- Little, W.A., 2000, "Low temperature electronics workshop: recent advances in low cost cryogenic coolers for electronics", Proc. 16th IEEE Semi-Therm Symposium, San Jose, CA, pp. 110-111.
- Ma, C.F., Bergles, A.E, 1986, "Jet impingement nucleate boiling", Int. J. Heat Mass Transfer, Vol. 29, pp. 1095-1101.
- Martin, H., 1977, "Heat and mass transfer between impinging gas jets and solid surfaces", Adv. in Heat Transfer, Vol. 13, pp. 1-60.
- Meyer, M.T., Mudawar, I., Boyack, C.E., Hale, C.A., 2006, "Single-phase and two-phase cooling with an array of rectangular jets", Int. J. Heat Mass Transfer, Vol. 49, pp. 17-29.
- Monde, M., 1987, "Critical heat flux in saturated forced convection boiling on a heated disk with an impinging jet", ASME J. Heat Transfer, Vol. 109, pp. 991-996.
- Monde, M., Kusuda, H., Uehara, H., 1980, "Burnout heat flux in saturated forced convection boiling with two or more impinging jets", Heat Transfer-Japanese Research, Vol. 9, pp. 18-31.
- Monde, M., Inoue, T., 1991, "Critical heat flux in saturated forced convective boiling on a heated disk with multiple impinging jet", ASME J. Heat Transfer, Vol. 113, pp. 722-727.
- Monde, M., Mitsutake, Y., 1996, "Critical heat flux in forced convective subcooled boiling with multiple impinging jets", ASME J. Heat Transfer, Vol. 118, pp. 241-243.

- Mudawar, I., 2001, "Assessment of high-heat-flux thermal management schemes", IEEE Trans. -Components and Packaging Tech., Vol. 24, pp. 122-141.
- Mudawar, I., Bowers, M.B., 1999, "Ultra-high critical heat flux (CHF) for subcooled water flow boiling-I: CHF data and parametric effects for small diameter tubes", Int. J. Heat Mass Transfer, Vol. 42, pp. 1405-1428.
- Mudawar, I., Incropera, T.A., Incropera, F.P., 1987, "Boiling heat transfer and critical heat flux in liquid films falling on vertically-mounted heat sources", Int. J. Heat Mass Transfer, Vol. 30, pp. 2083-2095.
- Mudawar, I., Maddox, D.E., 1989, "Critical heat flux in subcooled flow boiling of fluorocarbon liquid on a simulated electronic chip in a vertical rectangular channel", Int. J. Heat Mass Transfer, Vol. 32, pp. 379-394.
- Mudawar, I., Wadsworth, D.C., 1991, "Critical heat flux from a simulated chip to a confined rectangular impinging jet of dielectric liquid", Int. J. Heat Mass Transfer, Vol. 34, pp. 1465-1479.
- Naeemi, A., Meindl J.D., 2004, "An upper limit for aggregate I/O interconnect bandwidth of GSI chips constrained by power dissipation", Proc. IEEE Int. Interconnect Tech. Conf., San Francisco, CA. pp.157-159.
- Nakayama, W., Behnia, M., Mishima, H., 2000, "Impinging jet boiling of a fluorinert liquid on a foil heater array", ASME J. Electronic Packaging, Vol. 122, pp. 264-270.
- Park, T.H., Choi, H.G., Yoo, J.Y., Kim, S.J., 2003, "Streamline upwind numerical simulation of two-dimensional confined impinging slot jets", Int. J. Heat Mass Transfer, Vol. 46, pp. 251-262.
- Patankar, S.V., 1980, Numerical Heat Transfer and Fluid Flow, Hemisphere, Washington, DC.
- Peng, X.F., Wang, B.-X., 1993, "Forced convection and flow boiling heat transfer for liquid flowing through microchannels", Int. J. Heat Mass Transfer, Vol. 36, pp. 3421-3427.
- Qu, W., Mudawar, I., 2002, "Experimental and numerical study of pressure drop and heat transfer in a single-phase micro-channel heat sink", Int. J. Heat Mass Transfer, Vol. 45, pp. 2549-2565.

- Qu, W., Mudawar, I., 2003, "Measurement and prediction of pressure drop in two-phase micro-channel heat sinks", Int. J. Heat Mass Transfer, Vol. 46, pp. 2737-2753.
- Qu, W., Mudawar, I., 2004, "Measurement and correlation of critical heat flux in two-phase micro-channel heat sinks", Int. J. Heat Mass Transfer, Vol. 45, pp. 2549-2565.
- Saha, P., Zuber, N., 1974, "Point of net vapor generation and vapor void fraction in subcooled boiling", in: Heat Transfer 1974 Vol. 4, Proc. Int. Heat Transfer Conf., Tokyo, pp. 175-179.
- Schmidt, R.R., Notohardjono, B.D., 2002, "High-end server low-temperature cooling", IBM J. Res. & Dev., Vol. 49, pp. 739-751.
- Steinke, M.E., Kandlikar, S.G., 2004, "An experimental investigation of flow boiling characteristics of water in parallel microchannels", ASME J. Heat Transfer, Vol. 126, pp. 518-526.
- Sung, M.K., Mudawar, I., 2006, "Experimental and numerical investigation of single-phase heat transfer using a hybrid jet impingement/micro-channel cooling scheme", Int. J. Heat Mass Transfer, Vol. 49, pp. 682-694.
- Sung, M.K., Mudawar, I., 2006, "Correlation of critical heat flux in hybrid jet impingement/micro-channel cooling scheme", Int. J. Heat Mass Transfer, Vol. 49, pp. 2663-2672.
- Sung, M.K., Mudawar, I., *in press*, "Single-phase hybrid micro-channel/micro-jet impingement cooling", Int. J. Heat Mass Transfer.
- Sung, M.K., Mudawar, I., *in press*, "Single-phase and two-phase heat transfer characteristics of low temperature hybrid micro-channel/micro-jet-impingement cooling", Int. J. Heat Mass Transfer.
- Sung, M.K., Mudawar, I., *in press*, "Effects of jet pattern on single-phase cooling performance of hybrid micro-channel/micro-circular-jet-impingement thermal management scheme", Int. J. Heat Mass Transfer.
- Sung, M.K., Mudawar, I., *in press*, "Single-phase and two-phase cooling using hybrid micro-channel/slot-jet-module", Int. J. Heat Mass Transfer.
- Tay, A.A.O., Xue, H., Yang, C., 2002, "Cooling of electronic components with free jet impingement boiling", IEEE Inter. Society Conf. – Thermal Phenomena, pp. 387-394.

- Tuckerman, D.B., Pease, R.F.W., 1981, "High-performance heat sinking for VLSI", IEEE Electron. Dev. Letters EDL-2, pp. 126-129.
- Wadsworth, D.C., Mudawar, I., 1990, "Cooling of a multichip electronic module by means of confined two-dimensional Jets of dielectric liquid", ASME J. Heat Transfer, Vol. 112, pp. 891-898.
- Watson, E.J., 1964, "The radial spread of a liquid over a horizontal plane", J. Fluid Mech., Vol. 20, pp. 481-499.
- Wolf, D.H., Incropera, F.P., Viskanta, R., 1996, "Local jet impingement boiling heat transfer", Int. J. Heat Mass Transfer, Vol. 39, pp. 1395-1406.
- Yang, C., Tay, A.A.O., Xue, H., 2001, "An experimental study of liquid jet impingement cooling of electronic components with and without boiling", IEEE Int. Sym. – Electronics Material and Packaging, pp. 369-375.

APPENDICES

Appendix A. HFE 7100 Properties

The entire saturated and liquid HFE 7100 property data is presented in tabulated form in Appendix A. The nomenclature used for the column headings is defined as follows:

P_{sat}	Saturation pressure
T_{sat}	Saturation temperature at P_{sat}
T_f	Liquid temperature
h_{fg}	Latent heat of vaporization
$c_{p,f}$	Specific heat at constant pressure
ρ_f	Liquid density
ρ_g	Vapor density
μ_f	Liquid viscosity
k_f	Liquid conductivity
Pr_f	Liquid Prandtl number
σ	Surface tension

Table A.1 Saturated HFE 7100 property data.

P _{sat} [kPa]	T _s [°C]	h _f [kJ/kg]	c _p , [kJ/kg·K]	ρ _l [kg/m ³]	ρ _v [kg/m ³]	μ _r [kg/m·s]	k _r [W/m·K]	Pr _r	σ [N/m]
103.6	61.00	111.89	1.2550	1370.20	9.87	0.0003528	0.06178	7.17	0.011693
150	73.07	107.66	1.2791	1335.19	14.08	0.0003119	0.05942	6.71	0.010651
200	83.12	104.06	1.2992	1304.18	18.58	0.0002834	0.05745	6.41	0.009782
250	91.36	101.11	1.3157	1279.66	23.11	0.0002635	0.05584	6.21	0.009069
300	98.40	98.44	1.3298	1258.37	27.68	0.0002483	0.05446	6.06	0.008459
350	104.58	96.01	1.3422	1238.88	32.28	0.0002362	0.05326	5.95	0.007924
400	110.09	93.79	1.3532	1221.24	36.94	0.0002262	0.05218	5.86	0.007445
450	115.09	91.77	1.3632	1204.88	41.68	0.0002177	0.05120	5.79	0.007011
500	119.67	89.72	1.3723	1189.41	46.48	0.0002103	0.05031	5.74	0.006613
550	123.91	87.85	1.3808	1174.74	51.37	0.0002038	0.04948	5.69	0.006245
600	127.84	85.96	1.3887	1160.96	56.33	0.0001980	0.04871	5.65	0.005903
650	131.54	84.11	1.3961	1147.28	61.40	0.0001928	0.04799	5.61	0.005581
700	135.01	82.50	1.4030	1134.35	66.55	0.0001880	0.04731	5.58	0.005279
750	138.29	80.81	1.4096	1122.24	71.82	0.0001837	0.04667	5.55	0.004994
800	141.40	79.25	1.4158	1110.23	77.19	0.0001797	0.04606	5.52	0.004723
850	144.35	77.62	1.4217	1098.48	82.70	0.0001760	0.04548	5.50	0.004465
900	147.19	75.96	1.4274	1086.64	88.33	0.0001724	0.04493	5.48	0.004218
950	149.89	74.33	1.4328	1075.39	94.12	0.0001691	0.04440	5.46	0.003983
1000	152.47	72.73	1.4379	1064.12	100.03	0.0001659	0.04389	5.44	0.003757
1050	154.96	71.33	1.4429	1053.27	106.09	0.0001630	0.04341	5.42	0.003540
1100	157.35	69.77	1.4477	1042.31	112.36	0.0001601	0.04294	5.40	0.003332
1150	159.65	68.05	1.4523	1031.16	118.82	0.0001573	0.04249	5.38	0.003131
1200	161.88	66.50	1.4568	1020.35	125.48	0.0001547	0.04206	5.36	0.002936
1250	164.03	64.90	1.4611	1009.33	132.36	0.0001521	0.04164	5.34	0.002748
1300	166.11	63.42	1.4652	998.36	139.48	0.0001496	0.04123	5.32	0.002567
1350	168.13	61.80	1.4693	987.42	146.88	0.0001471	0.04083	5.29	0.002390
1400	170.09	60.14	1.4732	976.28	154.58	0.0001447	0.04045	5.27	0.002219
1450	171.99	58.52	1.4770	964.97	162.60	0.0001424	0.04008	5.25	0.002053
1500	173.83	56.77	1.4807	953.42	171.00	0.0001400	0.03972	5.22	0.001892
1550	175.63	55.03	1.4843	941.68	179.80	0.0001377	0.03937	5.19	0.001735
1600	177.38	53.33	1.4878	929.77	189.06	0.0001354	0.03903	5.16	0.001582
1650	179.08	51.61	1.4912	917.45	198.83	0.0001330	0.03869	5.13	0.001433
1700	180.74	49.50	1.4945	904.54	209.31	0.0001307	0.03837	5.09	0.001288
1750	182.35	47.62	1.4977	891.03	220.57	0.0001283	0.03805	5.05	0.001147
1800	183.93	45.48	1.5009	876.90	232.71	0.0001258	0.03775	5.00	0.001009
1850	185.47	43.08	1.5039	862.00	245.87	0.0001232	0.03744	4.95	0.000874
1900	186.97	40.53	1.5069	846.18	260.15	0.0001206	0.03715	4.89	0.000742
1950	188.43	37.92	1.5099	828.34	276.82	0.0001177	0.03687	4.82	0.000615
2000	189.86	34.92	1.5127	808.52	295.90	0.0001145	0.03659	4.73	0.000489
2050	191.27	31.55	1.5155	786.16	317.95	0.0001110	0.03631	4.63	0.000366
2110	192.91	26.82	1.5188	752.89	351.63	0.0001060	0.03599	4.47	0.000223
2150	193.96	21.36	1.5209	716.71	390.50	0.0001007	0.03578	4.28	0.000130
2189.3	195.00	15.79	1.5230	679.90	430.19	0.0000953	0.03558	4.08	0.000039

Table A.2 Liquid HFE 7100 property data.

T _f [°C]	ρ _f [kg/m ³]	c _{p,f} [kJ/kg·K]	μ _f [kg/m·s]	k _f [W/m·K]	Pr _f
-110	1892.20	913.00	0.0858317	0.09522	823.01
-100	1864.10	933.00	0.0296337	0.09326	296.46
-90	1836.00	953.00	0.0136587	0.09131	142.56
-80	1807.90	973.00	0.0075951	0.08935	82.71
-70	1779.80	993.00	0.0047940	0.08740	54.47
-60	1751.70	1013.00	0.0033072	0.08544	39.21
-50	1723.60	1033.00	0.0024286	0.08349	30.05
-40	1695.50	1053.00	0.0018627	0.08153	24.06
-30	1667.40	1073.00	0.0014741	0.07958	19.88
-20	1639.30	1093.00	0.0011943	0.07762	16.82
-10	1611.20	1113.00	0.0009858	0.07567	14.50
0	1583.10	1133.00	0.0008265	0.07371	12.70
10	1555.00	1153.00	0.0007023	0.07176	11.28
25	1512.85	1173.00	0.0005627	0.06980	9.46
35	1484.75	1193.00	0.0004920	0.06785	8.65
45	1456.65	1213.00	0.0004346	0.06589	8.00
55	1428.55	1233.00	0.0003874	0.06394	7.47

Appendix B. Single-Phase and Two-Phase Data

The entire datadase for single-phase and two-phase experiments is presented in tabulated form in Appendix B including the single-phase nucleate boiling portions of the boiling curve and CHF. The nomenclature used for the column headings is defined as follows:

PSIA	Absolute pressure at inlet
PSID	Pressure drop from nozzle inlet to channel outlet
Tsub	Degree of fluid subcooling, $T_{in} - T_{sat}$
Tin	Fluid temperature at inlet
T1	First point temperature measured at thermocouple plate
T2	Second point temperature measured at thermocouple plate
T3	Third point temperature measured at thermocouple plate
T4	Outermost temperature measured at thermocouple plate
Tsurf	1-D corrected area-weighted average surface temperature
Velocity	Jet velocity, U_{jet}
Delta T	$T_{surf} - T_{in}$
Flux	Heat flux at the heated surface based on power input and the surface area

Table B.1 Single-phase and two-phase experimental data for slot jets.

	PSIA	PSID	Tsub	Tin	T1	T2	T3	T4	Tsurf	Velocity	Delta T	Flux
	19.02	0.01	48.20	20.00	34.79	34.85	34.90	35.08	34.92	0.43	14.92	11.50
	19.02	0.03	48.14	20.06	52.46	52.74	52.75	53.08	52.79	0.43	32.73	25.82
	18.92	0.03	48.16	20.04	64.93	65.31	65.77	66.05	65.58	0.43	45.53	43.38
	18.96	-0.01	48.22	19.98	74.56	75.09	76.08	76.41	75.64	0.43	55.66	63.16
	19.13	0.04	48.06	20.14	83.37	84.25	85.50	86.32	85.01	0.43	64.87	85.16
	19.61	1.00	48.22	19.98	92.46	91.66	94.02	94.53	93.20	0.43	73.23	108.21
	18.65	-0.18	48.18	20.02	99.31	99.13	101.34	101.74	100.47	0.43	80.45	126.87
	18.83	-0.39	48.17	20.03	104.79	104.77	107.08	108.10	106.30	0.43	86.27	143.35
	19.45	0.28	48.09	20.11	109.04	108.97	111.70	112.79	110.76	0.43	90.65	155.38
CHF												213.21
	18.95	0.04	68.18	-0.08	27.19	27.38	27.43	27.61	27.43	0.42	27.51	18.23
	19.09	0.03	68.18	-0.08	44.39	44.67	44.79	45.07	44.76	0.42	44.85	31.41
	18.97	0.04	68.17	-0.07	62.81	63.42	63.78	64.11	63.61	0.42	63.68	51.18
	18.96	0.04	68.14	-0.04	73.19	73.96	75.05	75.48	74.55	0.42	74.60	76.45
	18.98	0.10	68.26	-0.16	82.65	82.42	84.13	84.49	83.49	0.42	83.65	101.70
	19.26	0.09	68.12	-0.02	93.20	93.18	95.52	96.12	94.62	0.42	94.64	132.41
	19.15	0.33	68.14	-0.04	103.98	104.00	106.40	107.48	105.59	0.42	105.63	156.53
	19.35	0.29	67.97	0.13	113.02	113.12	115.64	117.17	114.87	0.42	114.75	176.34
CHF												186.24
	19.07	0.04	88.55	-20.45	10.72	10.89	11.03	10.97	10.93	0.41	31.37	19.22
	19.02	0.03	88.35	-20.25	32.95	33.27	33.44	33.62	33.36	0.41	53.61	34.63
	19.05	0.03	88.14	-20.04	55.71	56.18	56.37	56.75	56.31	0.41	76.35	52.22
	19.09	0.04	87.90	-19.80	67.32	67.91	68.54	69.14	68.32	0.41	88.11	74.21
	19.10	0.03	88.19	-20.09	76.10	76.79	77.90	78.84	77.53	0.41	97.62	98.36
	18.90	0.00	88.13	-20.03	85.38	85.37	87.31	86.33	86.19	0.41	106.23	125.82
	19.18	0.08	88.04	-19.94	94.79	94.55	97.41	97.50	96.18	0.41	116.13	153.26
	19.04	0.04	88.47	-20.37	103.55	103.34	106.96	107.38	105.47	0.41	125.84	180.68
	19.07	0.20	88.39	-20.29	115.51	115.62	118.67	120.21	117.66	0.41	137.96	201.53
CHF												222.38
	19.09	0.03	108.55	-40.55	-6.64	-6.43	-6.36	-6.61	-6.49	0.40	34.07	15.90
	18.90	0.03	108.14	-40.14	16.88	17.22	17.39	17.51	17.29	0.40	57.43	32.41
	19.02	0.02	108.47	-40.47	41.37	41.89	42.09	42.34	41.98	0.40	82.46	48.92
	18.89	0.02	107.01	-39.01	65.49	66.16	66.36	66.77	66.27	0.40	105.28	66.51
	18.85	0.04	107.77	-39.77	72.23	72.97	73.31	74.06	73.23	0.40	113.00	85.19
	18.93	0.04	106.55	-38.55	78.31	78.22	79.67	78.23	78.67	0.40	117.22	108.23
	18.90	0.05	106.29	-38.29	83.50	83.72	85.13	83.71	84.11	0.40	122.40	130.21
	18.91	0.03	106.52	-38.52	92.04	92.36	94.28	95.22	93.60	0.40	132.12	159.82
CHF	18.97	0.04	107.84	-39.84	100.42	100.33	103.80	104.34	102.38	0.40	142.22	187.25
	19.18	0.04	107.15	-39.15	107.54	107.54	111.53	112.09	109.87	0.40	149.02	208.09
	19.22	0.08	107.63	-39.63	113.77	113.71	118.03	119.09	116.36	0.40	155.99	226.80
	19.03	0.16	107.12	-39.12	122.93	122.95	127.14	128.33	125.55	0.40	164.67	245.46
												254.80

Table B.1 Continued.

	PSIA	PSID	Tsub	Tin	T1	T2	T3	T4	Tsurf	Velocity	Delta T	Flux
	19.05	0.17	48.29	18.87	30.65	30.71	30.74	30.87	30.10	0.85	11.23	10.14
	19.08	0.22	48.17	18.86	41.35	41.51	41.64	41.66	40.25	0.85	21.38	20.58
	19.08	0.14	48.14	18.94	52.65	52.92	53.15	53.11	50.97	0.85	32.03	31.83
	19.08	0.17	48.05	18.91	63.01	63.42	63.78	63.77	60.82	0.85	41.91	42.80
	19.11	0.11	48.03	19.00	68.21	68.64	69.27	69.31	65.47	0.85	46.47	54.32
	19.13	0.15	48.17	18.97	74.23	74.75	75.70	75.78	70.75	0.85	51.77	69.97
	19.02	0.15	48.10	18.87	79.41	80.16	81.15	81.89	75.24	0.85	56.37	86.73
	19.03	0.15	48.12	18.88	84.15	84.51	85.71	85.80	78.73	0.85	59.85	100.45
	19.10	0.16	48.00	18.94	89.27	89.55	91.26	91.10	82.98	0.85	64.04	116.35
	19.13	0.14	48.11	18.99	93.56	93.72	96.07	96.07	86.52	0.85	67.53	132.78
	19.00	0.09	47.99	18.91	97.58	97.63	100.64	100.79	89.86	0.85	70.95	148.13
	18.98	0.20	48.22	18.78	101.11	101.13	104.58	104.80	92.79	0.85	74.01	161.30
	19.20	0.22	48.07	18.98	103.88	103.87	107.67	108.13	95.15	0.85	76.17	171.16
	19.20	0.14	48.14	19.06	106.07	106.04	110.18	110.61	97.08	0.85	78.03	177.77
	19.35	0.23	48.28	19.12	109.38	109.27	113.80	114.24	99.78	0.85	80.66	189.80
	19.12	0.02	48.02	19.10	114.76	114.53	119.09	119.07	104.32	0.85	85.22	199.71
CHF												204.67
	18.99	0.10	68.37	-0.07	8.50	8.60	8.65	8.74	8.31	0.83	8.38	5.14
	19.06	0.08	68.20	0.10	17.08	17.31	17.41	17.54	16.47	0.83	16.37	13.93
	19.05	0.10	68.26	0.04	27.91	28.33	28.45	28.61	26.80	0.83	26.76	24.64
	19.08	0.08	68.24	0.06	37.04	37.56	37.76	37.91	35.48	0.83	35.41	33.69
	19.17	0.09	68.32	-0.02	44.96	45.56	45.80	45.99	43.04	0.83	43.06	40.82
	19.15	0.10	68.39	-0.09	53.66	54.10	54.36	54.64	51.12	0.83	51.21	49.04
	19.16	0.09	68.41	-0.11	60.91	61.35	61.60	61.94	57.64	0.83	57.75	60.57
	19.14	0.10	68.41	-0.11	65.91	66.30	66.62	67.06	61.82	0.83	61.93	73.78
	18.97	0.09	68.41	-0.11	71.04	71.38	71.89	72.52	65.99	0.83	66.10	90.52
	19.10	0.11	68.25	0.05	77.03	77.38	78.10	79.01	71.14	0.83	71.09	106.75
	19.11	0.12	68.18	0.12	80.68	81.05	81.96	82.94	74.24	0.83	74.11	117.55
	19.08	0.10	68.31	-0.01	85.33	85.65	86.70	87.93	78.00	0.83	78.01	133.00
	19.12	0.09	68.31	-0.01	90.74	90.89	92.42	93.84	82.16	0.83	82.17	155.25
	19.29	0.10	68.27	0.03	97.43	97.27	100.03	101.30	87.44	0.83	87.41	183.20
	19.22	0.11	68.31	-0.01	101.39	101.15	104.55	105.88	90.62	0.83	90.63	200.00
	19.19	0.13	68.33	-0.03	105.99	105.65	109.84	110.88	94.33	0.83	94.36	218.40
	19.49	0.11	68.17	0.13	112.27	111.29	116.38	117.54	99.53	0.83	99.40	235.00
CHF												243.30
	19.07	0.07	88.40	-20.20	-3.42	-3.28	-3.30	-3.10	-3.98	0.81	16.22	11.23
	19.01	0.08	88.26	-20.06	6.71	6.99	6.94	7.18	5.65	0.81	25.71	20.84
	18.96	0.05	88.27	-20.07	19.26	19.63	19.67	20.01	17.61	0.81	37.68	32.36
	18.94	0.07	88.33	-20.13	30.19	30.67	30.72	31.18	28.01	0.81	48.14	42.78
	19.12	0.06	88.30	-20.10	42.77	43.37	43.50	44.03	40.00	0.81	60.10	54.58
	19.04	0.08	88.27	-20.07	55.75	56.42	56.68	57.26	52.34	0.81	72.41	66.92
	19.04	0.08	88.21	-20.01	63.55	64.28	64.51	65.25	59.53	0.81	79.54	77.66

Table B.1 Continued.

	PSIA	PSID	Tsub	Tin	T1	T2	T3	T4	Tsurf	Velocity	Delta T	Flux
	19.05	0.17	48.29	18.87	30.65	30.71	30.74	30.87	30.10	0.85	11.23	10.14
	19.08	0.22	48.17	18.86	41.35	41.51	41.64	41.66	40.25	0.85	21.38	20.58
	19.08	0.14	48.14	18.94	52.65	52.92	53.15	53.11	50.97	0.85	32.03	31.83
	19.08	0.17	48.05	18.91	63.01	63.42	63.78	63.77	60.82	0.85	41.91	42.80
	19.11	0.11	48.03	19.00	68.21	68.64	69.27	69.31	65.47	0.85	46.47	54.32
	19.13	0.15	48.17	18.97	74.23	74.75	75.70	75.78	70.75	0.85	51.77	69.97
	19.02	0.15	48.10	18.87	79.41	80.16	81.15	81.89	75.24	0.85	56.37	86.73
	19.03	0.15	48.12	18.88	84.15	84.51	85.71	85.80	78.73	0.85	59.85	100.45
	19.10	0.16	48.00	18.94	89.27	89.55	91.26	91.10	82.98	0.85	64.04	116.35
	19.13	0.14	48.11	18.99	93.56	93.72	96.07	96.07	86.52	0.85	67.53	132.78
	19.00	0.09	47.99	18.91	97.58	97.63	100.64	100.79	89.86	0.85	70.95	148.13
	18.98	0.20	48.22	18.78	101.11	101.13	104.58	104.80	92.79	0.85	74.01	161.30
	19.20	0.22	48.07	18.98	103.88	103.87	107.67	108.13	95.15	0.85	76.17	171.16
	19.20	0.14	48.14	19.06	106.07	106.04	110.18	110.61	97.08	0.85	78.03	177.77
	19.35	0.23	48.28	19.12	109.38	109.27	113.80	114.24	99.78	0.85	80.66	189.80
	19.12	0.02	48.02	19.10	114.76	114.53	119.09	119.07	104.32	0.85	85.22	199.71
CHF											204.67	
	18.99	0.10	68.37	-0.07	8.50	8.60	8.65	8.74	8.31	0.83	8.38	5.14
	19.06	0.08	68.20	0.10	17.08	17.31	17.41	17.54	16.47	0.83	16.37	13.93
	19.05	0.10	68.26	0.04	27.91	28.33	28.45	28.61	26.80	0.83	26.76	24.64
	19.08	0.08	68.24	0.06	37.04	37.56	37.76	37.91	35.48	0.83	35.41	33.69
	19.17	0.09	68.32	-0.02	44.96	45.56	45.80	45.99	43.04	0.83	43.06	40.82
	19.15	0.10	68.39	-0.09	53.66	54.10	54.36	54.64	51.12	0.83	51.21	49.04
	19.16	0.09	68.41	-0.11	60.91	61.35	61.60	61.94	57.64	0.83	57.75	60.57
	19.14	0.10	68.41	-0.11	65.91	66.30	66.62	67.06	61.82	0.83	61.93	73.78
	18.97	0.09	68.41	-0.11	71.04	71.38	71.89	72.52	65.99	0.83	66.10	90.52
	19.10	0.11	68.25	0.05	77.03	77.38	78.10	79.01	71.14	0.83	71.09	106.75
	19.11	0.12	68.18	0.12	80.68	81.05	81.96	82.94	74.24	0.83	74.11	117.55
	19.08	0.10	68.31	-0.01	85.33	85.65	86.70	87.93	78.00	0.83	78.01	133.00
	19.12	0.09	68.31	-0.01	90.74	90.89	92.42	93.84	82.16	0.83	82.17	155.25
	19.29	0.10	68.27	0.03	97.43	97.27	100.03	101.30	87.44	0.83	87.41	183.20
	19.22	0.11	68.31	-0.01	101.39	101.15	104.55	105.88	90.62	0.83	90.63	200.00
	19.19	0.13	68.33	-0.03	105.99	105.65	109.84	110.88	94.33	0.83	94.36	218.40
	19.49	0.11	68.17	0.13	112.27	111.29	116.38	117.54	99.53	0.83	99.40	235.00
CHF											243.30	
	19.07	0.07	88.40	-20.20	-3.42	-3.28	-3.30	-3.10	-3.98	0.81	16.22	11.23
	19.01	0.08	88.26	-20.06	6.71	6.99	6.94	7.18	5.65	0.81	25.71	20.84
	18.96	0.05	88.27	-20.07	19.26	19.63	19.67	20.01	17.61	0.81	37.68	32.36
	18.94	0.07	88.33	-20.13	30.19	30.67	30.72	31.18	28.01	0.81	48.14	42.78
	19.12	0.06	88.30	-20.10	42.77	43.37	43.50	44.03	40.00	0.81	60.10	54.58
	19.04	0.08	88.27	-20.07	55.75	56.42	56.68	57.26	52.34	0.81	72.41	66.92
	19.04	0.08	88.21	-20.01	63.55	64.28	64.51	65.25	59.53	0.81	79.54	77.66

Table B.1 Continued.

	PSIA	PSID	Tsub	Tin	T1	T2	T3	T4	Tsurf	Velocity	Delta T	Flux
	19.02	0.06	88.30	-20.10	67.80	68.48	69.02	69.92	62.91	0.81	83.01	93.85
	19.01	0.08	88.27	-20.07	73.29	73.93	74.73	76.06	67.40	0.81	87.47	112.95
	19.08	0.08	88.30	-20.10	78.33	79.09	80.12	81.68	71.67	0.81	91.77	129.42
	19.06	0.06	88.24	-20.04	84.38	85.13	86.58	88.56	76.72	0.81	96.77	150.25
	19.04	0.07	88.18	-19.98	89.22	89.99	91.69	94.05	80.69	0.81	100.67	167.81
	19.08	0.06	88.16	-19.96	93.27	94.09	96.28	98.78	84.04	0.81	103.99	184.26
	19.10	0.08	88.16	-19.96	96.67	97.60	100.27	102.75	86.81	0.81	106.77	199.61
	19.11	0.07	88.22	-20.02	100.56	101.34	104.65	107.09	89.86	0.81	109.88	216.11
	19.08	0.06	88.16	-19.96	105.61	106.43	110.35	113.07	94.02	0.81	113.98	236.93
	19.07	0.09	88.32	-20.12	110.25	111.12	115.69	118.29	97.91	0.81	118.03	254.49
	18.79	0.13	88.18	-19.98	113.25	114.21	119.19	121.66	100.55	0.81	120.53	264.39
	19.15	0.08	88.19	-19.99	115.13	116.40	120.92	124.22	102.08	0.81	122.08	273.18
	19.15	0.08	88.32	-20.12	117.71	119.02	123.40	126.97	104.20	0.81	124.32	280.89
	19.21	0.14	88.16	-19.96	124.37	125.71	130.93	134.15	109.99	0.81	129.96	300.72
CHF												310.64
	19.07	0.11	108.08	-39.98	-15.16	-15.06	-15.01	-14.79	-15.97	0.79	24.01	15.31
	19.08	0.12	108.11	-40.01	-3.60	-3.42	-3.28	-3.05	-4.94	0.79	35.07	25.47
	19.10	0.11	108.20	-40.10	8.16	8.36	8.64	8.87	6.27	0.79	46.36	35.61
	19.12	0.11	108.26	-40.16	18.98	19.29	19.61	19.89	16.57	0.79	56.73	45.76
	19.10	0.10	108.20	-40.10	35.16	35.59	36.00	36.35	31.97	0.79	72.07	60.58
	19.10	0.11	108.21	-40.11	51.50	52.01	52.54	52.95	47.46	0.79	87.58	76.25
	19.03	0.10	108.09	-39.99	62.74	63.26	63.90	64.29	58.10	0.79	98.09	86.67
	19.08	0.10	108.20	-40.10	69.13	69.59	70.18	70.71	63.38	0.79	103.48	103.35
	19.05	0.12	108.09	-39.99	73.49	73.75	74.68	75.50	66.48	0.79	106.46	124.60
	19.06	0.10	108.24	-40.14	77.90	78.07	79.30	80.33	70.10	0.79	110.23	139.18
	19.01	0.10	108.31	-40.21	82.57	82.72	84.12	85.38	73.85	0.79	114.06	155.60
	19.05	0.10	108.26	-40.16	86.72	86.82	88.49	89.97	77.18	0.79	117.34	170.97
	19.07	0.10	108.23	-40.13	90.62	90.68	92.54	94.32	80.32	0.79	120.45	185.22
	19.17	0.09	107.89	-39.79	94.12	94.16	96.20	98.21	83.05	0.79	122.84	199.49
	19.17	0.10	107.99	-39.89	98.18	98.10	100.81	102.66	86.28	0.79	126.17	215.99
	19.22	0.11	108.10	-40.00	101.99	101.76	105.13	106.90	89.39	0.79	129.39	230.28
	19.01	0.14	108.27	-40.17	105.05	104.89	108.50	110.65	91.76	0.79	131.93	245.62
	19.09	0.12	108.08	-39.98	107.85	107.82	111.53	114.02	94.25	0.79	134.23	254.39
	19.07	0.13	108.16	-40.06	111.41	111.40	115.49	118.16	97.10	0.79	137.16	269.79
	19.10	0.11	108.32	-40.22	114.36	114.23	118.90	121.34	99.44	0.79	139.66	281.86
	18.84	0.11	108.04	-39.94	118.97	118.87	123.93	126.53	103.20	0.79	143.14	299.52
CHF												308.35
	19.12	0.17	127.72	-59.92	-16.54	-16.32	-16.04	-22.37	-19.46	0.78	40.46	26.30
	19.01	0.18	127.47	-59.67	11.41	11.70	12.15	12.16	8.75	0.78	68.42	49.36
	18.94	0.16	127.89	-60.09	42.67	42.97	43.74	44.26	38.58	0.78	98.66	76.83
	19.02	0.16	127.65	-59.85	70.13	70.52	71.58	72.60	64.85	0.78	124.70	100.99

Table B.1 Continued.

	PSIA	PSID	Tsub	Tin	T1	T2	T3	T4	Tsurf	Velocity	Delta T	Flux
	19.04	0.15	127.77	-59.97	81.30	82.35	82.84	80.90	73.85	0.78	133.83	127.32
	18.94	0.14	127.73	-59.93	85.99	86.95	87.32	82.95	76.39	0.78	136.33	149.24
	18.95	0.16	127.96	-60.16	91.36	92.11	93.13	89.10	80.42	0.78	140.58	174.48
	19.00	0.16	128.24	-60.44	96.97	97.61	99.26	96.72	84.76	0.78	145.20	204.11
	19.04	0.17	127.75	-59.95	102.33	103.00	105.25	104.99	89.57	0.78	149.52	227.17
	18.92	0.15	127.87	-60.07	106.94	107.66	110.74	111.96	93.51	0.78	153.59	251.30
	18.89	0.16	127.77	-59.97	112.02	112.88	116.52	118.31	97.55	0.78	157.53	276.57
	18.82	0.24	127.68	-59.88	116.71	117.64	121.77	123.94	101.47	0.78	161.35	295.36
	20.10	1.18	48.03	19.77	27.15	27.20	27.34	27.51	26.56	2.54	6.79	11.78
	20.10	1.34	47.85	19.95	34.30	34.48	34.75	34.99	33.16	2.54	13.20	23.59
	20.15	1.35	47.89	19.91	41.29	41.55	41.88	42.24	39.52	2.54	19.61	35.39
	20.13	1.33	47.96	19.84	49.55	49.89	50.40	50.83	47.09	2.54	27.25	49.10
	20.11	1.32	48.18	19.62	59.92	60.32	61.23	61.65	56.59	2.54	36.97	66.95
	20.04	1.39	47.83	19.97	68.39	68.92	69.99	70.57	64.35	2.54	44.38	81.79
	20.12	1.35	47.91	19.89	76.17	76.83	78.00	78.80	71.39	2.54	51.50	96.88
	20.02	1.29	47.79	20.01	80.45	81.28	82.33	83.57	74.90	2.54	54.89	111.93
	20.04	1.17	47.84	19.96	84.95	85.95	87.28	88.71	78.62	2.54	58.67	129.50
	20.02	1.25	47.65	20.15	89.79	90.79	92.64	94.45	82.37	2.54	62.22	152.52
	20.04	1.21	48.05	19.75	95.20	94.97	97.68	99.67	85.93	2.54	66.17	173.40
	20.05	1.31	47.87	19.93	99.49	99.66	102.26	104.57	89.25	2.54	69.32	194.21
	20.03	1.35	47.70	20.10	103.66	104.16	106.91	109.49	92.37	2.54	72.27	217.32
	19.94	1.18	47.86	19.94	106.58	107.10	110.27	113.12	94.56	2.54	74.62	233.73
	20.01	1.25	47.82	19.98	109.78	110.37	113.95	117.02	97.05	2.54	77.06	250.22
	20.05	1.25	47.96	19.84	113.21	113.89	117.87	121.16	99.57	2.54	79.73	269.99
	20.11	1.24	47.88	19.92	114.91	115.58	119.99	123.00	100.94	2.54	81.02	277.67
	20.24	1.18	68.04	0.06	8.32	8.39	8.51	8.73	7.75	2.47	7.69	11.77
	20.24	1.18	68.19	-0.09	14.43	14.56	14.79	15.09	13.36	2.47	13.46	21.65
	20.20	1.19	68.06	0.04	21.02	21.24	21.51	21.97	19.43	2.47	19.39	32.08
	20.11	1.19	68.10	0.00	31.97	32.34	32.80	33.42	29.50	2.47	29.50	49.91
	20.14	1.17	68.34	-0.24	44.30	44.80	45.86	46.36	40.92	2.47	41.16	70.79
	20.14	1.17	68.36	-0.26	53.11	53.74	54.54	55.58	48.88	2.47	49.14	85.61
	20.13	1.18	68.17	-0.07	62.25	63.00	63.93	65.15	57.28	2.47	57.35	100.71
	20.08	1.17	68.04	0.06	70.51	71.50	72.32	73.97	64.72	2.47	64.66	117.37
	20.10	1.13	68.25	-0.15	76.59	77.60	78.54	80.40	69.89	2.47	70.03	133.84
	20.14	1.13	67.97	0.13	82.31	83.32	84.60	86.65	74.44	2.47	74.32	155.76
	20.10	1.15	67.92	0.18	88.11	89.20	90.75	93.26	79.04	2.47	78.86	179.88
	20.13	1.15	67.91	0.19	92.63	93.80	95.54	98.54	82.73	2.47	82.54	197.44
	20.14	1.15	68.15	-0.05	96.59	97.76	99.74	103.19	85.53	2.47	85.58	219.43
	20.13	1.18	68.00	0.10	101.04	102.31	104.63	108.45	88.95	2.47	88.85	241.37
	20.15	1.16	67.93	0.17	105.38	106.71	109.49	113.71	92.08	2.47	91.92	266.61
	20.29	1.19	68.08	0.02	110.07	111.44	114.82	119.47	95.62	2.47	95.60	291.97
	20.25	1.17	68.07	0.03	112.57	113.71	117.47	122.34	97.21	2.47	97.19	307.35
	20.20	1.18	87.87	-19.97	-6.96	-6.85	-6.66	-6.54	-7.78	2.45	12.19	16.43
	20.17	1.15	87.92	-20.02	1.64	1.83	2.09	2.41	0.12	2.45	20.14	29.88
	20.17	1.16	87.94	-20.04	12.72	13.04	13.45	14.05	10.38	2.45	30.41	46.88

Table B.1 Continued.

	PSIA	PSID	Tsub	Tin	T1	T2	T3	T4	Tsurf	Velocity	Delta T	Flux
	20.18	1.15	87.82	-19.92	22.98	23.46	23.99	24.80	19.89	2.45	39.82	62.52
	20.17	1.18	87.78	-19.88	32.71	33.31	34.01	35.00	28.84	2.45	48.73	78.47
	20.15	1.16	87.88	-19.98	41.84	42.58	43.41	44.54	37.27	2.45	57.25	93.02
	20.13	1.18	88.00	-20.10	50.63	51.52	52.48	53.80	45.39	2.45	65.49	107.41
	20.11	1.15	87.98	-20.08	59.54	60.56	61.66	63.16	53.62	2.45	73.71	121.69
	20.05	1.15	88.01	-20.11	70.38	71.55	72.84	74.55	63.55	2.45	83.66	140.34
	20.07	1.16	88.06	-20.16	77.46	78.80	79.94	82.11	69.76	2.45	89.92	156.80
	20.08	1.15	87.98	-20.08	82.53	83.87	85.11	87.53	73.76	2.45	93.84	175.43
	20.04	1.16	87.97	-20.07	87.19	88.53	90.04	92.85	77.34	2.45	97.41	196.28
	20.04	1.15	87.62	-19.72	91.74	93.14	94.84	98.04	81.02	2.45	100.74	213.87
	20.01	1.17	88.02	-20.12	95.80	97.47	99.83	103.07	84.28	2.45	104.40	235.80
	20.05	1.12	87.92	-20.02	100.75	101.45	104.44	107.27	87.39	2.45	107.41	255.54
	19.97	1.15	87.75	-19.85	104.13	104.69	107.97	111.10	89.83	2.45	109.69	272.02
	19.95	1.14	88.08	-20.18	109.22	109.79	113.78	117.21	93.50	2.45	113.67	301.78
	19.94	1.13	88.19	-20.29	112.63	113.22	117.67	121.38	96.06	2.45	116.35	320.43
	20.01	1.13	87.95	-20.05	115.41	116.23	120.83	124.81	98.27	2.45	118.32	334.70
	20.21	1.26	107.92	-40.02	-25.08	-24.96	-24.70	-25.12	-25.94	2.40	14.08	15.60
	20.16	1.25	107.96	-40.06	-13.81	-13.52	-13.16	-13.58	-15.54	2.40	24.52	32.34
	20.13	1.25	108.03	-40.13	-3.05	-2.60	-2.12	-2.07	-5.47	2.40	34.66	48.25
	20.12	1.25	107.80	-39.90	8.17	8.75	9.37	10.00	5.03	2.40	44.93	64.71
	20.21	1.25	108.02	-40.12	17.51	18.22	18.96	19.86	13.67	2.40	53.78	79.56
	20.24	1.22	108.03	-40.13	27.69	28.58	29.43	30.52	23.11	2.40	63.24	95.21
	20.19	1.23	107.91	-40.01	38.73	39.76	40.69	42.09	33.33	2.40	73.34	111.82
	20.16	1.22	108.09	-40.19	48.96	50.11	51.15	52.82	42.74	2.40	82.93	128.29
	20.18	1.22	108.16	-40.26	60.02	61.28	62.99	64.51	53.04	2.40	93.30	146.93
	20.13	1.21	107.82	-39.92	69.65	71.01	72.96	74.56	61.92	2.40	101.84	162.30
	20.15	1.20	107.81	-39.91	78.60	79.03	81.43	83.21	69.05	2.40	108.96	183.09
	20.12	1.21	107.76	-39.86	82.13	83.07	85.01	87.13	71.93	2.40	111.79	197.40
	20.16	1.22	107.99	-40.09	87.58	88.55	90.73	93.23	76.37	2.40	116.46	217.17
	20.05	1.20	108.08	-40.18	93.82	94.84	97.29	100.27	81.17	2.40	121.35	244.59
	20.04	1.20	108.07	-40.17	98.79	99.83	102.53	105.95	85.07	2.40	125.25	265.46
	20.13	1.18	108.00	-40.10	102.83	103.92	106.86	110.52	88.15	2.40	128.26	284.20
	20.04	1.18	108.10	-40.20	106.82	107.88	111.22	115.12	91.06	2.40	131.26	305.10
	20.03	1.20	107.88	-39.98	112.70	113.74	117.74	121.96	95.48	2.40	135.46	334.71
	21.60	1.84	49.17	20.03	28.16	28.28	28.40	28.68	27.40	3.42	7.37	15.89
	21.59	1.95	49.23	19.97	36.45	36.71	36.89	37.42	34.92	3.42	14.96	31.53
	21.53	1.90	49.10	20.10	44.29	44.68	44.92	45.70	42.00	3.42	21.91	46.89
	21.50	1.89	49.26	19.94	52.33	52.91	53.18	54.26	49.30	3.42	29.36	62.80
	21.49	1.89	49.10	20.10	59.71	60.38	61.01	62.03	56.02	3.42	35.92	77.38
	21.41	1.87	49.05	20.15	67.76	67.98	69.03	70.10	62.98	3.42	42.83	92.47
	21.39	1.85	49.27	19.93	78.48	78.89	79.99	76.95	71.51	3.42	51.58	114.03
	21.42	1.84	49.37	19.83	85.83	86.43	87.51	83.27	77.19	3.42	57.36	138.22
	21.41	1.81	49.16	20.04	91.91	92.56	93.91	92.22	82.45	3.42	62.40	164.55
	21.44	1.85	49.33	19.87	97.86	98.55	100.30	101.83	87.81	3.42	67.93	190.85
	21.43	1.86	49.12	20.08	102.80	103.51	105.65	108.27	91.66	3.42	71.59	216.11
	21.46	1.88	49.12	20.08	106.79	107.54	110.06	113.27	94.80	3.42	74.72	235.85

Table B.1 Continued.

	PSIA	PSID	Tsub	Tin	T1	T2	T3	T4	Tsurf	Velocity	Delta T	Flux
	21.48	1.83	49.28	19.92	111.62	112.42	115.49	119.05	98.13	3.42	78.22	266.59
	21.56	1.93	49.31	19.89	115.71	116.56	120.21	123.90	101.09	3.42	81.20	290.84
	21.38	1.93	68.36	0.22	9.47	9.61	9.76	9.98	8.71	3.30	8.49	15.89
	21.23	1.86	68.75	-0.17	16.93	17.20	17.42	17.90	15.49	3.30	15.67	29.89
	21.23	1.89	68.60	-0.02	28.14	28.60	28.90	29.67	25.67	3.30	25.69	50.45
	21.22	1.90	68.59	-0.01	39.47	40.09	40.51	41.62	35.92	3.30	35.93	71.90
	21.22	1.95	68.37	0.21	50.01	50.80	51.28	52.79	45.45	3.30	45.24	91.93
	21.22	1.90	68.71	-0.13	59.00	59.94	61.00	62.31	53.71	3.30	53.85	109.68
	21.21	1.93	68.66	-0.08	68.82	69.81	71.11	72.69	62.58	3.30	62.66	128.33
	21.22	1.93	68.51	0.07	78.49	79.57	81.01	83.02	71.18	3.30	71.12	149.17
	21.14	1.88	68.88	-0.30	84.33	84.27	86.28	87.09	74.81	3.30	75.11	168.92
	21.21	1.86	68.54	0.04	90.02	90.64	92.27	90.90	78.92	3.30	78.88	190.87
	21.19	1.89	68.86	-0.28	96.55	97.19	99.16	97.42	83.67	3.30	83.95	220.52
	21.17	1.91	68.77	-0.19	102.08	102.80	104.99	105.69	88.25	3.30	88.43	247.97
	21.17	1.91	68.51	0.07	106.54	107.32	109.88	112.74	92.03	3.30	91.96	270.98
	21.16	1.91	68.80	-0.22	112.03	112.89	115.94	120.09	96.21	3.30	96.43	301.86
	21.05	1.92	88.61	-19.91	-8.83	-8.68	-8.51	-9.05	-9.76	3.28	10.15	15.88
	21.11	1.89	88.68	-19.98	0.63	0.88	1.09	1.38	-1.05	3.28	18.93	32.63
	21.13	1.85	88.75	-20.05	10.42	10.82	11.15	11.85	7.93	3.28	27.98	49.91
	21.20	1.89	88.80	-20.10	22.49	23.10	23.56	24.63	18.99	3.28	39.10	71.07
	21.19	1.85	88.83	-20.13	34.04	34.88	35.48	36.85	29.53	3.28	49.66	92.48
	21.23	1.91	88.74	-20.04	44.42	45.49	46.08	47.90	38.97	3.28	59.01	111.88
	21.19	1.88	88.67	-19.97	55.59	56.83	57.52	59.73	49.11	3.28	69.08	132.75
	21.19	1.91	88.87	-20.17	63.83	65.15	65.95	68.47	56.57	3.28	76.74	148.07
	21.21	1.88	88.74	-20.04	74.09	75.50	76.97	79.34	65.91	3.28	85.95	168.92
	21.21	1.86	88.80	-20.10	81.35	82.86	84.41	86.94	72.15	3.28	92.25	187.55
	21.13	1.87	88.65	-19.95	88.03	88.24	90.65	90.64	75.95	3.28	95.90	212.83
	21.18	1.82	88.83	-20.13	93.72	94.55	96.54	94.82	80.47	3.28	100.60	235.86
	21.16	1.83	88.72	-20.02	99.63	100.55	102.83	100.31	84.93	3.28	104.96	262.20
	21.20	1.87	88.81	-20.11	105.27	106.28	108.77	107.03	89.00	3.28	109.11	289.77
	21.20	1.87	88.88	-20.18	108.28	109.32	112.07	109.76	91.20	3.28	111.38	305.15
	21.35	1.97	108.82	-40.02	-24.02	-23.78	-23.61	-27.23	-25.96	3.19	14.06	20.83
	21.31	1.97	108.80	-40.00	-10.86	-10.51	-10.07	-14.67	-14.20	3.19	25.80	42.79
	21.32	1.97	108.76	-39.96	1.12	1.71	2.22	2.11	-2.12	3.19	37.84	62.55
	21.29	1.94	108.84	-40.04	11.56	12.12	13.04	14.10	7.62	3.19	47.66	81.23
	21.26	1.93	108.85	-40.05	23.27	23.82	25.00	26.39	18.29	3.19	58.34	100.98
	21.28	1.96	108.74	-39.94	35.84	36.53	37.98	39.69	29.81	3.19	69.75	122.93
	21.27	1.92	108.85	-40.05	46.75	48.17	48.97	51.24	39.86	3.19	79.91	142.69
	21.26	1.90	108.80	-40.00	57.92	58.70	60.33	63.06	49.80	3.19	89.80	162.40
	21.27	1.91	108.72	-39.92	68.52	70.72	72.80	73.77	59.84	3.19	99.76	183.25
	21.20	1.91	108.61	-39.81	80.97	81.30	83.91	83.40	69.24	3.19	109.05	210.70
	21.23	1.91	108.83	-40.03	87.38	87.67	90.58	89.00	74.31	3.19	114.34	233.74
	21.25	1.87	108.82	-40.02	94.63	95.71	98.17	95.07	80.10	3.19	120.11	263.36
	21.21	1.93	108.81	-40.01	100.71	101.82	104.60	98.14	84.76	3.19	124.76	288.73
	21.26	1.86	108.67	-39.87	105.47	106.59	109.64	101.49	88.34	3.19	128.21	309.60

Table B.1 Continued.

	PSIA	PSID	Tsub	Tin	T1	T2	T3	T4	Tsurf	Velocity	Delta T	Flux
27.86	4.24	55.89	19.91	30.69	30.85	31.02	31.39	29.39	5.15	9.48	25.81	
27.83	4.20	55.65	20.15	43.08	43.47	43.91	44.72	40.44	5.15	20.30	54.36	
27.86	4.19	56.03	19.77	52.32	52.92	53.42	54.72	48.31	5.15	28.53	76.37	
27.87	3.98	55.98	19.82	62.89	63.69	64.86	65.88	57.83	5.15	38.01	101.62	
27.86	4.17	56.14	19.66	74.42	74.22	76.32	73.04	67.37	5.15	47.71	127.93	
27.78	4.10	56.09	19.71	85.09	85.62	87.35	81.96	76.80	5.15	57.09	154.27	
27.79	4.03	55.83	19.97	95.33	96.01	97.77	91.21	85.33	5.15	65.35	183.86	
27.79	4.03	55.92	19.88	102.35	103.13	105.03	100.43	90.64	5.15	70.76	213.55	
27.83	4.04	55.87	19.93	109.24	110.04	112.35	113.45	95.71	5.15	75.78	246.47	
27.83	4.16	56.11	19.69	115.10	115.99	118.60	120.92	99.88	5.15	80.19	277.22	
27.29	3.92	75.04	0.31	12.87	13.13	13.38	11.29	11.58	5.00	11.27	26.30	
27.30	3.91	75.47	-0.12	24.42	24.86	25.29	26.00	21.65	5.00	21.78	53.73	
27.30	3.92	75.37	-0.02	34.68	35.29	35.89	37.03	30.77	5.00	30.79	75.76	
27.30	3.94	75.24	0.11	48.15	49.05	49.72	51.42	42.53	5.00	42.42	107.60	
27.31	3.96	75.12	0.23	60.29	61.37	62.82	64.45	53.56	5.00	53.34	134.46	
27.32	3.96	75.42	-0.07	74.25	74.10	76.61	75.20	65.12	5.00	65.20	165.24	
27.26	3.94	75.29	0.06	86.31	87.10	89.16	84.65	75.95	5.00	75.89	193.69	
27.26	3.90	75.71	-0.36	95.57	96.56	98.58	93.63	83.49	5.00	83.85	223.35	
27.33	3.93	75.43	-0.08	103.38	104.35	106.66	102.15	89.38	5.00	89.45	256.27	
27.30	3.92	75.24	0.11	111.21	112.36	114.95	112.27	95.30	5.00	95.19	291.53	
26.76	3.76	94.74	-20.10	-6.51	-6.32	-6.05	-6.85	-7.80	4.90	12.31	25.44	
26.68	3.84	94.58	-19.94	8.69	9.19	9.60	10.04	5.74	4.90	25.68	57.31	
26.66	3.81	94.63	-19.99	21.76	22.49	23.11	24.38	17.33	4.90	37.32	85.87	
26.67	3.89	94.76	-20.12	36.69	37.70	38.58	40.39	30.71	4.90	50.83	116.59	
26.56	3.77	94.57	-19.93	50.92	52.25	53.12	55.67	43.14	4.90	63.07	149.50	
26.56	3.76	94.43	-19.79	64.01	66.74	68.93	69.92	56.08	4.90	75.86	182.42	
26.65	3.87	94.46	-19.82	81.64	81.47	84.79	82.68	69.72	4.90	89.54	216.46	
26.55	3.81	94.55	-19.91	96.27	97.52	99.71	97.67	82.32	4.90	102.23	258.14	
26.62	3.87	94.59	-19.95	105.46	106.99	109.27	105.94	89.38	4.90	109.33	296.70	
26.56	3.94	114.66	-40.29	-24.35	-24.13	-23.80	-29.06	-25.64	4.80	14.65	26.40	
26.56	3.94	114.25	-39.88	-7.46	-6.89	-6.51	-10.00	-10.49	4.80	29.39	59.37	
26.54	3.90	114.17	-39.80	5.38	6.19	6.80	7.92	1.02	4.80	40.82	85.74	
26.52	3.88	114.13	-39.76	22.35	23.50	24.35	26.25	16.21	4.80	55.97	120.84	
26.53	3.85	114.66	-40.29	38.87	40.32	41.44	44.01	30.92	4.80	71.21	155.99	
26.52	3.84	114.52	-40.15	54.18	55.98	56.96	60.57	44.32	4.80	84.47	189.96	
26.56	3.90	114.50	-40.13	72.53	73.03	75.87	76.49	60.17	4.80	100.30	228.40	
26.53	3.81	114.81	-40.44	89.55	91.09	93.42	92.98	75.31	4.80	115.75	267.91	
26.58	3.86	114.23	-39.86	101.09	103.11	105.34	103.72	84.85	4.80	124.71	305.38	
39.26	7.96	65.83	19.90	29.79	29.97	30.26	30.53	28.35	7.28	8.45	27.90	
38.97	7.74	65.84	19.89	40.86	41.25	41.77	42.67	37.86	7.28	17.97	57.59	
39.03	7.77	65.96	19.77	51.35	51.96	52.62	54.05	46.75	7.28	26.98	87.25	
38.92	7.62	66.10	19.63	62.37	63.81	65.34	65.82	56.96	7.28	37.33	119.08	
38.95	7.63	65.69	20.04	74.35	73.98	76.50	74.31	66.15	7.28	46.11	147.60	
38.95	7.73	65.76	19.97	88.66	89.42	91.40	87.18	78.44	7.28	58.47	190.38	

Table B.1 Continued.

	PSIA	PSID	Tsub	Tin	T1	T2	T3	T4	Tsurf	Velocity	Delta T	Flux
	39.04	7.79	66.01	19.72	101.75	102.74	105.00	101.96	89.46	7.28	69.74	228.85
	38.96	7.79	65.95	19.78	113.44	114.94	117.12	115.41	98.99	7.28	79.21	269.42
	37.28	7.22	85.16	-0.24	10.01	10.26	11.09	6.67	9.06	7.14	9.31	25.71
	37.66	7.40	85.04	-0.12	22.12	22.59	23.04	23.14	19.08	7.14	19.20	58.67
	37.75	7.33	84.86	0.06	32.87	33.53	34.19	35.55	28.72	7.14	28.67	86.13
	37.79	7.47	85.06	-0.14	45.56	46.56	47.48	49.38	39.84	7.14	39.99	120.16
	37.71	7.43	84.89	0.03	58.44	59.65	60.51	63.78	50.93	7.14	50.90	156.50
	37.25	7.12	85.05	-0.13	73.80	75.05	77.31	80.52	64.46	7.14	64.59	198.21
	37.29	7.13	85.42	-0.50	89.27	88.57	92.39	94.83	76.39	7.14	76.89	238.81
	37.26	7.08	84.57	0.35	113.26	114.33	117.24	120.18	96.94	7.14	96.60	311.39
	37.17	7.05	104.99	-20.17	-5.94	-5.68	-5.39	-7.40	-7.67	6.90	12.50	33.60
	37.56	7.08	105.00	-20.18	6.72	7.16	7.74	8.76	3.24	6.90	23.42	66.46
	37.56	7.14	104.85	-20.03	21.92	22.51	23.65	25.37	16.38	6.90	36.42	106.03
	37.44	7.16	105.17	-20.35	38.18	38.96	40.62	43.06	30.55	6.90	50.90	146.61
	37.38	7.13	104.98	-20.16	54.33	56.20	57.60	60.87	44.79	6.90	64.95	189.42
	38.02	7.46	104.82	-20.00	71.67	73.12	76.32	79.86	59.93	6.90	79.93	234.44
	38.03	7.31	104.46	-19.64	87.12	87.08	90.78	94.34	72.12	6.90	91.76	270.70
	38.28	7.40	104.62	-19.80	103.12	104.43	107.45	111.56	86.06	6.90	105.86	315.84
	37.13	7.18	124.10	-39.93	-23.83	-23.58	-23.30	-24.49	-25.56	6.80	14.37	33.38
	37.12	7.15	123.96	-39.79	-8.21	-7.65	-7.22	-6.82	-11.94	6.80	27.85	70.74
	36.88	7.00	124.10	-39.93	10.78	11.77	12.58	14.84	4.73	6.80	44.65	116.89
	36.87	6.98	124.14	-39.97	28.36	29.77	30.94	34.04	20.24	6.80	60.21	158.61
	36.89	7.02	124.33	-40.16	45.79	47.67	48.93	52.99	35.36	6.80	75.52	202.49
	36.98	7.02	124.45	-40.28	65.05	67.27	69.82	74.02	52.51	6.80	92.80	251.93
	36.95	7.02	124.61	-40.44	87.20	86.77	91.24	94.21	70.08	6.80	110.52	305.89

Table B.2 Single-phase and two-phase experimental data for equal-size-jet pattern.

	PSIA	PSID	Tsub	Tin	T1	T2	T3	T4	Tsurf	Velocity	Delta T	Flux
	19.54	0.70	48.20	19.88	33.20	N/A	33.23	33.17	32.20	0.95	12.32	16.06
	19.54	0.71	48.20	19.88	50.22	N/A	50.31	50.02	47.98	0.95	28.09	35.84
	19.52	0.68	48.23	19.86	65.65	N/A	65.84	65.48	62.14	0.95	42.29	56.72
	19.57	0.71	47.97	20.11	77.84	N/A	78.12	78.09	72.76	0.95	52.65	84.19
	19.41	0.66	48.14	19.94	88.81	N/A	89.22	90.21	82.01	0.95	62.06	117.12
	19.59	0.76	47.91	20.18	96.98	N/A	97.71	99.61	88.74	0.95	68.56	146.76
	19.63	0.75	48.14	19.95	101.27	N/A	102.52	105.18	92.30	0.95	72.35	166.51
	19.73	0.82	48.02	20.07	105.44	N/A	107.71	111.09	95.95	0.95	75.89	188.47
	20.31	0.80	48.19	19.89	109.07	N/A	112.01	116.05	99.01	0.95	79.11	204.96
CHF												213.21
	18.97	0.91	68.22	-0.23	25.41	25.72	25.78	N/A	23.68	0.92	23.91	32.95
	18.89	0.67	68.14	-0.14	50.37	49.96	51.53	N/A	46.98	0.92	47.12	63.68
	19.03	0.58	68.01	-0.02	71.56	71.47	73.62	N/A	66.34	0.92	66.36	92.27
	18.98	0.53	68.25	-0.25	80.04	79.53	82.35	N/A	72.96	0.92	73.22	119.67
	18.90	0.50	68.17	-0.18	87.40	86.79	90.44	N/A	78.56	0.92	78.74	150.39
	18.93	0.47	67.98	0.01	94.79	94.05	98.62	N/A	84.05	0.92	84.04	183.31
	18.93	0.45	67.98	0.01	100.98	99.94	105.57	N/A	88.67	0.92	88.65	209.67
	19.03	0.45	67.79	0.20	110.32	108.95	115.46	N/A	96.01	0.92	95.81	241.53
CHF												257.46
	19.59	0.56	88.46	-20.36	-1.26	N/A	-1.24	-1.12	-2.20	0.92	18.16	16.01
	19.51	0.56	88.53	-20.43	12.88	N/A	12.95	13.07	10.97	0.92	31.40	32.52
	19.54	0.58	88.25	-20.15	29.54	N/A	29.63	29.72	26.54	0.92	46.69	50.10
	19.52	0.60	88.29	-20.19	46.95	N/A	47.11	47.04	42.73	0.92	62.93	69.85
	19.58	0.72	88.35	-20.25	63.70	N/A	64.03	63.51	58.07	0.92	78.31	91.76
	19.59	0.75	88.12	-20.02	71.56	N/A	71.82	71.32	64.74	0.92	84.77	110.46
	19.59	0.80	88.02	-19.92	81.17	N/A	80.50	80.55	72.35	0.92	92.27	136.83
	19.78	0.90	88.15	-20.05	89.15	N/A	91.82	93.24	80.52	0.92	100.56	169.85
	19.85	0.95	88.02	-19.92	97.35	N/A	100.07	102.55	87.22	0.92	107.14	199.46
	20.49	0.98	88.28	-20.18	105.47	N/A	108.96	112.20	94.04	0.92	114.22	230.21
	20.97	1.01	88.17	-20.07	113.83	N/A	117.59	122.09	101.03	0.92	121.10	260.94
CHF												276.30
	19.70	0.85	107.74	-40.01	16.15	15.87	16.66	N/A	12.52	0.90	52.52	62.57
	19.55	0.71	107.73	-39.99	52.15	51.38	54.35	N/A	46.26	0.90	86.25	104.31
	19.39	0.59	107.55	-39.81	77.52	76.44	80.62	N/A	68.53	0.90	108.34	149.30
	19.30	0.56	107.80	-40.07	86.36	85.17	90.32	N/A	75.03	0.90	115.09	189.89
	19.42	0.53	107.86	-40.12	95.34	93.83	100.05	N/A	81.59	0.90	121.71	229.44
	19.31	0.49	107.58	-39.85	105.58	104.03	111.28	N/A	89.28	0.90	129.12	274.46
	19.25	0.50	107.57	-39.83	113.51	111.69	119.67	N/A	95.41	0.90	135.24	303.12
	19.17	0.45	107.38	-39.64	124.77	122.56	131.10	N/A	104.66	0.90	144.30	332.75
CHF												347.56
	34.42	15.17	48.35	19.70	29.16	N/A	29.32	29.65	28.11	2.89	8.41	20.42
	34.26	15.07	48.07	19.98	38.70	N/A	39.18	39.70	36.58	2.89	16.60	41.33
	34.06	14.89	48.10	19.95	49.48	N/A	50.30	51.11	46.05	2.89	26.10	66.58

Table B.2 Continued.

	PSIA	PSID	Tsub	Tin	T1	T2	T3	T4	Tsurf	Velocity	Delta T	Flux
	34.07	14.92	48.22	19.83	62.55	N/A	63.92	65.07	57.69	2.89	37.86	96.26
	34.89	15.71	48.11	19.94	75.99	N/A	77.76	79.20	69.39	2.89	49.45	129.18
	33.43	14.26	48.39	19.66	86.56	N/A	88.80	91.02	78.47	2.89	58.82	162.08
	33.63	14.35	48.29	19.76	95.38	N/A	98.16	101.61	85.77	2.89	66.01	197.19
	33.57	14.33	48.30	19.75	101.65	N/A	104.85	109.70	90.77	2.89	71.02	228.00
	33.55	14.36	48.35	19.70	109.28	N/A	113.02	119.33	96.55	2.89	76.85	268.56
	33.56	14.34	48.10	19.95	115.77	N/A	120.02	127.74	101.49	2.89	81.54	304.94
	24.83	5.98	67.74	0.03	16.23	15.90	16.80	N/A	14.10	2.80	14.07	34.04
	24.25	5.41	67.63	0.14	29.29	28.70	30.53	N/A	25.30	2.80	25.16	64.76
	23.56	4.73	67.84	-0.08	47.51	46.51	49.88	N/A	41.10	2.80	41.17	105.42
	23.02	4.23	67.88	-0.11	68.30	66.87	71.90	N/A	59.15	2.80	59.26	151.51
	22.73	3.87	67.80	-0.04	83.28	81.62	87.50	N/A	71.37	2.80	71.41	196.49
	22.51	3.71	67.81	-0.05	93.38	91.44	98.38	N/A	78.67	2.80	78.72	242.60
	22.34	3.54	67.77	0.00	99.81	97.81	105.62	N/A	82.83	2.80	82.84	282.15
	22.20	3.38	67.72	0.05	106.11	103.69	112.84	N/A	86.78	2.80	86.73	320.65
	21.97	3.23	67.93	-0.16	113.07	110.17	120.67	N/A	91.14	2.80	91.30	362.40
	21.92	3.12	67.84	-0.07	122.09	118.85	130.46	N/A	97.60	2.80	97.67	404.09
	21.91	3.13	67.51	0.25	135.43	131.66	144.33	N/A	108.49	2.80	108.23	441.39
CHF												480.88
	25.06	6.03	88.22	-20.16	11.63	10.92	12.89	N/A	7.87	2.74	28.04	63.65
	24.42	5.46	88.34	-20.28	30.83	29.66	33.25	N/A	24.63	2.74	44.91	106.50
	23.94	4.93	88.05	-19.99	50.05	48.49	53.81	N/A	42.82	2.74	62.81	145.97
	23.51	4.49	88.11	-20.05	69.92	68.08	74.45	N/A	58.29	2.74	78.34	192.07
	23.13	4.16	88.32	-20.26	84.75	82.76	89.73	N/A	70.36	2.74	90.61	237.09
	22.96	3.99	88.17	-20.11	94.85	92.47	100.31	N/A	77.65	2.74	97.75	281.03
	22.65	3.69	88.04	-19.98	110.51	107.02	117.38	N/A	87.51	2.74	107.48	371.15
	22.49	3.51	88.15	-20.09	126.05	121.34	135.23	N/A	97.55	2.74	117.65	460.01
	22.33	3.39	87.81	-19.75	133.84	128.69	143.78	N/A	102.87	2.74	122.61	499.53
	32.44	13.06	108.50	-39.94	-22.64	N/A	-22.14	-21.65	-23.94	2.60	16.00	28.10
	31.47	11.99	108.57	-40.01	-7.73	N/A	-6.76	-6.16	-10.59	2.60	29.43	57.74
	30.57	11.32	108.57	-40.01	6.31	N/A	7.71	8.53	2.07	2.60	42.08	85.20
	30.65	11.42	108.76	-40.20	22.95	N/A	24.78	26.16	16.92	2.60	57.12	120.34
	30.66	11.23	108.50	-39.94	39.88	N/A	42.16	43.91	32.00	2.60	71.93	155.42
	30.85	11.43	108.72	-40.16	55.42	N/A	58.16	60.29	45.87	2.60	86.02	188.38
	30.95	11.56	108.53	-39.97	71.00	N/A	74.24	76.76	59.67	2.60	99.64	223.52
	31.05	11.67	108.54	-39.98	84.00	N/A	87.56	91.34	70.92	2.60	110.90	260.85
	30.96	11.57	108.79	-40.23	97.11	N/A	101.41	106.98	82.14	2.60	122.37	308.17
	39.93	18.41	52.50	-19.91	27.37	N/A	27.65	28.25	26.42	4.70	46.33	20.49
	39.62	18.18	52.89	-19.52	36.31	N/A	36.99	38.16	34.25	4.70	53.77	44.71
	38.85	17.47	52.31	-20.10	48.17	N/A	49.31	51.10	44.57	4.70	64.67	76.54
	37.52	16.20	52.61	-19.80	58.79	N/A	60.06	62.98	53.84	4.70	73.64	105.09
	36.56	15.14	52.51	-19.90	72.36	N/A	74.04	78.07	65.65	4.70	85.54	142.39
	36.19	14.82	52.80	-19.61	82.94	N/A	85.05	90.05	74.79	4.70	94.41	173.11
	35.55	14.19	52.37	-20.04	95.41	N/A	97.82	104.70	85.10	4.70	105.15	219.23

Table B.2 Continued.

	PSIA	PSID	Tsub	Tin	T1	T2	T3	T4	Tsurf	Velocity	Delta T	Flux
35.02	13.64	52.58	-19.83	104.90	N/A	107.87	116.14	92.78	4.70	112.60	260.90	
34.12	12.79	52.84	-19.57	112.60	N/A	115.75	125.71	98.61	4.70	118.18	300.61	
35.15	14.10	72.40	-0.10	23.17	22.43	24.53	N/A	20.25	4.72	20.36	63.62	
33.47	12.42	72.43	-0.13	39.03	37.99	41.68	N/A	33.55	4.72	33.68	107.58	
32.69	11.58	72.30	0.00	55.05	53.70	58.76	N/A	47.47	4.72	47.47	151.48	
31.82	10.69	72.46	-0.16	70.34	68.72	74.70	N/A	58.64	4.72	58.79	194.25	
30.70	9.56	72.49	-0.19	86.36	84.66	91.63	N/A	71.99	4.72	72.18	240.37	
0.23	-20.96	72.45	-0.15	97.46	94.63	103.33	N/A	79.94	4.72	80.09	284.39	
29.90	8.65	72.33	-0.03	106.28	102.97	112.82	N/A	85.83	4.72	85.86	330.51	
29.79	8.53	72.34	-0.04	114.33	110.31	121.39	N/A	90.50	4.72	90.54	381.02	
29.56	8.28	72.48	-0.18	120.78	116.24	128.32	N/A	94.77	4.72	94.96	413.93	
29.63	8.30	72.50	-0.20	128.42	123.45	136.70	N/A	99.39	4.72	99.59	462.21	
29.49	8.16	72.45	-0.15	135.41	129.91	144.33	N/A	103.62	4.72	103.77	505.01	
38.38	17.65	91.38	-19.94	-10.73	N/A	-9.42	-8.62	-11.50	4.43	8.43	23.82	
40.10	19.34	91.67	-20.23	2.76	N/A	3.53	5.18	0.29	4.43	20.52	54.55	
41.74	20.97	91.40	-19.96	17.98	N/A	19.17	21.69	13.78	4.43	33.74	90.81	
42.05	21.26	91.38	-19.94	33.31	N/A	34.83	38.28	27.27	4.43	47.21	128.09	
41.78	21.00	91.63	-20.19	47.05	N/A	49.08	53.35	39.11	4.43	59.30	167.62	
40.86	20.04	91.40	-19.96	61.97	N/A	64.49	69.64	52.09	4.43	72.04	207.11	
39.92	19.05	91.73	-20.29	79.77	N/A	81.39	89.05	66.69	4.43	86.99	256.52	
39.14	17.89	91.77	-20.33	94.63	N/A	97.17	105.45	79.75	4.43	100.08	302.72	
43.18	22.55	111.26	-40.16	-25.79	N/A	-25.27	-24.64	-27.09	4.35	13.07	29.23	
42.96	22.36	110.90	-39.80	-13.07	N/A	-11.90	-10.73	-15.78	4.35	24.02	61.06	
43.06	22.42	111.16	-40.06	2.88	N/A	4.63	7.18	-1.52	4.35	38.54	99.52	
43.05	22.43	110.89	-39.79	18.25	N/A	20.79	24.17	12.14	4.35	51.94	135.73	
43.42	22.82	110.81	-39.71	36.12	N/A	38.07	42.68	27.56	4.35	67.27	178.54	
43.00	22.42	111.00	-39.90	51.08	N/A	53.63	58.74	40.59	4.35	80.49	216.99	
42.34	21.53	111.06	-39.96	63.94	N/A	67.33	73.38	51.96	4.35	91.93	254.26	
40.65	19.85	111.59	-40.49	82.70	N/A	85.94	93.64	67.96	4.35	108.46	304.92	

Table B.3 Single-phase and two-phase experimental data for decreasing-jet pattern.

	PSIA	PSID	Tsub	Tin	T1	T2	T3	T4	Tsurf	Velocity	Delta T	Flux
	19.28	0.19	48.35	19.85	34.17	N/A	34.37	34.44	33.30	0.82	13.46	16.19
	19.08	0.17	48.31	19.89	51.50	N/A	51.95	51.94	49.56	0.82	29.67	35.97
	19.20	0.22	48.29	19.91	68.29	N/A	69.13	69.27	65.27	0.82	45.36	57.92
	19.15	0.24	48.19	20.01	75.55	N/A	76.44	77.30	71.49	0.82	51.48	78.80
	19.22	0.21	48.28	19.92	84.28	N/A	85.60	87.46	79.11	0.82	59.19	105.14
	19.25	0.19	48.23	19.97	92.55	N/A	94.38	97.53	86.12	0.82	66.15	135.87
	19.04	0.06	48.44	19.76	100.41	N/A	102.83	107.17	92.66	0.82	72.90	168.77
	19.27	0.32	48.42	19.78	108.61	N/A	111.66	117.10	99.63	0.82	79.85	199.50
CHF												214.86
	19.34	0.45	68.04	-0.01	30.37	30.14	31.13	N/A	28.48	0.81	28.50	33.98
	19.28	0.43	68.06	-0.04	54.67	54.22	56.24	N/A	51.27	0.81	51.31	61.42
	19.30	0.40	67.95	0.08	73.93	73.17	75.75	N/A	68.24	0.81	68.16	93.29
	19.20	0.38	68.00	0.02	82.84	81.67	85.09	N/A	75.14	0.81	75.12	123.99
	19.29	0.37	67.86	0.16	90.15	88.65	92.97	N/A	80.67	0.81	80.51	152.52
	19.26	0.35	68.07	-0.05	96.85	95.04	100.17	N/A	85.64	0.81	85.69	179.93
	19.34	0.33	67.88	0.15	103.44	101.30	107.50	N/A	90.42	0.81	90.27	209.57
	19.31	0.33	67.99	0.03	110.76	108.39	115.38	N/A	95.73	0.81	95.69	242.53
	19.29	0.28	67.95	0.07	119.33	116.80	124.26	N/A	102.58	0.81	102.51	269.97
CHF												301.92
	19.42	0.47	88.38	-20.28	14.12	13.84	14.45	N/A	11.94	0.80	32.22	33.97
	19.34	0.43	88.18	-20.08	38.91	38.33	40.19	N/A	35.15	0.80	55.23	61.40
	19.23	0.38	88.45	-20.35	65.82	64.87	67.84	N/A	60.02	0.80	80.37	94.36
	19.17	0.38	88.26	-20.16	74.76	73.54	77.03	N/A	67.25	0.80	87.41	120.67
	19.14	0.35	88.11	-20.01	82.54	80.97	85.38	N/A	73.02	0.80	93.04	152.50
	19.09	0.35	88.03	-19.93	89.34	87.49	92.71	N/A	78.12	0.80	98.05	179.91
	19.18	0.30	88.14	-20.04	96.53	94.40	100.44	N/A	83.34	0.80	103.38	211.74
	19.15	0.32	88.13	-20.03	104.37	101.94	108.75	N/A	89.10	0.80	109.13	244.68
	19.20	0.32	88.12	-20.02	111.14	108.30	116.01	N/A	94.02	0.80	114.03	273.23
	19.24	0.33	88.06	-19.96	118.20	115.17	123.58	N/A	99.33	0.80	119.29	301.89
	19.25	0.27	87.98	-19.88	125.63	122.36	131.69	N/A	104.92	0.80	124.80	332.62
	19.31	0.26	87.71	-19.61	134.54	131.15	141.17	N/A	112.15	0.80	131.75	361.17
CHF												386.41
	19.57	0.47	108.15	-40.25	25.54	25.03	26.98	N/A	21.73	0.78	61.98	63.54
	19.45	0.43	107.97	-40.07	51.62	50.82	53.97	N/A	46.07	0.78	86.14	93.23
	19.41	0.39	107.97	-40.07	72.79	71.76	75.52	N/A	65.31	0.78	105.38	123.93
	19.33	0.38	107.45	-39.55	78.95	77.65	81.62	N/A	69.66	0.78	109.21	150.26
	19.21	0.36	107.56	-39.66	87.86	86.09	91.27	N/A	76.08	0.78	115.74	189.74
	19.24	0.36	108.01	-40.11	97.40	95.21	101.51	N/A	83.13	0.78	123.24	229.31
	19.22	0.35	107.30	-39.40	106.51	103.89	111.30	N/A	89.75	0.78	129.15	268.80
	19.12	0.33	107.40	-39.50	114.48	111.41	119.76	N/A	95.36	0.78	134.86	305.17
	19.10	0.23	107.82	-39.92	121.79	118.49	127.80	N/A	100.70	0.78	140.63	338.10
	19.06	0.27	107.28	-39.38	129.67	126.32	136.32	N/A	106.61	0.78	145.99	372.14
	19.20	0.37	107.35	-39.45	139.02	135.36	146.38	N/A	113.95	0.78	153.40	405.09
												440.16

Table B.3 Continued.

	PSIA	PSID	Tsub	Tin	T1	T2	T3	T4	Tsurf	Velocity	Delta T	Flux
	20.94	2.04	48.19	19.96	N/A	32.60	32.60	33.09	31.12	2.48	11.16	23.77
	20.91	2.00	48.38	19.77	N/A	45.28	45.28	46.13	42.34	2.48	22.57	46.78
	20.93	2.01	48.19	19.96	N/A	56.71	56.71	57.91	52.49	2.48	32.53	67.65
	20.86	1.93	48.34	19.81	N/A	69.17	69.17	70.69	63.48	2.48	43.67	90.73
	20.76	1.85	48.28	19.87	N/A	82.81	82.81	84.92	75.49	2.48	55.62	119.28
	20.73	1.85	48.30	19.85	N/A	89.63	89.63	93.44	80.77	2.48	60.92	150.02
	20.63	1.77	48.31	19.84	N/A	97.66	97.66	102.54	86.84	2.48	67.00	181.80
	20.66	1.78	48.18	19.97	N/A	105.47	105.47	111.83	92.51	2.48	72.54	219.16
	20.72	1.70	48.29	19.86	N/A	111.52	111.52	119.11	96.78	2.48	76.92	249.89
	20.80	1.75	48.31	19.84	N/A	121.13	121.13	130.68	103.87	2.48	84.03	297.21
	22.56	3.73	68.43	-0.23	31.50	30.96	32.51	N/A	28.00	2.48	28.23	61.42
	22.25	3.45	68.46	-0.26	52.24	51.30	54.51	N/A	46.27	2.48	46.52	105.34
	21.81	3.10	68.43	-0.23	72.63	71.30	75.86	N/A	63.42	2.48	63.65	151.43
	21.58	2.81	68.24	-0.04	85.66	83.84	89.43	N/A	73.54	2.48	73.58	196.39
	21.44	2.63	68.33	-0.13	96.31	93.93	100.74	N/A	81.14	2.48	81.28	243.62
	21.27	2.49	68.37	-0.17	103.85	101.01	109.05	N/A	85.99	2.48	86.16	286.57
	21.21	2.38	68.48	-0.28	111.56	108.27	117.41	N/A	90.84	2.48	91.12	331.55
	21.10	2.33	68.36	-0.16	118.80	115.15	125.44	N/A	95.45	2.48	95.61	374.41
	21.08	2.27	68.30	-0.10	126.82	122.92	134.30	N/A	100.91	2.48	101.01	417.19
	21.08	2.24	68.36	-0.16	134.33	130.32	142.63	N/A	106.41	2.48	106.57	452.28
	21.10	2.25	68.31	-0.11	147.82	143.74	156.88	N/A	116.99	2.48	117.10	501.67
	22.30	3.47	88.52	-20.72	15.22	14.59	16.36	N/A	11.33	2.40	32.05	62.45
	22.06	3.23	88.10	-20.30	37.78	36.76	39.92	N/A	31.09	2.40	51.40	108.59
	21.78	3.02	87.94	-20.14	59.35	57.94	62.87	N/A	50.05	2.40	70.20	153.59
	21.56	2.80	88.00	-20.20	77.72	75.93	81.60	N/A	65.72	2.40	85.93	195.28
	21.42	2.67	87.76	-19.96	89.57	87.25	94.15	N/A	74.48	2.40	94.44	243.60
	21.27	2.54	88.19	-20.39	98.86	96.04	104.12	N/A	81.03	2.40	101.42	286.51
	21.22	2.39	88.25	-20.45	108.26	104.99	114.13	N/A	87.42	2.40	107.87	333.72
	21.11	2.31	88.16	-20.36	116.58	112.78	123.19	N/A	93.01	2.40	113.37	376.54
	21.11	2.28	87.80	-20.00	124.64	120.52	131.88	N/A	98.34	2.40	118.35	420.43
	21.04	2.24	88.29	-20.49	132.13	127.73	140.17	N/A	103.38	2.40	123.88	461.01
	21.00	2.20	88.07	-20.27	139.47	134.86	148.09	N/A	108.31	2.40	128.58	500.54
	21.52	2.70	108.12	-40.18	-18.52	N/A	-17.96	-17.89	-20.12	2.23	20.06	32.58
	21.52	2.77	108.27	-40.33	0.30	N/A	1.54	1.80	-2.93	2.23	37.40	66.60
	21.45	2.64	107.93	-39.99	21.21	N/A	22.98	24.83	16.47	2.23	56.46	102.86
	21.38	2.57	107.99	-40.05	40.67	N/A	42.92	45.33	34.23	2.23	74.28	137.96
	21.31	2.52	107.89	-39.95	58.33	N/A	61.20	64.14	50.44	2.23	90.40	169.79
	21.39	2.49	108.14	-40.20	76.95	N/A	80.12	84.09	67.26	2.23	107.46	204.89
	21.31	2.43	108.03	-40.09	88.28	N/A	91.71	97.13	76.69	2.23	116.78	246.64
	21.15	2.24	108.35	-40.41	102.06	N/A	106.07	113.52	88.01	2.23	128.42	300.56
	28.30	6.74	52.85	19.85	33.11	N/A	33.59	34.46	31.62	4.00	11.76	32.53
	28.10	6.48	52.67	20.03	45.81	N/A	46.79	48.35	42.99	4.00	22.96	62.20
	27.97	6.46	52.58	20.12	59.58	N/A	61.08	63.39	55.17	4.00	35.05	96.24

Table B.3 Continued.

PSIA	PSID	Tsub	Tin	T1	T2	T3	T4	Tsurf	Velocity	Delta T	Flux
27.72	6.21	52.88	19.82	73.86	N/A	75.63	79.30	67.80	4.00	47.98	131.33
27.47	5.93	52.90	19.80	87.92	N/A	90.23	94.76	80.03	4.00	60.23	170.84
27.20	5.68	53.22	19.48	97.09	N/A	99.96	105.25	87.60	4.00	68.13	205.96
26.93	5.41	53.04	19.66	108.08	N/A	111.61	118.67	96.52	4.00	76.87	253.17
26.45	4.93	52.83	19.87	116.55	N/A	120.47	129.12	103.09	4.00	83.23	295.01
29.40	7.03	74.26	-0.35	25.03	24.45	26.43	N/A	21.24	4.10	21.58	62.45
28.45	6.19	73.95	-0.04	43.60	42.62	46.06	N/A	37.39	4.10	37.43	108.55
28.06	5.80	73.60	0.32	59.74	58.30	63.17	N/A	51.16	4.10	50.85	149.16
27.65	5.40	73.72	0.19	76.41	74.70	80.71	N/A	64.72	4.10	64.53	193.02
27.15	4.91	74.00	-0.09	91.86	89.57	96.88	N/A	76.99	4.10	77.08	242.45
26.74	4.52	74.22	-0.30	102.05	99.28	107.63	N/A	84.41	4.10	84.72	285.37
26.52	4.28	74.01	-0.10	110.23	107.11	116.34	N/A	89.96	4.10	90.06	327.09
26.43	4.20	73.94	-0.02	118.78	115.18	125.54	N/A	95.57	4.10	95.59	373.22
26.32	4.09	74.18	-0.27	126.78	122.81	134.10	N/A	100.65	4.10	100.92	419.32
26.25	4.02	74.01	-0.10	133.71	129.55	141.77	N/A	105.23	4.10	105.32	458.81
26.25	4.04	74.03	-0.12	141.66	137.11	150.42	N/A	110.30	4.10	110.41	504.91
25.78	4.91	91.52	-20.01	-3.52	N/A	-3.15	-3.07	-5.34	3.85	14.67	34.73
28.32	7.50	91.54	-20.03	11.96	N/A	12.68	13.32	8.32	3.85	28.35	69.85
26.72	5.82	91.67	-20.16	27.99	N/A	29.62	32.23	23.17	3.85	43.33	106.11
25.20	4.31	91.46	-19.95	44.37	N/A	46.61	50.00	37.89	3.85	57.83	142.32
25.58	4.71	91.58	-20.07	60.57	N/A	63.95	68.62	52.45	3.85	72.51	182.92
26.77	6.13	91.58	-20.07	77.54	N/A	80.35	86.45	67.35	3.85	87.42	220.25
27.42	6.52	91.44	-19.93	91.85	N/A	94.90	102.36	79.70	3.85	99.63	260.84
26.66	5.74	91.70	-20.19	103.89	N/A	107.75	115.84	89.38	3.85	109.57	309.30
28.12	7.46	111.15	-39.74	-21.63	N/A	-21.48	-20.93	-23.50	3.73	16.24	35.80
28.04	7.26	111.37	-39.96	-5.24	N/A	-4.71	-3.46	-8.99	3.73	30.97	73.10
27.98	7.16	111.64	-40.23	11.97	N/A	13.57	14.72	6.56	3.73	46.79	109.36
27.76	6.93	111.45	-40.04	28.75	N/A	31.44	34.68	21.88	3.73	61.93	146.67
27.76	6.93	111.97	-40.56	43.05	N/A	46.18	50.24	34.92	3.73	75.47	179.62
27.62	6.75	111.43	-40.02	60.95	N/A	65.15	70.44	51.28	3.73	91.29	220.22
27.44	6.61	111.62	-40.21	79.86	N/A	83.66	90.75	68.00	3.73	108.20	264.14
27.25	6.43	111.47	-40.06	92.36	N/A	97.10	104.87	78.72	3.73	118.78	301.59

Table B.4 Single-phase and two-phase experimental data for increasing-jet pattern.

	PSIA	PSID	Tsub	Tin	T1	T2	T3	T4	Tsurf	Velocity	Delta T	Flux
	19.31	0.33	48.33	19.92	36.04	N/A	36.12	36.20	34.97	0.77	15.05	18.32
	19.35	0.32	48.22	20.03	51.83	N/A	52.02	52.03	49.80	0.77	29.77	34.79
	19.17	0.28	48.15	20.10	68.06	N/A	68.38	68.20	64.91	0.77	44.81	53.44
	19.13	0.31	48.30	19.95	77.13	N/A	77.77	78.64	72.89	0.77	52.94	78.73
	19.20	0.25	48.22	20.03	89.37	N/A	90.00	92.29	83.55	0.77	63.52	110.56
	19.18	0.11	48.36	19.89	97.32	N/A	98.45	101.65	90.17	0.77	70.28	141.30
	19.32	0.25	48.30	19.95	104.24	N/A	105.68	109.67	95.86	0.77	75.92	167.63
	19.30	0.23	48.30	19.95	116.64	N/A	117.68	122.40	106.53	0.77	86.58	195.03
CHF												208.73
	19.28	0.35	67.99	-0.06	19.56	N/A	19.63	19.80	18.40	0.76	18.46	20.42
	19.30	0.30	67.91	0.02	37.99	N/A	38.21	38.35	35.61	0.76	35.60	41.31
	19.34	0.29	68.24	-0.31	57.76	N/A	58.14	58.12	54.09	0.76	54.40	63.29
	19.28	0.28	68.06	-0.13	73.53	N/A	74.17	74.61	68.69	0.76	68.82	86.36
	19.22	0.27	68.15	-0.22	81.81	N/A	82.71	84.21	75.78	0.76	76.00	112.71
	19.23	0.34	68.13	-0.20	92.40	N/A	93.62	96.08	85.02	0.76	85.23	142.34
	19.23	0.28	68.04	-0.11	102.19	N/A	103.69	107.10	93.18	0.76	93.29	176.34
	19.22	0.35	67.95	-0.02	111.81	N/A	113.49	118.23	101.02	0.76	101.04	212.59
	19.18	0.34	68.26	-0.33	121.64	N/A	123.09	128.17	109.30	0.76	109.63	236.74
CHF												248.81
	19.34	0.41	88.21	-20.21	12.21	11.95	12.15	N/A	10.06	0.74	30.27	31.83
	19.27	0.37	88.31	-20.31	38.31	37.72	38.62	N/A	34.11	0.74	54.43	63.66
	19.20	0.34	88.13	-20.13	65.45	64.35	66.84	N/A	59.59	0.74	79.72	91.15
	19.22	0.28	88.21	-20.21	77.72	76.34	79.56	N/A	69.86	0.74	90.07	122.98
	19.06	0.27	88.17	-20.17	86.95	85.29	89.61	N/A	77.27	0.74	97.44	153.68
	19.25	0.26	88.11	-20.11	96.18	93.89	99.17	N/A	84.42	0.74	104.53	183.28
	19.14	0.22	88.01	-20.01	102.83	100.17	105.98	N/A	89.28	0.74	109.28	209.63
	19.24	0.24	88.01	-20.01	111.86	108.88	115.42	N/A	96.06	0.74	116.07	244.77
CHF												262.34
	19.18	0.44	108.11	-40.21	28.36	27.68	28.67	N/A	24.12	0.72	64.32	63.66
	19.25	0.35	107.80	-39.90	67.90	66.59	69.46	N/A	61.16	0.72	101.06	104.30
	19.23	0.31	108.08	-40.18	81.72	79.93	83.72	N/A	71.98	0.72	112.16	150.37
	19.10	0.27	107.64	-39.74	93.06	90.79	95.96	N/A	80.80	0.72	120.54	190.96
	19.15	0.23	107.37	-39.47	103.66	100.82	107.13	N/A	88.87	0.72	128.35	229.43
	18.98	0.24	107.80	-39.90	113.16	109.88	116.71	N/A	95.97	0.72	135.87	264.53
	19.20	0.21	107.15	-39.25	124.47	120.54	127.90	N/A	104.77	0.72	144.02	298.68
CHF												338.20
	22.37	3.48	48.50	19.80	31.33	N/A	31.46	31.90	30.27	2.31	10.47	21.59
	22.36	3.44	48.31	19.99	43.40	N/A	43.70	44.41	41.14	2.31	21.16	43.53
	22.23	3.32	48.34	19.96	55.70	N/A	56.13	57.13	52.23	2.31	32.27	65.49
	22.06	3.16	48.35	19.95	72.21	N/A	72.83	74.62	67.09	2.31	47.13	97.36
	21.88	2.95	48.38	19.92	82.65	N/A	83.63	86.28	76.09	2.31	56.16	126.98
	21.66	2.71	48.44	19.86	91.99	N/A	93.40	97.51	83.90	2.31	64.04	163.19
	21.47	2.52	48.42	19.88	100.02	N/A	102.07	107.46	90.40	2.31	70.52	200.49

Table B.4 Continued.

	PSIA	PSID	Tsub	Tin	T1	T2	T3	T4	Tsurf	Velocity	Delta T	Flux
	21.47	2.52	48.39	19.91	108.25	N/A	110.85	117.90	97.04	2.31	77.14	238.91
	21.17	2.07	48.55	19.75	115.69	N/A	118.76	127.30	103.00	2.31	83.25	274.04
	21.47	2.50	68.39	-0.13	33.40	32.73	34.44	N/A	29.44	2.31	29.57	63.64
	21.22	2.22	68.72	-0.46	55.10	53.96	57.19	N/A	48.67	2.31	49.14	105.41
	20.96	2.01	68.40	-0.14	77.62	75.79	80.08	N/A	68.06	2.31	68.20	149.29
	20.79	1.81	68.46	-0.20	89.39	87.15	92.64	N/A	76.90	2.31	77.11	196.46
	20.70	1.64	68.61	-0.35	98.67	95.97	102.50	N/A	83.30	2.31	83.65	241.50
	20.55	1.51	68.40	-0.14	106.96	103.81	111.52	N/A	88.89	2.31	89.03	284.40
	20.45	1.42	68.35	-0.09	114.50	110.87	119.60	N/A	93.80	2.31	93.88	325.03
	20.44	1.33	68.32	-0.06	122.02	117.95	127.92	N/A	98.72	2.31	98.78	366.77
	20.39	1.32	68.40	-0.14	131.27	126.68	137.59	N/A	105.15	2.31	105.29	409.55
	20.44	1.28	68.38	-0.12	146.11	140.92	151.52	N/A	116.93	2.31	117.06	449.05
CHF												468.80
	21.98	3.22	87.91	-20.18	15.34	14.58	15.94	N/A	11.25	2.24	31.43	63.65
	21.74	2.89	87.93	-20.20	36.51	35.22	37.88	N/A	29.79	2.24	49.99	106.49
	21.22	2.46	87.74	-20.01	61.48	59.41	64.37	N/A	51.87	2.24	71.88	150.35
	20.85	2.14	87.92	-20.19	79.26	77.06	82.39	N/A	66.83	2.24	87.02	195.36
	20.54	1.87	87.70	-19.97	91.73	88.90	95.69	N/A	76.54	2.24	96.52	238.19
	20.35	1.70	87.99	-20.26	101.20	97.97	105.84	N/A	83.05	2.24	103.31	285.49
	20.37	1.56	87.99	-20.26	109.89	106.22	115.31	N/A	88.92	2.24	109.18	330.51
	20.28	1.46	88.02	-20.29	117.35	113.22	123.46	N/A	93.88	2.24	114.16	370.05
	20.18	1.39	88.03	-20.30	126.49	121.78	133.26	N/A	99.82	2.24	120.12	419.46
	20.09	1.33	87.90	-20.17	135.93	130.65	143.03	N/A	106.25	2.24	126.42	464.39
	19.97	1.27	87.92	-20.19	150.18	144.22	156.23	N/A	117.36	2.24	137.54	503.95
	22.32	3.51	108.17	-40.06	-18.77	N/A	-18.77	-18.44	-20.52	2.10	19.54	30.38
	22.38	3.46	108.31	-40.20	-0.32	N/A	-0.03	1.21	-3.68	2.10	36.52	63.29
	22.42	3.45	108.09	-39.98	19.82	N/A	20.48	22.23	14.73	2.10	54.71	97.36
	22.43	3.48	108.06	-39.95	41.22	N/A	42.04	44.31	34.02	2.10	73.97	135.76
	22.37	3.38	108.40	-40.29	60.30	N/A	61.81	64.81	51.48	2.10	91.77	171.99
	22.33	3.35	108.21	-40.10	76.16	N/A	77.22	81.03	65.49	2.10	105.59	201.58
	22.33	3.35	108.28	-40.17	90.90	N/A	92.54	97.85	78.40	2.10	118.57	243.32
	22.15	3.16	107.99	-39.88	99.14	N/A	101.77	107.86	85.26	2.10	125.14	278.46
	22.00	3.05	108.18	-40.07	105.32	N/A	108.42	115.34	90.30	2.10	130.37	304.94
	31.71	9.93	52.96	20.02	32.49	N/A	32.71	33.41	30.92	3.73	10.90	30.32
	31.65	9.93	52.96	20.02	46.52	N/A	47.07	48.42	43.37	3.73	23.35	62.17
	31.58	9.86	53.16	19.82	59.10	N/A	59.95	61.90	54.48	3.73	34.65	91.83
	31.25	9.53	52.96	20.02	71.49	N/A	72.26	75.24	65.24	3.73	45.21	121.47
	30.75	9.07	53.10	19.88	85.07	N/A	86.30	89.94	77.07	3.73	57.18	157.68
	30.17	8.47	53.10	19.88	96.45	N/A	98.24	103.29	86.51	3.73	66.64	200.48
	29.32	7.60	53.22	19.76	107.20	N/A	109.40	116.07	95.07	3.73	75.31	246.62
	28.13	6.48	53.48	19.50	116.58	N/A	119.63	128.19	102.53	3.73	83.03	295.05
	27.50	6.34	72.80	-0.33	27.39	26.54	28.56	N/A	23.39	3.82	23.71	63.60
	26.85	5.67	72.89	-0.42	46.56	45.10	48.89	N/A	39.76	3.82	40.18	109.74

Table B.4 Continued.

	PSIA	PSID	Tsub	Tin	T1	T2	T3	T4	Tsurf	Velocity	Delta T	Flux
	26.49	5.21	72.45	0.02	64.03	62.04	66.68	N/A	54.32	3.82	54.30	151.44
	25.97	4.68	72.63	-0.16	82.51	80.19	85.49	N/A	69.97	3.82	70.14	195.34
	25.50	4.13	72.75	-0.28	95.55	92.79	99.34	N/A	80.07	3.82	80.35	242.55
	25.01	3.59	72.61	-0.14	113.82	110.33	121.45	N/A	93.47	3.82	93.61	332.70
	24.90	3.48	72.54	-0.07	121.93	118.06	127.99	N/A	98.09	3.82	98.15	377.73
	24.87	3.44	72.65	-0.18	130.02	125.72	136.83	N/A	103.36	3.82	103.54	422.72
	24.68	3.29	72.48	-0.01	137.12	132.56	144.53	N/A	108.17	3.82	108.18	460.00
	24.63	3.17	72.37	0.10	144.08	139.30	151.95	N/A	112.74	3.82	112.64	498.46
	29.74	8.71	93.18	-20.25	-4.68	N/A	-4.69	-3.66	-6.34	3.53	13.91	31.41
	30.14	9.10	93.17	-20.24	9.77	N/A	10.18	11.75	6.63	3.53	26.88	62.14
	30.40	9.37	93.16	-20.23	25.53	N/A	26.27	28.49	20.61	3.53	40.84	97.30
	30.72	9.64	93.04	-20.11	41.26	N/A	42.16	45.08	34.53	3.53	54.64	131.33
	30.89	9.77	93.19	-20.26	58.20	N/A	59.50	63.14	49.56	3.53	69.82	169.70
	31.08	9.98	92.93	-20.00	74.67	N/A	75.81	80.89	64.03	3.53	84.03	205.92
	30.84	9.72	93.02	-20.09	87.74	N/A	89.58	95.74	75.49	3.53	95.58	244.37
	30.12	9.00	93.17	-20.24	101.76	N/A	104.58	112.34	87.29	3.53	107.53	297.19
	30.68	9.68	111.76	-40.04	-22.26	N/A	-22.63	-22.25	-24.33	3.47	15.71	32.51
	30.69	9.69	111.88	-40.16	-6.95	N/A	-7.34	-6.20	-10.82	3.47	29.34	65.46
	30.58	9.58	111.94	-40.22	9.76	N/A	10.42	12.53	4.50	3.47	44.72	101.70
	30.60	9.58	112.00	-40.28	25.68	N/A	26.72	29.68	18.72	3.47	58.99	136.84
	30.58	9.55	111.87	-40.15	43.10	N/A	44.60	48.51	34.31	3.47	74.46	175.22
	30.50	9.48	111.69	-39.97	60.70	N/A	62.15	67.08	49.66	3.47	89.64	214.77
	30.48	9.41	111.69	-39.97	80.19	N/A	81.78	88.46	66.87	3.47	106.84	260.84
	30.33	9.24	111.51	-39.79	92.93	N/A	95.35	102.97	78.09	3.47	117.88	298.31

Table B.5 Critical heat flux data for equal-jet pattern.

	PSIA	PSID	Tsub	Tin	T1	T2	T3	T4	Tsurf	Velocity	Delta T	Flux
	22.29	1.35	52.14	19.64	34.30	33.02	33.29	N/A	32.36	1.12	12.72	20.86
	22.52	1.39	51.87	19.86	69.33	66.03	66.82	N/A	64.52	1.12	44.66	71.32
	22.38	1.39	51.88	19.83	83.29	78.15	78.93	N/A	76.41	1.12	56.58	98.79
	22.53	1.45	51.88	19.82	92.47	85.54	86.33	N/A	83.60	1.12	63.79	121.83
	22.55	1.36	51.82	19.85	104.50	94.61	95.68	N/A	92.30	1.12	72.46	156.93
	22.43	1.28	51.69	19.94	117.63	103.76	105.24	N/A	101.39	1.12	81.45	193.14
	22.50	1.40	51.52	20.09	126.57	109.93	111.72	N/A	107.43	1.12	87.33	219.53
	22.38	1.33	51.46	20.13	136.00	116.67	118.94	N/A	113.89	1.12	93.76	248.09
	22.56	1.54	51.40	20.17	147.17	124.66	127.16	N/A	121.62	1.12	101.45	276.61
CHF												290.87
	22.23	1.37	72.48	-0.60	15.70	15.60	15.80	N/A	14.62	1.10	15.22	21.72
	22.39	1.35	72.33	-0.48	32.80	33.00	33.30	N/A	30.65	1.10	31.13	48.10
	22.44	1.46	72.30	-0.47	49.70	49.60	50.40	N/A	46.39	1.10	46.86	72.27
	22.68	1.68	72.16	-0.35	67.00	66.70	67.86	N/A	62.39	1.10	62.74	97.60
	22.40	1.58	72.11	-0.32	81.70	81.30	82.50	N/A	75.64	1.10	75.96	125.02
	22.60	1.47	71.87	-0.11	90.10	89.60	91.00	N/A	82.52	1.10	82.62	155.77
	22.56	1.46	72.05	-0.32	99.80	99.00	100.80	N/A	90.13	1.10	90.45	197.48
	22.48	1.51	72.12	-0.43	108.60	107.80	110.20	N/A	98.03	1.10	98.46	242.51
CHF	22.51	1.46	72.25	-0.59	124.00	123.20	126.40	N/A	109.80	1.10	110.39	284.32
												305.22
	22.44	1.36	92.17	-20.46	-4.65	-4.03	-4.49	N/A	-5.40	1.06	15.06	19.51
	22.37	1.35	92.12	-20.43	14.79	15.63	15.22	N/A	12.79	1.06	33.22	47.01
	22.40	1.43	91.98	-20.31	32.66	33.36	33.39	N/A	29.37	1.06	49.69	73.36
	22.19	1.34	92.11	-20.45	49.60	49.30	50.40	N/A	44.95	1.06	65.41	95.42
	22.46	1.54	91.95	-20.31	66.10	65.90	67.10	N/A	60.34	1.06	80.65	122.50
	22.30	1.17	91.96	-20.36	82.60	82.60	84.10	N/A	75.33	1.06	95.69	157.99
	22.50	1.58	92.07	-20.50	94.40	94.20	96.20	N/A	85.22	1.06	105.72	197.51
	22.25	1.41	92.19	-20.66	105.90	105.30	107.60	N/A	93.67	1.06	114.33	243.62
	22.41	1.56	92.03	-20.53	117.20	116.70	119.70	N/A	103.01	1.06	123.54	287.70
	22.65	1.54	92.09	-20.62	131.00	130.80	134.20	N/A	115.43	1.06	136.05	321.75
												338.78
CHF												
	22.70	1.27	107.74	-41.09	-1.06	-1.08	-0.71	N/A	-3.32	1.02	37.77	48.14
	22.08	1.11	107.73	-40.34	31.45	30.95	32.40	N/A	27.05	1.02	67.39	94.34
	21.78	0.94	107.55	-40.32	70.42	69.98	71.48	N/A	63.24	1.02	103.56	156.89
	21.59	0.83	107.80	-39.89	88.30	87.84	89.46	N/A	77.79	1.02	117.68	234.86
	21.54	0.78	107.86	-39.89	99.89	99.10	101.22	N/A	86.83	1.02	126.72	292.09
	21.55	0.81	107.58	-39.92	108.51	107.28	110.25	N/A	93.75	1.02	133.67	331.62
	21.65	0.87	107.57	-39.87	117.02	115.52	119.36	N/A	100.79	1.02	140.66	366.78
	21.83	0.93	107.38	-39.23	132.02	129.32	132.78	N/A	110.27	1.02	149.50	404.11
CHF												422.78
	26.80	5.58	52.63	19.37	43.46	42.35	42.65	N/A	39.98	2.20	20.60	47.20
	26.90	5.78	52.41	19.59	68.05	66.41	67.06	N/A	61.49	2.20	41.90	94.44
	26.98	6.05	52.35	19.65	88.41	84.83	85.61	N/A	77.43	2.20	57.79	143.79

Table B.5 Continued.

	PSIA	PSID	Tsub	Tin	T1	T2	T3	T4	Tsurf	Velocity	Delta T	Flux
	27.15	6.15	52.43	19.57	106.40	99.36	100.10	N/A	89.75	2.20	70.18	193.17
	27.38	6.36	52.32	19.68	122.02	111.63	112.83	N/A	99.96	2.20	80.28	241.49
	27.64	6.53	52.27	19.73	138.28	123.75	125.58	N/A	110.25	2.20	90.52	289.63
	27.81	6.60	52.22	19.78	154.25	136.07	138.73	N/A	120.27	2.20	100.49	345.89
	27.83	6.77	52.08	19.92	167.13	145.92	148.98	N/A	126.73	2.20	106.81	387.63
	27.65	6.53	52.17	19.83	174.30	154.99	158.09	N/A	133.09	2.20	113.26	424.91
	27.80	6.72	52.21	19.79	178.01	168.80	171.72	N/A	142.35	2.20	122.56	464.39
CHF												484.13
	25.73	4.80	72.13	-0.24	26.83	23.36	23.85	N/A	21.51	2.12	21.76	45.01
	25.85	4.85	71.89	0.00	56.46	49.39	50.25	N/A	45.25	2.12	45.25	97.72
	25.87	4.87	72.14	-0.25	81.36	73.80	74.91	N/A	68.17	2.12	68.42	144.89
	26.30	5.18	71.54	0.35	101.47	90.29	91.34	N/A	82.73	2.12	82.39	194.27
	26.39	5.29	72.11	-0.22	117.66	102.27	103.41	N/A	93.34	2.12	93.56	242.61
	26.50	5.40	71.89	0.00	133.19	113.82	115.38	N/A	104.05	2.12	104.05	294.31
	26.60	5.46	72.10	-0.21	147.49	124.33	126.31	N/A	113.03	2.12	113.24	340.41
	26.64	5.61	71.81	0.08	164.84	137.26	139.92	N/A	120.96	2.12	120.88	393.12
	26.62	5.64	71.80	0.09	164.99	147.25	150.09	N/A	129.15	2.12	129.06	435.89
	27.02	5.90	71.73	0.16	165.18	155.40	158.28	N/A	134.34	2.12	134.18	467.70
	27.02	5.94	71.48	0.41	182.34	166.75	170.09	N/A	144.70	2.12	144.29	512.74
CHF												555.56
	24.20	3.18	91.64	-20.42	37.65	36.65	37.26	N/A	32.12	2.00	52.54	98.70
	24.70	3.75	91.56	-20.34	64.60	62.63	64.11	N/A	55.75	2.00	76.10	156.86
	24.85	4.07	91.39	-20.17	94.89	91.37	92.95	N/A	79.75	2.00	99.93	256.76
	24.98	4.27	91.55	-20.33	105.22	100.84	102.79	N/A	87.28	2.00	107.61	301.89
	25.01	4.33	90.93	-19.71	116.38	110.89	113.60	N/A	95.35	2.00	115.06	352.41
	24.89	4.17	91.61	-20.39	129.00	122.62	125.96	N/A	104.88	2.00	125.27	405.11
	25.10	4.36	91.51	-20.29	141.36	134.05	137.78	N/A	114.29	2.00	134.58	452.32
	25.05	4.37	91.49	-20.27	159.26	150.72	155.10	N/A	128.50	2.00	148.77	511.62
	25.15	4.35	91.46	-20.24	182.11	172.46	176.93	N/A	148.32	2.00	168.56	554.43
CHF												575.83
	24.20	3.18	112.06	-40.81	12.09	11.11	11.67	N/A	6.55	2.00	47.36	98.66
	24.70	3.75	111.99	-40.74	60.96	58.77	59.97	N/A	49.51	2.00	90.25	201.81
	24.85	4.07	111.65	-40.40	95.34	91.61	93.23	N/A	77.81	2.00	118.21	300.79
	24.98	4.27	111.59	-40.34	121.87	115.20	117.75	N/A	96.85	2.00	137.19	410.60
	25.01	4.33	111.59	-40.34	138.63	131.13	134.40	N/A	112.35	2.00	152.69	473.16
	24.89	4.17	111.62	-40.37	150.67	142.40	145.99	N/A	121.83	2.00	162.20	516.00
	25.10	4.36	111.50	-40.25	165.83	156.59	160.88	N/A	134.11	2.00	174.37	567.71
	25.05	4.37	111.71	-40.46	184.68	173.40	178.09	N/A	149.57	2.00	190.03	608.34
CHF												628.66
	31.87	10.95	52.15	19.56	41.24	39.38	39.72	N/A	37.51	3.10	17.95	47.22
	31.92	10.95	52.27	19.44	61.15	59.32	60.03	N/A	55.22	3.10	35.78	94.43
	31.92	10.89	52.13	19.58	81.42	79.44	80.18	N/A	72.81	3.10	53.23	144.89
	32.02	10.92	51.99	19.72	98.84	95.21	95.95	N/A	86.33	3.10	66.61	195.36
	32.00	10.96	52.08	19.63	112.92	107.70	108.75	N/A	96.77	3.10	77.14	244.78

Table B.5 Continued.

	PSIA	PSID	Tsub	Tin	T1	T2	T3	T4	Tsurf	Velocity	Delta T	Flux
	32.27	11.22	51.95	19.76	128.07	120.75	122.27	N/A	107.84	3.10	88.08	296.48
	32.48	11.33	51.76	19.95	141.54	132.41	134.94	N/A	117.90	3.10	97.95	344.77
	32.54	11.68	52.08	19.63	155.82	144.34	146.82	N/A	127.58	3.10	107.96	397.49
	32.39	11.59	51.80	19.91	161.88	153.91	156.96	N/A	134.33	3.10	114.42	444.65
	32.48	11.42	51.70	20.01	173.46	165.20	168.56	N/A	143.37	3.10	123.36	492.93
	32.18	11.08	51.75	19.96	186.21	176.61	180.74	N/A	152.74	3.10	132.78	545.65
	31.40	10.47	51.94	19.77	195.33	185.02	189.30	N/A	159.57	3.10	139.80	580.88
CHF												598.50
	29.72	8.85	72.16	-0.37	8.65	9.54	8.75	N/A	7.89	2.95	8.26	21.70
	30.04	9.14	72.18	-0.39	19.29	20.22	19.64	N/A	17.65	2.95	18.04	46.99
	30.24	9.39	71.97	-0.18	29.71	30.61	30.27	N/A	26.60	2.95	26.77	72.25
	30.62	9.81	71.92	-0.13	39.23	40.16	39.96	N/A	35.38	2.95	35.51	95.36
	31.55	10.66	71.95	-0.16	63.30	64.37	64.43	N/A	56.54	2.95	56.69	153.54
	31.93	11.07	72.04	-0.25	82.11	83.13	83.50	N/A	72.74	2.95	73.00	207.34
	32.12	11.29	72.04	-0.25	97.49	96.56	97.62	N/A	84.20	2.95	84.45	257.89
	31.84	10.97	71.84	-0.05	107.44	106.25	107.87	N/A	91.32	2.95	91.37	312.90
	31.30	10.38	72.02	-0.23	113.91	113.35	116.39	N/A	96.65	2.95	96.88	359.04
	30.86	9.92	72.04	-0.25	122.22	120.47	125.46	N/A	102.46	2.95	102.71	408.43
	30.89	9.71	71.98	-0.19	130.93	129.20	134.89	N/A	109.19	2.95	109.38	454.53
	30.98	9.90	71.97	-0.18	135.36	133.86	139.68	N/A	112.63	2.95	112.81	478.68
	27.80	6.65	72.17	-0.38	139.27	137.15	143.75	N/A	115.04	2.95	115.42	506.10
	27.85	6.62	71.91	-0.12	146.77	144.51	150.15	N/A	119.70	2.95	119.82	550.02
	27.92	6.58	72.27	-0.48	154.32	152.07	159.29	N/A	126.14	2.95	126.61	587.47
	28.10	6.70	72.24	-0.45	160.46	157.89	163.57	N/A	129.06	2.95	129.51	630.27
	28.01	6.53	72.18	-0.39	169.82	170.54	175.65	N/A	138.30	2.95	138.69	678.61
	28.14	6.93	73.20	-1.41	185.94	183.63	192.84	N/A	151.76	2.95	153.16	723.50
CHF												745.94
	25.09	3.97	91.40	-20.83	21.04	20.41	20.95	N/A	16.46	2.97	37.29	93.24
	28.09	7.15	91.30	-20.73	47.31	46.19	47.13	N/A	38.82	2.97	59.54	157.99
	28.18	7.23	91.24	-20.67	67.60	65.99	66.92	N/A	56.19	2.97	76.86	207.41
	28.28	7.34	91.14	-20.57	95.05	93.06	94.28	N/A	78.26	2.97	98.83	309.68
	30.73	11.68	91.02	-20.45	108.16	103.82	105.08	N/A	86.87	2.97	107.32	361.34
	29.97	9.16	91.03	-20.46	115.53	111.85	113.27	N/A	92.61	2.97	113.07	405.20
	31.12	10.72	91.24	-20.67	131.74	125.23	128.67	N/A	104.65	2.97	125.32	462.29
	30.80	10.78	91.08	-20.51	148.37	140.01	145.01	N/A	117.77	2.97	138.28	517.22
	29.45	9.15	91.04	-20.47	166.46	157.14	161.57	N/A	132.12	2.97	152.59	570.01
	29.54	8.78	90.99	-20.42	176.92	166.95	171.60	N/A	139.75	2.97	160.17	617.20
	29.40	9.20	91.27	-20.70	185.54	174.14	178.72	N/A	145.24	2.97	165.94	655.56
	27.88	8.10	91.40	-20.83	201.76	189.24	195.27	N/A	158.38	2.97	179.21	712.60
	28.07	8.57	91.15	-20.58	212.30	199.21	207.08	N/A	167.87	2.97	188.45	742.24
CHF												757.06
	49.71	28.50	52.55	19.69	37.38	36.00	36.39	N/A	34.27	4.90	14.58	46.09
	49.75	28.55	52.59	19.65	55.22	53.76	54.48	N/A	49.94	4.90	30.29	94.43
	49.98	28.74	52.85	19.39	73.61	71.24	72.53	N/A	65.51	4.90	46.12	146.00
	50.38	29.11	52.81	19.43	90.59	85.97	87.43	N/A	78.51	4.90	59.09	194.23

Table B.5 Continued.

	PSIA	PSID	Tsub	Tin	T1	T2	T3	T4	Tsurf	Velocity	Delta T	Flux
	50.20	28.93	52.68	19.56	110.70	99.75	101.38	N/A	92.28	4.90	72.72	240.38
	50.38	29.08	52.61	19.63	125.19	113.05	114.89	N/A	103.68	4.90	84.05	293.21
	50.38	29.08	52.70	19.54	139.26	125.22	127.29	N/A	111.63	4.90	92.09	341.50
	50.48	29.21	52.76	19.48	152.32	136.06	138.49	N/A	120.85	4.90	101.37	385.43
	52.00	30.73	52.55	19.69	166.16	146.56	149.70	N/A	129.91	4.90	110.21	433.69
	53.08	31.78	52.59	19.65	176.83	154.67	158.17	N/A	136.81	4.90	117.15	470.98
	53.00	31.70	52.60	19.64	181.56	164.39	168.23	N/A	143.29	4.90	123.65	518.23
	52.89	31.66	52.59	19.65	195.89	173.48	177.92	N/A	151.42	4.90	131.77	563.26
	50.82	29.42	52.69	19.55	200.01	188.60	194.71	N/A	160.97	4.90	141.42	645.71
	48.82	27.39	52.64	19.60	208.27	196.29	202.15	N/A	166.19	4.90	146.59	693.98
	47.40	26.03	52.49	19.75	216.19	203.72	209.37	N/A	171.65	4.90	151.90	732.35
	44.42	23.03	52.43	19.81	222.55	210.72	215.31	N/A	176.20	4.90	156.39	767.45
CHF												785.00
	42.20	20.86	72.77	-0.31	15.36	16.24	15.79	N/A	13.50	4.72	13.80	45.88
	43.24	21.98	72.76	-0.30	32.67	33.55	33.38	N/A	28.37	4.72	28.67	96.42
	44.54	72.83	72.83	-0.37	53.45	54.25	54.53	N/A	46.28	4.72	46.65	155.71
	46.54	25.32	73.09	-0.63	71.41	72.29	73.01	N/A	62.00	4.72	62.62	205.14
	47.45	25.52	72.32	0.14	86.46	87.33	88.46	N/A	74.50	4.72	74.36	258.97
	47.47	26.34	72.89	-0.43	97.98	98.38	100.44	N/A	83.58	4.72	84.01	308.52
	47.10	25.86	72.89	-0.43	108.65	107.13	111.58	N/A	91.44	4.72	91.87	356.85
	45.38	24.11	72.87	-0.41	114.77	115.29	118.18	N/A	95.61	4.72	96.02	411.76
	43.50	22.15	72.69	-0.23	121.95	122.35	125.81	N/A	100.56	4.72	100.80	458.97
	41.63	20.24	72.77	-0.31	131.17	129.24	135.29	N/A	106.70	4.72	107.01	508.38
	39.94	18.62	73.22	-0.76	139.17	137.31	143.75	N/A	112.31	4.72	113.08	559.99
	38.00	16.49	72.96	-0.50	147.78	145.84	153.74	N/A	118.73	4.72	119.23	616.09
	36.52	15.08	72.77	-0.31	155.78	154.08	161.40	N/A	124.61	4.72	124.91	655.64
	34.17	12.61	72.63	-0.17	162.66	160.25	169.25	N/A	129.07	4.72	129.24	708.28
	34.00	12.31	72.48	-0.02	171.46	169.28	178.41	N/A	136.05	4.72	136.06	748.88
	33.80	12.24	72.57	-0.11	176.65	174.71	184.38	N/A	140.35	4.72	140.46	775.23
	33.52	11.90	72.89	-0.43	186.32	185.26	195.09	N/A	148.68	4.72	149.11	816.94
CHF												837.79
	42.93	21.99	28.33	-20.65	21.86	20.32	21.25	N/A	15.83	4.71	36.48	103.06
	42.80	22.07	27.81	-20.13	58.26	55.37	57.58	N/A	46.75	4.71	66.87	201.81
	43.56	22.60	28.01	-20.33	89.41	85.09	87.25	N/A	71.56	4.71	91.90	302.97
	43.58	22.65	27.80	-20.12	116.06	110.16	112.48	N/A	91.76	4.71	111.88	406.18
	43.30	22.41	27.73	-20.05	140.68	133.24	136.09	N/A	109.92	4.71	129.97	513.76
	43.69	22.56	27.93	-20.25	162.96	153.94	157.32	N/A	126.38	4.71	146.63	608.30
	43.00	21.76	28.05	-20.37	188.67	176.91	181.42	N/A	145.13	4.71	165.50	712.59
	41.26	20.26	27.85	-20.17	201.44	188.27	194.22	N/A	154.75	4.71	174.92	766.39
	40.27	19.27	27.69	-20.01	212.03	198.00	205.87	N/A	162.92	4.71	182.93	819.08
	38.04	16.99	28.22	-20.54	219.45	206.24	213.60	N/A	167.99	4.71	188.53	873.02
CHF												899.99
	42.26	19.28	95.73	-20.62	5.35	5.07	5.79	N/A	1.63	5.70	22.25	72.20
	44.55	21.55	95.65	-20.54	33.40	32.76	34.70	N/A	25.74	5.70	46.29	158.96
	45.72	22.81	95.49	-20.38	56.37	55.14	57.98	N/A	45.04	5.70	65.42	230.38

Table B.5 Continued.

	PSIA	PSID	Tsub	Tin	T1	T2	T3	T4	Tsurf	Velocity	Delta T	Flux
	48.44	25.56	95.50	-20.39	78.96	77.86	80.45	N/A	63.79	5.70	84.18	305.20
	49.51	26.56	95.46	-20.35	98.95	97.17	101.87	N/A	80.42	5.70	100.78	380.98
	49.00	26.08	95.39	-20.28	114.24	112.07	117.49	N/A	92.01	5.70	112.29	454.51
	47.39	24.39	95.50	-20.39	130.22	128.57	134.47	N/A	104.50	5.70	124.89	535.80
	45.92	22.97	94.96	-19.85	144.10	141.68	149.00	N/A	114.65	5.70	134.50	610.58
	44.05	20.92	95.20	-20.09	156.59	153.73	161.97	N/A	123.55	5.70	143.64	683.06
	43.29	20.26	94.83	-19.72	165.03	162.67	171.11	N/A	129.80	5.70	149.52	735.73
	42.34	19.27	95.85	-20.74	173.81	171.65	180.51	N/A	136.54	5.70	157.28	782.95
	41.36	18.26	95.14	-20.03	181.39	180.44	188.47	N/A	142.48	5.70	162.51	825.76
	41.55	18.07	95.37	-20.26	187.77	185.52	195.61	N/A	146.72	5.70	166.99	867.64
	41.58	18.05	95.77	-20.66	197.46	190.51	199.25	N/A	150.40	5.70	171.07	898.35
	39.64	16.29	95.86	-20.75	201.64	200.32	209.98	N/A	157.38	5.70	178.13	940.79
	39.34	15.99	96.30	-21.19	209.69	207.77	214.79	N/A	162.12	5.70	183.31	970.43
	39.70	16.17	95.61	-20.50	211.85	214.83	221.46	N/A	167.11	5.70	187.61	987.96
	39.70	16.25	95.61	-20.50	218.95	214.73	228.61	N/A	170.61	5.70	191.12	1016.49
	39.51	15.99	95.63	-20.52	227.31	226.65	231.02	N/A	175.67	5.70	196.19	1043.94
	39.57	15.15	96.13	-21.02	230.04	225.44	240.34	N/A	179.28	5.70	200.30	1068.09
CHF												1080.16
	53.00	27.84	98.90	-20.88	12.04	12.86	N/A	N/A	7.59	6.50	28.47	95.23
	53.29	28.17	98.86	-20.84	47.01	49.35	N/A	N/A	37.71	6.50	58.55	205.03
	54.10	29.28	98.85	-20.83	78.03	80.73	N/A	N/A	63.80	6.50	84.63	305.10
	55.03	30.51	98.67	-20.65	108.96	112.96	N/A	N/A	90.17	6.50	110.82	407.24
	56.82	32.34	98.73	-20.71	134.41	139.14	N/A	N/A	110.49	6.50	131.20	514.84
	57.18	32.61	98.85	-20.83	153.71	159.37	N/A	N/A	125.20	6.50	146.03	613.75
	56.17	31.28	98.61	-20.59	171.55	177.56	N/A	N/A	138.28	6.50	158.88	710.39
	55.29	29.91	98.63	-20.61	190.56	195.87	N/A	N/A	151.45	6.50	172.06	817.96
	54.17	28.32	98.65	-20.63	206.70	216.01	N/A	N/A	164.67	6.50	185.29	914.37
	52.63	26.79	99.09	-21.07	216.66	226.55	N/A	N/A	172.01	6.50	193.08	971.45
	51.76	25.53	98.97	-20.95	228.10	238.66	N/A	N/A	180.54	6.50	201.48	1035.07
	51.11	24.94	99.18	-21.16	239.70	250.76	N/A	N/A	190.20	6.50	211.36	1077.87
	49.38	23.11	98.81	-20.79	245.72	256.52	N/A	N/A	193.56	6.50	214.36	1127.35